Modelling of Diffusional Phenomena in Structural Alloys for High Temperature Applications



Yilun Gong

Department of Materials

University of Oxford

This dissertation is submitted for the degree of

Doctor of Philosophy

St Anne's College

October 2017

I would like to dedicate this thesis to my loving parents.

Declaration

I hereby declare that except where specific reference is made to the work of others, the contents of this dissertation are original and have not been submitted in whole or in part for consideration for any other degree or qualification in this, or any other university. This dissertation is my own work and contains nothing which is the outcome of work done in collaboration with others, except as specified in the text and Acknowledgements.

Yilun Gong

October 2017

Publications

Y. Gong, H. Larsson, R. Naraghi, J. Ågren and R.C. Reed. 'On the selective oxidation in Ni-Cr System'. *Acta Materialia*, in progress.

X. Zhang, B. Grabowski, F. Körmann, A.V. Ruban, **Y. Gong**, R.C. Reed, T. Hickel and J. Neugebauer. 'Temperature dependence of the stacking-fault Gibbs energy for Al, Cu, and Ni'. *Physical Review B*, in progress.

Y. Gong, B. Grabowski, A. Glensk, F. Körmann, J. Neugebauer and R.C. Reed. 'Temperature dependence of the Gibbs energy of vacancy formation of fcc Ni'. *Physical Review B*, **97**, 214106, (2018).

P.A.J. Bagot, A. Radecka, A.P. Magyar, **Y. Gong**, D.C. Bell, G.D.W. Smith, M.P. Moody, D. Dye and D. Rugg. 'The effect of oxidation on the subsurface microstructure of a Ti-6Al-4V alloy'. *Scripta Materialia*, **148**, 24–28, (2018).

Y. Gong, D.J. Young, P. Kontis, Y.L. Chiu, H. Larsson, A. Shin, J.M. Pearson, M.P. Moody and R.C. Reed. 'On the breakaway oxidation of Fe9Cr1Mo steel in high pressure CO_2'. *Acta Materialia*, **130**, 361–374, (2017).

H. Larsson, T. Jonsson, R. Naraghi, **Y. Gong**, R.C. Reed and J. Ågren. 'Oxidation of iron at 600 °C–experiments and simulations'. *Materials and Corrosion*, **68**, 133–142 (2017).

P. Kontis, S. Pedrazzini, **Y. Gong**, P.A.J. Bagot, M.P. Moody and R.C. Reed. 'The effect of boron on oxide scale formation in a new polycrystalline superalloy'. *Scripta Materialia*, **127**, 156–159, (2017).

Acknowledgements

First I would like to thank my supervisor Prof. Roger Reed who gave huge support to my research; he gave me big pictures at high levels and encouraged me to work with the best people in different areas; his drivenness and devotion changed me significantly. I also would like to thank Dr. Nils Warnken who first introduced me into the diffusion/phase transformation world during my undergraduate study at the University of Birmingham; his meticulousness influenced me tremendously.

Also I would like to thank all the help from our group members including Dr. Fauzan Adziman, Dr. David Crudden, Dr. Jianglin Huang, Dr. Paraskevas Kontis, Dr. Enrique Alabort Martinez, Dr. Hang Wang, Dr. Zailing Zhu, Daniel Barba Cancho, Koji Kageyama, André Németh, Sabin Sulzer, Yuanbo Tang, and Karen Bamford for her well-organising.

I would like to thank all my collaborators and partners in 9Cr EDF project including Dr. Aya Shin, Dr. Jonathan Pearson and Eleanor Laney from EDF Energy, Prof. David Young from New South Wales University, Dr. Sumner Joy and Dr. Nigel Simms from Cranfield University, Dr. Peter Robinson from Quintessa, Prof. Hugh Evans, Dr. Yu-Lung Chiu, and Dr. Mary Taylor from the University of Birmingham, Dr. Mudith Karunaratne, Dr. Xinjie Yan and Dr. Rebecca Higginson from the Loughborough University, Prof. Gordon Tatlock from the University of Liverpool, Dr. Fran Jones from Frazer-Nash Consultancy, Dr. Fabien Rouillard from the French Alternative Energies and Atomic Energy Commission (CEA), Dr. Yang Liu and Dr. Peter Deem from Amec Foster Wheeler, Prof. David Knowles from Atkins and the University of Bristol. Special thanks should give to Prof. Young

who taught me a lot on high temperature corrosion; he is an excellent teacher, mentor and collaborator.

I also would like to thank nice people I have been working with at KTH and Thermo-Calc in Sweden, including Dr. Henrik Larsson, Dr. Lars Höglund, Prof. John Ågren, Reza Naraghi, Prof. Malin Selleby, Prof. Mats Hillert, Dr. Lina Kjellqvist and Prof. Bo Sundman (now at CEA). Special thanks should give to Henrik who taught me every details of DICTRA simulations with huge patience.

I also would like to thank smart people at MPIE, Germany including Dr. Blazej Grabowski, Dr. Albert Glensk, Dr. Fritz Körmann, Prof. Jörg Neugebauer and Prof. Dierk Raabe, particularly Blazej who led me to his fascinating research/coding world and taught me with great patience.

I would like to thank excellent people I have been working with during my internship stay at NIMS, Japan, including Dr. Rudder Wu, Dr. Hiroshi Harada, Keiko Suzuta and Dr. Hong Gao, particularly Rudder who not only helped me on experiments, but also let me enjoy the Japanese culture.

I would like to thank great people I have been working with in Oxford, including but not limited to Prof. Michael Moody, Dr. Paul Bagot, Dr. Andrew London and Dr. Brian Setiadinata from the atom probe group, Gabriella Chapman and Greg Cook from EM Group (for saving me so many times from emergent EM sessions), Prof. Chris Grovenor and Dr. Kexue Li from Nano-SIMS group.

I also would like to thank Dr. Bruce Pint from the Oak Ridge National Laboratory (ORNL) who offered me different possibilities. He is a nice and knowledgeable person.

I also would like to thank all my dear friends, specially my roommate Dr. Zuliang Hong who gave a huge support during my thesis writing-ups.

Last but most importantly, Chinese Scholarship Council (CSC) and EDF Energy UK are greatly acknowledged for support of fundings.

Abstract

This thesis is concerned with the physical metallurgy/corrosion of high temperature structural alloys, of the type used for some of the most demanding engineering applications yet devised by mankind. Both iron-based steels and nickel-based superalloys are used for such applications; the common thread in this thesis from the science perspective is the role played by defects such as vacancies which lead to degradation due to diffusional phenomena such as oxidation and creep. Modelling for typical diffusional behaviour is carried out at various length scales in this work.

First, the vacancy formation free energy in fcc-nickel is calculated by using highly-accurate *ab initio* thermodynamics including relevant temperature effects such as phonon vibrations and magnetisms. Predictions show good agreement with experiments, with non-Arrhenius behaviour due to the anharmonicity suggested by calculations.

Second, the oxidation kinetics is predicted for the Ni-Cr-O system by coupling CALPHAD thermodynamics and diffusional kinetics. A general (oxidation) diffusion model coupled with the homogenisation model is applied, allowing the treatment of metal, oxide and metal/oxide interface to be unified. Predicted oxidation kinetics considering oxide phases (halite, corundum and spinel) and metallic phases (fcc and bcc) show reasonable agreement with experiments. Proposed quantification of entropy-production potentially allows the long-debated question concerning the rate-controlling steps (phases) in high temperature corrosion process to be answered.

Last, the failure (breakaway oxidation) mechanisms of a critical Fe9Cr1Mo nuclear component exposed to CO_2 are studied by high-resolution characterisations. Based upon

theories of carbon diffusion in ferrite and Boudouard surface reaction, the temperature-dependent lifetime – linked with carbon saturation in metal – is rationalised at accelerated conditions and is extrapolated to service conditions.

Table of contents

List of figures **xiii**

List of tables **xvii**

Nomenclature **xix**

1 Introduction and Motivation for Research **1**

1.1 Importance of Metallic Alloys for Structural High Temperature Applications 1

1.2 Metallic Alloys for High Temperature Structural Applications 4

1.2.1 Nuclear Power Reactors 4

1.2.2 Aero-engine 5

1.2.3 Industrial Gas Turbines 7

1.3 The Phenomenology of Diffusion 7

1.4 Role of Modelling 9

1.5 Scope of Proposed Research 9

2 Literature Survey **12**

2.1 Numerical Modelling Approaches for Diffusional Reactions 12

2.1.1 CALPHAD 12

2.1.2 Density Functional Theory 15

2.1.3 *Ab initio* Thermodynamics 18

2.2 Importance of Diffusion 25

2.2.1 Fick's Laws . . . 25
2.2.2 Diffusion in Multi-component System . . . 26
2.2.3 Diffusion in Oxides . . . 28
2.2.4 Diffusion-controlled Phase Transformation . . . 35
2.2.5 Solving Phenomenological Diffusion Equation(s) . . . 38

3 On the Prediction of Vacancy Formation Energy in fcc-Nickel 43

3.1 Introduction . . . 43
3.2 Background . . . 45
3.3 Computational Methodology . . . 48
3.3.1 General Free Energy Approach . . . 48
3.3.2 Total Energy, Electronic and Quasiharmonic Contribution . . . 51
3.3.3 Coupling of Electrons with Vibrations . . . 54
3.3.4 Magnetic Excitations . . . 55
3.4 Results and Discussions . . . 56
3.4.1 On the Influence of Excitation Mechanisms on Vacancy Formation Free Energy . . . 56
3.4.2 On the Temperature Dependence of Vacancy Formation Entropy . 57
3.4.3 Magnetism . . . 59
3.5 Summary and Conclusions . . . 61

4 Modelling of Oxidation of Ni-Cr Alloys 65

4.1 Introduction . . . 65
4.2 Background . . . 66
4.3 Numerical Modelling Approach . . . 70
4.3.1 Oxide Diffusion Model . . . 70
4.3.2 Grain Boundary Diffusion . . . 71
4.3.3 Homogenisation Model . . . 72
4.3.4 Numerical Implementation . . . 73

4.3.5 Entropy Production . . . 76
4.4 Thermodynamic and Kinetic Descriptions . . . 77
4.4.1 Halite-(Ni,Cr)O . . . 78
4.4.2 Corundum-$(Cr,Ni)_2O_3$ . . . 82
4.4.3 Spinel-$NiCr_2O_4$ . . . 86
4.5 Numerical Results . . . 89
4.6 Summary & Conclusions . . . 94

5 CO_2 Oxidation of 9Cr Steel 102
5.1 Introduction . . . 103
5.2 Experimental Procedures . . . 105
5.3 Theoretical Modelling . . . 109
5.3.1 Oxide Growth Model (OGM) . . . 109
5.3.2 DICTRA Simulations . . . 113
5.3.3 Substrate Penetration Model (SPM) . . . 114
5.4 Experimental Results . . . 116
5.5 Modelling Results . . . 122
5.5.1 Oxidation Kinetics . . . 122
5.5.2 Carburisation Kinetics . . . 125
5.6 Discussion . . . 129
5.6.1 On the Degradation Reactions Observed . . . 129
5.6.2 On the Role of Carbon and its Treatment in Numerical Modelling 132
5.6.3 Implications for Remnant Life Assessment . . . 134
5.7 Summary & Conclusions . . . 138

6 Summary, Conclusions and Future Directions 142
6.1 Summary . . . 142
6.2 Future Directions . . . 143
6.2.1 DFT Thermodynamics . . . 143

6.2.2 Modelling of Oxidation Kinetics 145
6.2.3 CO_2 Oxidation of 9Cr Steel 147

References **149**

List of figures

1.1 Fracture toughness and yield strength of typical materials. 2

1.2 Strength limitations of conventional high temperature alloys. 3

1.3 Schematic diagram of the Advanced Gas-cooled Reactor. 4

1.4 Illustration of material usage in a typical civil aero-engine. 6

1.5 View into the industrial gas turbine SGT-800. 8

1.6 Typical modelling techniques across various time/length scales. 10

2.1 Comparison of the classical and quantum mechanical harmonic oscillator. 20

2.2 Different types of non-stoichiometric ionic oxides. 30

2.3 Schematic illustration of the interface region and surrounding cells at the beginning and at the end of a time-step. 37

2.4 Graphical representation of the approximations of the first and second derivatives by differences. 39

2.5 Graphical representation in space-time of the explicit, implicit and mixed schemes. 40

3.1 Calculated Gibbs energy of vacancy formation and equilibrium vacancy mole fraction of fcc-Ni compared with existing experimental data and DFT calculations. 44

3.2 Calculated vacancy formation entropy of fcc-Ni compared with existing experimental data. 58

3.3 (a) Trajectories of the 12 nearest neighbours (1NNs) of a vacancy; (b) distribution function of the distance between 1NNs and the vacancy and corresponding effective potential. 58

3.4 Calculated evolution of local magnetic moments (within sphere of 1.286 Å radius) of all atoms in a 3^3 supercell as a function of LD time at $T =$ 1600 K with $a = 3.58$ Å by using DFT with low convergence parameters; comparisons are made between bulk (black), with one vacancy (red), and $T = 0$ K calculations (mono-vacancy: blue; bulk: pink). 60

3.5 Averaged magnetic moment as a function of volume at $T = 0$ K and at the melting temperature of 1728 K for the vacancy and perfect bulk $3 \times 3 \times 3$ supercells. 61

4.1 Influence of Cr content in Ni-Cr alloys on oxidation kinetics at P_{O_2}=0.1 atm between 800 to 1200 °C 68

4.2 Schematic diagram showing the transition from transient to steady state oxidation for Ni-Cr alloys 68

4.3 Illustration of 1D geometric layout used in modelling approach. 69

4.4 Illustration of parallelled interpolation scheme. 75

4.5 Illustration of adaptive meshing method adopted in this work. 77

4.6 Oxygen tracer diffusion coefficient in halite NiO phase. 79

4.7 Nickel tracer diffusion coefficient in halite NiO phase. 80

4.8 Temperature-dependent chromium tracer diffusion coefficient in halite NiO. 80

4.9 Chromium-content-dependent chromium tracer diffusion coefficient in halite NiO phase. 81

4.10 P_{O_2}-dependent chromium tracer diffusion coefficient in halite NiO phase. 81

4.11 Defect concentrations in corundum Cr_2O_3 phase at 1100 °C. 83

4.12 Calculated defect concentrations in corundum Cr_2O_3 phase. 84

4.13 Chromium tracer diffusion coefficient in corundum Cr_2O_3 phase. 84

4.14 Oxygen tracer diffusion coefficient in corundum Cr_2O_3 phase. 85
4.15 Nickel tracer diffusion coefficient in corundum Cr_2O_3 phase 86
4.16 Nickel tracer diffusion coefficient in spinel $NiCr_2O_4$ phase. 87
4.17 Chromium tracer diffusion coefficient in spinel $NiCr_2O_4$ phase. 88
4.18 Oxygen tracer diffusion coefficient in spinel $NiCr_2O_4$ phase. 88
4.19 Predicted equilibrium phase mole fractions for Ni-5Cr, Ni-15Cr, Ni-30Cr and Ni-50Cr alloys at different P_{O_2} at 1000 °C. 89
4.20 Predicted evolution of phase distribution for alloy Ni-0.05 wt.%Cr at 800 °C. 90
4.21 Weight gain curve for alloy Ni-0.05 wt.%Cr exposed at 800 °C from predictions (black) and corresponding parabolic fitting (red). 91
4.22 Predicted oxidation kinetics for different Ni-Cr alloys at 800 °C, 900 °C and 1000 °C. 91
4.23 Illustration of contribution of interface diffusion on effective oxygen mobility at the internal oxide zone (IOZ). 93
4.24 Calculated entropy production for pure iron oxidised at 600 °C in dry oxygen. 94

5.1 Geometry, dimension and backscattered SEM image of fin tube specimen. 106
5.2 Thermodynamic predictions of exposure gas conditions. 107
5.3 Weight gain measurements of samples exposed at 580 °C, 600 °C, 620 °C and 640 °C. 108
5.4 Illustration of the oxide growth model (OGM) with defined physical parameters annotated. 110
5.5 (a) Backscattered SEM image of oxide cross-section showing layered structure consisting of magnetite-Fe_3O_4, banded spinel phase region and shallow IOZ; (b) Backscattered SEM and (d) EDX images of IOZ during the transition between protective/breakaway oxidation below (c) corresponding phase map with possible sites of atom probe analysis marked with red box. 118

5.6 Elemental studies of internal oxidation zone (IOZ) by TEM. 119
5.7 Comparison of the centre of the fin before and after exposure. 120
5.8 Identification of elemental carbon in oxide close to spinel/alloy interface. 121
5.9 Atom probe reconstructions of samples from the internal oxidation zone. . 122
5.10 Measurements of oxide phase regions by Nano-SIMS. 123
5.11 Comparisons of predicted and measured thickness of spinel and magnetite phase regions. 124
5.12 Prediction of oxide thickness at different temperatures and different times. 126
5.13 Predicted volume fraction of carbides at different times. 127
5.14 Predicted evolution of carbon content at oxide/alloy interface and fin centre. 128
5.15 P_{O_2} and a_C phase diagram with suggested diffusion paths. 131
5.16 Predicted weight gain contributed by oxidation and carburisation at the time of carbon saturation, in comparison with measured weight gain at breakaway (WGB) data. 134
5.17 Contour plot of time required for carbon saturation as a function of effective chemical diffusivity of carbon and surface reaction parameter. 136
5.18 Calculated surface reaction parameter. 137
5.19 Predicted time to breakaway initiation from an empirical ln{TTB}-1/T linear fitting and carbon saturation model with different carbon saturation criteria. 138

6.1 Illustration of contribution of interface diffusion on effective oxygen mobility at the internal oxide zone (IOZ). 146
6.2 Illustration of microstructure in spinel phase region, based on preliminary characterisation. 147

List of tables

2.1 Kröger-Vink notation and corresponding sublattice formalism describing typical defect structure in binary oxides. 31

2.2 The effect of substitutionally dissolved foreign cations on the defect equilibrium. 32

3.1 Experimental determined vacancy formation enthalpy (H^f_{Va}) and entropy (S^f_{Va}) of fcc-Ni. 47

3.2 Previously calculated *ab initio* vacancy formation enthalpy (H^f_{Va}) and entropy (S^f_{Va}) of fcc-Ni. 47

3.3 Convergence parameters for the $T = 0\,\mathrm{K}$ calculations and the resulting vacancy formation enthalpy H^f at atmospheric pressure. 50

3.4 Convergence parameters for the electronic free energy calculations and the resulting Gibbs energy of vacancy formation G^f at the melting point (1728 K) and at atmospheric pressure. 50

3.5 Convergence parameters for the quasiharmonic calculations and the resulting Gibbs energy of vacancy formation G^f at the melting point (1728 K) and at atmospheric pressure. 52

3.6 Convergence parameters for the TU-TILD potential to DFT calculations and the resulting Gibbs energy of vacancy formation G^f at the melting point (1728 K) and at atmospheric pressure. 53

3.7 Occurrence of spin flips for 3^3 supercell calculations coupling TU-TILD potential with DFT with low convergence parameters. 54

4.1 Thermodynamic descriptions of assessed oxides in Ni-Cr-O system. . . . 96
4.2 Atomic mobility of assessed oxides in Ni-Cr-O system. 99
4.3 R^2 of fit of predicted weight gain curves to the parabolic law. 100

5.1 Measured composition of steel (wt.%); carbon and sulphur are measured by the combustion analysis while the rest by the Inductively Coupled Plasma Optical Emission Spectometry (ICPOES). Data courtesy of EDF Energy. 141
5.2 Chemical composition (at.%) of $M_2(C,N)$ from internal oxidised zone (IOZ) as measured by TEM-EDX. Measurements courtesy of Y.L. Chiu. . 141
5.3 Chemical composition of chromite, $M_{23}C_6$ carbide and ferrite phase from the internal oxidised zone (IOZ) as measured by atom probe tomography. 141

Nomenclature

Roman Symbols

A	surface area (of alloy which is exposed to environment)
a	lattice parameter (Chapter 3)
a_k	thermodynamic activity of species k (Chapter 5)
a_s	number of sites on (stoichiometric coefficient of) sublattice s (Chapter 2 &4)
a_s^r	number of sites on (stoichiometric coefficient of) sublattice s in phase r (Chapter 2 &4)
$A\left(z^{i\mathbb{A}}\right)$	cross-sectional area of phase region $\mathbb{A}$ at the interfacial region
b_{jk}	number of moles of component j per mole formula unit of species k
C	concentration
$C_{i,\text{int}}^k$	interfacial concentrations in a volume-fixed frame of reference of component i in phase k
$c_{i,\text{O}}$	concentration of the diffusing ion i per mole of anion (oxygen) sites
c_k	concentration of species k
c_k^j	concentration of grid point k at time step j
$c^\star$	boundary concentration
C_V	isochoric heat capacity
$\mathbf{D}$	dynamical matrix
D	diffusion coefficient
d	average grain size
D_0	pre-exponential factor, maximum diffusion coefficient

$D_{\mathrm{C}}^{\mathrm{eff}}$	effective chemical diffusion coefficient of carbon in ferrite considering blocking of carbide phases, Chapter 5
$\mathbf{D}_{\mathbf{G}^{\mathrm{sc}}}$	reciprocal dynamical matrix
D_k	chemical diffusion coefficient of species k
$D^{\star}$	tracer diffusion coefficient
E	electric potentail
e	elementary charge
$E_{0\mathrm{K}}$	total energy at $T = 0\,\mathrm{K}$
E_{cut}	plane wave energy cut-off energy
E_{dc}	double counting corrections
$E_{\mathrm{high}}^{\mathrm{DFT}}$	total energy calculated from DFT with high convergence parameters (referenced to those from $T = 0\,\mathrm{K}$)
$E_{\mathrm{low}}^{\mathrm{DFT}}$	total energy calculated from DFT with low convergence parameters (referenced to those from $T = 0\,\mathrm{K}$)
E^{h}	total energy calculated from Einstein harmonic potential (referenced to those from $T = 0\,\mathrm{K}$)
$E_{N,e}$	total energy of the system of interacting particles including nuclei and electrons
E^{pot}	total energy calculated from classical interatomic potentials (referenced to those from $T = 0\,\mathrm{K}$)
E^{qh}	total energy calculated from quasiharmonic dynamic matrix (referenced to those from $T = 0\,\mathrm{K}$)
$\mathrm{erf}()$	error function, $\mathrm{erf}(x) = \frac{1}{\sqrt{\pi}} \int_{-x}^{x} \exp\left(-t^2\right) \mathrm{d}t$
$\mathscr{F}$	Faraday constant
F	force
F	Helmholtz free energy
F^{ah}	anharmonic Helmholtz free energy
$F_{\mathrm{cl}}^{\mathrm{atom}}$	vibrational Helmholtz free energy of classical harmonic oscillator

f^{corr}	correlation factor
F^{el}	electronic Helmholtz free energy of a static lattice
$F^{\mathrm{el-vib}}$	adiabatic Helmholtz free energy coupling between electrons and atomic vibrations
f^{gb}	volume fraction of grain boundary
f_i	Fermi-Dirac function
$F^{\mathrm{mag-vib}}$	the magnetic contribution to the Helmholtz free energy containing the impact of atomic vibrations
f_{m}^{α}	mole fraction of α phase
$f^{\mathrm{m},\phi}$	mole fraction of phase ϕ
$F_{O_{\mathrm{h}}}$	Fourier number of diffusion equation: $F_{O_{\mathrm{h}}} = D\Delta t/h^2$
$F_{O_{\mathrm{h}}}^{\mathrm{e}}$	explicit Fourier number of diffusion equation: $F_{O_{\mathrm{h}}}^{\mathrm{e}} = (1-\eta)F_{O_{\mathrm{h}}}$
$F_{O_{\mathrm{h}}}^{\mathrm{e}}$	implicit Fourier number of diffusion equation: $F_{O_{\mathrm{h}}}^{\mathrm{i}} = \eta F_{O_{\mathrm{h}}}$
F^{qh}	quasiharmonic Helmholtz free energy
$F_{\mathrm{qm}}^{\mathrm{atom}}$	vibrational Helmholtz free energy of quantum mechanical harmonic oscillator
$f_{\mathrm{SiO_2}}^{\mathrm{int}}$	fraction of spinel/alloy interface across which diffusion is blocked
$f^{\mathrm{v},\phi}$	volume fraction of phase ϕ
G	Gibbs free energy
g	geometry factor describing vacancy mole fraction
${}^{\mathrm{E}}G$	excess Gibbs energy
G_{Va}^{f}	Gibbs energy of formation of vacancies
$\Delta^{\mathrm{ideal}}G$	change in Gibbs energy upon mixing of idea solution
${}^{\mathrm{phys}}G$	contribution to the Gibbs energy due to physical properties
${}^{\circ}G_{\mathrm{ref}}$	reference Gibbs energy upon mechanical mixture of all species in a phase
$\hat{H}$	Hamiltonian
h	spacing of grid point of space discretisation
H_{Va}^{f}	enthalpy of formation of vacancies
ΔH_{m}	enthalpy of atomic migration

I_i	constituent array of i^{th} order
$\mathbb{J}$	Jacobian matrix
$J_k^{i\mathbb{A}}$	diffusive flux of component k in phase region $\mathbb{A}$ into the interfacial region in a volume-fixed frame of reference
$J_{i,\text{int}}^k$	interfacial fluxes in a volume-fixed frame of reference of component i in phase k
J_j^r	diffusive flux of component j in phase r
J_k	diffusive flux of species k
k	relative contribution of the average compositional gradient and the size of finite volume when defining the mesh quality function
k_B	Boltzmann constant
k_c	parabolic thickening constant
k_p	parabolic weight gain constant
K_{sp}	solubility product
L_{I_i}	interaction parameters defined by constituent array I_i
$L_{i,j}$	interaction parameters between species i and j
L_k	phenomenological kinetic parameter of species k
Δm	weight gain
$\mathbf{M}$	mass vector
M	magnetic moment
M_j^{bulk}	lattice mobility of element j
m_e	electron mass
M_j^{eff}	effective mobility of element j considering gain boundary diffusion
M_j^{gb}	grain-boundary mobility of element j
M_I	mass of nucleus I
M_j^r	effective mobility of component j in phase r
M_k	mobility of component k
$M_{k\text{Va}}^{rs}$	mobility of species k on sublattice s in phase r

$n_{i,\mathrm{O}}$	mole fraction of ion i per mole of anion (oxygen) sites
N_k	amount of component k
N_n	number of nuclei
N^{UP}	number of up-sampled configurations
$O()$	error term in an approximation to a mathematical function
P	pressure
P_k	partial pressure of species k
Q	activation energy
q	grain shape numerical factor: 1 for parallel grains, 3 for square grains
q_k	charge of species k
Q_{M}	mesh quality function
R	gas constant
$\mathbf{R}_i$	coordinates of the nuclei
$\mathbf{r}_i$	coordinates of the electrons
$\mathbf{R}_i^0$	coordinates of the nuclei at equilibrium
s	SiO_2 blocking factor
S^{conf}	configurational entropy
S^{el}	electronic entropy of a static lattice
$S^{\mathrm{el\text{-}vib}}$	entropy due to adiabatic coupling between electrons and atomic vibrations
S^f_{Va}	entropy of formation of vacancies
S^{mag}	magnetic entropy
S^{vib}	atomic vibrational entropy
Δt	time step
T	temperature
t	time
$\hat{T}^{\mathrm{el}}$	kinetic energy for the electrons
$\hat{T}^{\mathrm{nul}}$	kinetic energy for the nuclei
$\mathbf{U}$	displacement vector

U	internal energy
u_i^k	substitutional site-fraction (u-fraction) of component i in phase k
U^{el}	electronic internal energy of a static lattice
V	volume
v	atom-vacancy exchange frequency
v_0	effective atom-vacancy exchange frequency
$v^{\mathbb{A}/\mathbb{B}}$	interface moving between phase $\mathbb{A}$ and phase $\mathbb{B}$
$v_{\mathrm{eff}}^{\mathrm{KS}}$	Kohn-Sham potential
$\hat{V}^{\mathrm{el}}$	electron-electron repulsion energy
$\hat{V}^{\mathrm{e\text{-}n}}$	electron-nucleus attraction energy
v_{ext}	external potential (due to fixed nuclei) contributing to Kohn-Sham potential
v_{H}	Hartree potential contributing to Kohn-Sham potential
$\hat{V}^{\mathrm{nuc}}$	nucleus-nucleus repulsion energy
V_S	molar volume
v_{sp}	moving velocity of spinel/alloy interface relative to the original alloy/gas interface. (Chapter 5)
$v_{V,T}$	effective potentials between the vacancy and its 1NNs, at a constant volume and pressure
v_{XC}	exchange-correlation functional contributing to Kohn-Sham potential
$X_{\mathrm{C}}^{\mathrm{crit}}$	critical carbon mole fraction as carbon carbon saturation
x_i	mole fraction of component i
$X^{\mathrm{NN}}, Y^{\mathrm{NN}}$	coordinate of nearest neighbours (1NNs) of a vacancy (mapped to the first quadrant of the xy plane)
x_{ox}	oxide thickness
x_{Va}	equilibrium mole fraction of vacancies
y_i^s	site-fraction of constituent i on sublattice s
y_k^{rs}	site fraction of species k on sublattice s in phase r
Z	partition function

Z_I	proton number of nucleus I
z_{Va}^{rs}	site fraction of vacancy on sublattice s in phase r if vacancy is a defined constituent on the sublattice, otherwise it is equal to unity
z_x	space x coordinate, Chapter 1&5
z_y	space y coordinate, Chapter 1&5

Greek Symbols

α_j	activation energy reduction factor of element j for grain boundary diffusion
$\alpha_{\mu,\mathrm{C}}$	surface reaction coefficient of carbon at the spinel/alloy interface
β	a general 'lumped' factor describing the processes of carbon transport through the oxides, the kinetics of the Boudouard reaction and the kinetics of carbon transport across the oxide/alloy interface (Chapter 5)
β	thermodynamic beta; $\beta = 1/(k_B T)$
δ	grain boundary width
ε_0	electric constant
ε_{F}	Fermi energy
ε_i	energy of non-interacting electron i
η_k	electrochemical potential of species k
γ	parameter describing the occupancies of Fermi-Dirac function f_i: $\gamma = 1$ for spin-polarised systems and $\gamma = 2$ for spin-unpolarised systems
$\Gamma_j^{\star}$	effective transport properties of element j by applying the homogenisation function
$\hbar$	reduced Planck constant
κ	electrical conductivity
λ	linear coupling parameter
μ_k	chemical potential of species k
Ω	volume of supercell
ω_0	vibration frequency of independent harmonic oscillators

$\omega_{\mathbf{k}}$	vibration frequency of oscillators with wave vector $\mathbf{k}$
$\Omega_{k\mathrm{Va}}$	rate of exchange between a k atom and its neighbouring vacancy
ϕ_i	Kohn-Sham orbital (wave function) of non-interacting electron i
${}^{v}\Phi^{i,j}$	v^{th} order coefficient describing the interaction between i and j in the *Redlich-Kister polynomials*
ψ_k	electrostatic potential of species k
$\Psi_{N,e}$	many-body wave function of nuclei and electrons
ρ	volumetric mass density
$\rho\left(\mathbf{r}\right)$	electron density
$\rho_{V,T}\left(d\right)$	distribution function of the distance (d) between the vacancy and its 1NNs, at a constant volume and pressure
Θ	measurable property correlated to defect equilibria
ζ	implicity

Other Symbols

$< ... >$	canonical ensemble average

Kröger-Vink notation M_s^c:

- M corresponds to the species, such as atoms, vacancies (V), interstitials (i), electrons (e) or electron holes (h).
- s indicates the lattice site that the species occupies, such as atoms, lattice interstice (i), cation site (C or M) or anion site (A or X).
- c corresponds to the electronic charge of the species relative to the site that it occupies. $\cdot$ means a net single positive charge; ' means a net single negative charge; $\times$ means null charge.

Acronyms / Abbreviations

1NN	nearest neighbours
ah	anharmonic

AM05	Armiento-Mattsson functional
AP	analysis point
APB	anti-phase boundary
APT	atom probe tomography
BC	bond coating
bcc	body centered cubic
CALPHAD	**CAL**culation of **PHA**se **D**iagrams
CEF	compound energy formalism
COD	coefficient of determination
CSL	coincident site lattice
DD	differential dilatometry
DFT	density functional theory
DICTRA	**DI**ffusion-**C**ontrolled phase **TRA**nsformation
DOS	density of states
$\Delta\rho$	residual electrical resistivity
DSC	differential scanning calorimetry
EAM	embedded atom method
EDX	energy-dispersive X-ray spectroscopy
e^+-LT	positron lifetime spectroscopy
fcc	face centered cubic
FDM	finite difference method
FEG	field emission gun
FEM	finite element method
FIB	focused ion beam
FM	ferromagnetic
FVM	finite volume method
GB	grain boundary
GGA	generalised-gradient approximation

hcp	hexagonal close packed
HEG	homogeneous electron gas
HRTEM	high-resolution transmission electron microscope
ICPOES	inductively coupled plasma optical emission spectometry
IGTs	industrial gas turbines
IOZ	internal oxidation zone
kp	k-points
LDA	local density approximation
LD	Langevin dynamics
LGT	local Grüneisen theory
LPM	lifetime prediction methodology
LRO	long-range order
MC	Monte Carlo
MD	molecular dynamics
MEAM	modified embedded atom method
NanoSIMS	nanoscale secondary ion mass spectrometry
NEB	nudged elastic band
NM	non-magnetic
OGM	oxide growth model
PAC	peak angular correlation
PAS	positron annihilation spectroscopy
PAW	projector augmented wave
PBE	Perdew-Burke-Ernzerhof functional
PW91	Perdew-Wang functional
qh	quasiharmonic
qm	quantum mechanical
SAD	selected area diffraction
SCF	self consistent field

SDD	silicon drift detector
SEM	scanning electron microscope
SE	secondary electron
SFE	stacking fault energy
SGTE	Scientific Group Thermodata Europe
SPM	substrate penetration model
QM/MM	quantum mechanics/molecular mechanics
SQS	quasi-random structures
SRO	short-range order
STP	standard temperature and pressure
TBC	thermal barrier coating
tcp	topologically close packed
TCS	time required for carbon saturation
TEM	transmission electron microscope
TGA	thermal gravimetric analysis
TI	thermodynamic integration
TRL	technology readiness levels
TTB	time to breakaway
TU-TILD	two-stage upsampled thermodynamic integration using Langevin dynamics
UP-TILD	up-sampled thermodynamic integration using Langevin dynamics
VASP	Vienna *ab initio* simulation package
WGB	weight gain at breakaway

Chapter 1

Introduction and Motivation for Research

1.1 Importance of Metallic Alloys for Structural High Temperature Applications

Metallic alloys underpin nearly all sectors of commercial enterprise and industrial activity, e.g. energy production & conversion, transportation, construction & manufacturing, and space & satellite communications. In particular, metallic structural components are widely used for high temperature applications mainly due to their excellent combined mechanical properties (stiffness, strength, toughness and fatigue resistance) and environmental stability (oxidation/corrosion resistance). The major reason for this position is that metals possess a superior combination of fracture toughness and yield strength when compared to other materials, see fig. 1.1; it is particularly true when exposed at elevated temperatures.

Nevertheless, pure metals are soft: therefore, they are usually alloyed to achieve higher levels of strength and thermal & environmental resistance. Different metallic systems offer different ranges of properties. For example, Ti-alloys are widely used for the fan blade of aero-engines due to their appealing combination of low density and high strength.

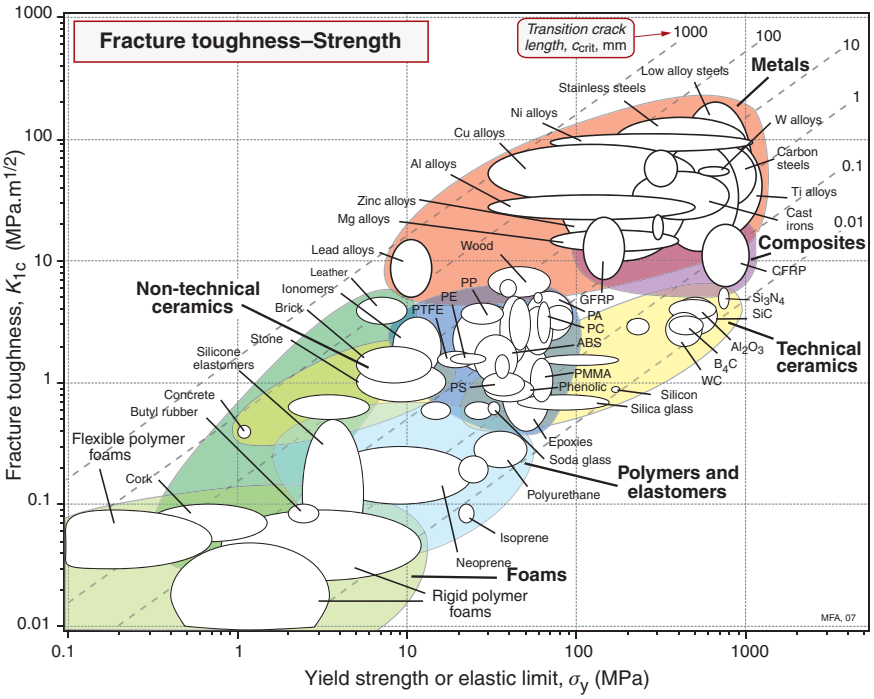


Fig. 1.1 Fracture toughness and yield strength of typical materials [1]; note metals show good combination of fracture toughness and yield strength.

For the pressure vessel of nuclear plant, however, steel is a more suitable choice because of its high strength, good radiation-resistance at high temperatures, low cost, and ease of manufacture. For applications which operate at ultra-high temperatures (> 700 °C) – turbine blades/discs of aero-engines – Ni-based superalloy are employed, see fig. 1.2 comparing 100 kh creep-rupture stress of different alloys.

The remarkable mechanical and heat-resistant properties of alloys such as modern superalloys can be attributed to their unique chemical and microstructural features [3–6] which have evolved over 90 years. The early heat-resistant nickel base alloys were the Ni-20% Cr alloys used for electrical heating elements in the early 20th century [7] mainly due to the high melting point of Ni (1450 °C) and the formation of protective Cr_2O_3 scale. Later, the Al and Ti contents were increased to enhance γ'-precipitation hardening effects and significant amounts of refractory (mostly) elements were added for solid solution strengthening. The refinements of processing techniques and the search for better high temperature strength/creep/oxidation resistance materials have never stopped.

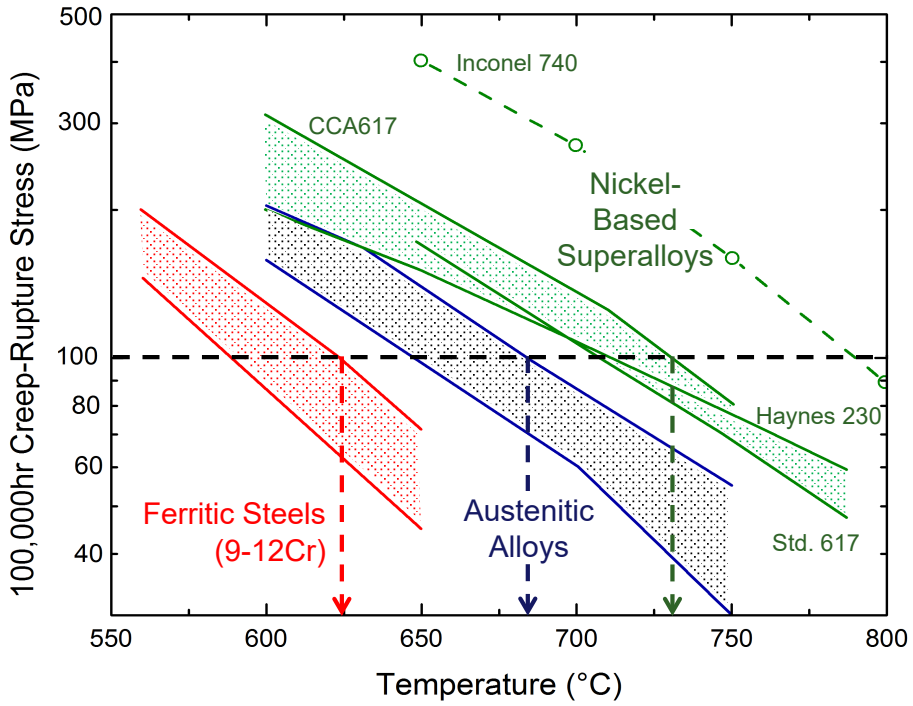


Fig. 1.2 Strength limitations of conventional high temperature alloys [2].

This thesis is concerned with the physical metallurgy/corrosion of high temperature structural alloys, of the type used for some of the most demanding engineering applications. Both iron-based steels and nickel-based superalloys are used for such applications; the common thread in this thesis from the science perspective is the role played by defects such as vacancies which lead to degradation due to diffusional phenomena such as oxidation and creep. In what follows in this chapter, we consider first the technical relevance of the applications, before following up by considering the phenomenology of diffusion. In the final part of this chapter, the scope and aims of this thesis are considered, particularly emphasising the role of numerical modelling in promoting greater understanding of the complex phenomena involved and improved predictive power of the effects which are important.

1.2 Metallic Alloys for High Temperature Structural Applications

1.2.1 Nuclear Power Reactors

In 2015, 70 TWh of electricity was generated by nuclear power in the United Kingdom, supplying 21% of the total electricity capacity of the country [8]. Of all eight nuclear plants currently running in UK, seven are second-generation advanced gas-cooled (AGR) nuclear reactors which use graphite as the neutron moderator and carbon dioxide as coolant, see fig. 1.3.

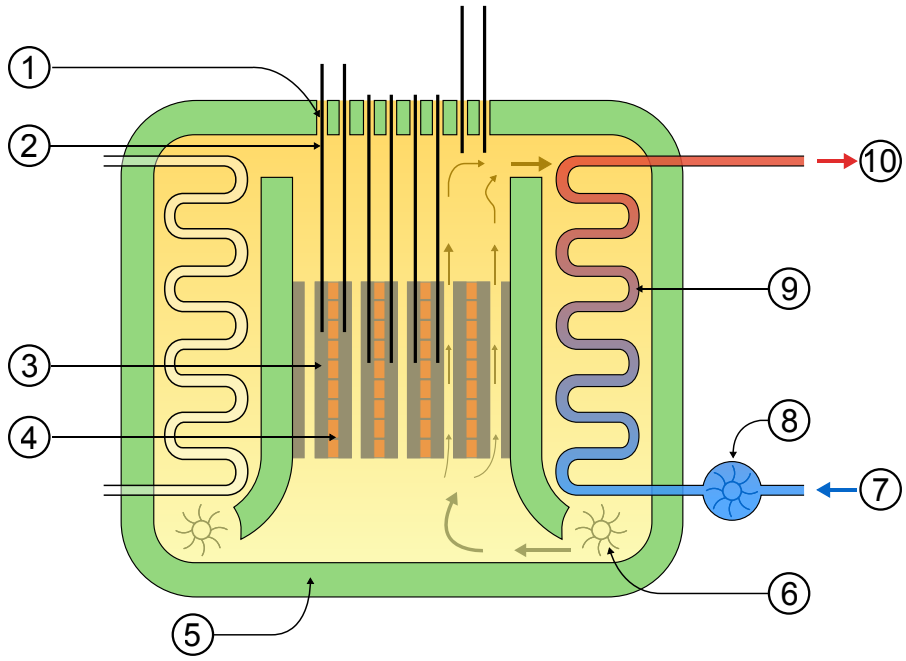


Fig. 1.3 Schematic diagram of the Advanced Gas-cooled Reactor [9]. Note that the heat exchanger is contained within the steel-reinforced concrete combined pressure vessel and radiation shield. 1. Charge tubes; 2. Control rods; 3. Graphite moderator; 4. Fuel assemblies; 5. Concrete pressure vessel and radiation shielding; 6. Gas circulator; 7. Water; 8. Water circulator; 9. Heat exchanger; 10. Steam.

To avoid graphite corrosion and carbon deposition on metallic components, the gas composition is designed with e.g. 1% CO, 260 vpm CH_4, 151 wpm H_2O, 100 vpb COS and balance CO_2, for the AGR reactor operated at the Hartlepool (HRA) plant [10].

Typical designed outlet gas temperature is up to 640 °C; the service pressure is 41 bar (only Dungeness B is running under 31 bar).

Such harsh environments provide severe challenges to the materials being used for the boilers and heat exchangers where coolant is running on one side and water/steam on another. Various alloys are used for these critical components, such as mild & low alloy steels, 9Cr-1Mo steels, 12Cr steels, 18/8 stainless steels and high Ni alloys, taking into account their weldability, creep resistance and corrosion resistance. All these materials are prone to sluggish diffusion-controlled phase transformation such as oxidation and carburisation during long-term service. However, it was not until 1971 that so-called breakaway oxidation and associated acceleration of chemical degradation (i.e. fast diffusion-controlled phase transformation) were found on 9Cr-1Mo steels at elevated temperatures (laboratory conditions) [11].

An experimental programme was then started by British Energy in 1998, trying to initiate breakaway (mostly by increasing exposure temperatures) so that the mechanisms for breakaway and the factors which cause it could be investigated [12]. Theoretical modelling nowadays is required to predict and to extrapolate to low temperature regions, aiming to improve assessment of component life time under service conditions. This matter is considered in detail in chapter 5.

1.2.2 Aero-engine

Nickel-based superalloys are widely used in the hottest parts of the engine including the combustion chamber, the last few compressor stages before the combustion chamber and the turbine stages (see fig. 1.4). As higher operating temperatures means higher thermal efficiency, the strong demand for highly efficient aero-engines has been pushing the development of nickel-based superalloys to withstand higher and higher temperatures.

This is achieved either by adding various alloying elements such as Co, Fe, Cr, Mo, Ru, Re, and W for solid solution strengthening in the γ matrix, Al, Ti and Ta for strengthening

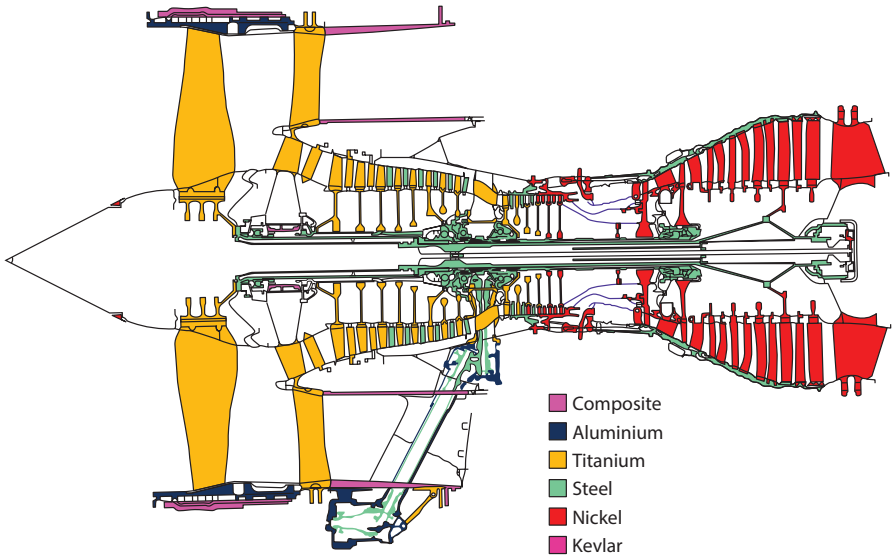


Fig. 1.4 Illustration of material usage in a typical Rolls-Royce civil aero-engine [13].

by precipitation of coherent ordered γ' phase, Ti and W to stop the cross-slip in γ matrix by lowering its stacking fault energy (SFE), C and B for grain boundary strengthening by formation of carbides or borides, and Y for slowing the surface degradation due to corrosive attack, or by improving the processing techniques such as removing weak grain boundaries by directional solidification with grain-selectors, slowing the heat transfer by electron-beam physical vapour deposition (EB-PVD) of thermal barrier coating (TBC), sustaining a protective thermally-grown oxide (TGO) layer by introducing bond coating (BC), reducing porosity of metallic components by the Hot Isostatic Pressing (HIPing) in powder metallurgy.

Most of the above efforts, to a significant degree, are linked to high temperature diffusional phenomena in the fcc-Ni phase (in the presence of various types of defects and/or alloying elements and/or under different stress levels); it is crucial, thus, to determine its atomic diffusivity and associated vacancy concentrations, either by high-temperature experiments such as the diffusion couple for inter-diffusion coefficient and positron annihilation spectroscopy for vacancy concentrations, or with the help of modern electronic structure calculations conducted at the ground state ($T = 0\,\mathrm{K}$); a temperature gap, however, still exists between measurements and predictions. Not until recently however – with the

development of high performance computing and advances of phonon calculations – has it been possible to incorporate finite-temperature effects into theoretical calculations; this allows in principle more accurate design of new grades of superalloys. In chapter 3, this matter is considered in greater detail, with a particular emphasis on finite temperature calculations using the latest electronic structure theory.

1.2.3 Industrial Gas Turbines

Steels were utilised effectively as high temperature materials in industrial gas turbines (IGTs, fig. 1.5) during the second and third decades of the 20th century before the strong interest in applying advanced nickel-based superalloys emerged, driven by increasing operating temperatures. Different from alloys used in aero-engines (particularly the turbine blade), alloys designed for IGTs usually require superior corrosion resistance due to lower quality of the fossil fuel being used [13–15]. Typically, large amounts of Cr and Al are added in the alloys to achieve better oxidation/corrosion resistance. Thus it is important to assess how these elements improve the alloy's resistance to surface degradation and what the minimum doses required are. So far, no quantitative models are available to predict high temperature oxidation of alloys, particularly coupling the defect structure and associated kinetics both in oxides and alloys. Such theory and modelling techniques are developed in chapter 4.

1.3 The Phenomenology of Diffusion

The common thread in this thesis is the phenomenon of diffusion which occurs in the structural alloys used for these applications. Diffusion is a transport mechanism for matter whereby molecules or ions intermix. Concentration C is usually used to describe the local state of a species; according to Fick's laws, its time (t) and space dependency (z_x) can be

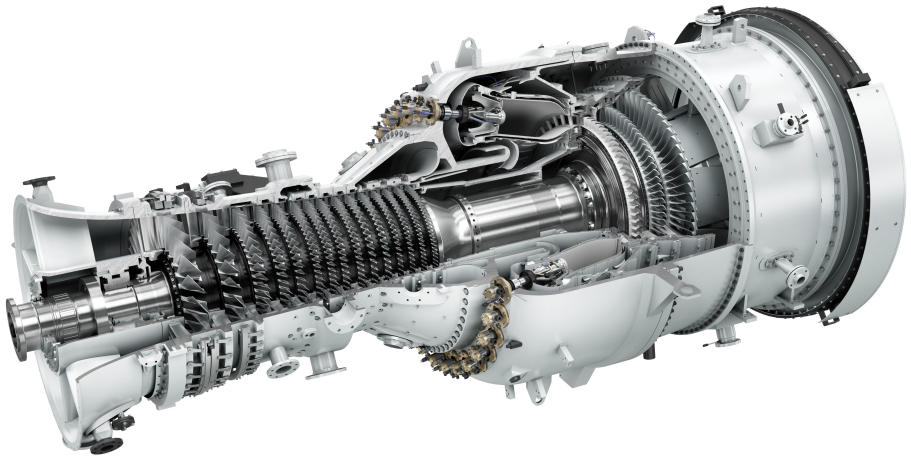


Fig. 1.5 View into the industrial gas turbine SGT-800 (Courtesy of Siemens).

described by:

$$\frac{\partial C}{\partial t} = D\frac{\partial^2 C}{\partial z_x^2} \tag{1.1}$$

where the magnitude of diffusion coefficient D is ultimately dependent upon the diffusion mechanism. There are two common mechanisms applicable depending on the type of site occupied by an atom: atoms can exchange their position with a neighbouring vacancy in what is known as the vacancy-mechanism. Alternatively, in the interstitial mechanism much smaller interstitial atoms migrate through the interatomic channels. At finite temperatures, atoms in a solid oscillate about a given site. Diffusion is then possible if the kinetic energy of a vibration is sufficient to overcome the potential barrier associated with a diffusion jump. As the kinetic energy of vibrations decreases with temperature, D can be given consistent with the Arrhenius relationship:

$$D = D_0 \exp\left(-Q/RT\right) \tag{1.2}$$

where D_0 is a quantity measuring the fundamental vibrational frequency of the lattice known as the frequency factor (also called pre-exponential factor) and Q is the activation energy or barrier energy; R is the gas constant [16]. Similar to a chemical reaction, several

sequential steps are usually involved during a diffusional process; this will be detailed in section 3.2. For diffusion in oxides which usually have more complex crystal structure, the electric field is also significant; relevant physical background and description will be detailed in section 2.2.3.

1.4 Role of Modelling

A model is a simplified description – especially a mathematical one – of a system or process, to assist calculations and predictions [17]. In another words, it is a representation of reality which mimics the way in which nature behaves. It can either be empirical or physical, but a physical model, which is based on the established laws or principles of physics and chemistry, has the predictive capability [17]. Physical modelling of materials problems is a broad topic necessitating studies across wide range of length/time scales, see fig. 1.6, and it is becoming increasingly interdisciplinary. With the help of fast development of computational power, the gaps between each modelling techniques is becoming smaller and smaller: coupled multi-scale modelling is becoming possible: for example, parameterised vacancy formation free energy from DFT Molecular Dynamics Simulation can be inserted into DICTRA or Phase-Field (coupled with CALPHAD) calculations. It should also be emphasised that modelling and experiment are complementary: they are working closer and closer nowadays; model-driven/guided experimentation, which best optimises experimental resources, is becoming a trend.

1.5 Scope of Proposed Research

As discussed above, diffusional behaviour is commonly reported in high temperature structural alloys. However, even though huge research efforts have been conducted on metallic systems, the accuracy of descriptions for thermodynamic/mobility databases, and the understanding of the role of diffusion in both ceramics and metallic component

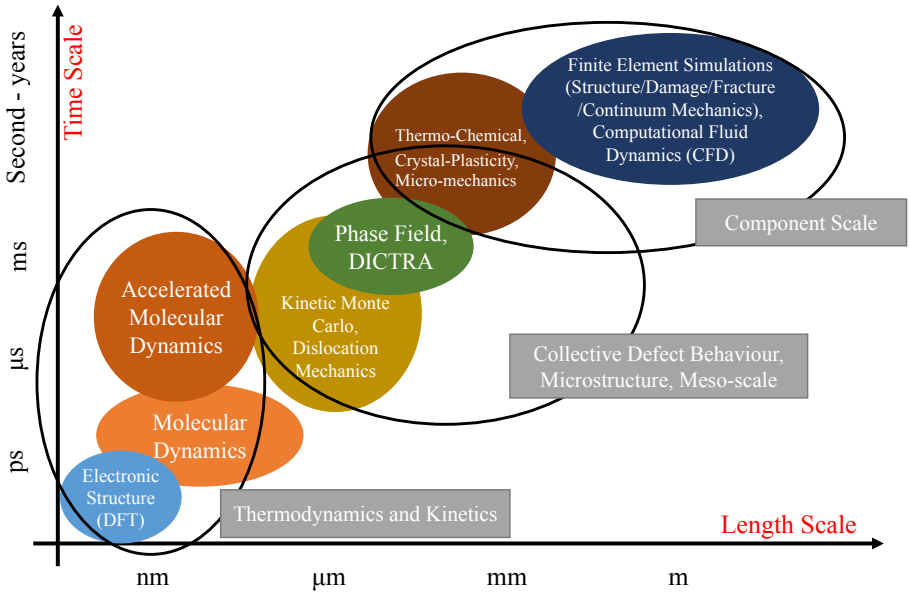


Fig. 1.6 Typical modelling techniques across various time/length scales, after [17, 18].

on surface degradation still needs to be improved greatly. The research here has been conducted with this in mind.

The aim of the current thesis is to convey more accurate predictive capability of high temperature diffusional behaviour in structural materials by modelling at various length scales. The following, linked to three industrial applications outlined in section 1.2, defines the scope of this thesis:

- The vacancy formation free energy in fcc-nickel is calculated by using highly-accurate *ab initio* thermodynamics in chapter 3. This deals with modelling on the atomistic level.

- The oxidation kinetics is predicted for the Ni-Cr system by coupling CALPHAD thermodynamics and diffusional kinetics accounting for defect structures/kinetics in oxide phases (halite, corundum and spinel) and the alloy underneath in chapter 4. This is modelling on the microstructural level.

- Based upon theories of carbon diffusion and Boudouard reaction, temperature-dependent lifetime of a critical Fe-9Cr1Mo nuclear component exposed to CO_2 –

linked with carbon saturation – is predicted in chapter 5. This can be regarded as coupled modelling on the microstructural and mesoscopic levels.

Chapter 2

Literature Survey

2.1 Numerical Modelling Approaches for Diffusional Reactions

This section will describe several materials modelling techniques traditionally used in materials science linked to diffusional reactions, from meso-scale continuous CALPHAD/DICTRA approach, to quantum mechanics looking at atomic/electronic scales.

2.1.1 CALPHAD

Since the late sixties, a new scientific field called computational thermodynamics (or CALPHAD, a portmanteau for **CAL**culation of **PHA**se **D**iagrams) has developed with pioneering works of Kaufman, Ansara and Hillert [19]. The basic idea is to describe the equilibrium state of materials by quantifying and minimising their basic thermodynamic properties, usually Gibbs free energy as a function of pressure, temperature and composition, for phases in the considered system. These quantities are represented by consistent and general mathematical expressions of sound physical meanings (i.e. *thermodynamic models*), with parameters being optimised based on selected thermochemical data (measured by using e.g. calorimetry or electrochemistry), phase diagram (equilibrium

composition & phase fractions) and *ab initio* calculations. This optimisation process is usually referred to as *thermodynamic assessment*. Even with assessed data for low order systems (i.e. binary and ternary), the CALPHAD method shows powerful predictive capabilities extrapolating to multi-component complex systems. Significantly driven by industry, a large scientific community has grown up around CALPHAD consisting of people working with software (algorithm and user interface), physical models and database development to improve the accuracy, the efficiency and the applicability to a wide range of materials. The following paragraph detail some commonly used thermodynamic models which have been utilised in the present work.

Ideal Solution When different species are mixed without considering any inter-molecular or inter-atomic forces, the solution is called an *ideal solution*. The change in Gibbs energy upon mixing the pure species comes only from the increase in its entropy:

$$\Delta^{\text{ideal}}G = -T\Delta S = -RT\sum_i x_i \ln x_i \tag{2.1}$$

Gaseous phases are often modelled in this way.

(Sub-)regular Solution Model If the interactions between mixed species are considered, associated non-zero enthalpy of mixing will contribute to the Gibbs energy of a phase:

$$G = H - TS = {}^{\circ}G_{\text{ref}} + \Delta^{\text{ideal}}G + {}^{\text{E}}G \tag{2.2}$$

where ${}^{\circ}G_{\text{ref}} = \sum x_i {}^{\circ}G_i$ is the *reference Gibbs energy* corresponding to a mechanical mixture of all species in a phase. The terms x_i and G_i are the molar fraction and Gibbs energy of the pure species i, respectively. ${}^{\text{E}}G$ is the *excess Gibbs energy* which denotes the deviation

from ideal behaviour. e.g. for binary system:

$$^{\mathrm{E}}G = \sum_i \sum_{j>i} x_i x_j L_{i,j} \tag{2.3}$$

where the interaction parameters $L_{i,j}$ can be a constant in the regular solution model (with entropy effects symmetric with respect to composition) or can be expanded with *Redlich-Kister polynomials* in the sub-regular solution model [20]:

$$L_{i,j} = \sum_{v=0}^{n} {}^{v}\Phi^{i,j} \left(x_i - x_j\right)^v \tag{2.4}$$

where ${}^{v}\Phi^{i,j}$ is the v^{th} order coefficient describing the interacting between i and j.

Compound Energy Formalism (CEF) A *sublattice phase* can be envisaged as being composed of interlocking sublattices on which the various components can mix. The *sublattice model* is flexible and is particularly useful to describe ordering in metallic system, solutions with complex crystallographic structure (e.g. oxides) and interstitials; for detailed application of the sublattice model, see [21, 22]. The compound energy formalism [23], using general mathematical expressions describing the sublattice model, is often used in the CALPHAD method. To make the mathematics easier, the concept of *constituent array* is introduced [22]. A *constituent array* specifies one or more constituents on each sublattice and is denoted I, while the individual constituents are denoted i, sometimes with a superscript s to denote the sublattice s. The Gibbs energy of each phase is thus described as:

$$G = \sum_{I_0} P_{I_0}(Y) \, {}^{\circ}G_{I_0} + RT \sum_s a_s \sum_i y_i^s \ln\left(y_i^s\right) + {}^{\text{phys}}G + {}^{\mathrm{E}}G \tag{2.5}$$

where I_0 is a constituent array of zeroth order and $P_{I_0}(Y)$ is the corresponding product of the site fractions. The zeroth order constituent array means there is only one constituent on each sublattice (i.e. compound or the *end members*). ${}^{\circ}G_{I_0}$ represents the reference Gibbs energy of the compound I_0. The factor a_s is the number of sites on sublattice s and y_i^s

denotes the site-fraction of constituent i on sublattice s. ${}^{\text{phys}}G$ represents the contribution to the Gibbs energy due to physical properties including the magnetic transitions [24, 25] and ${}^{\text{E}}G$ is the excess Gibbs energy expanded as:

$$ {}^{\text{E}}G = \sum_{i=1}^{n} \sum_{I_i} P_{I_i}(Y) L_{I_i} \tag{2.6} $$

where I_i is a constituent array of i^{th} order and L_{I_i} is the interaction parameters defined by I_i. The interaction parameters can be represented by a Redlich–Kister expansion [20].

The equilibrium state is found by minimising the total Gibbs free energy including all described phases, subject to a set of linear constraints such as thermodynamic conditions, mass balance and charge balance (electroneutrality, if ionic species present as constituents, e.g. solid oxide described in chapter 4) of each phase [26]; this is usually achieved by the *Newton–Raphson scheme*. Software such as Thermo-Calc [27], OpenCalphad [28] and PANDAT [29] possess numerical routines for this.

2.1.2 Density Functional Theory

The foundation of quantum theory is the *many-body* problem of interacting nuclei and electrons which are governed by the *Schrödinger equation* [30]

$$ \hat{H}_{N,e} \Psi_{N,e}(\{\mathbf{R}_i\}, \{\mathbf{r}_i\}) = E_{N,e} \Psi_{N,e}(\{\mathbf{R}_i\}, \{\mathbf{r}_i\}) \tag{2.7} $$

where $E_{N,e}$ is the total energy of the system of interacting particles, $\mathbf{R}_i$ are the coordinates of the N_n nuclei and $\mathbf{r}_i$ those of the N_e electrons. $\Psi_{N,e}$ is the many-body wave function and the Hamiltonian $\hat{H}_{N,e}$ is given by the following equation:

$$ \hat{H}_{N,e} = \hat{T}^{\text{el}} + \hat{T}^{\text{nuc}} + \hat{V}^{\text{el}} + \hat{V}^{\text{nuc}} + \hat{V}^{\text{e-n}} \tag{2.8} $$

The operators on the right are the kinetic energy for the electrons (nuclei) $\hat{T}^{\mathrm{el}}$ ($\hat{T}^{\mathrm{nuc}}$), the electron-electron repulsion $\hat{V}^{\mathrm{el}}$, the nucleus-nucleus repulsion $\hat{V}^{\mathrm{nuc}}$, and the electron-nucleus attraction $\hat{V}^{\mathrm{e\text{-}n}}$ which are given by:

$$\hat{T}^{\mathrm{el}}\left(\{\mathbf{r}_i\}\right) = -\sum_{i}^{N_e} \frac{\hbar^2}{2m_e} \nabla_i^2 \tag{2.9}$$

$$\hat{T}^{\mathrm{nuc}}\left(\{\mathbf{R}_I\}\right) = -\sum_{I}^{N_n} \frac{\hbar^2}{2M_I} \nabla_I^2 \tag{2.10}$$

$$\hat{V}^{\mathrm{el}}\left(\{\mathbf{r}_i\}\right) = \frac{1}{2} \sum_{i}^{N_e} \sum_{j \neq i}^{N_e} \frac{e^2}{4\pi\varepsilon_0 \left|\mathbf{r}_i - \mathbf{r}_j\right|} \tag{2.11}$$

$$\hat{V}^{\mathrm{nuc}}\left(\{\mathbf{R}_I\}\right) = \frac{1}{2} \sum_{I}^{N_n} \sum_{J \neq I}^{N_n} \frac{Z_I Z_J e^2}{4\pi\varepsilon_0 \left|\mathbf{R}_I - \mathbf{R}_J\right|} \tag{2.12}$$

$$\hat{V}^{\mathrm{e\text{-}n}}\left(\{\mathbf{r}_i\}, \{\mathbf{R}_I\}\right) = -\sum_{i}^{N_e} \sum_{I}^{N_n} \frac{Z_I e^2}{4\pi\varepsilon_0 \left|\mathbf{r}_i - \mathbf{R}_I\right|} \tag{2.13}$$

Here $\hbar$ is the reduced Planck constant, m_e the electron mass, e the elementary charge, ε_0 the electric constant, and M_I (Z_I) the mass (proton number) of nucleus I.

In practice, to balance the accuracy and computational cost, the many-body Schrödinger equation is solved numerically by approximating the interactions defined in eq. (2.8); for example the *Born-Oppenheimer approximation* [31] significantly reduces the computational complexity by decoupling electronic terms from descriptions of the nuclei in eq. (2.7), i.e. the configuration of nuclei enters only as external parameters during the minimisation of electronic energy (ground state).

Followed by the pioneering works of Hohenberg, Kohn and Sham, the *density functional theory* (DFT) [32, 33] has evolved as one of the most popular methods for the calculation of electronic structures. By defining electron density as the key variable, the many-body problem is mapped onto a system of noninteracting electrons moving in an effective potential which is determined by the electron density, consistent with:

$$\left\{ -\frac{\hbar}{2m} \nabla^2 + v_{\mathrm{eff}}^{\mathrm{KS}}\left(\mathbf{r}\right) \right\} \varphi_i\left(\mathbf{r}\right) = \varepsilon_i \varphi_i\left(\mathbf{r}\right) \tag{2.14}$$

where $\varphi_i(\mathbf{r})$ is the *Kohn-Sham orbital (wave function)* with corresponding energy ε_i, which can be used to construct the electron density $\rho(\mathbf{r})$:

$$\rho(\mathbf{r}) = \sum_i f_i |\varphi_i(\mathbf{r})|^2 \tag{2.15}$$

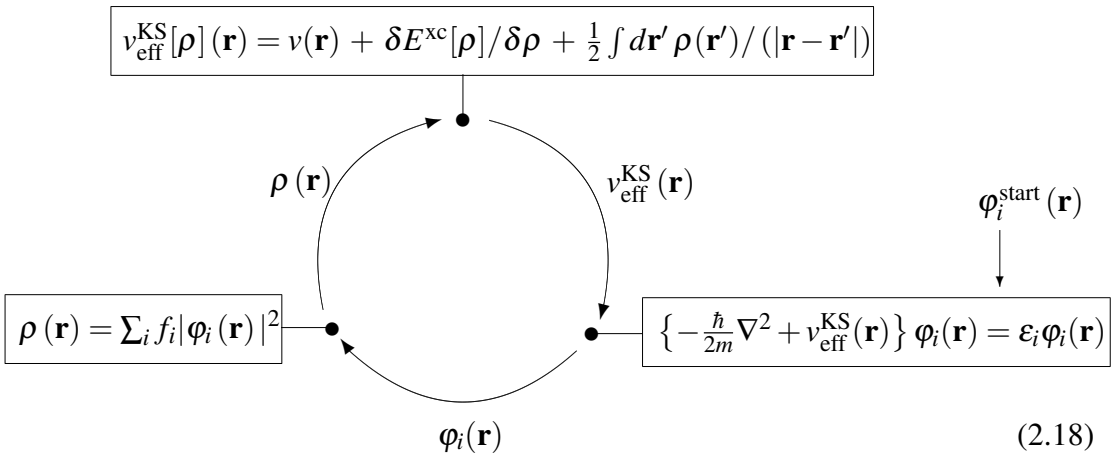
where f_i is the *Fermi-Dirac function* which describes the probability of occupancy of energy levels by Fermions and guarantees the antisymmetry with respect to particle interchange for non-interacting electrons:

$$f_i = \left[1 + \exp\left(\frac{\varepsilon_i - \varepsilon_\mathrm{F}}{k_\mathrm{B}T}\right)\right]^{-1} \tag{2.16}$$

where ε_F is the Fermi energy or level. The *Kohn-Sham potential* $v_\mathrm{eff}^\mathrm{KS}$ is defined by

$$v_\mathrm{eff}^\mathrm{KS}(\mathbf{r}) = v_\mathrm{ext}(\mathbf{r}) + v_\mathrm{H}(\mathbf{r}) + v_\mathrm{XC}(\mathbf{r}) \tag{2.17}$$

where the external potential $v_\mathrm{ext}(\mathbf{r})$ (due to fixed nuclei) and the Hartree potential $v_\mathrm{H}(\mathbf{r})$ which describes the classical electrostatic Coulomb interactions is explicitly defined, while the form of the *exchange-correlation* functional $v_\mathrm{XC}(\mathbf{r})$ which contains all many-particle interactions are not known exactly. Equations (2.14) to (2.17) are solved iteratively so that $\varphi_i(\mathbf{r})$, $v_\mathrm{eff}^\mathrm{KS}$ and $\rho(\mathbf{r})$ converge, as shown below in the *self consistency cycle* (2.18).



(2.18)

Perdew *et al* classified the functional form of $v_\mathrm{XC}(\mathbf{r})$ according to the number and kind of their local ingredients [34]; the *local density approximation* (LDA) in which

$v_{\mathrm{XC}}(\mathbf{r})$ depends only on the local electronic density [33] and the *generalised-gradient approximation* (GGA) in which the $v_{\mathrm{XC}}(\mathbf{r})$ depends on both the local electron density and its gradient [35–37] are two good approaches for metallic systems. For LDA approximation, $v_{\mathrm{XC}}(\mathbf{r})$ is obtained by fitting to a Homogeneous Electron Gas (HEG) [35]. For GGA approximation, a range of parameterisations are available in which those formulated by Perdew and Wang (PW91) [38] and by Perdew, Burke and Ernzerhof (PBE) [37] are two most prominent approaches.

Nowadays, with the development of commercial (e.g. CASTEP [39], VASP [40, 41]) and open-source (e.g. Quantum ESPRESSO [42]) software packages, computation of the energies and properties at $T = 0\,\mathrm{K}$ has become very straightforward. The calculated total energy as a function of volume and crystal structure can be directly linked to various properties, e.g. bulk modulus [43], stacking-fault energy (SFE) [44], anti-phase boundary (APB) energy [45] and the gamma surface for dislocation dynamics modelling [46].

2.1.3 *Ab initio* Thermodynamics

To bridge CALPHAD with DFT, extensions of DFT from the ground state ($T = 0\,\mathrm{K}$) to finite temperature requires the total entropy S^{total} to be calculated

$$S(V,T) = S^{\mathrm{total}} = S^{\mathrm{conf}} + S^{\mathrm{vib}} + S^{\mathrm{el}} + S^{\text{el-vib}} + S^{\mathrm{mag}} \tag{2.19}$$

where S^{conf}, S^{vib}, S^{el}, $S^{\text{el-vib}}$ and S^{mag} are the configurational entropy, atomic vibrational entropy, electronic entropy, entropy due to the adiabatic coupling of electrons and atomic vibrations [47], and the magnetic entropy, respectively. They can be achieved either by approximate phonon theories of lattice vibrations, or by solving higher orders (i.e. beyond the second order of Taylor expansion) exactly by using numerical methods; the latter can be classified into two conceptually distinct routes: classical statistical approaches including the *Monte Carlo method* (MC) & the *Molecular Dynamics simulations* (MD) [48], and the *quantum mechanical perturbation theory*.

Approximate theories of lattice vibrations

The quantum theory was firstly applied to the motion of atoms in the solid by Einstein – the *Einstein solid* [49] – which assumes all atoms were independent harmonic oscillators with the same frequency ω_0. It gives the Helmholtz free energy of each atom oscillating in three dimensions by:

$$F_{\mathrm{qm}}^{\mathrm{atom}}(T) = 3\frac{\hbar\omega_0}{2} + 3k_{\mathrm{B}}T\ln\left(1-\exp\left(-\beta\hbar\omega_0\right)\right) \tag{2.20}$$

where $\beta = (k_{\mathrm{B}}T)^{-1}$, k_{B} is the Boltzmann constant. Comparing with that from a classical harmonic oscillator:

$$F_{\mathrm{cl}}^{\mathrm{atom}}(T) = 3k_{\mathrm{B}}T\ln\left[\frac{\hbar\omega_0}{k_{\mathrm{B}}T}\right] \tag{2.21}$$

it differs by a zero point energy at $T = 0\,K$ due to the Heisenberg's uncertainty principle, as shown in the example calculations for Ni with assumed $\hbar\omega_0 = 22\,\mathrm{meV}$ (compare to a phonon dispersion of Ni in [50]) by using both approaches in fig. 2.1 (a); the entropy $S(T) = -\left(\frac{\partial F}{\partial T}\right)_V$ calculated for the quantum mechanical harmonic oscillator gives better consistency with the thermodynamic third law (i.e. $S(T = 0\,K) = 0$); the isochoric heat capacity $C_V(T) = T\left(\frac{\partial S}{\partial T}\right)_V$ derived from the quantum mechanical harmonic oscillator shows better consistency with experimental measurements [50].

Equation (2.20) can be generalised to coupled harmonic oscillators by summing over all wave vectors $\mathbf{k}$:

$$F_{\mathrm{qm}}^{\mathrm{vib}}(T) = \frac{1}{N}\sum_{\mathbf{k}}^{3N}\left\{\frac{\hbar\omega_{\mathbf{k}}}{2} + k_{\mathrm{B}}T\ln\left[1-\exp\left(-\beta\hbar\omega_{\mathbf{k}}\right)\right]\right\} \tag{2.22}$$

The *quasiharmonic* approach [51, 52] (reviewed in [53]) is based on the volume-dependent harmonic potentials; the central equation is a Taylor expansion of the electronic

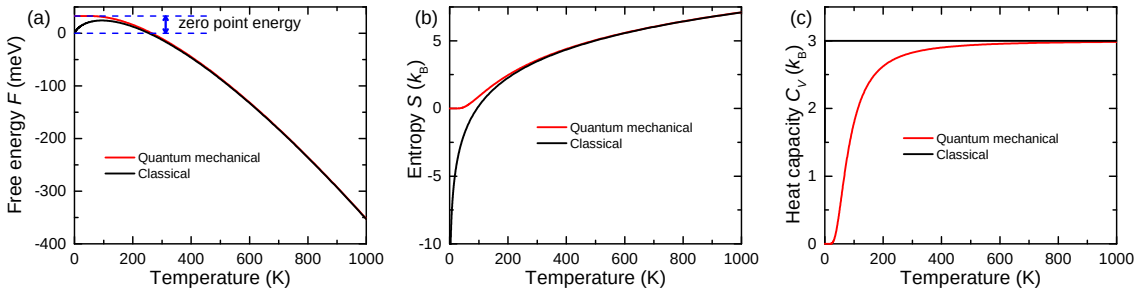


Fig. 2.1 Comparison of the classical and quantum mechanical harmonic oscillator assuming a single frequency $E = h\nu = \hbar\omega_0 = 22\,\mathrm{meV}$, for (a) Helmholtz free energy $F^{\mathrm{atom}}(T)$, (b) Entropy $S(T)$ and (c) Isochoric heat capacity $C_V(T)$.

free energy F^{el} around the $T = 0\,\mathrm{K}$ equilibrium nuclei positions $\left\{\mathbf{R}_I^0\right\}$:

$$F^{\mathrm{el}}\left(\{\mathbf{R}_I\},\Omega,T\right) = F_0^{\mathrm{el}}(\Omega,T) + \underbrace{\frac{1}{2!}\sum_{I,J}^{N_n}\sum_{\alpha,\beta}^{3} U_{I,\alpha}U_{J,\beta}\left[\frac{\partial^2 F^{\mathrm{el}}\left(\{\mathbf{R}_I\},\Omega,T\right)}{\partial R_{I,\alpha}\partial R_{J,\beta}}\right]_{\{\mathbf{R}_I^0\}}}_{F^{\mathrm{h}}} + \underbrace{\frac{1}{3!}\sum_{I,J,K}^{N_n}\sum_{\alpha,\beta,\gamma}^{3} U_{I,\alpha}U_{J,\beta}U_{K,\gamma}\left[\frac{\partial^3 F^{\mathrm{el}}\left(\{\mathbf{R}_I\},\Omega,T\right)}{\partial R_{I,\alpha}\partial R_{J,\beta}\partial R_{K,\gamma}}\right]_{\{\mathbf{R}_I^0\}} + \ldots}_{F^{\mathrm{ah}}} \tag{2.23}$$

where Ω denotes the volume of the supercell; $I,J,K\ldots$ run over all N_n nuclei, $\alpha,\beta,\gamma\ldots$ run over all three coordinates. The harmonicity is contributed by the second order term while the anharmonicity is refereeing to explicit deviations of the atomic potential from a simple harmonic dependence. Defining the dynamical matrix $\mathbf{D}$, with the components:

$$D_{I\alpha,J\beta}(\Omega,T) := \frac{1}{M_I}\left[\frac{\partial^2 F^{\mathrm{el}}\left(\{\mathbf{R}_I\},\Omega,T\right)}{\partial R_{I,\alpha}\partial R_{J,\beta}}\right]_{\{\mathbf{R}_I^0\}} \tag{2.24}$$

we have

$$F^{\mathrm{qh}} := \mathbf{UD}(\Omega,T)\,\mathbf{UM}/2 \tag{2.25}$$

where the displacement vectors $\mathbf{U}$ and mass vector $\mathbf{M}$ comprise hereby the displacements and masses of all nuclei $\{\mathbf{U}_I\}$ and $\{M_I\}$, respectively. The dynamical matrix can be calculated, for example, by the *direct force constant* method [54] which obtains the real space $\mathbf{D}$ by utilising finite differences of forces:

$$D_{I\alpha,J\beta}\left(\Omega,T\right) = -\frac{1}{M_I}\left[\frac{\partial F^{\mathrm{HF}}_{I,\alpha}\left(\{\mathbf{R}_I\},\Omega,T\right)}{\partial R_{J,\beta}}\right]_{\{\mathbf{R}^0_I\}} \tag{2.26}$$

where the force F can be calculated giving a suitable displacement ΔR (typically within $0.01 a_0$)

$$F^{\mathrm{HF}}_{I,\alpha}\left(\{\mathbf{R}_I\},\Omega,T\right) = \frac{1}{\Delta R}\left[F^{\mathrm{el}}\left(R_{1,1},\ldots,R_{I,\alpha}+\Delta R,\ldots,R_{N_n,3},\Omega,T\right) - F^{\mathrm{el}}\left(\{\mathbf{R}_I\},\Omega,T\right)\right] \tag{2.27}$$

HF forces from Kohn-Sham calculations for different Ω

$$D^{0\mathrm{K}}_{I\alpha,J\beta}(\Omega) = -(M_I\Delta R)^{-1}\, F^{\mathrm{HF,0K}}_{I,\alpha}(R^0_{1,1},\ldots,R^0_{J,\beta}+\Delta R,\ldots,R^0_{N_n,3},\Omega) \tag{2.28}$$

$$D^{0\mathrm{K}}_{\mathbf{G}^{\mathrm{sc}},\alpha\beta}(\Omega) = N_n^{-1}\sum_{I,J}^{N_n} D^{0\mathrm{K}}_{I\alpha,J\beta}(\Omega)\, e^{i\mathbf{G}^{\mathrm{sc}}\cdot\left(\mathbf{R}^0_I-\mathbf{R}^0_J\right)} \tag{2.29}$$

$$\mathbf{D}^{0\mathrm{K}}_{\mathbf{G}^{\mathrm{sc}}}(\Omega)\,\mathbf{w}_{\mathbf{G}^{\mathrm{sc}},s} = (\omega^{0\mathrm{K}}_{\mathbf{G}^{\mathrm{sc}},s})^2(\Omega)\,\mathbf{w}_{\mathbf{G}^{\mathrm{sc}},s} \tag{2.30}$$

Kohn-Sham calculations for different Ω and T

$$F(\Omega,T) \approx F^{\mathrm{el}}(\{\mathbf{R}^0_I\},\Omega,T) + \underbrace{\sum_{\mathbf{G}^{\mathrm{sc}}}^{\mathrm{prBZ}'}\sum_{s}^{3}\left\{\frac{1}{2}\hbar\,\omega^{0\mathrm{K}}_{\mathbf{G}^{\mathrm{sc}},s}(\Omega) + k_{\mathrm{B}}T\ln\left[1-\exp\left\{-\beta\hbar\,\omega^{0\mathrm{K}}_{\mathbf{G}^{\mathrm{sc}},s}(\Omega)\right\}\right]\right\}}_{= F^{\mathrm{qh,0K}}(\Omega,T) = E^{\mathrm{zp,0K}}(\Omega) + TS^{\mathrm{qh,0K}}(\Omega)} \tag{2.31}$$

$$F(\Omega,T)\,/N_n = F(V,T)\,. \tag{2.32}$$

Then by Fourier transforming the real space dynamical matrix $\mathbf{D}$ to reciprocal dynamical matrix $\mathbf{D}_{\mathbf{G}^{\mathrm{sc}}}$ (eq. (2.29)), we can obtain the phonon frequencies $\omega^{0\mathrm{K}}_{\mathbf{G}^{\mathrm{sc}},s}$ by diagonalising $\mathbf{D}_{\mathbf{G}^{\mathrm{sc}}}$ (eq. (2.30)). Then by combining with previously derived eq. (2.22), we can have the

quasiharmonic free energy (eq. (2.31)). The diagram above summarises the key quantities in deriving the quasiharmonic free energy (adopted from [55]). The quasi-harmonic approximation is conceptually well defined; various open-source software packages (e.g. Phonopy [56]) can achieve phonon calculations at harmonic and quasi-harmonic levels.

Solving for lattice vibrations numerically exactly

The quantum perturbation theory explicitly includes the high order terms in the Taylor expansion of Born-Oppenheimer surface successively order by order, thus capturing the anharmonic contributions, as seen in recent reviews [57, 58]. However, this type of approach requires a large amount of atomic configurations to be sampled to achieve the desired accuracy (say, below 1 meV/atom), making it computationally expensive.

The classical statistical approaches (by e.g. MD or MC), however, explicitly samples the full nuclei phase space; an additional *thermodynamic integrations* scheme [59, 60] is required to obtain the vibrational entropy contribution. It allows coupling between different systems with distinct partition functions, e.g. an Einstein reference, to e.g. the full DFT potential. Typically a linear coupling is used:

$$U_\lambda = (1-\lambda)U_0 + \lambda U_1 \tag{2.33}$$

where U_0 is the energy of the reference system, U_1 of the target system (i.e. full DFT), and λ the coupling parameter. The classical statistical mechanics gives:

$$\frac{\mathrm{d}F}{\mathrm{d}\lambda} = \left\langle \frac{\mathrm{d}U_\lambda}{\mathrm{d}\lambda} \right\rangle_\lambda \tag{2.34}$$

where $\langle ... \rangle_\lambda$ is the canonical ensemble average for a given potential U_λ. The difference of the free energy of two systems thus is then given by:

$$\Delta F = \int_0^1 \langle U_1 - U_0 \rangle_\lambda \, \mathrm{d}\lambda \tag{2.35}$$

Typically, an extended version of classical MD, Langevin dynamics (LD) [61], is used to allow for controlling the temperatures in the system. The *up-sampled thermodynamic integration using Langevin dynamics* (UP-TILD) method [62] has been proposed to speed up DFT-MD calculations by dividing them into two consecutive steps: (1) thermodynamic integration from a reference potential (e.g. Einstein) to low converged *ab initio* sampling by using LD; (2) perturbative approach – the up-sampling – to calculate the free energy difference between low&high converged DFT potentials, based on the previously obtained sampling points as a function of λ. An intermediate reference state – by using interatomic potentials, e.g. embedded atom method (EAM) [63] or modified EAM (MEAM) [64–66] – was introduced into the first step in the *two-stage upsampled thermodynamic integration using Langevin dynamics* (TU-TILD) method [67] to further speed up calculations. The TU-TILD method can be summarised as:

$$F^{\mathrm{ah}} = \int_0^1 \mathrm{d}\lambda_1 \left[\left\langle E^{\mathrm{pot}} - E^{\mathrm{qh/h}} \right\rangle_{\lambda_1} \right] + \int_0^1 \mathrm{d}\lambda_2 \left[\left\langle E^{\mathrm{DFT}}_{\mathrm{low}} - E^{\mathrm{pot}} \right\rangle_{\lambda_2} + \langle \Delta E \rangle^{\mathrm{UP}}_{\lambda_2} \right] \tag{2.36}$$

where the first term provides the difference between the free energies described by the DFT quasiharmonic dynamical matrix (or harmonic potential) and by the interatomic potential; the total energy is calculated from the interatomic potential E^{pot} and from the harmonic or quasiharmonic dynamical matrix $E^{\mathrm{qh/h}}$ (both referenced to their own total energy at $T = 0\,\mathrm{K}$) using the linearly coupled force from both approaches in the first LD simulation. The second LD simulation uses the forces varying linearly from potential forces ($\lambda_2 = 0$) to full DFT forces ($\lambda_2 = 1$), giving the the second ensemble average. N^{UP} up-sampled configurations are averaged to assess the offset of the Born-Oppenheimer surface $\langle \Delta E \rangle^{\mathrm{UP}}$:

$$\langle \Delta E \rangle^{\mathrm{UP}}_{\lambda_2} = \frac{1}{N^{\mathrm{UP}}} \sum_i^{N^{\mathrm{UP}}} \left(E^{\mathrm{DFT}}_{\mathrm{high}} - E^{\mathrm{DFT}}_{\mathrm{low}} \right) \tag{2.37}$$

It should be noted that the interatomic potential is fitted specifically to the DFT calculations for the equilibrium configuration (at different volumes), thus giving equilibrium starting

point for the second LD simulations if a *pre-equilibrium* procedure (using the interatomic potential) is applied prior to LD steps.

Electronic free energy and its coupling with lattice vibrations

Electronic free energy can be approximated by the finite temperature extension of DFT [68] which weights the charge density (entering into the SCF cycle) with the Fermi-Dirac occupation number (eqs. (2.15) and (2.16)). The electronic free energy F^{el} is thus given as:

$$F^{\mathrm{el}}(T) = U^{\mathrm{el}}(T) - TS^{\mathrm{el}}(T) \tag{2.38}$$

with the internal energy $U^{\mathrm{el}}(T)$ written as [69]:

$$U^{\mathrm{el}}(T) = \sum_i f_i \varepsilon_i - E_{\mathrm{dc}} \tag{2.39}$$

where E_{dc} is double counting corrections. The configurational entropy is written as:

$$S^{\mathrm{el}}(T) = -\gamma k_{\mathrm{B}} \sum_i [f_i \ln f_i + (1-f_i)\ln(1-f_i)] \tag{2.40}$$

where $\gamma = 1$ is for spin-polarised systems and $\gamma = 2$ for spin-unpolarised systems.

Detailed comparisons for $3d$, $4d$, and $5d$ transition metals by the SCF finite temperature DFT approach, the fixed density-of-states (DOS) approximation [47] and the Sommerfeld approximation [70] have been summarised in [47].

The free energy due to coupling between electrons and lattice viberations $F^{\mathrm{el-vib}}(V,T)$ can be approximated by averaging the electronic free energy (referenced to the electronic internal energy U^{el} at $T = 0\,\mathrm{K}$) of every N up-sampled atomic configuration in the TU-

TILD method [47]:

$$F^{\mathrm{el-vib}}(T) = \frac{1}{N}\sum_{i}^{N}\Delta F_i^{\mathrm{el}}(T) \tag{2.41}$$

$$\Delta F_i^{\mathrm{el}}(T) = F_i^{\mathrm{el}}(T) - U_i^{\mathrm{el}}(T = 0\,\mathrm{K}) \tag{2.42}$$

In practice $F_i^{\mathrm{el}}(T)$ calculations are done by Fermi-smearing while the $U_i^{\mathrm{el}}(T = 0\,\mathrm{K})$ need to be calculated by using the Methfessel-Paxton scheme [71] for better numerical stabilities.

2.2 Importance of Diffusion

This section will detail modelling for high temperature diffusion, including the theoretical background of diffusion in binary and multicomponent metallic and oxide systems, diffusion-controlled phase transformations, and analytical/numerical methods solving diffusion equations.

2.2.1 Fick's Laws

Diffusion is closely related to the irreversible process of mixing. It was firstly observed that the liquid/gas tend to mix no matter if stirring and convection are avoided. The initial basis for diffusion theory was proposed by Adolf Fick in 1855 [72] assuming that the diffusive flux of solute to be proportional to the concentration gradient. e.g. in an isothermal isobaric one-phase binary system with diffusion of a species k:

$$J_k = -D_k \nabla c_k \tag{2.43}$$

where D_k is the chemical diffusion coefficient, J_k the flux of k, c_k the concentration of k.

Equation (2.43) is only valid for an ideal solution. It was then realised that the driving force for diffusion should be the gradient of chemical potential μ_k, i.e. the force acting on

k atoms [73, 74]:

$$J_k = -L_k \nabla \mu_k \tag{2.44}$$

where L_k is a phenomenological kinetic parameter which is link to D_k (by applying the chain law) as:

$$D_k = L_k \frac{\partial \mu_k}{\partial c_k} \tag{2.45}$$

Approximating the flux proportional to force (i.e. *the linear relation*) near equilibrium, eq. (2.44) is analogous with Ohm's law for electrical conduction and Fourier's law for heat conduction, and its continuity can be maintained by the mass conservation law, i.e. the *Fick's Second Law* which reads:

$$\dot{c_k} = \nabla \cdot (-J_k) \tag{2.46}$$

2.2.2 Diffusion in Multi-component System

To couple various irreversible processes, a more general description of the flux eq. (2.44) under the linear relation was then formulated by Onsager [75, 76]:

$$J_k = -\sum_j \left(L_{kj} X_j\right) \tag{2.47}$$

where J_k stands for any type of flux, e.g. diffusion of a species, of heat or electric charge and X_j is a force, e.g. a gradient of chemical potential, temperature or electric potential. Here j stands for dimension and (or) type of forces. Equation (2.47) can also be applied to the diffusion in a multi-component system

$$J_k = -\sum_{j=1}^{N} \left(L_{kj} \nabla \mu_j\right) \tag{2.48}$$

with its entropy production (*dissipation function*) given by [77]:

$$\dot{S} = \frac{1}{T}\sum_{k=1}^{N} J_k \nabla \mu_k \tag{2.49}$$

It should be noted that $\dot{S}$ is a physical quantity which measures how the system approaches equilibrium by irreversible processes, and it is invariant to frame of reference (e.g. *number-fixed*, *volume-fixed* or *lattice-fixed frame of reference*).

For crystalline phases, if assuming diffusion occurs by atoms jumping into neighbouring vacant lattice sites without any correlation effects (as detailed in section 3.2) and there is a random distribution of vacancies which are in equilibrium, the flux eq. (2.48) can be re-written in a lattice-fixed frame of reference as [78]:

$$J_k = -c_k y_{\mathrm{Va}} \Omega_{k\mathrm{Va}} \nabla \mu_k \tag{2.50}$$

where y_{Va} is the fraction of vacant lattice sites on the sublattice where k is dissolved, $\Omega_{k\mathrm{Va}}$ is the rate of exchange between a k atom and its neighbouring vacancy. The off-diagonal terms of L_{kj} are cancelled assuming no chemical driving force of one component to the diffusive flux of another component [77].

Two situations follow from eq. (2.50) considering the site of solution k:

- k is substitutional: as $y_{\mathrm{Va}} \to 0$, the mobility is defined as $M_k = y_{\mathrm{Va}}\Omega_{k\mathrm{Va}}$ with flux derived as $J_k = -c_k M_k \nabla \mu_k$.
- k is interstitial: the mobility is defined $M_k = \Omega_{k\mathrm{Va}}$, so the flux is $J_k = -c_k y_{\mathrm{Va}} M_k \nabla \mu_k$ with y_{Va} close to unity.

where the mobility M_k is described in an Arrhenius way following the absolute reaction theory [79]:

$$M_k = \frac{M_k^{\circ}}{RT} \exp\left(-\frac{Q_k}{RT}\right) \tag{2.51}$$

where M_k° and Q_k are the frequency factor and the activation energy, respectively.

The above phenomenological model (starting from eq. (2.50)) is widely used in the *DIffusion-Controlled phase TRAnsformation* (DICTRA) software package to describe phases without complex crystalline structure (i.e. no phase constituents other than elements are allowed), and both compositional-dependent parameters (M_k° and Q_k) are stored in the mobility database, following the similar description of CEF in CALPHAD, i.e. the sum of a linear combination of the end-point values and a Redlich-Kister polynomial.

2.2.3 Diffusion in Oxides

Modelling of diffusion in oxides requires the description of both their defect chemistry and their electro-chemical transport. The theoretical framework was first outlined by Carl Wagner (from [80] to [81]) who assumed that the migration of ions in oxide are mostly mediated by vacancies (at both substitutional and interstitial sites) whose concentrations are strongly dependent on defect equilibria. He also assumed the diffusive flux to be driven by the gradient of both chemical potential and electric potential:

$$J_k = -L_k \left(\nabla \mu_k + q_k \mathscr{F} \nabla E \right) \tag{2.52}$$

where E is the electric potential, q_k the charge of species k and $\mathscr{F}$ is the Faraday constant. These give the *Wagner's theory* which provides a mechanistic understanding of high-temperature oxidation kinetics of metals.

Defect structures of oxides

Following Wagner's pioneering work on oxidation kinetics, Per Kofstad systematically reviewed the chemistry of defects in oxides [82, 83]. Different from the defects present in metals – as all the metal oxide are ionic in nature – the charged particles and vacancies should be considered as well, with the global electroneutrality always being maintained dur-

ing the reaction. The Kröger-Vink (K-V) notation [84] (summarised in the Nomenclature) is typically used to express the defect structure.

For highly stoichiometric ionic compounds, two major types of intrinsic point defects are the Schotty and Frenkel defects.

- **Schotty defects**: With equivalent amounts of vacancies on both cationic and anionic sub-lattices, both anions and cations are expected to be mobile.

$$\varnothing \Leftrightarrow V_O^{\cdot\cdot} + V_M^{''} \tag{2.53}$$

- **Frenkel defects**: Either cations or anions are mobile with equal activities of cations vacancies & interstitials or anions vacancies & interstitials, respectively.

$$\text{Mobile cations} : \varnothing \Leftrightarrow M_i^{\cdot\cdot} + V_M^{''} \tag{2.54}$$

$$\text{Mobile anions} : \varnothing \Leftrightarrow O_i^{''} + V_O^{\cdot\cdot} \tag{2.55}$$

Most oxides, however, are non-stoichiometric in nature to support simultaneous migration of ions and electrons during the oxidation reaction. Either anions or cations are presumed to exhibit variable valencies on its sub-lattice in order to maintain the electroneutrality of compounds. Similar to the classification of semiconductors, two classes of oxide are defined based on the type of majority carriers:

- **n-type**: The electrical charge is transferred mainly by negative carriers. Either metal excess ($M_{1+\delta}O$) or oxygen deficit ($MO_{1-\delta}$) may exhibit. (1) Metal excess. Part of unpartnered metal ions from a perfect oxide crystal leave the cation lattice and enter interstitial sites, together with negative charged oxygen ions entering the conduction band. Interstitial metal ions may show different charges, which influence the dependency of electrical conductivity on the partial pressure of oxygen. (2) Oxygen deficit. It can be explained as the discharge and subsequent evaporation

of an oxygen ion; the electrons enter the conduction band and a vacancy is created on the anion lattice. Neutral ($V_O^{\times}$), singly charged ($V_O^{\cdot}$) and doubly charged ($V_O^{\cdot\cdot}$) vacancies may coexist in the oxide.

- **p-type**: The electrical charge is transferred mainly by positive carriers. Either metal deficit ($M_{1-\delta}O$) or oxygen excess may exhibit ($MO_{1+\delta}$). (1) Metal deficit. Vacancies are formed on the cation lattice, together with electron holes ($h^{\cdot}$) in the form of metal ions with higher valence. (2) Oxygen excess. Interstitial oxygen ions and electron holes are presented.

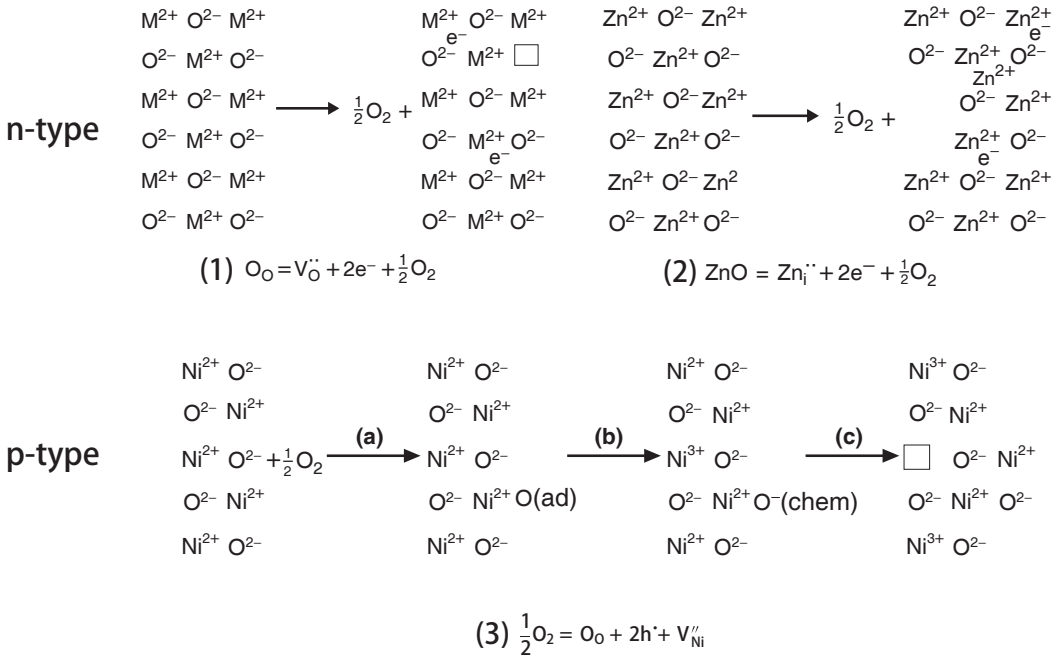


Fig. 2.2 Different types of non-stoichiometric ionic oxides: (1) Oxygen-deficit n-type; (b) Metal-excess n-type; (c) Metal-deficit p-type [85].

Figure 2.2 shows examples of different types of non-stoichiometric oxides. From each defect equilibrium as noted, it is possible to correlate a property measurement (Θ) – such as the electrical conductivity (κ), diffusivity (D) and density (ρ) – with thermodynamic activities of charge carriers ($[e']$ or $[h^{\cdot}]$) which are functions of partial pressure of oxygen

(P_{O_2}) depending on the charge of dominated carriers.

$$\text{n-type} : \Theta \propto [e'] \propto P_{O_2}^{-1/k}, \quad k > 0 \tag{2.56}$$

$$\text{p-type} : \Theta \propto [h^{\cdot}] \propto P_{O_2}^{1/k}, \quad k > 0 \tag{2.57}$$

Following the CALPHAD spirit, Naraghi [86] recently used the general sublattice formalism (CEF) to describe defect structure in typical oxides, as summarised in table 2.1; the Kröger-Vink diagrams, which show the P_{O_2} dependencies of defect concentrations, thus can be well described.

Table 2.1 Kröger-Vink notation and sublattice formalism describing typical defect structure in binary oxides [86]. k describes the P_{O_2}-dependency of correlated properties as defined in eqs. (2.56) and (2.57).

Oxide type	Defect structure	Kröger-Vink notation	Sublattice formalism	k
n-type	Oxygen deficit $MO_{1-\delta}$	$O_O \Leftrightarrow V_O^{\cdot\cdot} + 2e' + \frac{1}{2}O_2$	$\left[M^{+2}, M^{+1}\right]_1 \left[O^{-2}, Va\right]_1$	-6
		$O_O \Leftrightarrow V_O^{\cdot} + e' + \frac{1}{2}O_2$	$\left[M^{+2}, M^{+1}\right]_1 \left[O^{-2}, Va^{-1}\right]_1$	-4
		$O_O \Leftrightarrow V_O^{\times} + \frac{1}{2}O_2$	$\left[M^{+2}\right]_1 \left[O^{-2}, Va^{-2}\right]_1$	-2
	Metal excess $M_{1+\delta}O$	$M_M^{\times} O_O^{\times} \Leftrightarrow \frac{1}{2}O_2 + M_i^{\cdot\cdot} + 2e'$	$\left[M^{+2}, M^{+1}\right]_1 \left[Va, M^{+2}\right]_1 \left[O^{-2}\right]_1$	-6
		$M_M^{\times} O_O^{\times} \Leftrightarrow \frac{1}{2}O_2 + M_i^{\cdot} + e'$	$\left[M^{+2}, M^{+1}\right]_1 \left[Va, M^{+1}\right]_1 \left[O^{-2}\right]_1$	-4
		$M_M^{\times} O_O^{\times} \Leftrightarrow \frac{1}{2}O_2 + M_i^{\cdot}$	$\left[M^{+2}\right]_1 [Va, M]_1 \left[O^{-2}\right]_1$	-2
p-type	Metal deficit $M_{1-\delta}O$	$\frac{1}{2}O_2 \Leftrightarrow O_O + 2h^{\cdot} + V_M''$	$\left[M^{+2}, M^{+3}, Va\right]_1 \left[O^{-2}\right]_1$	6
		$\frac{1}{2}O_2 \Leftrightarrow O_O + h^{\cdot} + V_M'$	$\left[M^{+2}, M^{+3}, Va^{+1}\right]_1 \left[O^{-2}\right]_1$	4
		$\frac{1}{2}O_2 \Leftrightarrow O_O + V_M^{\times}$	$\left[M^{+2}, Va^{+2}\right]_1 \left[O^{-2}\right]_1$	2
	Oxygen excess $MO_{1+\delta}$	$\frac{1}{2}O_2 \Leftrightarrow O_i'' + 2h^{\cdot}$	$\left[M^{+2}, M^{+3}\right]_1 \left[O^{-2}\right]_1 \left[Va, O^{-2}\right]_1$	6
		$\frac{1}{2}O_2 \Leftrightarrow O_i' + 1h^{\cdot}$	$\left[M^{+2}, M^{+3}\right]_1 \left[O^{-2}\right]_1 \left[Va, O^{-1}\right]_1$	4
		$\frac{1}{2}O_2 \Leftrightarrow O_i'$	$\left[M^{+2}\right]_1 \left[O^{-2}\right]_1 [Va, O]_1$	2

When impurities (of cations) present in oxides, the effective valence of cations, concentrations or thermodynamic activities of each species, and the diffusional kinetics may be changed; such effects are summarised in table 2.2.

Table 2.2 The effect of substitutionally dissolved foreign cations on the defect equilibrium (summarised based on [87]).

Oxide type	Defect structure	Dissolving cations with higher valence		Dissolving cations with lower valence	
n-type	Oxygen deficit	$[e^{'}] \downarrow$	$[V_O^{\cdot\cdot}] \uparrow$	$[e^{'}] \uparrow$	$[V_O^{\cdot\cdot}] \downarrow$
	Metal excess		$[M_i^{\cdot\cdot}] \uparrow$		$[M_i^{\cdot\cdot}] \downarrow$
p-type	Metal deficit	$[h^{\cdot}] \uparrow$	$[V_M^{''}] \downarrow$	$[h^{\cdot}] \downarrow$	$[V_M^{''}] \uparrow$
	Oxygen excess		$[O_i^{''}] \downarrow$		$[O_i^{''}] \uparrow$

Transport Mechanisms

The transport of species in the oxide takes place either through point defects (e.g. vacancies and interstitial ions) or along line and surface defects (e.g. grain boundaries, dislocations, inner and outer surfaces). The relative contributions of the different types of diffusion depend on the temperature, partial pressure or activities of the constituents, microstructure etc.

Based on Wagner's work on diffusion in oxides, Hallström *et al* extended the current CALPHAD lattice vacancy-mediated diffusion model (as described in section 2.2.2) to account for the diffusion of a specific species in each sub-lattice, and applied to the Fe-O systems [88–90]; the so-called *general diffusion model* thus unifies the descriptions for diffusion in metal & oxides. The flux of component j in phase r is given as:

$$J_j^r = -M_j^r c_j \nabla \mu_j \tag{2.58}$$

where the effective mobility M_j^r of component j in phase r is then given by:

$$M_j^r = \frac{\sum_s a_s^r \sum_k b_{jk} y_k^{rs} z_{\mathrm{Va}}^{rs} M_{k\mathrm{Va}}^{rs}}{\sum_s a_s^r \sum_k b_{jk} y_k^{rs}} \tag{2.59}$$

where s is sublattice index and k is species index. The other parameters are defined as follows:

- $M_{k\mathrm{Va}}^{rs}$ is the mobility of species k on sublattice s in phase r.
- a_s^r is the number of sites on sublattice s in phase r.
- b_{jk} is the number of moles of component j per mole formula unit of species k.
- y_k^{rs} is the site fraction of species k on sublattice s in phase r
- z_{Va}^{rs} is identical with y_{Va}^{rs} if vacancy is a defined constituent on the sublattice, otherwise it is set equal to one.

If any species transport independently within its original sub-lattice (i.e. no jumps across different sub-lattices) and are mediated by the vacancy presented in such sub-lattice, we can have the flux description of each species consistent with eq. (2.50) defined for each sub-lattice where the chemical potential is defined with respect to the site fraction. Under local-equilibrium conditions (assumption), the chemical potential of a component (with respect to the mole fraction of a component) is equal to the chemical potential of each its species (with respect to the site fraction of such species). It is thus reasonable to calculate the effective flux of a component only by summing up the mobility contributed from each its species (e.g. different charge states) at each sub-lattice (i.e. the effective mobility defined in eq. (2.59)). Details of the model have been published in [91] as part of this work in this thesis; it can also be found in section 4.3.1.

Above kinetic parameters can be directly linked with tracer diffusion experiments. If assuming the tracer distributes randomly among each sublattice, we can have following

expression based on the Einstein relation (kinetic theory) [74, 92]:

$$D_j^{*r} = RTM_j^r \tag{2.60}$$

It should be noted that above CALPHAD approaches for lattice diffusion in oxides assumes that the electrons are much more mobile than ions so the electron flux necessary for keeping the charge balance is not limiting the movement of ions [93, 94]; and the scale is thick compared with the *Debye length*, i.e. the distances over which *space charge effects* (electrical double layer) occur.

The grain boundary diffusion in oxide generally shows smaller energy barriers (activation energy) than the lattice diffusion does (not for Al_2O_3 [95–98]), making it the dominant mass transport mechanism at the temperature regime of interest in high temperature corrosion. Ideally, the grain boundary diffusion model assumes the enhancement of diffusion coefficients in a region that has the shape of a slab parallel to the grain boundary, with the thickness of the slab considered as the grain-boundary width. This region can either be identified by experiments (macroscopic diffusion experiments [99] or microscopic TEM characterisations [100]) or by its assumed crystal structures [101].

Unlike the lattice diffusion, since detailed grain boundary structures vary significantly depending on crystal structures and grain boundary morphologies (orientations), no universal transport mechanism has been accepted yet in terms of defect structures (equilibrium) and defect migrations. However, recent *ab-initio* simulations attempted to approach the energetic properties (e.g. formation energy) and electronic properties (e.g. electronic band structure) of grain boundaries for α-Al_2O_3 [97, 102], Cr_2O_3 [103] and spinel-(Ni,Fe)Cr_2O_4 [104] by constructing different type of atomic structures. The constructions were achieved by using so-called coincidence site lattice (CSL) theory [105, 106] for tilt and twist grain boundaries, or by randomising grain orientations in a super-cell, or based on the type of grain boundary planes and associated interface symmetries. By that, Heuer [98, 97] further suggested that grain boundary diffusion in α-Al_2O_3 could occur via

glide/climb of grain boundary dislocations, grain boundary ledges, and other structural (linear) defects, instead of basic *random walk theory* for point defects. The migration of grain boundary disconnections could explain the enhancement of grain boundary diffusion.

2.2.4 Diffusion-controlled Phase Transformation

Mathematically, the diffusion-controlled phase transformation is a *Stefan problem* which is defined as a free-boundary value problem for partial differential equations (PDEs) when the position of the boundary is also not known a priori [107]. Within each phase, the evolution of composition (and/or the phase fraction) is governed by the diffusion equation; local equilibrium conditions are imposed to the phase interfaces.

Sharp Interface Model

The sharp interface model assumes the composition at the phase boundaries to be discontinuous. It generally requires the phase interface to be tracked explicitly, which makes the geometrical representation to be difficult. Local equilibrium and mass balance are assumed at the interface with two sets of governing equations applied:

- Continuous diffusion equation is applied for each bulk region at each side of the phase interface, as detailed in eq. (2.46).
- Flux balance is applied to the phase interface:

$$(c_k^{\alpha} - c_k^{\beta})v = J_k^{\alpha} - J_k^{\beta} \tag{2.61}$$

  where v is the interface moving velocity; c_k^{α} & c_k^{β} and J_k^{α} & J_k^{β} are the equilibrium concentration and the diffusive flux of component k at each side of phase interface between phase α and phase β, respectively.

For multicomponent systems with more than one alloying elements, more than one tie-lines will present, making the equilibrium state to be dependent on the kinetics as

well. An iteration method can be introduced to find the correct tie-line, in order to make the interface moving velocity calculated from eq. (2.61) for each component k to be the same (or numerically smaller than an error criteria σ), as describe in [108]. The moving boundary problem (Stefan problem) can be numerically achieved by the *Murray and Landis space transformation* [109], or its generalisation [110] which is implemented in DICTRA.

Homogenisation Model

Even though the treatment of phase interface in classic sharp-interface model described previously is computationally efficient and thermodynamically consistent, as the tie-line finding process required is numerically difficult (risky), especially for multi-component systems usually with unsatisfied convergence, attempts have been made to introduce a phase interface sub-system – a finite volume – in which the phase fractions were assumed to vary in accordance with equilibrium [111]; any phase interface kinetics thus are ignored. As this method does not require the tie-line finding process without explicitly tracking the interfacial position, it can theoretically reduce the time complexity of computing. Furthermore, since it does not require the kinetics and the thermodynamics to be closely coupled (iterative way), some thermodynamical situations can be more easily treated. Numerical details of this approach are systematically reviewed and discussed in [112].

The *homogenisation model* stems from the multi-phase approaches which treat diffusion in regions where multiple phases are mixed with each others [113, 114]. Local equilibrium assumptions are typically applied to the whole diffusional region so that local phase fractions and effective kinetics (local-microstructural dependent) can be properly evaluated; this is particularly essential for 1D models which typically cannot capture the geometrical complexity of phase evolutions. The multi-phase idea was then combined with the finite volume interface idea, giving the general approach for treating the multi-phase moving boundary problem under local equilibrium conditions [115], as illustrated in fig. 2.3. The

interface moving velocity for $\mathbb{B} \rightarrow \mathbb{A}$ transformation $v^{\mathbb{A}/\mathbb{B}}$ was given as:

$$\frac{v^{\mathbb{A}/\mathbb{B}}}{V_S} = \frac{\sum_{\alpha\in\mathbb{A}}\sum_k \frac{\partial f_{\mathrm{m}}^{\alpha}}{\partial N_k}\left[J_k^{i\mathbb{A}}A\left(z^{i\mathbb{A}}\right) - J_k^{i\mathbb{B}}A\left(z^{i\mathbb{B}}\right)\right] - \sum_{\delta\in\mathbb{B}}\sum_k \frac{\partial f_{\mathrm{m}}^{\delta}}{\partial N_k}\left[J_k^{i\mathbb{A}}A\left(z^{i\mathbb{A}}\right) - J_k^{i\mathbb{B}}A\left(z^{i\mathbb{B}}\right)\right]}{\sum_{\alpha\in\mathbb{A}}\sum_k \frac{\partial f_{\mathrm{m}}^{\alpha}}{\partial N_k}\left[u_k^{i\mathbb{A}}A\left(z^{i\mathbb{A}}\right) - u_k^{i\mathbb{B}}A\left(z^{i\mathbb{B}}\right)\right] - \sum_{\delta\in\mathbb{B}}\sum_k \frac{\partial f_{\mathrm{m}}^{\delta}}{\partial N_k}\left[u_k^{i\mathbb{A}}A\left(z^{i\mathbb{A}}\right) - u_k^{i\mathbb{B}}A\left(z^{i\mathbb{B}}\right)\right]} \tag{2.62}$$

where $\mathbb{A}$ and $\mathbb{B}$ are two phase regions (with multiple phase present) which are separated by

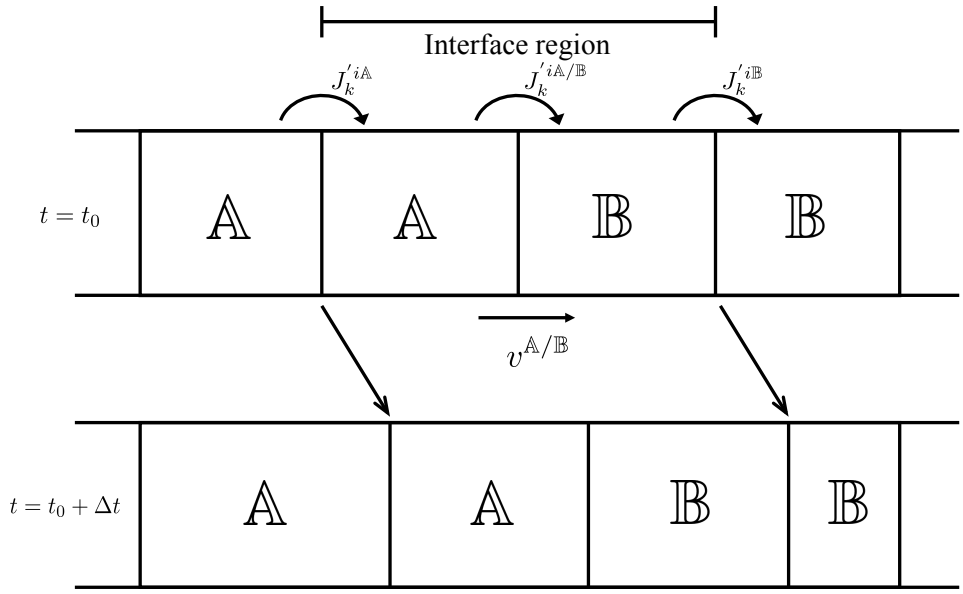


Fig. 2.3 Schematic illustration of the interface region and surrounding cells at the beginning and at the end of a time-step; modified based on [112, 115].

a phase interface, V_S the molar volume of substitutional components, u the substitutional site-fraction, $J_k^{i\mathbb{A}}$ the flux of component k in phase region $\mathbb{A}$ into the interfacial region in a volume-fixed frame of reference, f_{m}^{α} the mole fraction of α phase at the interfacial region, N_k the amount of component k at the interfacial region, $A\left(z^{i\mathbb{A}}\right)$ the cross-sectional area of phase region $\mathbb{A}$ at the interfacial region.

The numerical frameworks for simulating diffusion-controlled phase transformation are pretty well developed after [115], except the phase interface is still solved in the volume-fixed frame of reference which is required for keeping the volume & volume fraction at the interfacial region as a constant; satisfied numerical accuracy can only be achieved in this way. However large error will then evolve when treating oxidation due

to its large volume expansion (difference in molar volume). The solution would be to develop a unified flux equation for both bulk region and the interfacial region as they are both under local equilibrium assumption anyway. The equations are solved completely in the lattice-fixed frame of reference coupling with assessed molar volume data, allowing the phase transformation strain to be well predicted. A preliminary attempt is detailed in [91].

2.2.5 Solving Phenomenological Diffusion Equation(s)

Analytical approaches

Analytical solutions are usually used due to their simplicity and efficiency. For a simple 1D diffusion equation without any source terms:

$$\dot{c} = D\frac{\mathrm{d}^2 c}{\mathrm{d}z^2} \tag{2.63}$$

and boundary conditions:

$$c\left(z>0, t=0\right) = 0 \tag{2.64}$$

$$c\left(z=0, t\right) = c^{\star} \tag{2.65}$$

One can find [116]:

$$c\left(z,t\right) = c^{\star}\left(1-\mathrm{erf}\left(\frac{z}{2\sqrt{Dt}}\right)\right) \tag{2.66}$$

where $\mathrm{erf}\left(\right)$ is the *error function*. For more general/complex form of boundary conditions and equations, the *Fourier transformation* is typically used to approximate the solution. Alternatively, the parabolic diffusion equation can be solved by various numerical techniques, such as finite difference method (FDM), finite element method (FEM) and finite volume method (FVM) for better flexibilities.

Finite difference method (FDM)

The mathematical formalism and implementation of FDM are the simplest among the above three methods. The central idea is to approximate the differential equations with difference equations. One can approximate the second derivative of c respect to z on the right hand side of eq. (2.63) as:

$$c_k'' = \frac{c_{k+1} - 2c_k + c_{k-1}}{h^2} + O\left(h^2\right) \tag{2.67}$$

where k is the index of grid point along the z axis after uniform discretisation of the space with spacing of h, as shown in fig. 2.4. By further discretising the time, one can write the

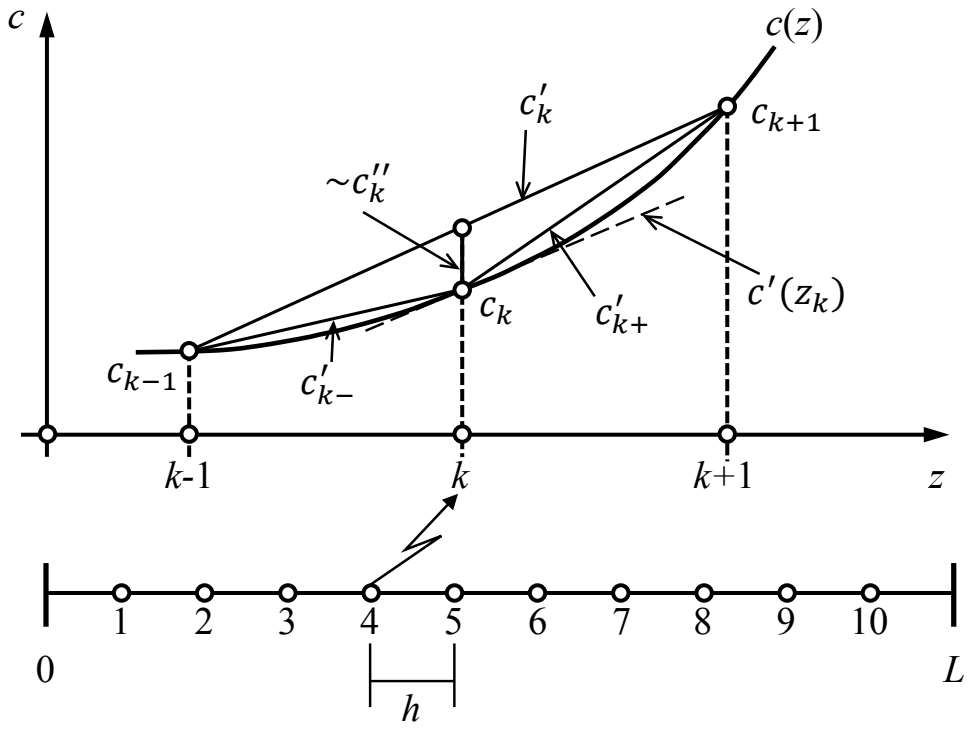


Fig. 2.4 Graphical representation of the approximations of the first and second derivatives by differences [117].

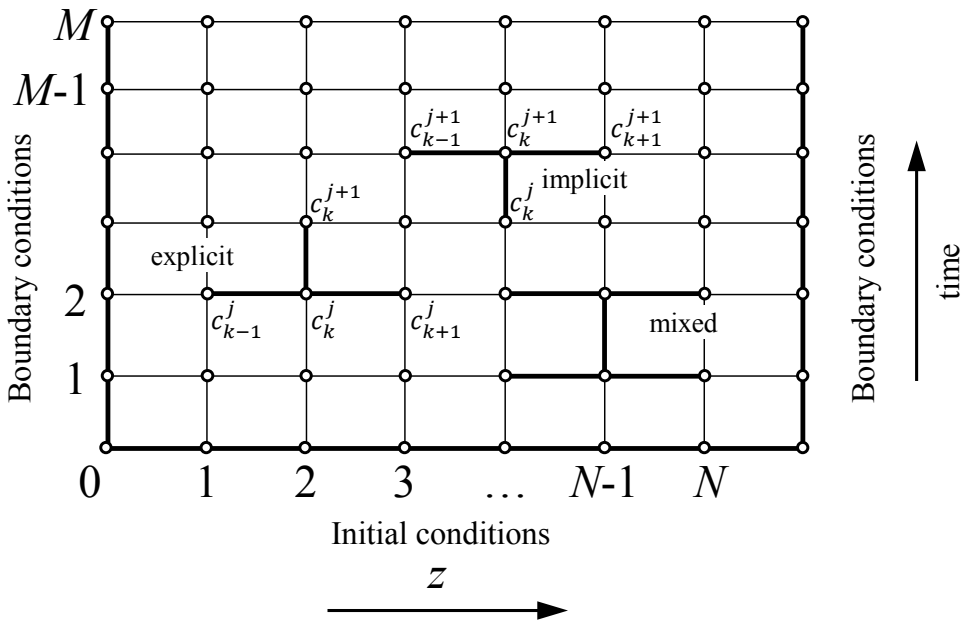


Fig. 2.5 Graphical representation in space-time of the explicit, implicit and mixed schemes [117].

discretised form of eq. (2.63) as:

$$(1-\zeta)\left[-c_{k-1}^{j}+2c_k^j-c_{k+1}^j\right]+\zeta\left[-c_{k-1}^{j+1}+2c_k^{j+1}-c_{k+1}^{j+1}\right]+\frac{1}{F_{O_\mathrm{h}}}\left[c_k^{j+1}-c_k^j\right]=0 \tag{2.68}$$

where c_k^j denotes the concentration of grid point k at time step j, F_{O_h} the *Fourier number* given as $D\Delta t/h^2$. ζ is the implicity, as shown in fig. 2.5:

- $\zeta = 0$ (explicit): based on concentrations of previous time step which are known.
- $\zeta = 1$ (implicit): based on concentrations of current time step which are unknown.
- $0 < \zeta < 1$ (mixed): based on concentrations of both current & previous time steps; $\zeta = 0.5$ corresponds to the *Crank-Nicolson* scheme.

The implicit & mixed method leads to a tridiagonal system of equations which can be solved by the simplified Gaussian elimination – Thomas algorithm (i.e. tridiagonal matrix algorithm) [118] (for linear cases). For example, eq. (2.63) with fixed boundary

concentration $c^\star$ at both end sides gives following system of equations:

$$\begin{bmatrix} 1+2F^{\mathrm{i}}_{O_{\mathrm{h}}} & -F^{\mathrm{i}}_{O_{\mathrm{h}}} & & & & 0 \\ -F^{\mathrm{i}}_{O_{\mathrm{h}}} & 1+2F^{\mathrm{i}}_{O_{\mathrm{h}}} & -F^{\mathrm{i}}_{O_{\mathrm{h}}} & & & \\ & -F^{\mathrm{i}}_{O_{\mathrm{h}}} & 1+2F^{\mathrm{i}}_{O_{\mathrm{h}}} & -F^{\mathrm{i}}_{O_{\mathrm{h}}} & & \\ & & \cdots & \cdots & \cdots & \\ & & & -F^{\mathrm{i}}_{O_{\mathrm{h}}} & 1+2F^{\mathrm{i}}_{O_{\mathrm{h}}} & -F^{\mathrm{i}}_{O_{\mathrm{h}}} \\ 0 & & & & -F^{\mathrm{i}}_{O_{\mathrm{h}}} & 1+2F^{\mathrm{i}}_{O_{\mathrm{h}}} \end{bmatrix} \begin{bmatrix} c_1^{j+1} \\ c_2^{j+1} \\ \cdots \\ \cdots \\ c_{N-1}^{j+1} \\ c_N^{j+1} \end{bmatrix} =$$
$$\begin{bmatrix} 1-2F^{\mathrm{e}}_{O_{\mathrm{h}}} & +F^{\mathrm{e}}_{O_{\mathrm{h}}} & & & & 0 \\ +F^{\mathrm{e}}_{O_{\mathrm{h}}} & 1-2F^{\mathrm{e}}_{O_{\mathrm{h}}} & +F^{\mathrm{e}}_{O_{\mathrm{h}}} & & & \\ & +F^{\mathrm{e}}_{O_{\mathrm{h}}} & 1-2F^{\mathrm{e}}_{O_{\mathrm{h}}} & +F^{\mathrm{e}}_{O_{\mathrm{h}}} & & \\ & & \cdots & \cdots & \cdots & \\ & & & +F^{\mathrm{e}}_{O_{\mathrm{h}}} & 1-2F^{\mathrm{e}}_{O_{\mathrm{h}}} & +F^{\mathrm{e}}_{O_{\mathrm{h}}} \\ 0 & & & & +F^{\mathrm{e}}_{O_{\mathrm{h}}} & 1-2F^{\mathrm{e}}_{O_{\mathrm{h}}} \end{bmatrix} \begin{bmatrix} c_1^{j} \\ c_2^{j} \\ \cdots \\ \cdots \\ c_{N-1}^{j} \\ c_N^{j} \end{bmatrix} + \begin{bmatrix} F_{O_{\mathrm{h}}} c^\star \\ 0 \\ \cdots \\ \cdots \\ 0 \\ F_{O_{\mathrm{h}}} c^\star \end{bmatrix} \tag{2.69}$$

where $F^{\mathrm{e}}_{O_{\mathrm{h}}} = (1-\zeta)F_{O_{\mathrm{h}}}$, $F^{\mathrm{i}}_{O_{\mathrm{h}}} = \zeta F_{O_{\mathrm{h}}}$. Extension to multi-component systems is possible by defining c as $(n-1)\times 1$ vectors and $F_{O_{\mathrm{h}}}$ & D as a $(n-1)\times(n-1)$ matrix where n is the number of components. However, its numerical stability and flexibility for non-linear cases is a challenge.

Finite volume method (FVM)

FVM is similar to FDM except that each discretised concentration point is defined within a *control volume* where its integral is evaluated by using the divergence theorem. By guaranteeing automatically the conservation of the fundamental equations at the discrete level, it is particularly flexible to mesh arbitrary geometries; the homogenisation model implemented in DICTRA is based on FVM [119]. The discretised form of flux eq. (2.58)

for component k between two neighbouring cells $n-1$ and n thus is given as [113]:

$$\tilde{J}_k^n = \sqrt{[M_k c_k]^n [M_k c_k]^{n-1}} \frac{\Delta \mu_k^n}{\Delta z_n} \tag{2.70}$$

The *Newton–Raphson* scheme is applied to approach eq. (2.70) iteratively. Defining a normalised quantity f_k^n as:

$$f_k^n = \frac{\Delta N_k^n}{N_k^n \Delta t} \tag{2.71}$$

where ΔN_k^n is the change of molar content of component k in all cells n during time-step Δt. The multi-variable function to solve for each iteration is:

$$\mathbf{F} = \mathbf{f} - \mathbf{f}' = \mathbf{0} \tag{2.72}$$

where primed quantities are obtained from initial guess and subsequent update by Newton–Raphson iteration whereas the un-primed quantities are calculated from the fluxes in the system. Equation (2.72) yields the linear system of equations:

$$\mathbf{F} \simeq \mathbf{F_0} + \mathbb{J}_\mathbf{F} \delta \mathbf{f}' = \mathbf{0} \tag{2.73}$$

where the *Jacobian* matrix $\mathbb{J}_\mathbf{F}$ can be evaluated either by perturbing $\Delta \mathbf{N}'$ or from analytical derivatives of mobility with respect to composition which now are potentially possible based on [120].

Chapter 3

On the Prediction of Vacancy Formation Energy in fcc-Nickel

3.1 Introduction

Nickel is the preferred solvent in the superalloys for high temperature applications–for example the turbomachinery employed for jet propulsion and power generation, or alternatively critical components for heat exchangers or the petrochemical plant. What is the rationale for this? Undoubtedly the widespread abundance of this element and its low cost are factors of economic importance. The fundamental basis for its mechanical stability can be traced to the face-centred cubic (fcc) crystal structure which is stable up to melting [13]. Consequently rates of time-dependent plasticity–so-called creep deformation–are low. Moreover, the chemical driving force for phase instability driven by substitutional diffusion is favourably small.

As atomic diffusion is mostly mediated by vacancies, the magnitude of the vacancy formation energy in nickel is of profound importance for high temperature applications. Nevertheless, at present the magnitude of this critical quantity–and indeed its variation with temperature–is the subject of significant uncertainty. The experimental detection limit for vacancies is 10^{-5} when applying techniques such as differential dilatometry (DD)

which is able to obtain *absolute* vacancy concentrations. Applying indirect techniques the experimental detection limit can be maximally increased to about 10^{-6} which restricts the experimentally accessible temperature range to about 1000 K for Ni as illustrated in fig. 3.1 by the gray shaded area. On the theory side, modern electronic structure calculations which make use of density function theory (DFT) are usually carried out at absolute zero or need to approximate temperatures effects by e.g. the quasiharmonic approximation. Only recently it has been shown that vibrational contributions beyond the harmonic level can result in qualitative changes to vacancy formation [121]. Further development is however necessary to incorporate all relevant finite temperature effects into these computations, e.g. magnetic excitations.

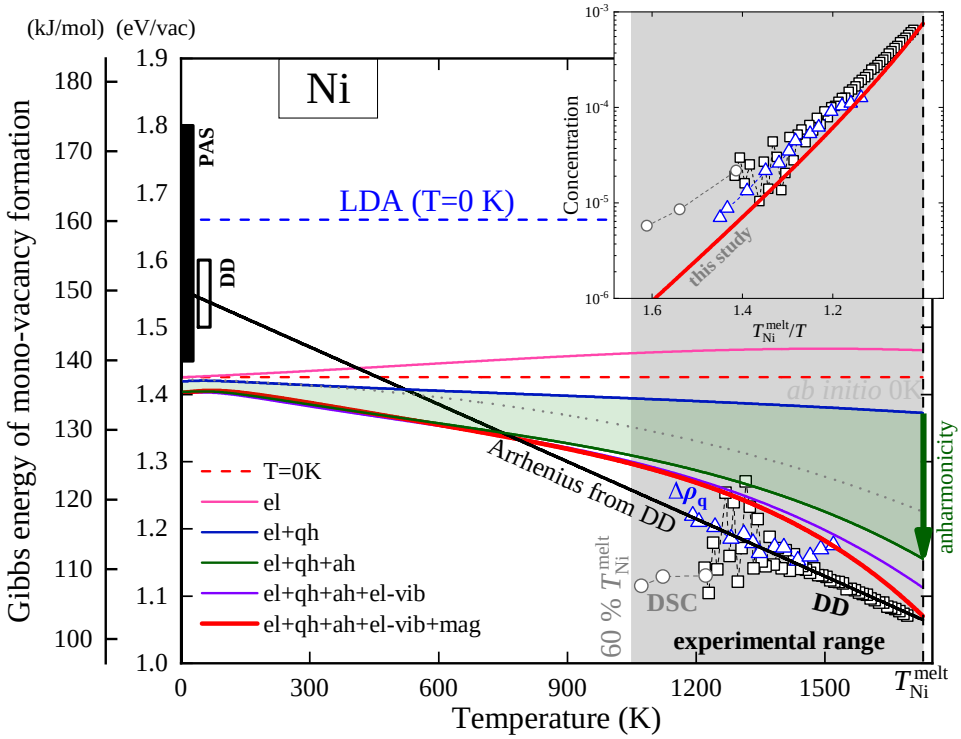


Fig. 3.1 Calculated Gibbs energy of vacancy formation and equilibrium vacancy mole fraction of fcc-Ni compared with existing experimental data [122–125] and DFT calculation [126].

In this chapter, fully *ab initio* DFT calculations are performed to determine the temperature dependent vacancy formation energy of nickel. First, we show that there are discrepancies between the existing high temperature experimental assessments and theoreti-

cal results obtained from DFT at absolute zero. Next, finite temperature calculations–which include the effects of magnetism and phonon vibrations–are performed. It is demonstrated that the existing experimental data at high temperature and the absolute zero DFT calculations can be rationalised. Our results have implications for the design of new grades of nickel-based superalloys for industrial applications.

3.2 Background

Application Typical degradations at high temperature is mostly controlled by atomic diffusion: vacancy absorption/emission (atomic migration) during climbing process of dislocations (dislocation creep) [127], short range atomic reordering during the lengthening of micro-twins [128–130], imbalance of diffusive flux of atoms which causes the formation of pores (Kirkendall porosity) [131], ionic diffusion within surface protective oxides during environmental attack by corrosive species [132], degradation of thermal barrier coating (TBC)/bond coating (BC) by their inter-diffusion with the alloy substrate [133], nucleation and coarsening of precipitates such as detrimental topologically close-packed (tcp) phases [134].

Link to Diffusional Phenomena It is accepted that the mechanism of vacancy-mediated diffusion requires two distinct phenomena: (1) formation of vacancy defects in an otherwise perfect crystalline lattice, and (2) a thermally-activated jump in which the diffusing atom and the nearest neighbour vacancy exchange position on the lattice. The former is characterised by the dilute limit mole fraction of vacancies which can be estimated consistent with [135] assuming thermodynamic equilibrium according to:

$$x_{\mathrm{Va}} = g \exp\left(\frac{-G^{f}_{\mathrm{Va}}}{k_{\mathrm{B}}T}\right) \tag{3.1}$$

where g is a geometry factor (e.g. $g = 1$ for mono- and $g = 6$ for di-vacancies in fcc) and G^f_{Va} the temperature (and pressure) dependent Gibbs energy of formation of vacancies. Note that if one assumes an Arrhenius-like behaviour – i.e. the enthalpy and entropy of formation H^f_{Va} and S^f_{Va} are independent of temperature – one can reformulate eq. (3.1) as the Arrhenius equation:

$$\begin{aligned} x_{\mathrm{Va}} =& g \exp\left(\frac{T S^f_{\mathrm{Va}} - H^f_{\mathrm{Va}}}{k_{\mathrm{B}} T}\right) \\ =& g \exp\left(\frac{S^f_{\mathrm{Va}}}{k_{\mathrm{B}}}\right) \exp\left(\frac{-H^f_{\mathrm{Va}}}{k_{\mathrm{B}} T}\right) \\ =& A \exp\left(\frac{-H^f_{\mathrm{Va}}}{k_{\mathrm{B}} T}\right) \end{aligned} \tag{3.2}$$

The thermally-activated jump can be characterised by the atom-vacancy exchange frequency v according to [136]:

$$v = v_0 \exp\left(-\frac{\Delta H_{\mathrm{m}}}{k_{\mathrm{B}} T}\right) \tag{3.3}$$

where v_0 is the effective frequency associated with the vibration of the atom in the direction of the vacancy and ΔH_{m} is the enthalpy of the migration. The tracer diffusion coefficient is thus given as [137]:

$$D^{\star} = a^2 x_{\mathrm{Va}} v f^{\mathrm{corr}} \tag{3.4}$$

where a is the equilibrium lattice parameters, f^{corr} the correlation factor describing the reduced efficiency of diffusion due to atomic jumps back to original sites.

Experimental Measurements Reported in Literature Measurements of H^f_{Va} have been attempted by various techniques, including positron annihilation spectroscopy (PAS) [138, 139], differential dilatometry (DD) [123], residual electrical resistivity ($\Delta\rho$) [140, 124] and calorimetry (e.g. DSC) [125]. However, very few if any of these are able to determine

c_{Va} or S^f_{Va} with the greatest accuracy; this, for example, limits the temperature range where the decrease of bulk lifetime in PAS can be observed and from which vacancy formation energy can be extracted [138]. Table 3.1 summarises experimentally-determined H^f_{Va} and S^f_{Va} values to date.

Table 3.1 Experimental determined vacancy formation enthalpy (H^f_{Va}) and entropy (S^f_{Va}) of fcc-Ni.

Year	Method	H^f_{Va} [eV]	S^f_{Va} [k_{B}]	Reference
1969	Electrical resistivity $\Delta\rho_{\mathrm{q}}$, quenched sample	1.60	-	Mamalui *et al* [141, 139]
1976	Electrical resistivity $\Delta\rho_{\mathrm{q}}$, quenched 60 μm diameter wire	1.58(1)	-	Wycisk *et al* [140]
1977	Peak angular correlation (PAC)	1.72	-	Dlubek *et al* [142]
1977	Peak angular correlation (PAC)	1.74	-	Nanao *et al* [143]
1977	Positron annihilation spectroscopy (PAS)	1.73 ... 1.45(7)	-	Campbell *et al* [144]
1978	Electrical resistivity $\Delta\rho_{\mathrm{q}}$, quenched 30 μm diameter wire	1.63(5)	-	Wycisk *et al* [124]
1979	Peak angular correlation (PAC)	1.55(5)	-	Matter *et al* [145]
1979	Positron annihilation spectroscopy (PAS)	1.72	-	Maier *et al* [146]
1980	Positron lifetime spectroscopy (e^+-LT)	1.54(2)	-	Lynn *et al* [147]
1981	Positron annihilation spectroscopy (PAS)	1.80(10)	-	Smedskjaer *et al* [148]
1982	Positron annihilation spectroscopy (PAS)	1.78(10)	-	Schaefer *et al* [149, 150]
1982	Review of positron annihilation spectroscopy (PAS)	1.79(5)	-	Siegel *et al* [151, 152]
1983	Positron annihilation spectroscopy (PAS)	1.63(2)	-	Fluss *et al* [153]
1987	Unknown	1.4(2)	-	Glazkov [154]
1989	Positron annihilation spectroscopy (PAS)	1.7(1)	-	Troev *et al* [155]
1989	Positron lifetime spectroscopy (e^+-LT)	1.6(1)	-	Troev *et al* [155]
1997	Positron lifetime spectroscopy (e^+-LT)	1.73(7)	-	Wolff *et al* [138]
2001	Differential dilatometry (DD)	1.56(4)	3.3(5)	Scholz [123]

Computational Efforts Numerous DFT work has been reported to estimate the mono-vacancy formation enthalpy (H^f_{Va}) in fcc-Ni. Moreover, the influence of exchange-correlation functionals and correction schemes have been reviewed in [126]. Table 3.2 summarises calculated H^f_{Va} and S^f_{Va} values reported in previous work.

Table 3.2 Previously calculated *ab initio* vacancy formation enthalpy (H^f_{Va}) and entropy (S^f_{Va}) of fcc-Ni for both ferromagnetic (FM) and non-magnetic (NM) cases.

Year	Method	Spin	Excitations	H^f_{Va} [eV]	S^f_{Va} [k_{B}]	Reference
1992	LDA	NM	T=0 K	1.76	-	Dederichs *et al* [156]
1995	LDA	NM	T=0 K	1.77	-	Korhonen *et al* [157]
1999	LDA	NM	T=0 K	1.78	-	Korzhavyi *et al* [158]
2001	LDA	FM	T=0 K	1.81	-	Mizuno *et al* [159]
2001	LDA	NM	T=0 K	1.68	-	Mizuno *et al* [159]

Table 3.2 (continued)

Year	Method	Spin	Excitations	H^f_{Va} [eV]	S^f_{Va} [k_{B}]	Reference
2001	PW91	FM	T=0 K	1.54	-	Mizuno *et al* [159]
2001	PW91	NM	T=0 K	1.43	-	Mizuno *et al* [159]
2006	PW91	FM	T=0 K	1.37	-	Megchiche *et al* [160]
2006	LDA	FM	T=0 K	1.62	-	Megchiche *et al* [160]
2012	AM05	FM	T=0 K	1.69	-	Nazarov *et al* [126]
2012	LDA	FM	T=0 K	1.66	-	Nazarov *et al* [126]
2012	PBE	FM	T=0 K	1.44	-	Nazarov *et al* [126]
2012	PW91	FM	T=0 K	1.38	-	Nazarov *et al* [126]
2014	LDA	NM	Quasiharmonic	1.63 ... 1.70	−0.12 ... 0.51	Hargather *et al* [161]
2014	LDA	FM	Quasiharmonic	1.63 ... 1.66	−1.93 ... −1.71	Hargather *et al* [161]

Contradiction Estimates of S^f_{Va} determined by DD [123] are found to be larger than $3\,k_{\mathrm{B}}$. However, recent quasi-harmonic calculations [161, 125] suggested S^f_{Va} to be negative. In this work, relevant excitation mechanisms contributing to the free energy have been explicitly calculated. The anharmonicity beyond the quasi-harmonicity, originated from the breakdown of the inversion symmetry close to the vacancy, was found to be responsible for such large entropy.

3.3 Computational Methodology

3.3.1 General Free Energy Approach

The temperature and pressure dependent Gibbs energy of vacancy formation is given by [121]

$$G^f_{\mathrm{Va}}(P,T) = F^{\mathrm{vac}}(\Omega,T;N) - NF^{\mathrm{bulk}}(v,T) + Pv^f, \tag{3.5}$$

where $F^{\mathrm{vac}}(\Omega,T;N)$ is the free energy surface of the vacancy supercell with volume Ω and N atoms, $F^{\mathrm{bulk}}(v,T)$ the free energy surface of the perfect bulk for a single atom with volume v per atom, P the pressure, and $v^f = (\Omega - Nv)$ the volume of vacancy formation.

For both of the free energy surfaces $F^{\mathrm{vac}}(V,T)$ and $F^{\mathrm{bulk}}(V,T)$ (where V denotes here a generic volume dependence), the set of relevant contributions for a magnetic material such as Ni reads

$$\begin{aligned} F(V,T) =& E_{0\mathrm{K}}(V) + F^{\mathrm{el}}(V,T) + F^{\mathrm{qh}}(V,T) + \\ & F^{\mathrm{ah}}(V,T) + F^{\mathrm{el-vib}}(V,T) + F^{\mathrm{mag-vib}}(V,T), \end{aligned} \tag{3.6}$$

where $E_{0\mathrm{K}}$ is the total energy at $T = 0\,\mathrm{K}$, F^{el} the electronic free energy of a static lattice, F^{qh} and F^{ah} the quasiharmonic and explicitly anharmonic free energy contribution from atomic vibrations, $F^{\mathrm{el-vib}}$ the adiabatic coupling between electrons and atomic vibrations, and $F^{\mathrm{mag-vib}}$ the magnetic contribution to the free energy containing the impact of atomic vibrations. The term $E_{0\mathrm{K}}(V)$ is meant to include the total electronic and magnetic energy at $T = 0\,\mathrm{K}$, which implies that F^{el} and $F^{\mathrm{mag-vib}}$ contain only the explicitly temperature dependent electronic and magnetic contribution.

We are mainly interested in $G^f(T)$ in the experimentally accessible range, i.e. $60\ldots100\%$ of the melting temperature of Ni (1728 K [162]). This temperature range is far above the Curie temperature of Ni (631 K [163]) meaning that experimentally the paramagnetic state is measured. In principle, this fact would require to compute the terms entering eq. (3.6) using paramagnetic DFT calculations. Such calculations are particularly challenging for Ni because (in contrast to, for example, Fe) paramagnetic spin configurations treated by conventional unconstrained spin DFT generally converge into the non-magnetic state [164, 165]. Inclusion of longitudinal spin fluctuations is required to stabilise finite local magnetic moments [164]. Modelling these fluctuations necessitates *constrained* spin DFT calculations [166] which increase drastically the computational expenses.

However, it has been recently shown that both longitudinal as well as transverse magnetic excitations have only a minor impact on lattice vibrations for Nickel [165]. Further, the local magnetic moment obtained for a paramagnetic state stabilised by longitudinal spin fluctuations is close to the ferromagnetic value [164]. These findings suggest that for

Table 3.3 Convergence parameters for the $T = 0\,\mathrm{K}$ calculations and the resulting vacancy formation enthalpy H^f at atmospheric pressure, for both ferromagnetic (FM) and non-magnetic (NM) cases. E_{cut} denotes the plane wave energy cut-off. The notation for the lattice constants $(a_{\mathrm{start}}\text{-}a_{\mathrm{end}}, \delta a; a_1, a_2)$ means that the mesh is going from a_{start} to a_{end} in steps of δa, with additional lattice constants a_1 and a_2.

Supercell	Size	Spin	Atoms	E_{cut}(eV)	k-points (kp)	kp·atoms	Lattice constants (Å)	H^f(eV)
Vacancy	$2\times2\times2$	FM	31	400	$24\times24\times24$	428,544	3.42 - 3.64, 0.02; 3.55, 3.61	1.45
Bulk	$2\times2\times2$	FM	32	400	$24\times24\times24$	428,544	3.42 - 3.64, 0.02; 3.55, 3.61	
Vacancy	$3\times3\times3$	FM	107	400	$16\times16\times16$	438,272	3.42 - 3.64, 0.02; 3.55, 3.61	1.43
Bulk	$3\times3\times3$	FM	108	400	$16\times16\times16$	442,368	3.42 - 3.64, 0.02; 3.55, 3.61	
Vacancy	$4\times4\times4$	FM	255	400	$12\times12\times12$	440,640	3.42 - 3.64, 0.02; 3.55, 3.61	1.43
Bulk	$4\times4\times4$	FM	256	400	$12\times12\times12$	442,368	3.42 - 3.64, 0.02; 3.55, 3.61	
Vacancy	$3\times3\times3$	NM	107	400	$16\times16\times16$	438,272	3.42 - 3.64, 0.02; 3.55, 3.61	1.40
Bulk	$3\times3\times3$	NM	108	400	$16\times16\times16$	442,368	3.42 - 3.64, 0.02; 3.55, 3.61	

the computation of the free energy the ferromagnetic state is a reasonable approximation to the paramagnetic state. We thus computed the free energy contributions entering eq. (3.6) utilising collinear ferromagnetic calculations. Such an approach renders the computations much more amenable.

All calculations were performed using the projector augmented wave (PAW) method [167] as implemented in the Vienna Ab initio Simulation Package (VASP) [40, 41] with the provided PAW potentials [69]. The generalised gradient approximation (GGA) with Perdew-Burke-Ernzerhof (PBE) [37] parameterisation was utilised for the exchange-correlation functional.

Table 3.4 Convergence parameters for the electronic free energy calculations and the resulting Gibbs energy of vacancy formation G^f at the melting point (1728 K) and at atmospheric pressure, including the converged $T = 0\,\mathrm{K}$ contributions (i.e. only the electronic contribution varies in this table for a convenient comparison). E_{cut} denotes the plane wave energy cut-off.

Supercell	Size	Atoms	E_{cut}(eV)	k-points (kp)	kp·atoms	Lattice constants (Å)	Temperatures (K)	G^f(eV)
Vacancy	$2\times2\times2$	31	330	$6\times6\times6$	6,696	3.54, 3.58, 3.62, 3.64	300, 800, 1200, 1600, 1740	1.47
Bulk	$2\times2\times2$	32	330	$6\times6\times6$	6,912	3.54, 3.58, 3.62, 3.64	600, 1000, 1400, 1740	
Vacancy	$3\times3\times3$	107	450	$5\times5\times5$	13,375	3.54, 3.58, 3.62, 3.64	300, 800, 1200, 1600, 1740	1.47
Bulk	$3\times3\times3$	108	450	$5\times5\times5$	13,500	3.54, 3.58, 3.62, 3.64	300, 800, 1200, 1600, 1740	

3.3.2 Total Energy, Electronic and Quasiharmonic Contribution

We calculated $E_{0\mathrm{K}}(V)$ at 12 volumes with lattice parameters ranging from 3.42 Å to 3.64 Å, fully relaxing the atomic coordinates. The volume dependence was parameterised using the Vinet equation-of-state [168]. The Methfessel-Paxton scheme [71] with a smearing parameter of 0.10 eV was used. Table 3.3 shows the convergence parameters and the resulting enthalpies of formation revealing only a small change of -0.02 eV upon increasing the supercell from $2\times2\times2$ to $3\times3\times3$, and no change when increasing further to a $4\times4\times4$ supercell. The additional non-magnetic calculations for the $3\times3\times3$ supercell reveal only a small impact of magnetism on the enthalpy of vacancy formation (≈ 0.03 eV).

The electronic free energy F^{el} for the ferromagnetic static lattice was calculated using the self-consistent field (SCF) approach [47] within finite temperature DFT [68]. We used a mesh of 20 volume-temperature points and convergence parameters as given in table 3.4. Based on the mesh, the difference between the vacancy and bulk electronic free energy was fitted using a polynomial in volume and temperature ($\Delta F^{\mathrm{el}} = a_1T + a_2T^2 + a_3T^3 + a_4TV$ with fitting coefficients a_i, $i = 1\ldots4$). No difference in the Gibbs energy of formation is observed when using a $2\times2\times2$ or a $3\times3\times3$ supercell for the electronic free energy calculations (table 3.4, last column).

The quasiharmonic free energy contribution F^{qh} to the vacancy formation energy was obtained by the small displacement method [169, 59]. We used displacements of 0.03 Bohr radius (~ 0.016 Å) and treated all atoms spin-polarised. Table 3.5 lists the tested convergence parameters as well as the considered volumes. The volume dependence was fitted with a second order polynomial. We observe that the difference in the Gibbs energy of vacancy formation is between the $2\times2\times2$ and $3\times3\times3$ supercells in F^{qh} is below 0.01 eV at the melting point.

Table 3.5 Convergence parameters for the quasiharmonic calculations and the resulting Gibbs energy of vacancy formation G^f at the melting point (1728 K) and at atmospheric pressure, including the converged $T = 0$ K and electronic contributions (i.e. only the quasiharmonic contribution varies in this table for a convenient comparison). E_{cut} denotes the plane wave energy cut-off and *Augmentation* refers to the grid used for the calculation of the augmentation charges (gp/atom=grid points; see Ref. [170] for details). The notation for the lattice constants $(a_{\text{start}}\text{-}a_{\text{end}}, \delta a; a_1, a_2)$ means that the mesh is going from a_{start} to a_{end} in steps of δa, with additional lattice constants a_1 and a_2.

Supercell	Size	Atoms	E_{cut}(eV)	k-points (kp)	kp·atoms	Augmentation	gp/atom	Lattice constants (Å)	G^f(eV)
Vacancy	$2\times2\times2$	31	400	$10\times10\times10$	31,000	$240\times240\times240$	445,935	3.52 - 3.64, 0.02; 3.55, 3.61	1.38
Bulk	$2\times2\times2$	32	400	$10\times10\times10$	32,000	$240\times240\times240$	432,000	3.52 - 3.64, 0.02; 3.55, 3.61	
Vacancy	$2\times2\times2$	31	400	$16\times16\times16$	126,976	$240\times240\times240$	445,935	3.52 - 3.64, 0.02; 3.55, 3.61	1.38
Bulk	$2\times2\times2$	32	400	$16\times16\times16$	131,072	$240\times240\times240$	432,000	3.52 - 3.64, 0.02; 3.55, 3.61	
Vacancy	$3\times3\times3$	107	400	$10\times10\times10$	107,000	$360\times360\times360$	436,037	3.52 - 3.64, 0.02; 3.55, 3.61	1.37
Bulk	$3\times3\times3$	108	400	$10\times10\times10$	108,000	$360\times360\times360$	432,000	3.52 - 3.64, 0.02; 3.55, 3.61	
Vacancy	$3\times3\times3$	107	400	$12\times12\times12$	184,896	$360\times360\times360$	436,037	3.52 - 3.64, 0.02; 3.55, 3.61	1.37
Bulk	$3\times3\times3$	108	400	$12\times12\times12$	186,624	$360\times360\times360$	432,000	3.52 - 3.64, 0.02; 3.55, 3.61	

TU-TILD Scheme–Anharmonicity

The term F^{ah} has been calculated by using the Two-stage Upsampled Thermodynamic Integration using Langevin Dynamics (TU-TILD) method [67]. The TU-TILD method is a hierarchical approach to the estimation of the free energy surface by using the thermodynamic integration (TI) and perturbation theory. Three consecutive steps of calculations have been performed:

(1) TI coupling quasi-harmonic approaches to the TU-TILD potential with the Langevin molecular dynamics (LD); the TU-TILD potential is based on the embedded atom method (EAM) [63] optimised by using the MEAMfit fitting code [171] for fcc-nickel bulk at 1728 K. In this work, a simple harmonic (Einstein) approach rather than the quasi-harmonic approach is utilised as the reference potential, significantly reducing the computational time.

(2) TI coupling TU-TILD potential to DFT with relatively low convergence parameters to provide an efficient but still accurate enough sampling of the configuration

space; LD simulations were performed with a time step of 5 fs, using the Langevin thermostat with a friction parameter of 0.01 fs^{-1}.

(3) for each volume and temperature (and linear coupling parameter λ), uncorrelated snapshots extracted from the trajectories in step (2) were recalculated by DFT with higher convergence parameters; the energy offset of the Born-Oppenheimer surface due to DFT numerical convergence is thus assessed; this up-sampling step – a perturbative approach – allows the final free energy surface to be calculated with high accuracy.

Table 3.6 Convergence parameters for the TU-TILD potential to DFT calculations and the resulting Gibbs energy of vacancy formation G^f at the melting point (1728 K) and at atmospheric pressure, including the converged $T = 0$ K, electronic and quasiharmonic contributions (i.e. only the anharmonic contribution varies in this table for a convenient comparison). $E_{\text{cut}}^{\text{low/high}}$ and $k\text{-points}^{\text{low/high}}$ denote the plane wave energy cut-off and k-point mesh for the low/high DFT calculations.

Supercell	Size	Atoms	$E_{\text{cut}}^{\text{low}}$(eV)	$k\text{-points}^{\text{low}}$	$E_{\text{cut}}^{\text{high}}$(eV)	$k\text{-points}^{\text{high}}$	Lattice constants (Å)	Temperatures (K)	G^f(eV)
Vacancy	$2\times2\times2$	31	300	$3\times3\times3$	330	$6\times6\times6$	3.54, 3.58, 3.62, 3.64	300,800,1200,1600,1728	1.02
Bulk	$2\times2\times2$	32	300	$3\times3\times3$	330	$6\times6\times6$	3.54, 3.58, 3.62, 3.64	600,1000,1400,1728	
Vacancy	$3\times3\times3$	107	300	$3\times3\times3$	450	$5\times5\times5$	3.54, 3.58, 3.62, 3.64	300,800,1200,1600,1728	1.15
Bulk	$3\times3\times3$	108	300	$3\times3\times3$	450	$5\times5\times5$	3.54, 3.58, 3.62, 3.64	600,1000,1400,1728	

Above detailed convergence parameters are listed in table 3.6. Vacancy jumps (due to high mobility of vacancies) are expected at high temperatures consistent with the results of LD calculations. But as the (quasi-)harmonic approaches assume a fixed lattice structure, the calculations in step (1) (which couple the (quasi-) harmonic approach with TU-TILD potential) are not applicable at high temperatures. It is possible, in principle, to calculate the internal energy U at different temperatures by LD and then integrate U over temperature (from $T = 0$ when $S = 0$) to obtain the free energy:

$$\int_{\beta_1}^{\beta_2} U(\beta)\,\mathrm{d}\beta = \beta_2 F(\beta_2) - \beta_1 F(\beta_1) \tag{3.7}$$

It should be noted that the calculation of U requires large amount of configurational space to be sampled (i.e. sampling time to be long enough and the associated time step to be sufficiently small) to ensure its convergence; this is computationally expensive. Therefore in practice a compromise has to be made; in this work this has been done by coupling harmonic approaches with LD up to the temperature at which a vacancy is found to jump (T_{jump}) followed by an integration of internal energy over temperature from T_{jump} to the melting temperature. Rather conservatively, T_{jump} has been set to 800 K; Technical details and proof of eq. (3.7) are given in Appendix I. In some LD simulations coupling TU-TILD potentials with DFT with low convergence parameters, spin flips were found at high temperatures for larger supercells; it might be due to larger degree of freedoms in the system when the temperature is higher or there are more atoms in the system or the volume is larger. Table 3.7 shows the occurrence of spin flips of 21 calculations (3 random seeds times 7 linear coupling parameters λ) for each temperature and volume in a 3^3 supercell. One can clearly see higher possibility of spin flips at high temperatures and at larger volumes.

Table 3.7 Occurrence of spin flips for 3^3 supercell calculations coupling TU-TILD potential with DFT with low convergence parameters.

	300 K	800 K	1200 K	1600 K	1728 K
3.54 Å	0.00	0.00	0.09	0.61	0.72
3.58 Å	0.00	0.00	0.19	0.75	0.68
3.62 Å	0.00	0.00	0.38	0.75	0.63
3.64 Å	0.00	0.09	0.43	0.63	0.46

3.3.3 Coupling of Electrons with Vibrations

The free energy due to the coupling between electrons and lattice vibrations $F^{\text{el}-\text{vib}}(V,T)$ has been calculated by averaging the electronic free energy (referenced to the electronic

internal energy at $T = 0\,\mathrm{K}$) of all up-sampled atomic configurations in the TU-TILD scheme; this method is detailed by Zhang *et al* [47].

3.3.4 Magnetic Excitations

A full *ab initio* calculation of magnetic excitations is challenging (see, e.g. Ref. [172] for a recent overview). Ni is a particularly challenging material due to the presence of longitudinal spin fluctuations which usually require the application of constrained spin DFT [164].

Since we are predominantly interested in the high temperature regime, the magnetic free energy can be modelled by neglecting the magnetic short-range order (SRO) as [173, 174]:

$$F^{\mathrm{mag-vib}}(V,T) \approx -TS^{\mathrm{mag-vib}}, \tag{3.8}$$

where $S^{\mathrm{mag-vib}}$ denotes the magnetic entropy. A common approximation to the high-temperature limit of $S^{\mathrm{mag-vib}}$ is given by [175–177]

$$S^{\mathrm{mag-vib}} = -k_{\mathrm{B}} \ln\left(M(V,T)+1\right), \tag{3.9}$$

where $M(V,T)$ denotes the local magnetic moment (at a specific T and V). The expression above can be derived from the high-temperature limit of the quantum mechanical spin model and is nowadays commonly used in thermodynamic approaches.

In the present work we have obtained the magnetic moment M by averaging over all N^{UP} up-sampled atomic configurations (at specific T and V):

$$M(V,T) = \frac{1}{N^{\mathrm{UP}}} \sum_{i}^{N^{\mathrm{UP}}} M_i(V,T). \tag{3.10}$$

Above treatment ensures that the impact of atomic motion (via the MD) on the local magnetic moments is accurately captured.

Note that eq. (3.9) can only be rigorously derived for a localised magnetic system. Very recently alternative entropy equations to eq. (3.9) have been suggested [178, 179], namely $S^{\mathrm{mag-vib}} = -3k_{\mathrm{B}}\ln(M)$ and $-k_{\mathrm{B}}\ln(M)$, but which have been so far evaluated for very few selected systems only.

In contrast, eq. (3.9) has been routinely employed for decades to parameterise magnetic contributions within thermodynamic approaches such as CALPHAD, in particular for wide range of magnetic materials, ranging from more localised towards more itinerant systems. We therefore use eq. (3.9) in the present work too. Note that as will be shown below the impact of explicit magnetic excitations is overall minor.

3.4 Results and Discussions

3.4.1 On the Influence of Excitation Mechanisms on Vacancy Formation Free Energy

Figure 3.1 shows the calculated temperature-dependent mono-vacancy formation Gibbs energy and equilibrium vacancy mole fraction in fcc-Ni, contributed by the various excitation mechanisms, in comparison with experimental measurements. The electronic contribution (pink line) gives a formation energy larger than the $T = 0\,\mathrm{K}$ calculation (red dashed), while quasiharmonicity (blue line) shifts down the curve to slightly lower values. However, the shift is by far not enough to reproduce the experimental data and a discrepancy of almost 0.3 eV remains at the melting temperature. Anharmonicity (green line and shading) is the dominant contribution, shifting down the curve by about 0.2 eV and leading to a strong non-Arrhenius behaviour. The contributions from the electron-phonon coupling (purple line) and from the magnetic excitations (red line) further decrease the formation energy at high temperatures.

The final theory curve including all excitation mechanisms (red line) is in reasonable agreement with experimental data. The remaining discrepancy may stem from the er-

ror associated with both experiments [138, 123] and modelling; the strong interactions between vacancies and tracer elements such as oxygen [180, 181], hydrogen [182, 183] nitrogen [180] and carbon [184] have been rationalised recently. In terms of the modelling, it should be emphasised that the calculation of the formation energy of a point defect puts extreme demands on numerical accuracy and precision. Although we have tried to keep numerical errors well below 1 meV/atom in our calculations, even a tiny error of 0.1 meV/atom scales up to a 10 meV/defect error in the formation energy for a $3 \times 3 \times 3$ supercell. Further, we stress again the challenge in capturing the full magnetic contribution discussed above.

3.4.2 On the Temperature Dependence of Vacancy Formation Entropy

Figure 3.2 shows the calculated vacancy formation entropy, i.e. the negative derivative of the Gibbs energy of formation, in comparison with differential dilatometry measurements. The quasiharmonic approximation (blue line) gives only a very small entropy of formation. Considering all excitation terms listed in eq. (3.6), particularly the anharmonic contribution, gives a much larger entropy of formation in consistent with experimental measurements: strong anharmonicity is suggested here. As discussed by Glensk *et al* [121] for Al and Cu, this is largely due to the softening of the effective potential towards the vacancy, which locally destroys the inversion symmetry and introduces sizeable odd-order anharmonic contributions, although no linear temperature dependency–which is suggested in the local Grüneisen theory (LGT) [121]–is seen in the present case.

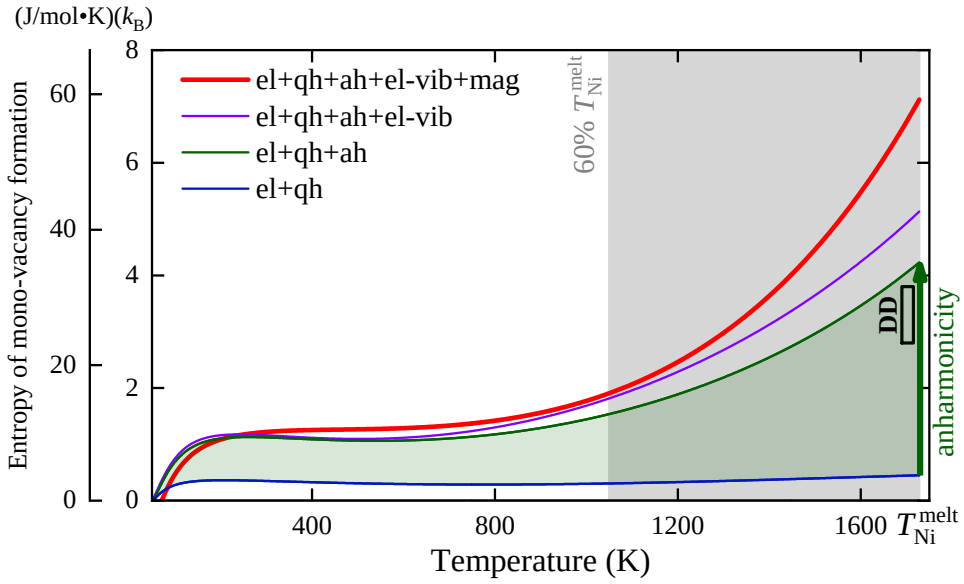


Fig. 3.2 Calculated vacancy formation entropy of fcc-Ni compared with existing experimental data [123].

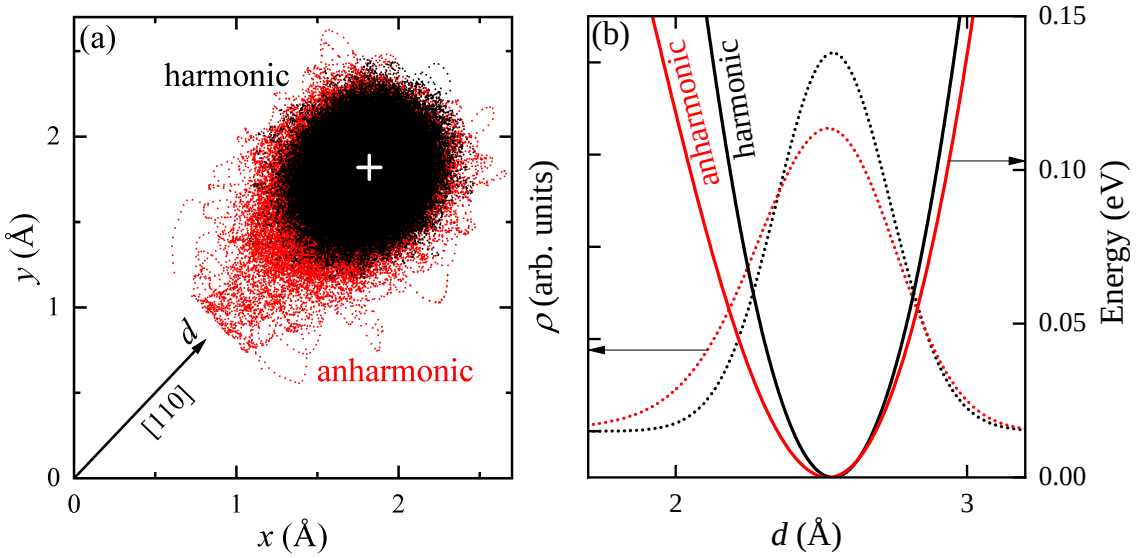


Fig. 3.3 (a) Trajectories of the 12 nearest neighbours (1NNs) of a vacancy (mapped to the first quadrant of the *xy* plane and truncated half-way if a vacancy jump happens) by quasiharmonic and anharmonic approaches at 1600 K and for a lattice constant of 3.58 Å; the equilibrium position is marked as a white cross; (b) distribution function of the distance between 1NNs and the vacancy (dashed lines) according to eq. (3.11), and corresponding effective potential (solid lines) according to eq. (3.12).

To highlight the softening of the effective potential, fig. 3.3a shows an example of the trajectories of the 12 nearest neighbours (1NNs) of a vacancy (mapped to the first quadrant

of the *xy* plane with coordinates of $X^{\mathrm{NN}}_{V,T;i}, Y^{\mathrm{NN}}_{V,T;i}$) based on quasiharmonic (black) and fully anharmonic (red) simulations at 1600 K. In the anharmonic data, one can clearly see a high possibility for the neighbours to move towards the vacancy. Figure 3.3b shows the corresponding distribution function of the distance between 1NNs and the vacancy

$$\rho_{V,T}(d) = \sum_i \delta\left(\sqrt{\left(X^{\mathrm{NN}}_{V,T;i}\right)^2 + \left(Y^{\mathrm{NN}}_{V,T;i}\right)^2} - d\right), \tag{3.11}$$

where $\delta(x)$ equals to 1 for $x = 0$ and otherwise 0, and the resulting effective potentials according to

$$v_{V,T}(d) = -k_{\mathrm{B}} T \ln\left(\rho_{V,T}(d)\right). \tag{3.12}$$

One can clearly see an anisotropy and softening towards the vacancy which cannot –by definition– be reproduced within the quasiharmonic approximation. These results are in nice consistency with previous findings for non-magnetic Al and Cu [121].

3.4.3 Magnetism

Figure 3.4 shows calculated evolution of local magnetic moments (1.286 Å radius) of all atoms in a 3^3 bulk supercell (black) and a 3^3 mono-vacancy supercell (red) as a function of LD time at $T = 1600$ K with $a = 3.58$ Å by using DFT with low convergence parameters, in comparison with $T = 0$ K calculations (mono-vacancy: blue; bulk: pink). One can see that the introduction of a vacancy increases the magnetic moment for $\sim 0.2\,\mu_{\mathrm{B}}$ of its 12 1NNs from the LD calculations. The lattice vibration decreases the average magnetic moment of all atoms.

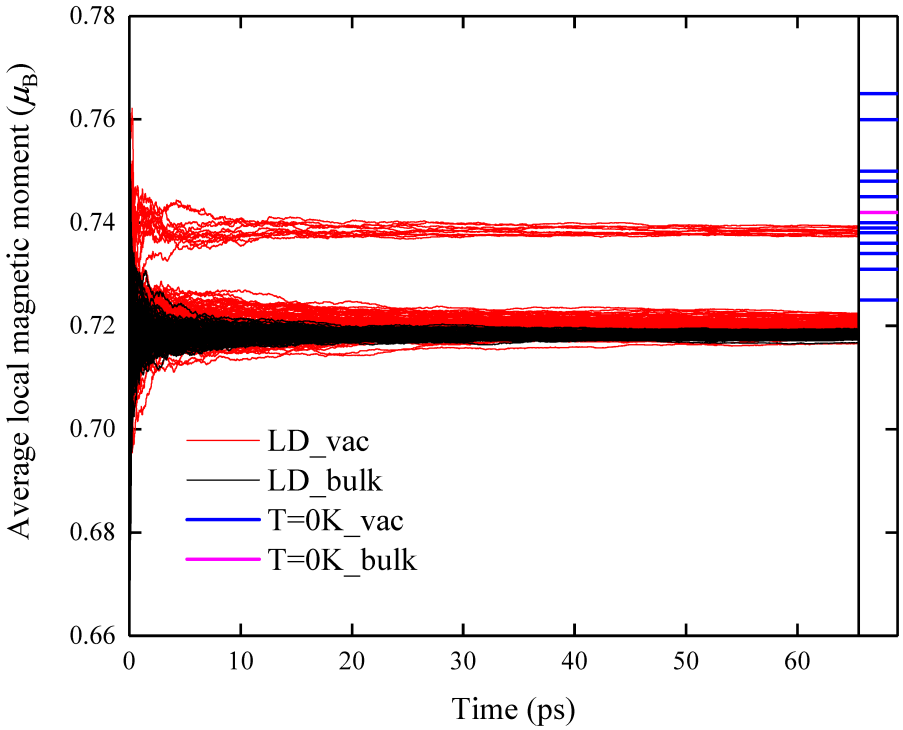


Fig. 3.4 Calculated evolution of local magnetic moments (within sphere of 1.286 Å radius) of all atoms in a 3^3 supercell as a function of LD time at $T = 1600\,\mathrm{K}$ with $a = 3.58$ Å by using DFT with low convergence parameters; comparisons are made between bulk (black), with one vacancy (red), and $T = 0\,\mathrm{K}$ calculations (mono-vacancy: blue; bulk: pink).

To rationalise the impact of the magnetic contribution at high temperatures (fig. 3.2), we have studied the averaged magnetic moments in our LD simulations. Overall we observe a similar behaviour for the vacancy and perfect bulk supercell (fig. 3.5): The magnetic moment *decreases* with increasing temperature, and *increases* with increasing volume. Both dependencies are small with changes of about $0.05\,\mu_B$ and tend to compensate each other if the effect of thermal expansion is considered. The difference between the vacancy and perfect bulk supercell is an order of magnitude smaller and becomes only apparent at the highest temperatures and volumes (red shading in fig. 3.5). The slightly higher magnetic moment of the vacancy supercell is mainly caused by the 1NNs of the vacancy. Despite being small, this difference in magnetic moment between the vacancy and perfect bulk supercell is responsible for the steep increase in the entropy of formation at high temperatures.

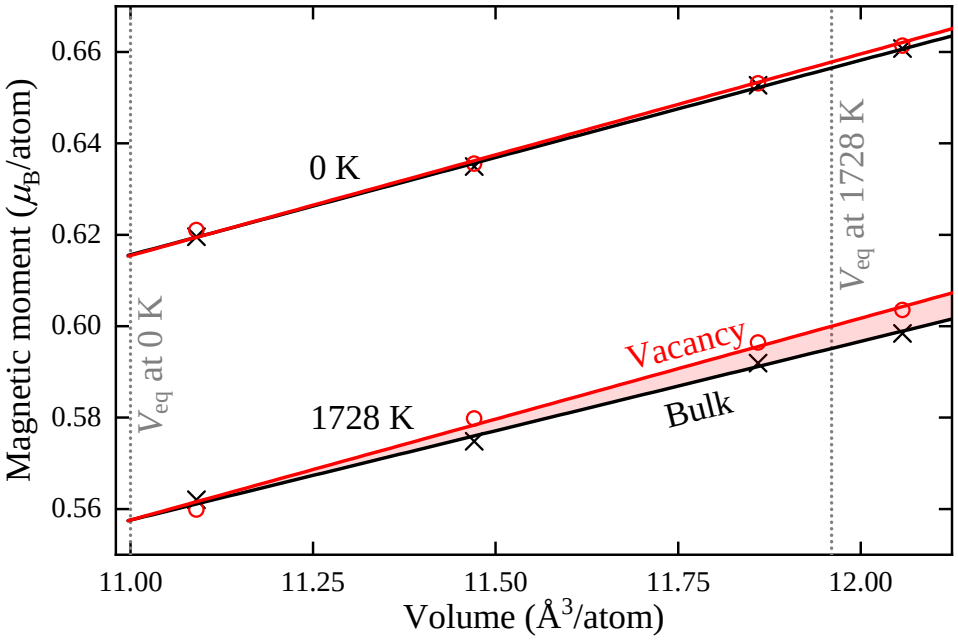


Fig. 3.5 Averaged magnetic moment as a function of volume at $T = 0$ K and at the melting temperature of 1728 K for the vacancy and perfect bulk $3 \times 3 \times 3$ supercells. The symbols represent explicit simulations and the solid lines are polynomial fits to guide the eye. The grey dotted lines denote the equilibrium volumes V_{eq}.

One should note that calculated magnetic excitation assumes a fully disordered paramagnetic system with stable local magnetic moments. The SRO, which may play a decisive role at high temperature [174], has not been considered here.

3.5 Summary and Conclusions

In this chapter, the vacancy formation free energy in fcc-Ni has been calculated using atomistic calculations by accounting for different excitation mechanisms, including the electronic, quasiharmonic, anharmonic, magnetic and the coupling between electrons and atonic vibrations. The anharmonicity and its coupling with electrons has been calculated by using the Two-stage Upsampled Thermodynamic Integration using the Langevin Dynamics (TU-TUILD) scheme which allows the free energy to be calculated with high accuracy.

In contrast with purely quasi-harmonic calculations which suggest a very small entropy of vacancy formation, much larger entropy of vacancy formation due to locally asymmetric

displacement potentials is revealed by the anharmonic calculations carried out here. The calculated results which account for all excitation mechanisms agree reasonably well with recent differential dilatometry (DD) measurements close to the melting temperature, and previously reported T=0 K *ab initio* calculations. The local Grüneisen theory (LGT) [121] does not seem to apply for fcc-nickel.

The work in this chapter supports the view that the mobility of vacancies at high temperatures is high in fcc-nickel; conventionally-used methods involving thermodynamic integration from a (quasi-)harmonic potential with its frequencies fixed to lattice positions are not suitable. Thermodynamic integration of internal energy over temperature method as employed here – which allows the free energy to be calculated for a given interatomic potential – addresses this issue, although its convergency needs to be carefully handled to prove that this has occurred. In this way, it has been shown that the large self-diffusion coefficient of fcc-Ni implied in this work can be quantified by extrapolation to finite temperatures.

It should be noted that the calculations have been conducted with and without considering spin-polarisation. Magnetism (of both ferromagnetic/paramagnetic form) is found to have negligible effect on the calculated vacancy formation enthalpy, although magnetic excitation – which may cause the deviation of calculated results from experimental measurements at high temperatures – needs to be studied further.

This work reported in this chapter is a first step towards the prediction of high temperature diffusion and defect evolution in nickel-based alloys to high accuracy. Such approaches may once mature aid in the design of new grades of superalloys.

Appendix I: Thermodynamic Integration over T

Following shows the derivation and proof of thermodynamic integration scheme over temperatures which allows the free energy at low temperatures to be extended to high temperatures for a given inter-atomic potential by integrating the internal energy U; U is calculated by the Langevin molecular dynamics coupled with TU-TILD potentials.

For a system in thermodynamic equilibrium, the Helmholtz free energy F in the canonical ensemble is defined as:

$$F(\beta) = -\frac{1}{\beta}\ln Z(\beta) \tag{3.13}$$

with the canonical partition function $Z(\beta)$ defined as:

$$Z(\beta) = \sum_i \exp(-\beta E_i) \tag{3.14}$$

where $\beta = 1/(k_B T)$.

The internal energy U is given by:

$$U(\beta) = \frac{1}{Z(\beta)}\sum_i E_i \exp(-\beta E_i) \tag{3.15}$$

$$= -\frac{1}{Z(\beta)}\sum_i \frac{\partial}{\partial\beta}\exp(-\beta E_i) \tag{3.16}$$

$$= -\frac{1}{Z(\beta)}\frac{\partial}{\partial\beta}\sum_i \exp(-\beta E_i) \tag{3.17}$$

$$= -\frac{1}{Z(\beta)}\frac{\partial}{\partial\beta}Z(\beta) \tag{3.18}$$

$$= -\frac{\partial}{\partial\beta}\ln Z(\beta) \tag{3.19}$$

Equations (3.13) and (3.19) give:

$$U(\beta) = \frac{\partial}{\partial\beta}\left[\beta F(\beta)\right] \tag{3.20}$$

Integrating eq. (3.20) gives:

$$\int_{\beta_1}^{\beta_2} U(\beta)\,\mathrm{d}\beta = \beta_2 F(\beta_2) - \beta_1 F(\beta_1) \tag{3.21}$$

In practice, U is calculated at every 20 K, followed by the polynomial parameterisation (over T) before the integration procedure.

Chapter 4

Modelling of Oxidation of Ni-Cr Alloys

4.1 Introduction

The nickel-based superalloys contain substantial quantities of chromium. This is particularly the case for the grades used for demanding environments, e.g. in the power generation, petrochemical or aerospace sectors [13]. Why is this? The overarching reason is the need for the provision of resistance to oxidation, which would otherwise occur very rapidly. Thus, pure Ni oxidises quickly to a porous, friable NiO which is prone to spallation. But if sufficient Cr is added, so-called selective oxidation occurs such that the formation of a protective layer of Cr_2O_3 is promoted [185]. Its growth is slow, which explains its value in conferring superior oxidation resistance to these materials.

Nevertheless, our understanding of the role of Cr in promoting this effect is incomplete. For instance, no quantitative model for the effect of Cr on oxidation resistance is available as yet. Thus for example – although the critical level of $\sim$12 wt.% Cr has been established empirically – there exists as yet no physical explanation or rationalisation of the critical level needed. In the search for physics-based approaches for alloy design, this is much needed. Clearly, any such model needs to appeal to the underlying thermodynamics and diffusion-based mass-transport phenomena on which the phase transformation for any superior oxidation resistance depends.

The work reported in the this chapter was carried out with the above in mind. We set out to build a quantitative modelling framework for the degradation of Ni-Cr alloys capable of explaining the critical level of Cr needed for selective oxidation to Cr_2O_3. A CALPHAD-based approach is chosen, on account of the need to treat the diffusional fluxes of Ni, Cr and O ions, but also in the hope of allowing future extension to the greater complexity of alloying prevalent in commercial alloys. In principle, this would then provide the predictive capability of environmental degradation behaviour which is needed.

4.2 Background

Diffusion-controlled parabolic oxidation kinetics When an Ni-Cr alloy is exposed to an oxygen-containing environment at high temperature, oxides are formed at the metal/gas interface; the thickness of oxide (and associated weight gain) increases with time, with the kinetics often found to be parabolic. Diffusion-controlled chemical reaction is therefore suggested by this observation, with oxygen penetrating through the oxide formed to react with the underlying metal (inward oxide growth) and/or with metal ions (cations) diffusing outwards to form oxide at the oxide/gas interface. The rate constant is found to be inversely proportional to the oxide thickness, consistent with:

$$\frac{\mathrm{d}x_{\mathrm{ox}}}{\mathrm{d}t} = \frac{k_c}{x_{\mathrm{ox}}} \tag{4.1}$$

which gives:

$$x_{\mathrm{ox}}^2 = 2k_c t \tag{4.2}$$

where x_{ox}, t and k_c are oxide thickness, time and parabolic thickening constant, respectively. Equation (4.2) can be reformulated as:

$$\left(\frac{\Delta m}{A}\right)^2 = k_p t \tag{4.3}$$

where A, Δm and k_p are surface area (of alloy which is exposed to environment), weight gain and parabolic weight gain constant respectively.

Compositional dependency and transient oxidation Figure 4.1 illustrates the measured parabolic weight gain constant as a function of temperature and Cr concentration in the Ni-Cr system [186, 185]. The acceleration of oxidation kinetics with increasing temperatures is mainly due to the nature of the thermally-activated processes and hence is consistent with, for example, absolute reaction rate theory [79]. The Cr-content dependency, however, has been categorised into three groups [185] based on the microstructure observed. Figure 4.2 illustrates the microstructural evolution from transient to steady-state oxidation for Ni-Cr alloys with (a) high and (b) low Cr concentration [187]. The high Cr concentration (typically larger than 30 wt.%), characterised by the formation of a continuous/protective Cr_2O_3 layer between the fast growing halite-NiO & spinel-$NiCr_2O_4$ and the substrate, leads to slow oxidation kinetics which are controlled by the diffusional kinetics of dense Cr_2O_3 (Group III, fig. 4.2(a)); on the other hand lower Cr concentrations are found to be insufficient to sustain the continuous Cr_2O_3 layer, thus causing the fast overgrowth of halite-NiO and porous spinel-$NiCr_2O_4$ on top of internal Cr_2O_3 (Group I, fig. 4.2(b)); in such alloys, the kinetics increase with increasing Cr concentration. Group II alloys – which show inhomogeneous oxygen attack on the alloy grain boundaries/bulk at initial-stage oxidation – usually take much longer to approach steady-state protective oxidation kinetics; chromium diffusion is happening laterally and simultaneously with net migration inwards/outwards and this effect probably plays a role in altering the kinetics [185].

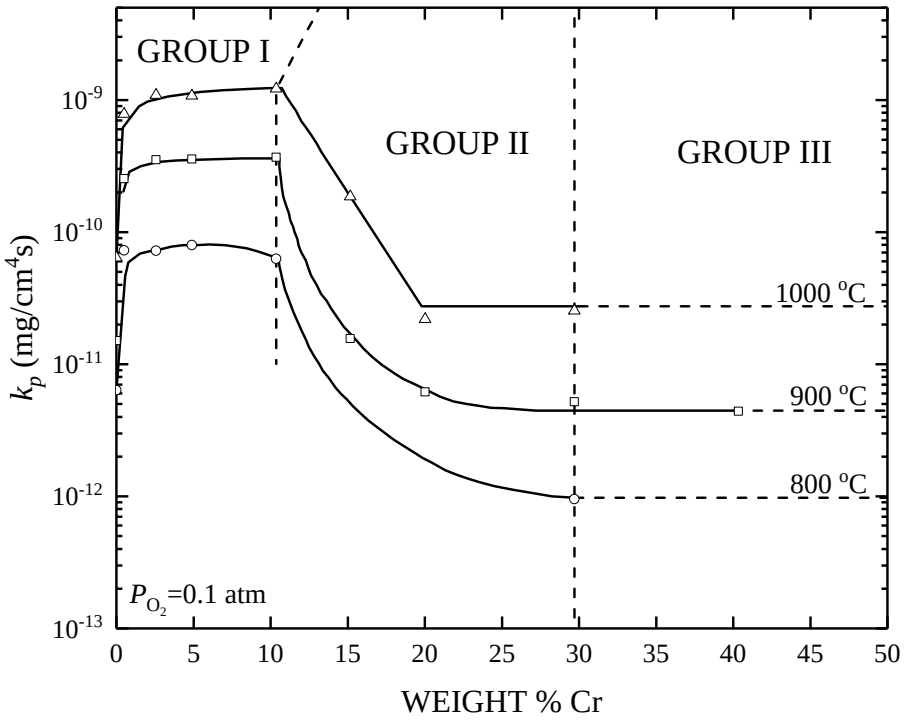


Fig. 4.1 Influence of Cr content in Ni-Cr alloys on oxidation kinetics at P_{O_2}=0.1 atm between 800 to 1200 °C, after [185].

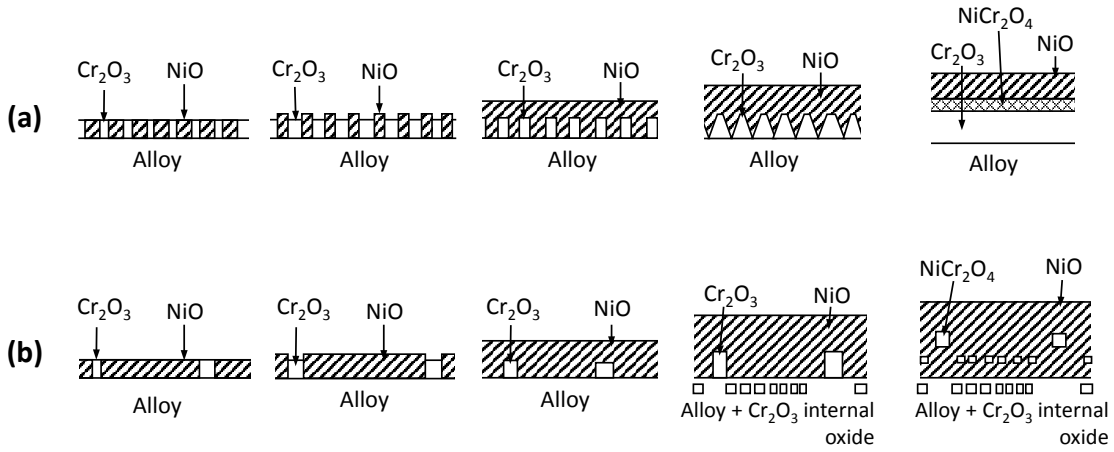


Fig. 4.2 Schematic diagram showing the transition from transient to steady state oxidation for Ni-Cr alloys with (a) high Cr concentration and (b) low Cr concentration, after [187].

Modelling approaches Since high temperature oxidation can be regarded as a diffusion-controlled phase transformation, models available in the literature thus far – of the type adopted in this work – are based upon such approaches. Hence the full diffusion field both in oxide and the underlying substrate needs to be evaluated, as illustrated in fig. 4.3

for a high Cr content alloy. Calculations are usually conducted by coupling estimates of thermodynamic (or electro-chemical) driving forces with atomic mobilities. Attempts have been made to apply the traditional sharp interface approach – which involves maintaining mass balance under the local equilibrium assumption at each moving phase interface – to the binary Fe-O and Cr-O systems [88, 90, 89], with some success. However, for multicomponent oxide systems – e.g. Ni-Cr-O and Fe-Cr-O – the process of tie-line estimation for each phase interface is always numerically challenging; moreover, the oxidation process usually shows a phase region which consists of mixture of multiple phases, e.g. halite-NiO together with spinel-$NiCr_2O_4$. The homogenisation model – stemming from a multi-phase approach which treats diffusion in regions where multiple phases are mixed with each other and application of local equilibrium assumptions to the entire diffusion field – circumvents these difficulties. It allows both local phase transformation (e.g. phase fraction of $NiO/NiCr_2O_4$ mixture) and evolution of global phase region interface (e.g. oxide/alloy interface) to be predicted without explicitly tracking the phase interface. Such method makes the simulation of oxidation of complex alloys possible. A good example is shown in [91] where the thickening of each oxide layer for the Fe-O system is well-predicted by such an approach. This homogenisation model approach is followed here.

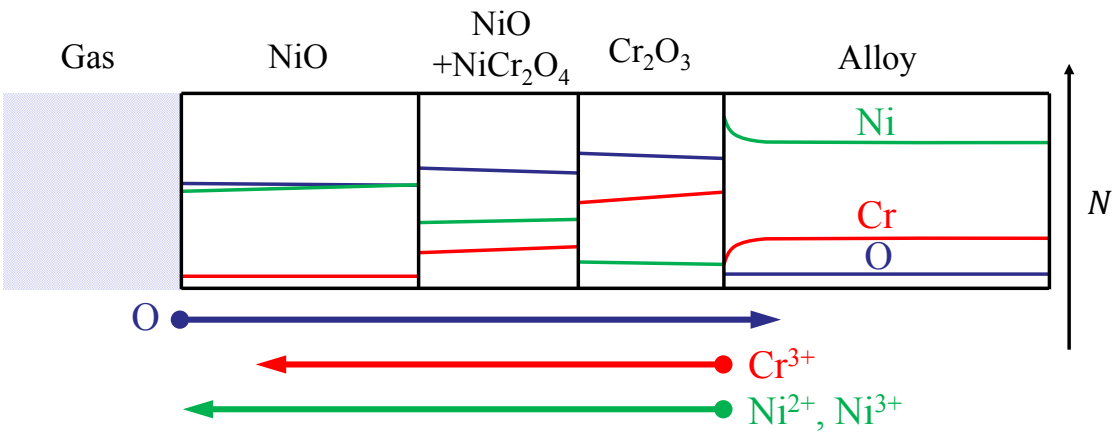


Fig. 4.3 Illustration of 1D geometric layout used in modelling approach.

4.3 Numerical Modelling Approach

4.3.1 Oxide Diffusion Model

The model proposed here assumes that the diffusion of each ionic species is mediated by the vacancies present on the sublattice on which it resides. Thus the kinetic coefficient M_i of ion i on each sublattice in the (oxygen) lattice fixed frame of reference can be expressed as:

$$M_i = \frac{1}{c_{i,\mathrm{O}}} \frac{a_s}{a_\mathrm{O}} y_i^s \left(y_\mathrm{Va}^s M_{i\mathrm{Va}}^s \right) \frac{1}{V_S} \tag{4.4}$$

where $c_{i,\mathrm{O}}$ is the concentration of the diffusing ion i per mole of anion sites; y_i^s and y_Va^s are the fraction of ion i and vacancies on the s sublattice, respectively; a_s and a_O denote the stoichiometric coefficients of sublattice and oxygen sublattice respectively; V_S the molar volume. M_i is related to the tracer or self-diffusion coefficient D_i^* by comparing the limiting case of zero electrical-potential gradient to Fick's first law consistent with:

$$M_i = \frac{D_i^\star}{RT} \tag{4.5}$$

By substituting eq. (4.4) in eq. (4.5) and integrating over all ionic species, the tracer diffusion coefficient of species i can be written as:

$$D_i^\star = RT \sum_s \frac{a_s}{a_\mathrm{O}} y_i^s y_\mathrm{Va}^s M_{i\mathrm{Va}}^s \frac{1}{n_i} \tag{4.6}$$

where n_i is the mole fraction of ion i per mole of anion (oxygen) sites, $M_{i\mathrm{Va}}$ the mobility factor which represents the thermally-activated jumps and which has the form:

$$M_{i\mathrm{Va}} = M_{i\mathrm{Va}}^0 \exp\left\{ \frac{-Q_{i\mathrm{Va}}}{RT} \right\} \frac{1}{RT} \Gamma^{mg} \tag{4.7}$$

where R is the gas constant, T the temperature, $M_{i\mathrm{Va}}^0$ is a frequency factor, $Q_{i\mathrm{Va}}$ is an activation enthalpy, and Γ^{mg} is a factor taking into account the effect of ferromagnetic

transition. If the ferromagnetic effect for the phase can be ignored, the mobility can be simplified to:

$$M_{i\mathrm{Va}} = \exp\left\{\frac{-Q_{i\mathrm{Va}} + RT\ln M^0_{i\mathrm{Va}}}{RT}\right\}\frac{1}{RT} = \exp\left\{\frac{\Delta G_{i\mathrm{Va}}}{RT}\right\}\frac{1}{RT} \tag{4.8}$$

In general the parameter $\Delta G_{i\mathrm{Va}}$ depends on the composition, the temperature T, and the pressure P. In the spirit of the CALPHAD approach the composition dependence of $\Delta G_{i\mathrm{Va}}$ is represented as

$$\Delta G_{i\mathrm{Va}} = \sum_{I_0} P_{I_0}\{Y\}\Phi_{I_0} + \sum_{i=1}^{n}\sum_{I_i} P_{I_i}\{Y\}\Psi_{I_i} \tag{4.9}$$

where Φ_{I_i} is the value at each endpoint of the compositional space (I_0) and Ψ_{I_i} is the interaction parameter defined by I_i.

In simulations it is the effective mobilities of the elements rather than the mobilities of ions that are considered (see section 4.3.3). Contributed by corresponding ionic species in each sublattice, the mobility M^r_j of element j in phase r is expressed consistent with eq. (2.59).

4.3.2 Grain Boundary Diffusion

In the temperature regime considered in this study, diffusion along grain boundary, acts as a short-circuit diffusion path, thus it plays a key role, particularly for corundum-Cr_2O_3 phase. Type A kinetics [188] is assumed here:

$$M^{\mathrm{eff}}_j = f^{\mathrm{gb}} M^{\mathrm{gb}}_j + \left(1 - f^{\mathrm{gb}}\right) M^{\mathrm{bulk}}_j \tag{4.10}$$

where M^{eff}_j, M^{gb}_j and M^{bulk}_j are the effective, grain-boundary and lattice mobility of element j respectively; the term f^{gb} represents the volume fraction of grain boundaries which can

be simply estimated by [189]:

$$f^{\mathrm{gb}} = q\delta/d \tag{4.11}$$

where q is the numerical factor depending on the grain shape (1 for parallel grains, 3 for square grains), δ the grain boundary width, d the average grain size. M_j^{gb} is evaluated as:

$$M_j^{\mathrm{gb}} = M_j^{\mathrm{bulk}} \exp\left\{\frac{-\alpha_j Q_j^{\mathrm{bulk}}}{RT}\right\} \tag{4.12}$$

where α_j is the activation energy reduction factor; Q_j^{bulk} is the 'effective' activation energy of bulk mobility which in practice, is evaluated by numerically perturbing T, as the element mobility in bulk is calculated by summing-up over all sub-lattices (see eq. (2.59)) and $\Delta G_{i\mathrm{Va}}$ may contain complex expressions.

4.3.3 Homogenisation Model

The homogenisation model [190, 191] implemented in the 1D DICTRA diffusion code has been used to evaluate the phase evolution and diffusion kinetics within the oxide scales and the underlying substrate. If any correlation effects of successive atom-vacancy jumps and all other kinetic and thermodynamic cross-effects are ignored, the flux J_k of an element k $\left[\mathrm{mol}\cdot\mathrm{m}^{-2}\cdot\mathrm{s}^{-1}\right]$ in the single phase region along spatial coordinate z in the lattice-fixed frame of reference can be modelled as:

$$J_k = -M_k c_k \frac{\partial \mu_k}{\partial z} \tag{4.13}$$

with continuity maintained consistent with:

$$\frac{\partial c_k}{\partial t} = \frac{\partial}{\partial z}(-J_k) \tag{4.14}$$

With the homogenisation model, multi-component multi-phase diffusion is modelled by assuming that at each point along the reaction front the local phase assemblage comes

to local equilibrium, consistent with the local equilibrium assumption. The transport properties of component (element) k within each phase ϕ are defined by:

$$\Gamma_k^{\phi} = M_k^{\phi} c_k^{\phi} \tag{4.15}$$

Then an estimate of the effective transport occurring in the multi-phase mixture $\Gamma_k^{\star}$ is obtained by applying a so-called homogenisation function which is locally dependent upon microstructure. If the rule of mixtures is used then:

$$\Gamma_k^{\star} = \sum_{\phi} f^{\phi} \Gamma_k^{\phi} \tag{4.16}$$

where $f^{\mathrm{v},\phi}$ is the local volume fraction of phase ϕ. The flux expression eq. (4.13) can then be rewritten as:

$$J_k = -\Gamma_k^{\star} \frac{\partial \mu_k^{\mathrm{l.eq}}}{\partial z} \tag{4.17}$$

where the superscript *l.eq.* has been added to emphasise that a locally-equilibrated chemical potential is assumed.

4.3.4 Numerical Implementation

The above system of equations (eqs. (4.14) to (4.17)) has been solved by the finite volume method (FVM) making use of flux equations derived from the discrete lattice model [192, 113, 91]:

$$J_k = \frac{-RT}{\Delta z} \sqrt{\Gamma_k^{\star 1} \Gamma_k^{\star 2}} 2 \sinh \left\{ \frac{\Delta \mu_k}{2RT} \right\} \tag{4.18}$$

where $\Gamma_k^{\star 1}$ and $\Gamma_k^{\star 2}$ are defined for two neighbouring control volumes, Δz and $\Delta \mu_k$ are the centre-to-centre distance and the chemical potential difference between them two, respectively. The expression $2RT \sinh\{\Delta \mu_k / 2RT\} / \Delta z$ has been chosen by appealing to absolute reaction theory; its first order Taylor expansion can be shown to be consistent with the chemical potential gradient (i.e. an approximation when $\Delta \mu_k / RT$ is small).

Due to the nonlinearity of the system of equations, the Newton-Raphson scheme is used. Furthermore, several numerical improvements have been implemented relative to what has been carried out previously [192, 113] for diffusion in oxide phase(s):

Assessed molar volume Oxygen acts as an interstitial in metals but a (substitutional) volume-carrier in oxides; hence the system of equations has been solved fully in a lattice-fixed frame of reference taking the influence of diffusive flux on local molar volumes (with assessed molar volumes) into account, regardless of which phases may be present in the system [91].

Diffusion across phase interfaces The flux across the oxide/metal interface is hindered by the low mobility of the base component (solvent) in the substrate if eq. (4.18) is utilised; the degree of phase transition $\sum_{\phi} \left|\Delta f^{\phi}\right| /2$ is introduced to address this issue by modifying eq. (4.18) as [91]:

$$J_k = \frac{-RT}{\Delta z}\left[\left(\frac{1}{2}\sum_{\phi}\left|\Delta f^{\phi}\right|\right) M_k^{\text{trans}} \sqrt{c_k^1 c_k^2} + \left(1-\frac{1}{2}\sum_{\phi}\left|\Delta f^{\phi}\right|\right)\sqrt{\Gamma_k^{\star 1}\Gamma_k^{\star 2}}\right] 2\sinh\left\{\frac{\Delta\mu_k}{2RT}\right\} \tag{4.19}$$

If larger phase transition occurs (i.e. $\sum_{\phi} \left|\Delta f^{\phi}\right| \to 2$), e.g. the moving oxide/substrate interface, more (assumed) trans-interface mobility M_k^{trans} (which is larger) is contributed. This special treatment arises for the general homogenisation model without explicitly tracking the phase interface; in fact the diffusion across the phase interface is assumed not to be the rate-determining process here.

Parallisation & interpolation scheme The interpolation scheme [193] (a typical space-time tradeoff) was utilised in [91] to speed-up calculations by storing pre-calculated thermodynamic equilibria at discretised thermodynamic variable (e.g. composition) space which is dynamically conserved. An alternative speed-up can be achieved by the parallelisation due to the independency of each equilibrium calculation, as suggested in [194]. Here both methods are combined together in a way that each slave process maintains

each individual sub-set of the whole pre-calculated thermodynamic variable space which is managed by one of the slave processes; this slave process communicates with the homogenisation model (master process) by providing all thermodynamic equilibrium information, as illustrated in fig. 4.4.

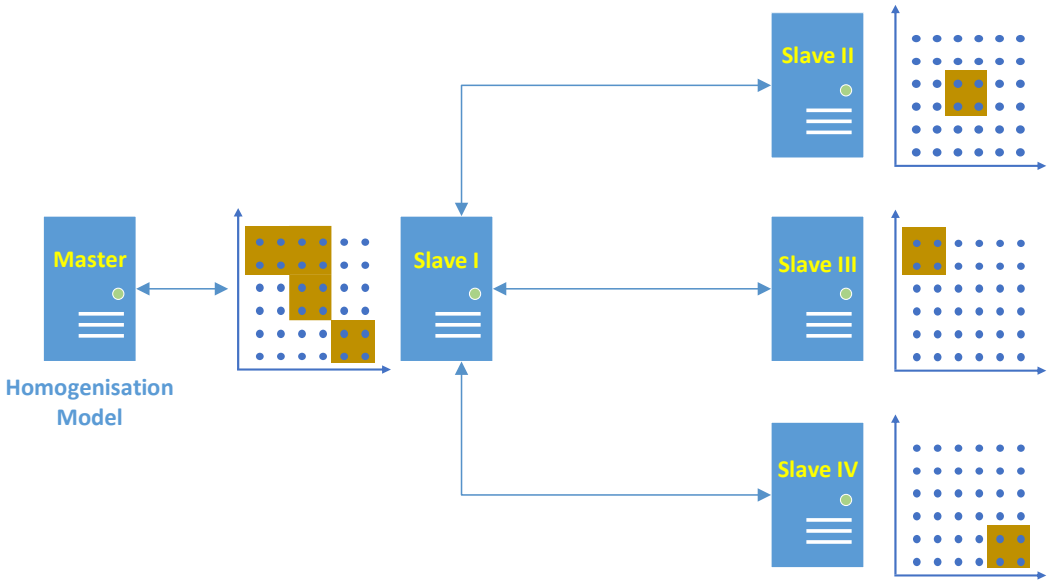


Fig. 4.4 Illustration of parallelled interpolation scheme: each slave process maintains each individual sub-set of the whole pre-calculated thermodynamic variable space which is managed by one of the slave processes; this slave process communicates with the homogenisation model (master process) by providing all thermodynamic equilibrium information.

Improved equilibrium solver The charge balance constraint for each phase is added in this work for finding the starting compositional values before the Gibbs-energy minimisation procedure; the full convex hull is computed (by the Quickhull algorithm [195]) and stored initially in order to speed up iso-thermal kinetic calculations; this algorithm in principle would also be useful for the Alloy-by-Design purpose where most materials properties are defined at a fixed temperature. One of the drawbacks of the convex hull approach compared to the lower bound value approach (which was implemented in Thermo-Calc)

is that it may enter into an irrational metastable compositional region; site-fractions of constituents are thus constrained by pre-defined ranges during calculations.

Adaptive meshing scheme It is found that a larger compositional gradient (along the space, $\mathrm{d}x/\mathrm{d}z$) or larger size of finite volumes ($\mathrm{d}z$) will lead to better convergency of the Newton-Raphson scheme. If we define the mesh quality function (Q_{M}), in a simple linear manner, as:

$$Q_{\mathrm{M}} = k\left(\frac{\mathrm{d}x}{\mathrm{d}z}\right)_{\mathrm{avg}} + \mathrm{d}z \tag{4.20}$$

where k is defined as the relative contribution of the average compositional gradient and the size of finite volume, then we can constrain the Q_{M} of every finite volumes within a upper and lower bound by merging/splitting of two neighbouring finite volumes, as demonstrated in fig. 4.5. This scheme is particularly useful for oxidation simulations where a fewer number of finite volumes are needed for the oxide region compared to that for the metal region.

4.3.5 Entropy Production

The energy dissipation rate due to diffusion can be calculated as [75, 76]:

$$\dot{S} = \frac{1}{T}\sum_{k} J_k \nabla \eta_k \tag{4.21}$$

where η is the electrochemical potential which is contributed by the chemical potential μ and the electrostatic potential ψ:

$$\eta_k = \mu_k + q_k \mathscr{F} \psi_k \tag{4.22}$$

where q is the charge of the species and $\mathscr{F}$ is the Faraday constant. To differentiate the entropy produced by different phases, it is possible to integrate $\dot{S}$ over space weighted by

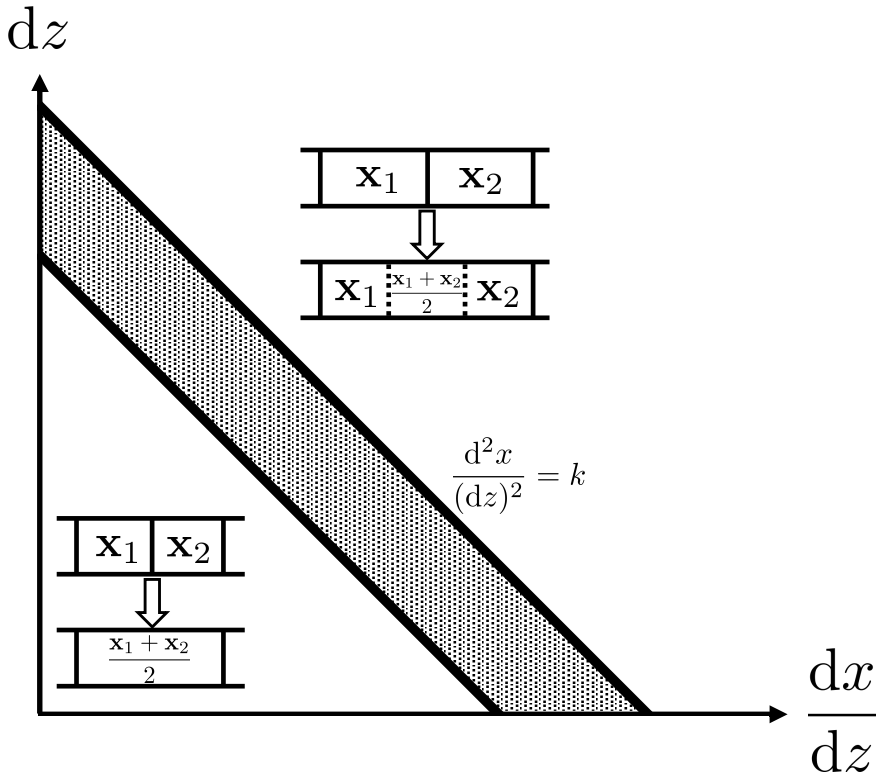


Fig. 4.5 Illustration of adaptive meshing method adopted in this work.

local equilibrium phase mole fractions $f^{\mathrm{m},\phi}$:

$$\dot{S}^{\phi} = -\frac{1}{T}\int_z \sum f^{\mathrm{m},\phi} J_k \frac{\partial \eta_k}{\partial z}\,\mathrm{d}z \tag{4.23}$$

The phase with largest $\dot{S}^{\phi}$ is suggested to be the one through which diffusion is rate-controlling.

4.4 Thermodynamic and Kinetic Descriptions

The thermodynamic descriptions (parameters) are shown in table 4.1. The mobility parameters are shown in table 4.2. The optimisations were done using the PARROT module implemented in the Thermo-Calc software [27]. In what follows, the parameters used are justified.

4.4.1 Halite-(Ni,Cr)O

Based upon the concept of a two sublattice model – one for cations and one for anions – halite has been modelled by Taylor and Dinsdale [196] according to:

$$\left[\mathrm{Cr^{3+}}, \mathrm{Ni^{2+}}, \mathrm{Ni^{3+}}, \mathrm{Va}\right]_1 \left[\mathrm{O^{2-}}\right]_1 \tag{4.24}$$

A disadvantage of this approach is that it is not possible to model oxygen transport on the second sublattice.

Hence, in this work, the possibility of vacancies is introduced onto the oxygen sublattice, i.e.

$$\left[\mathrm{Cr^{3+}}, \mathrm{Ni^{2+}}, \mathrm{Ni^{3+}}, \mathrm{Va}\right]_1 \left[\mathrm{O^{2-}}, \mathrm{Va}\right]_1 \tag{4.25}$$

Hence, this allows the vacancy-mediated diffusion of oxygen to be considered. The calculated oxygen tracer diffusion coefficient at $P_{\mathrm{O}_2} = 10^{-4}$ atm and $P_{\mathrm{O}_2} = 1$ atm are compared to experiments [197–202], as shown in fig. 4.6. Different activation energies at different temperatures (i.e. non-Arrhenius behaviour) are suggested by tracer diffusion experiments; it might be due to the non-Arrhenius vacancy formation energy at oxygen sub-lattice; further attempts should introduce parameterisation consistent with LGT [121] (i.e. $G^f_{\mathrm{Va}} = H^f_{\mathrm{Va}} - \frac{1}{2}T^2 {S^f_{\mathrm{Va}}}'$ rather than $G^f_{\mathrm{Va}} = H^f_{\mathrm{Va}} - TS^f_{\mathrm{Va}}$)

The migration of both $\mathrm{Ni^{2+}}$ ions and $\mathrm{Ni^{3+}}$ ions are considered. As electrons move much faster than ions, it is reasonable to neglect the different valence states when considering diffusion, i.e. $\mathrm{Ni^{2+}}$ and $\mathrm{Ni^{3+}}$ are assumed to have the same mobility. The calculated nickel tracer diffusion coefficient at $P_{\mathrm{O}_2} = 10^{-4}$ atm and $P_{\mathrm{O}_2} = 1$ atm are compared to experiments [203–210, 210–212], as shown in fig. 4.7. Reasonable agreement is demonstrated.

Cr tracer diffusion coefficient in halite-NiO has been measured by several workers, e.g. [213–216] for single crystals and [217] for polycrystals. Here we calculate the substitutional Cr diffusion which is mediated by the vacancies present at cationic sites,

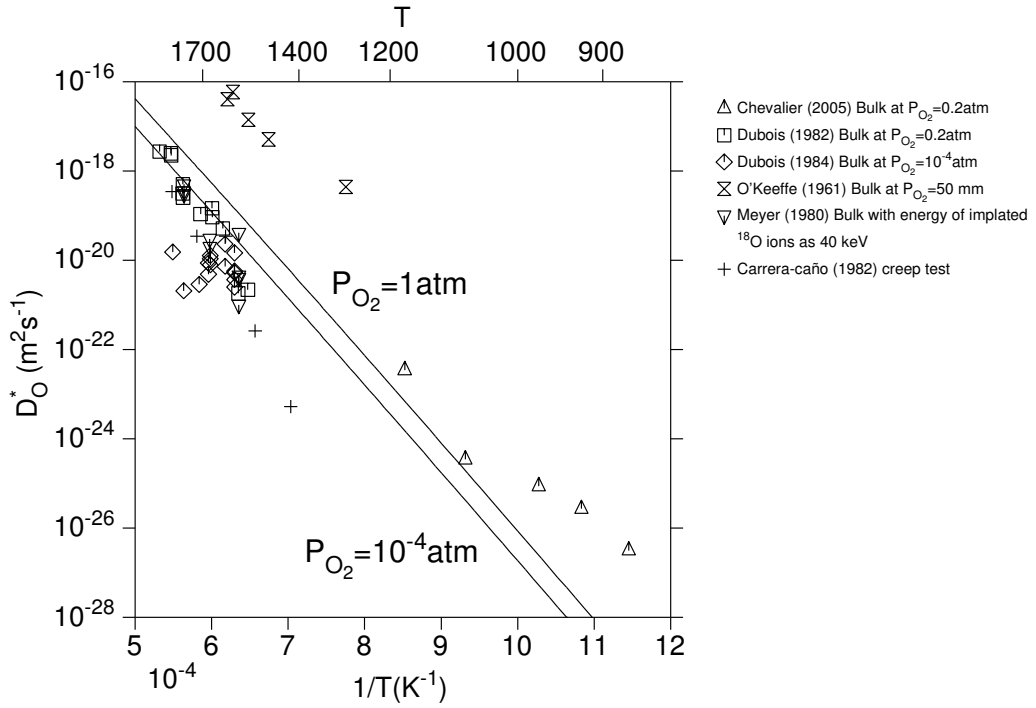


Fig. 4.6 The comparison of oxygen tracer diffusion coefficient in halite NiO phase between different experiments and calculations [197–202].

including V''_{Ni}, V'''_{Ni} and V'''_{Cr}. Figures 4.8 to 4.10 compare the calculations and experiments for the dependency of temperature, Cr concentration in (Ni,Cr)O and P_{O_2} on Cr tracer diffusion coefficient, respectively. The predictions show good agreement in terms of the temperature dependency and Cr-concentration dependency. However, the P_{O_2} dependency cannot be properly rationalised due to the contradiction of measurements [214] and [215]. Proper judgement of these two sets of measurements are required.

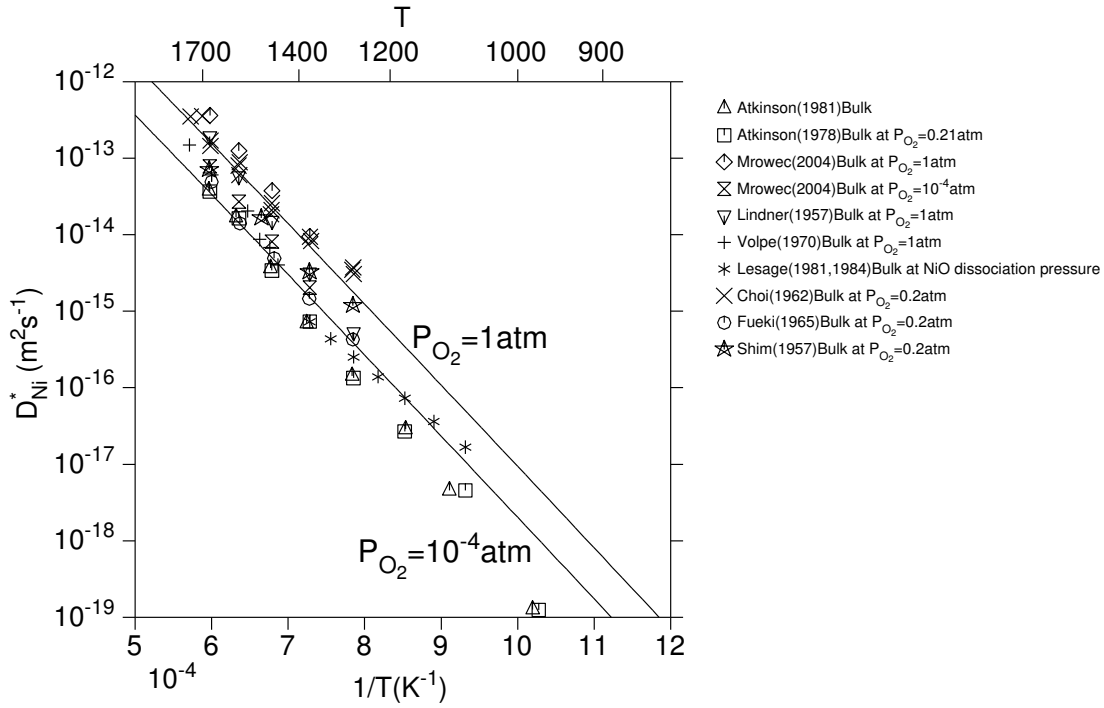


Fig. 4.7 The comparison of nickel tracer diffusion coefficient in halite NiO phase between calculations and experiments [203–210, 210–212].

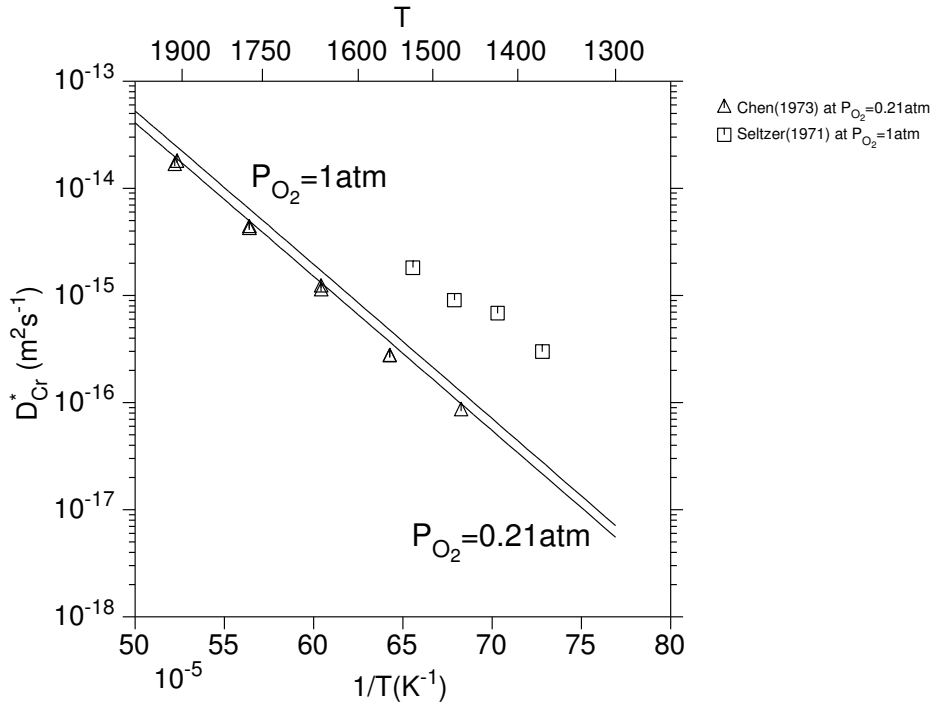


Fig. 4.8 The comparison of temperature-dependent chromium tracer diffusion coefficient in halite NiO phase between calculations and experiments [214, 215].

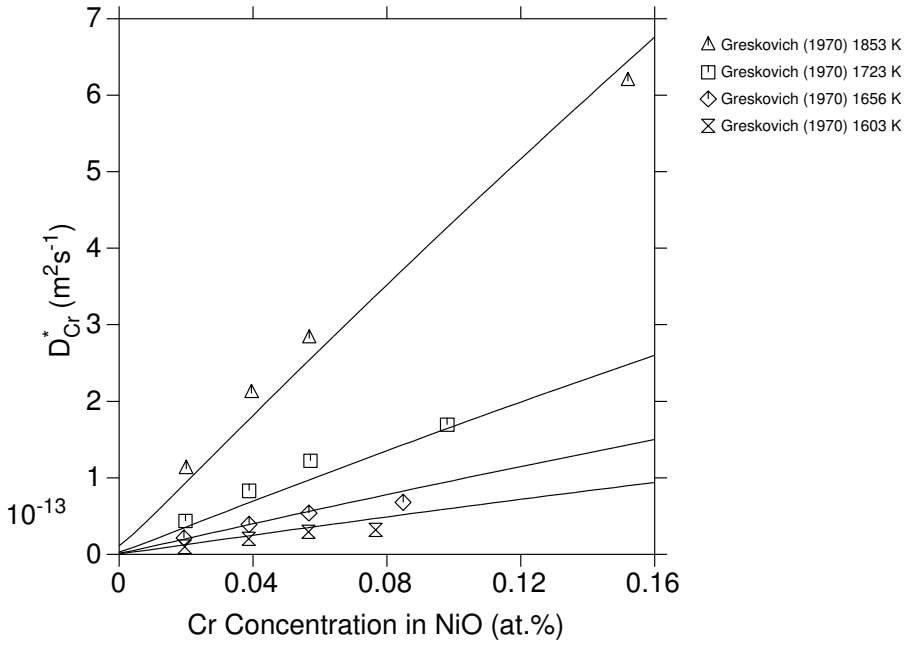


Fig. 4.9 The comparison of chromium-content-dependent chromium tracer diffusion coefficient in halite NiO phase between calculations and experiments [213].

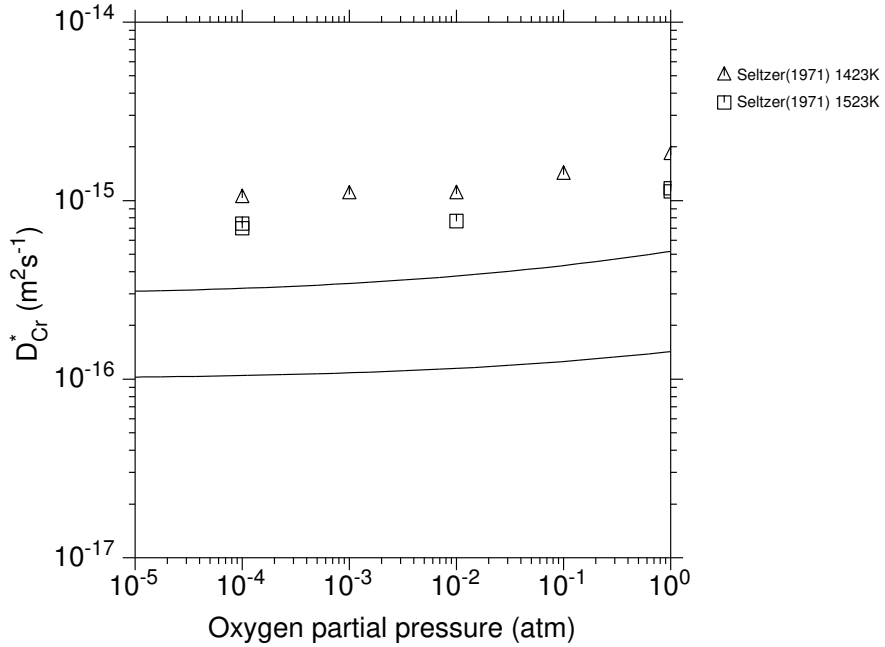


Fig. 4.10 The comparison of P_{O_2}-dependent chromium tracer diffusion coefficient in halite NiO phase between calculations and experiments [215].

4.4.2 Corundum-$(Cr,Ni)_2O_3$

The available kinetic assessment of Cr_2O_3 by Hallström [90] is based on the thermodynamic (defect) assessment of Taylor and Dinsdale [196, 218] which considers the Cr^{3+} interstitials at the octahedral sites at low oxygen activities, i.e.

$$\left[Cr^{3+}, Cr^{2+}\right]_2 \left[Cr^{3+}, Va\right]_1 \left[O^{2-}\right]_3 \tag{4.26}$$

where the first sublattice represents the two-thirds of the octahedral sites occupied by cations. The second sublattice is also octahedral and contains interstitial cations. The third sublattice represents the hexagonally close-packed oxygen ions. To allow for a P_{O_2} dependent oxygen mobility to be modelled, tentative attempts have been made previously to correlate oxygen vacancies with Cr interstitials [90] without modifying the thermodynamic descriptions.

In this work, vacancies are introduced in the oxygen sublattice, based on the recent thermodynamic reassessment by Povoden *et al* [219]:

$$\left[Cr^{3+}, Cr^{2+}\right]_2 \left[Cr^{3+}, Va\right]_1 \left[O^{2-}, Va\right]_3 \tag{4.27}$$

Hence the flux of oxygen can be expressed as:

$$J_O = -\left[y'''_{Va} y'''_O M_{OVa}\right] \frac{1}{V_m} \frac{\partial \mu_O}{\partial z} \tag{4.28}$$

where y'''_{Va} and y'''_O are the site fractions of vacancies and oxygen in the third sub-lattice, respectively. Equation (4.28) is consistent with the generalised expressions detailed in section 4.3.1. The oxygen vacancy formation enthalpy is chosen here, consistent with recent *ab initio* calculations by Carey *et al* [220], i.e. 4.11 eV and 2.45 eV for undoped and Ni-doped Cr_2O_3 respectively. Linear temperature dependent oxygen vacancy formation Gibbs free energy is assumed here, following the Arrhenius law. No experimental measurements

or finite temperature calculation have been reported yet; the entropy of oxygen vacancy formation is thus chosen so that the minimum vacancy concentration is within the numerical limit (10^{-12} by default) of the equilibrium solver (Thermo-Calc 2017a). Figures 4.11 and 4.12 show the calculated defect concentration (including Cr^{+3} interstitials and oxygen vacancies), as a function of temperature and P_{O_2} respectively. It should be noted that there is more than one charge state of an oxygen vacancy in Cr_2O_3 phase with different formation energies [221]; however only $V_O^{\cdot\cdot}$ is considered in this study for simplicity. Calculated and measured chromium [222–226] and oxygen [227, 222, 223, 228–231] tracer diffusion coefficients are compared in figs. 4.13 and 4.14 respectively. Predictions show good agreement with measurements on single crystals, even though large variance of measured diffusion coefficients are suggested.

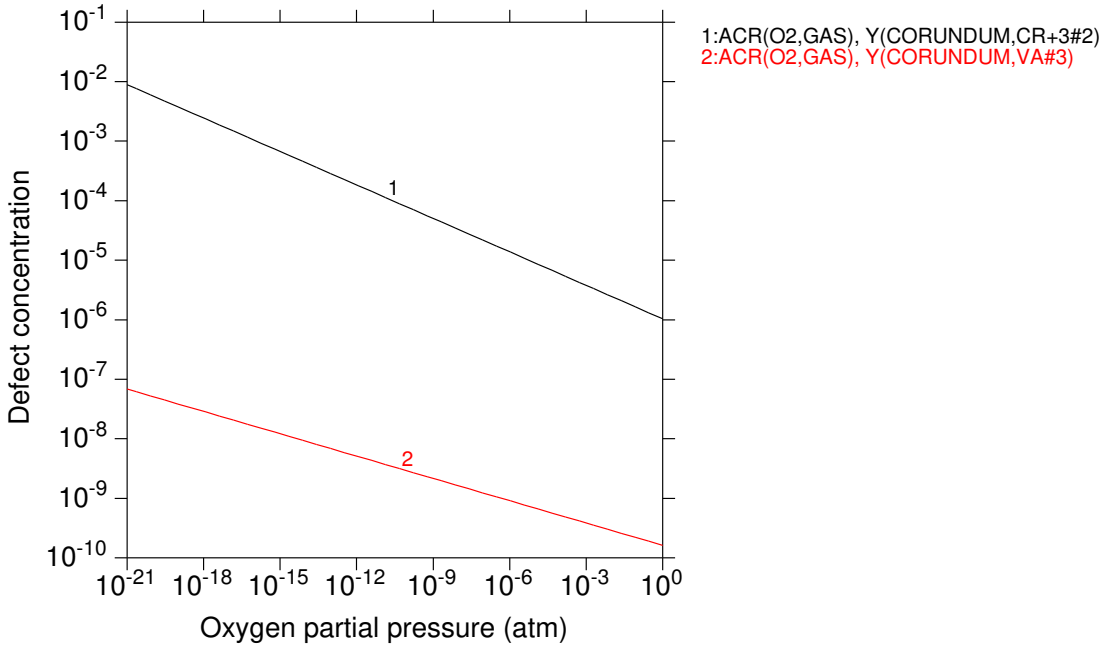


Fig. 4.11 Calculated defect concentrations in corundum Cr_2O_3 phase at 1100 °C; 1. Cr^{3+} interstitials and 2. oxygen vacancies.

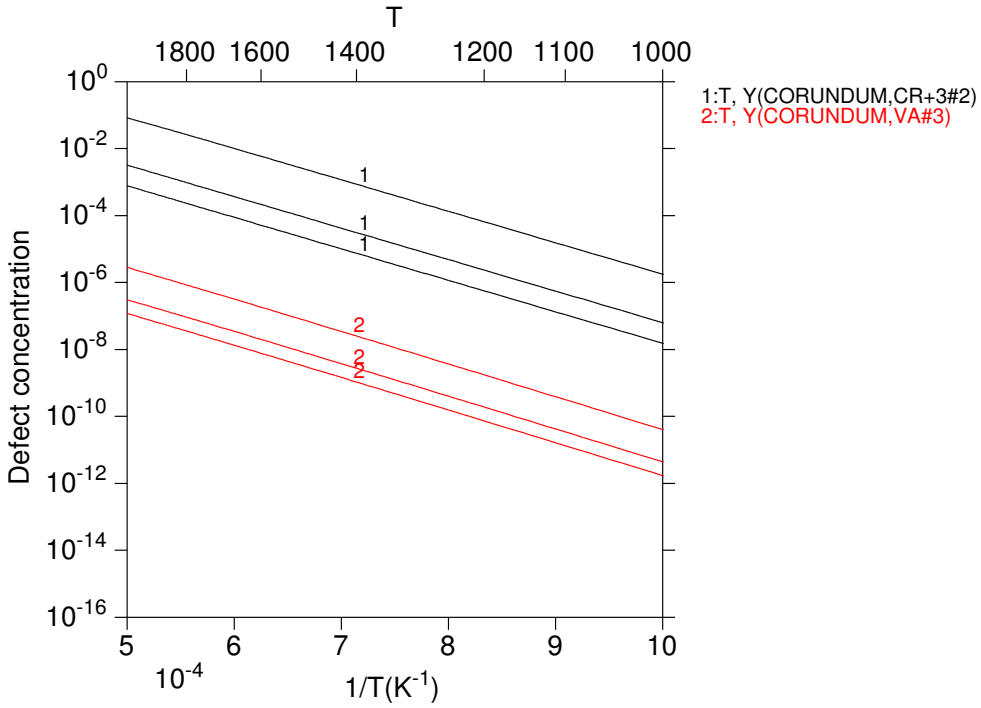


Fig. 4.12 Calculated defect concentrations in corundum Cr_2O_3 phase at $P_{O_2} = 5 \times 10^{-5}, 10^{-12}, 0.1$ atm; 1. Cr^{3+} interstitials and 2. oxygen vacancies.

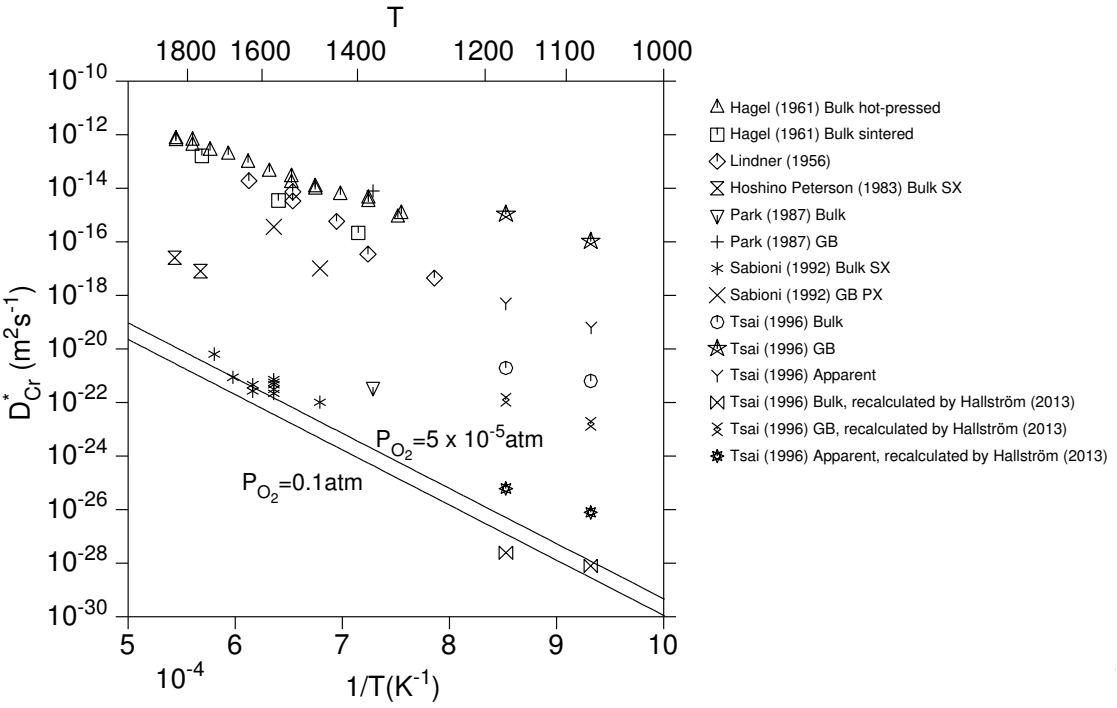


Fig. 4.13 The comparison of chromium tracer diffusion coefficient in corundum Cr_2O_3 phase between calculations and experiments [227, 222, 223, 228–231].

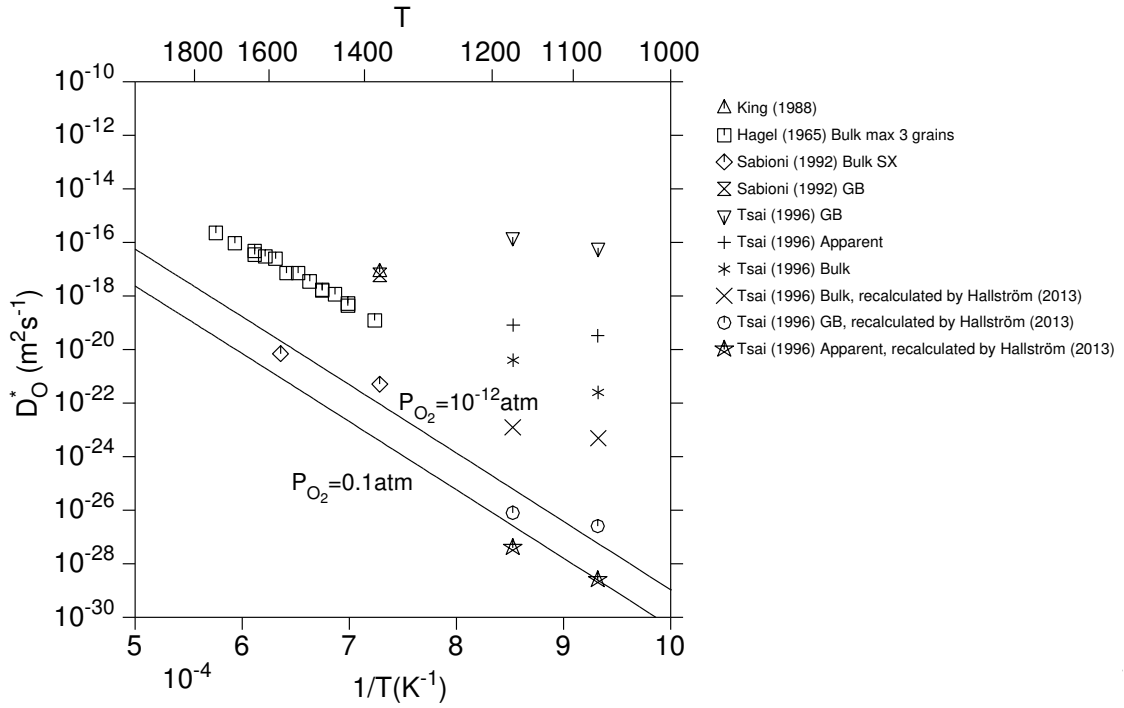


Fig. 4.14 The comparison of oxygen tracer diffusion coefficient in corundum Cr_2O_3 phase between calculations and experiments [222–226].

To allow for the treatment of diffusion of nickel through Cr_2O_3, the Ni^{2+} interstitials have been further added, consistent with [196]:

$$\left[Cr^{3+}, Cr^{2+}\right]_2 \left[Ni^{2+}, Cr^{3+}, Va\right]_1 \left[O^{2-}, Va\right]_3 \tag{4.29}$$

Calculated tracer diffusion coefficient of nickel in Cr_2O_3 is shown in fig. 4.15, as compared with experiments on single crystals [216].

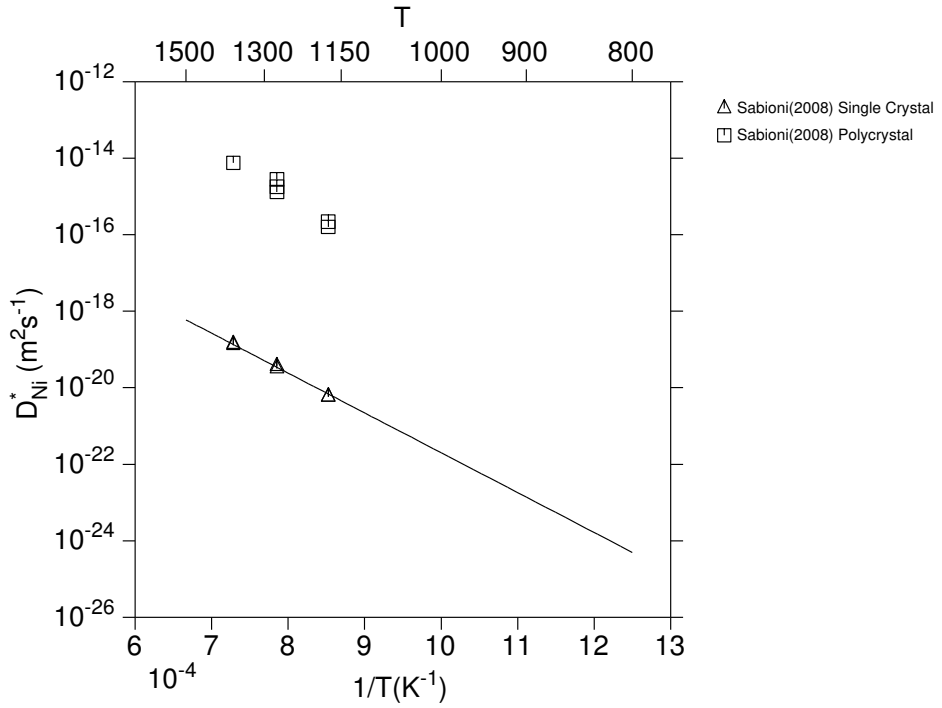


Fig. 4.15 The comparison of nickel tracer diffusion coefficient in corundum Cr_2O_3 phase at $P_{O_2} = 0.2$ atm between calculations and experiments [216].

4.4.3 Spinel-$NiCr_2O_4$

Here we have used a four sublattice model according to [232]

$$\left[Cr^{3+}, Cr^{2+}, Ni^{2+}\right]_1 \left[Cr^{3+}, Ni^{2+}, Va\right]_2 \left[Cr^{2+}, Va\right]_2 \left[O^{2-}\right]_4 \tag{4.30}$$

where the first sub-lattice represents the tetrahedral interstitial site; the second and the third sub-lattice represent the octahedral interstitial site; the fourth sub-lattice denotes the fcc oxygen sublattice. It should be noted that the introduction of the third sublattice is to generalise the spinel description consistent with Fe-Cr-O system and the concentration of octahedral Cr^{2+} ions at the third sub-lattice is very low in the $NiCr_2O_4$ phase.

The available kinetic data for the $NiCr_2O_4$ spinel phase are very sparse. No vacancy has been added to the oxygen sub-latticed for this phase due to lack of P_{O_2}-dependent oxygen tracer diffusion measurements and accepted results. The tracer diffusion coefficients

measured for poly-crystalline $NiCr_2O_4$ [233, 234, 228, 205] are adopted here. Figures 4.16 to 4.18 compare calculated and measured tracer diffusion coefficient of oxygen, chromium and nickel, respectively. All predictions show good agreement with measurements.

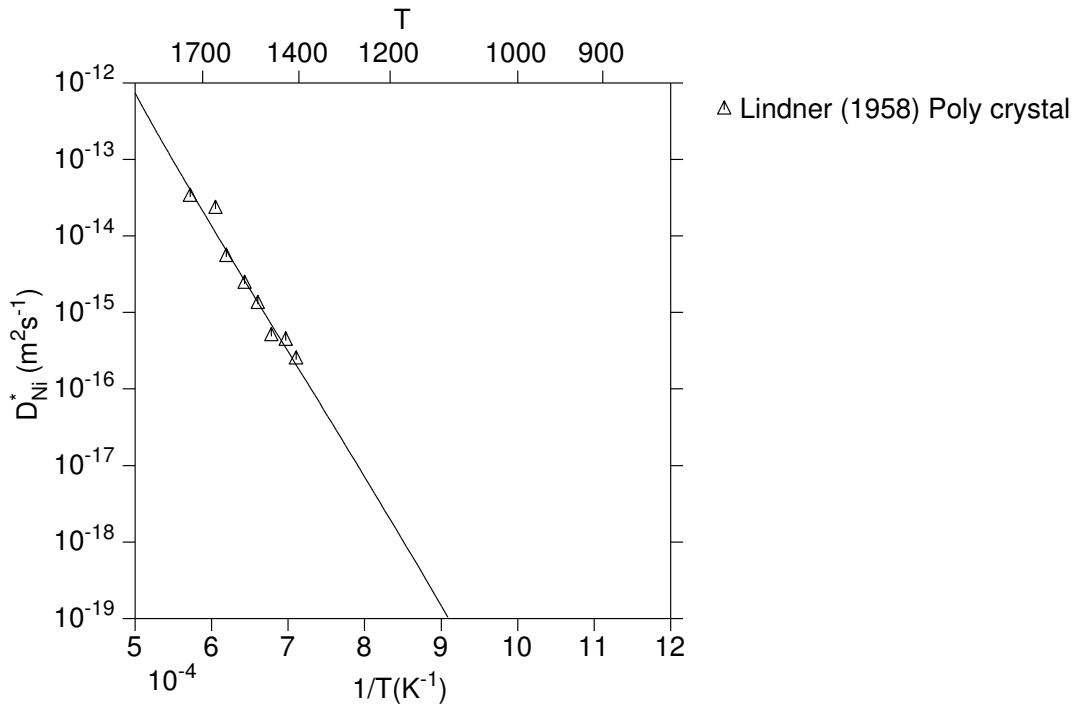


Fig. 4.16 The comparison of nickel tracer diffusion coefficient in spinel $NiCr_2O_4$ phase at $P_{O_2} = 0.1$ atm between calculations and experiments [235].

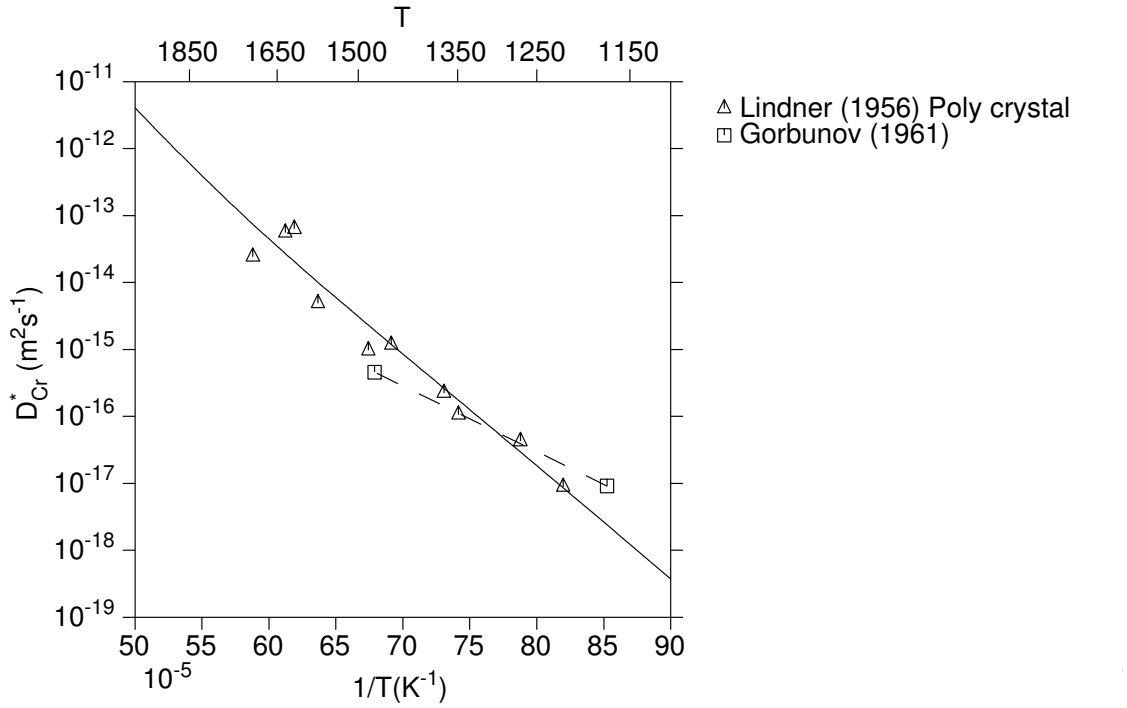


Fig. 4.17 The comparison of chromium tracer diffusion coefficient in spinel $NiCr_2O_4$ phase at $P_{O_2} = 0.2$ atm between calculations and experiments [228, 234].

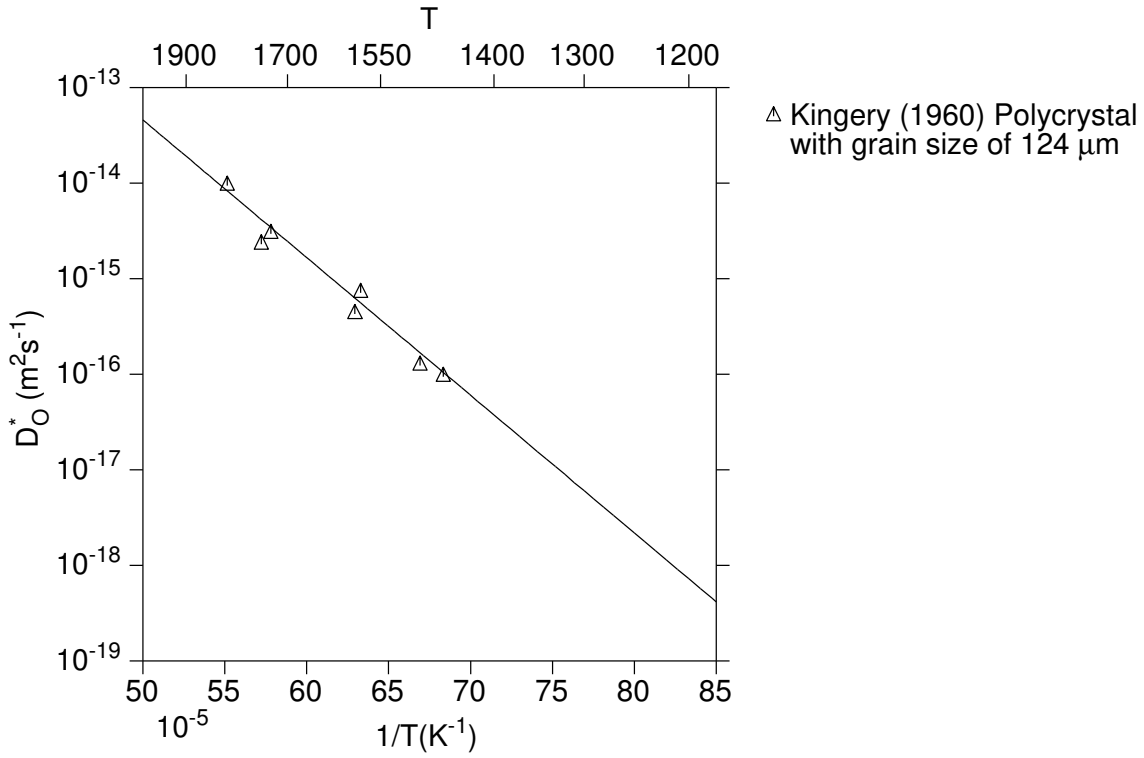


Fig. 4.18 The comparison of oxygen tracer diffusion coefficient in spinel $NiCr_2O_4$ phase at $P_{O_2} = 0.2$ atm between calculations and experiments [233].

4.5 Numerical Results

Figure 4.19 shows predicted equilibrium phase mole fractions for Ni-5Cr, Ni-15Cr, Ni-30Cr and Ni-50Cr alloys at 1000 °C, as a function of P_{O_2} (by replacing nickel in the system). One can see the prediction of formation of outer NiO and internal Cr_2O_3 for low Cr alloys, and outer Cr_2O_3 for high Cr alloys; this is broadly consistent with observed scale microstructure for alloys with different Cr concentration. However, it should be noted that these calculations assume no diffusion kinetics. In fact the semi-conducting properties of oxide phases and metallic diffusion in underlying substrate dominate the steady-state oxide layer structures and associated thickening kinetics.

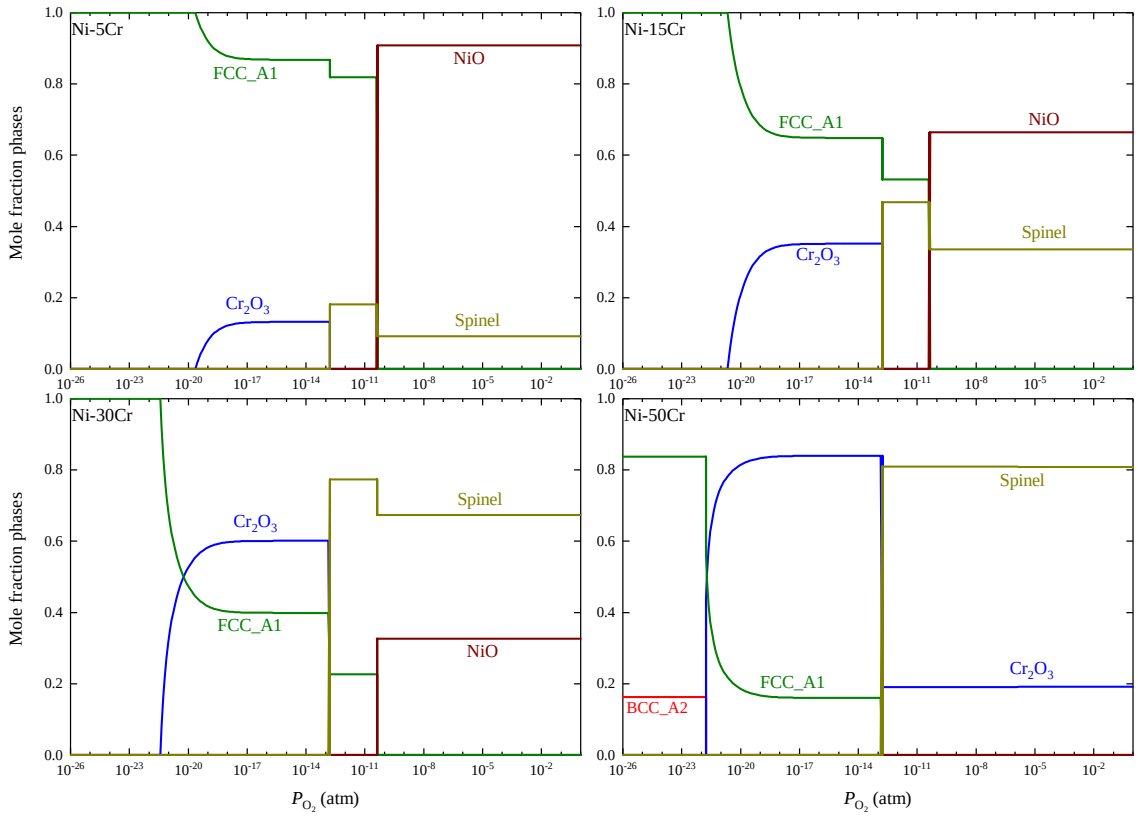


Fig. 4.19 Predicted equilibrium phase mole fractions for Ni-5Cr, Ni-15Cr, Ni-30Cr and Ni-50Cr alloys at different P_{O_2} at 1000 °C.

Kinetic simulations have been conducted for Ni-Cr alloys with Cr concentration ranging from 0 to 45wt% at temperatures 800 °C, 900 °C and 1000 °C, in order to predict the evolution of phases expected. It should be stressed that current simulations for oxidation

kinetics are computationally expensive due to the complex defect structure and non-linearity of the diffusion fields in oxides. Typical runtime of a simulation (for 1 h of oxidation) is around one week, paralleled to 32 cores in a single computing node with two Intel Xeon E5-2687W processors (3.10 GHz).

Figure 4.20 shows predicted evolution of phase distribution (taking the solid/gas interface as the reference) for alloy Ni-0.05 wt.%Cr exposed at 800 °C in air. One can see the growth of outer NiO layer, the precipitation of Cr_2O_3 particles in γ phase, and the formation of spinel at the NiO/γ interface.

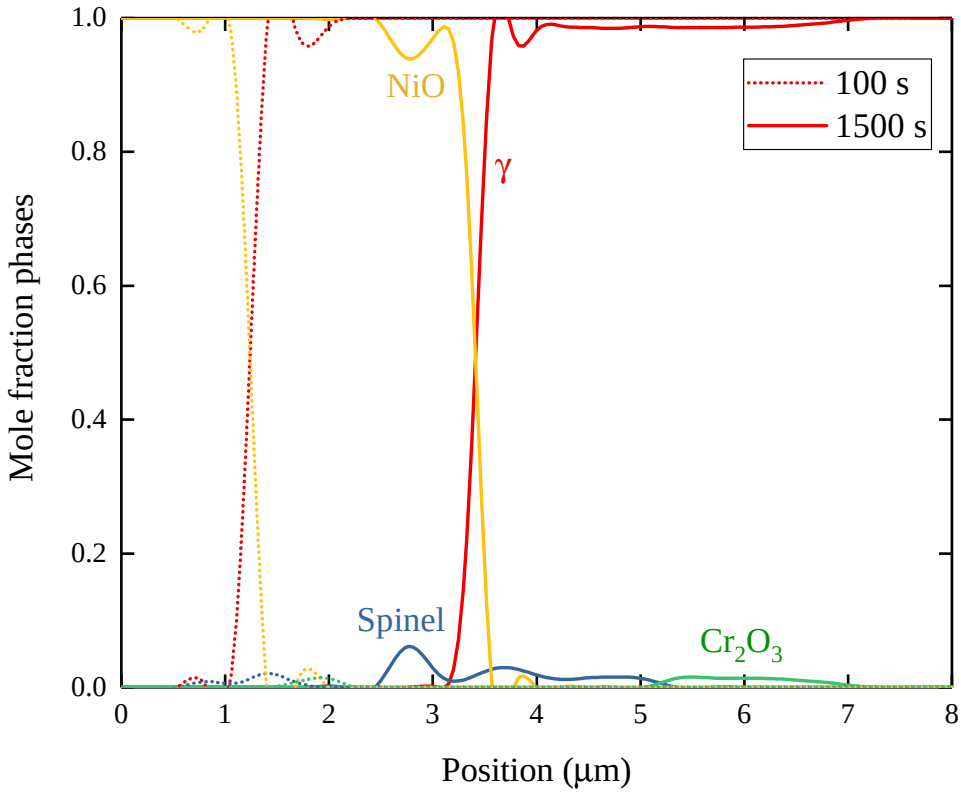


Fig. 4.20 Predicted evolution of phase distribution for alloy Ni-0.05 wt.%Cr at 800 °C.

For each alloy composition and temperature, the evolution of weight gain contributed by oxygen intake has been predicted; then by fitting to the parabolic law consistent with eq. (4.3), k_p is calculated. Figure 4.21 shows the weight gain curve for alloy Ni-0.05 wt.%Cr exposed at 800 °C from predictions and from corresponding parabolic fitting. It should be

noted that a more general mathematical form is applied here to take into account the rapid initial weight gain, as suggested in [236].

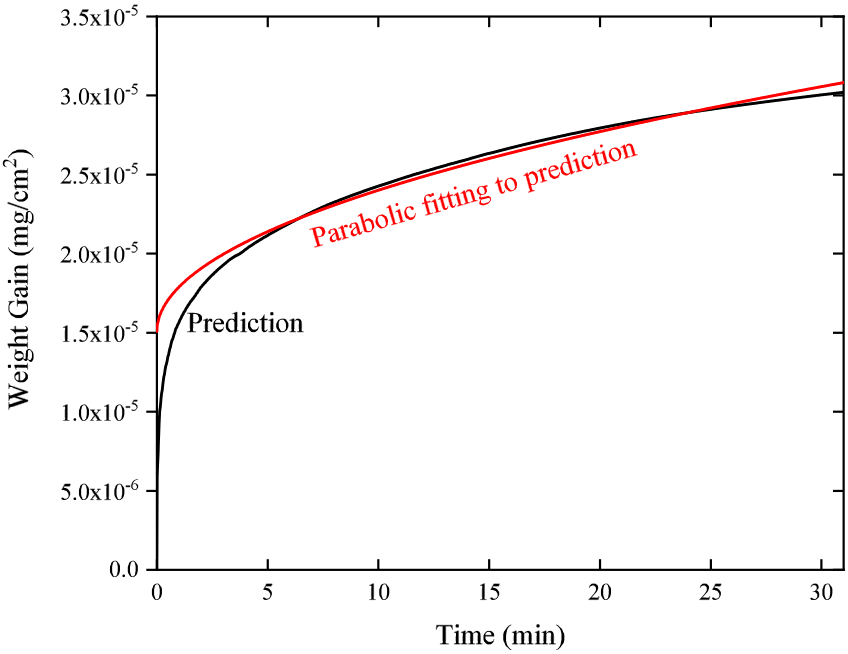


Fig. 4.21 Weight gain curve for alloy Ni-0.05 wt.%Cr exposed at 800 °C from predictions (black) and corresponding parabolic fitting (red).

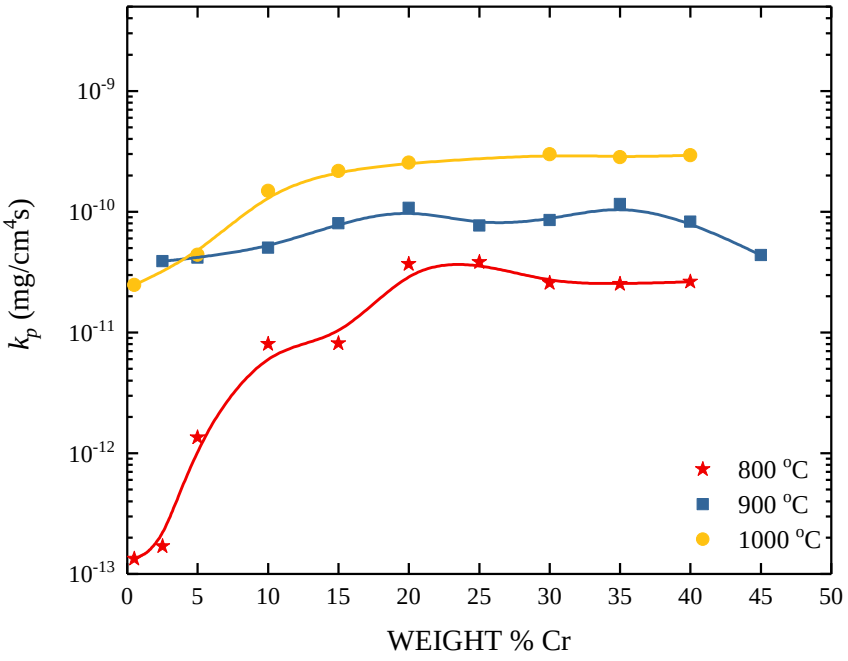


Fig. 4.22 Predicted oxidation kinetics for different Ni-Cr alloys at 800 °C, 900 °C and 1000 °C.

Figure 4.22 shows predicted k_p, with corresponding R^2 listed in table 4.3. One can see that all calculations follow the parabolic law. For Group I&II alloys, the higher k_p with higher Cr concentration is rationalised, accounting for the effects of Cr doping in NiO (which increases the vacancy concentration and oxygen mobility) and the introduction of spinel phase. For Group III alloys, however, k_p is over-predicted; continuous and protective Cr_2O_3 layer as observed in experiments [185] did not show in the simulation; this is due to unsatisfied description of oxygen diffusivity $D_{\mathrm{O}}^{\mathrm{eff}}$ at IOZ where the diffusion along the precipitate/matrix interface dominates as a short-circuit diffusion path; the competing between fast oxygen ingress at IOZ (to form internal Cr_2O_3) and counter-diffusion of Cr (to form enough Cr_2O_3 at the halite/metal interface to block oxygen ingress) needs to be rationalised.

Figure 4.23 illustrates the influence of local oxide fraction within IOZ on $D_{\mathrm{O}}^{\mathrm{eff}}$. Metal lattice shows higher oxygen diffusivity than oxides. Current homogenisation model, regardless what homogenisation function ($\Gamma_k^\star$) is applied, gives a monotonic decrease of $D_{\mathrm{O}}^{\mathrm{eff}}$ from the metal side to the oxide side; the interface diffusion, however, gives an increase of $D_{\mathrm{O}}^{\mathrm{eff}}$ close to the metal side. Physical quantities including oxygen solubility and diffusivity in metal and in oxide have been modelled within the current CALPHAD framework with parameters consistently being improved; the flux description (eq. (4.19)), however, needs to be adjusted to account for the interface diffusion, as a function of size and shape of precipitates at IOZ.

By calculating the entropy production (integrated over time&space) for each phase, it is possible to evaluate the rate-controlling steps (phases), see fig. 4.24 of an example calculation for simulations of oxidation of pure iron at 600 °C in dry air (i.e. Fe-O binary system) [91]. Ferrite shows high $\dot{S}$ initially due to rapid oxygen diffusion into pure iron (as interstitials) just after the exposure to O_2, followed by the formation of oxides at around 10 s. For long-term exposure, diffusion through Fe_3O_4 is the rate-controlling step, even though FeO shows the largest thickness both in experiment and modelling [91]. Extension of such calculations to multi-component alloy systems (e.g. Ni-Cr-O) assessed in this chapter

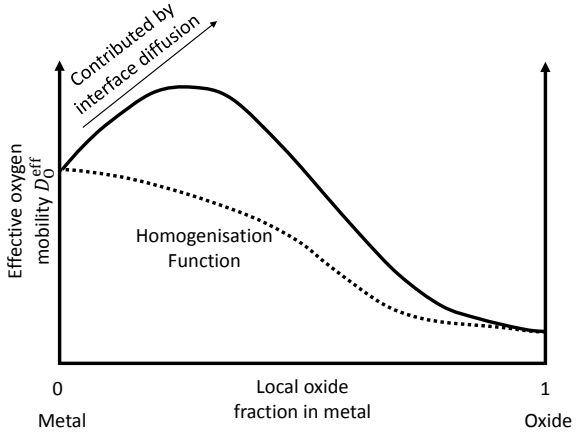


Fig. 4.23 Illustration of contribution of interface diffusion on effective oxygen mobility at the internal oxide zone (IOZ).

requires the flux across the interface (e.g. eq. (4.19)) to be more accurately evaluated, and is still under development. Nevertheless, the evaluation of entropy production for multi-component alloy systems with formation of complex oxides and inter-diffusion in the alloy potentially allow the long-debating question concerning the rate-controlling steps (phases) in corrosion process to be answered.

By applying the diffusional theory and associated chemistry of defects in oxide (such as the doping of Cr in NiO which increases cation vacancies), simulations conducted in this work allow the kinetics of long-term oxidation (e.g. k_p in fig. 4.1) to be reasonably predicted. The initial oxidation, however, cannot be properly predicted due to the lack of description of nucleation and (catalytic) surface reaction in the simulation. Extensive experimental characterisations have been conducted [186, 187, 237, 238] to explain observed compositional-dependency of oxidation kinetics focusing on the role of microstructure and its influence on the short-circuit diffusion path. One example of recent observation by *in-situ* TEM [238] on early stage oxidation suggested that increased short-circuit diffusion path created by the spinel-$NiCr_2O_4$ island interfaces is a plausible reason for enhanced oxidation kinetics with Cr addition for Group I alloys. 2D/3D modelling or mean-field approach might be required.

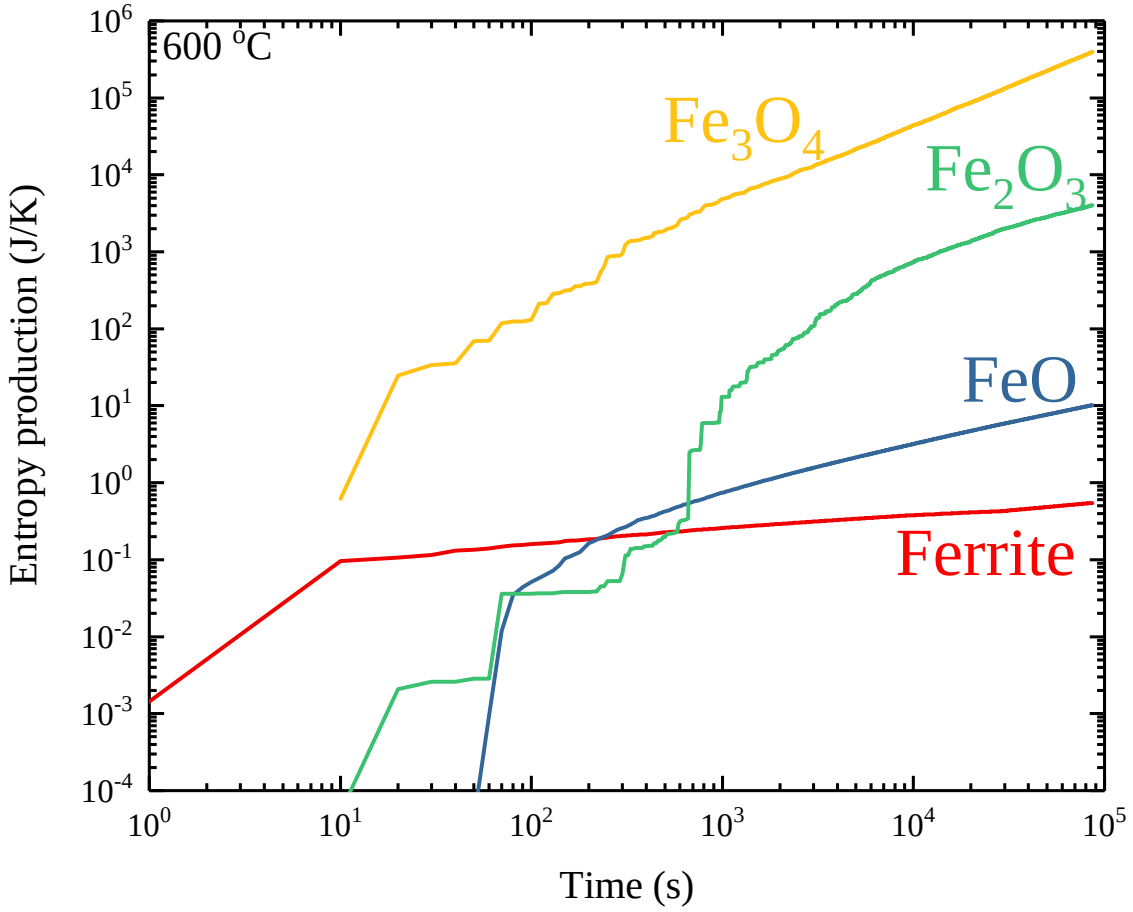


Fig. 4.24 Calculated entropy production for pure iron oxidised at 600 °C in dry air.

4.6 Summary & Conclusions

- The present chapter represents fundamental study of the high temperature oxidation properties of Ni-Cr alloys, particularly looking at the influence of both alloying chemistry in metal and defect chemistry of oxide scales on diffusional kinetics and associated phase transformation (i.e. oxide growth).

- Thermodynamic and kinetic descriptions are proposed for possible phases including halite, spinel and corundum, following the CALPHAD spirit; anion vacancies are introduced in the thermodynamic assessment to describe the P_{O_2}-dependent oxygen mobilities.

- To resolve the numerical challenge involving diffusion in oxides, an improved homogenisation model and thermodynamic equilibrium solver have been utilised; modifications include applying assessed molar volume, generalisation of flux description for diffusion across phase interfaces, parallisation & interpolation scheme, and optimised starting compositional values for Gibbs-energy minimisations.

- Diffusion simulations reported in this chapter potentially allow the energy dissipation (entropy production, $\dot{S}^{\phi}$) to be evaluated; a method of quantifying $\dot{S}^{\phi}$ is proposed, in principle being able to answer the long-debating question concerning the rate-controlling steps (phases) in corrosion process.

- In comparison with experiments, the compositional dependency of oxidation kinetics has been estimated by calculations, even though K_p are over-predicted at protective Cr_2O_3 region (Group III alloys with high Cr concentration); further studies should focus on the evolution of scale grain structures, the physics behind grain boundary diffusion in oxides, oxygen permeability (interface diffusion) at IOZ and nucleation; see section 6.2.2 for more details.

Tables & Figures

Table 4.1 Thermodynamic descriptions of assessed oxides in Ni-Cr-O system. Units are consistent with CALPHAD standard, see [22].

Thermodynamic description	References
Corundum	
$\left(Cr^{3+}, Cr^{2+}\right)_2 \left(Ni^{2+}, Cr^{3+}, Va\right)_1 \left(O^{2-}, Va\right)_3$	
${}^{\circ}G^{\text{Corundum}}_{Cr^{3+}:Ni^{2+}:O^{2-}} - 2H^{\text{SER}}_{Cr} - H^{\text{SER}}_{Ni} - 3H^{\text{SER}}_{O} = +\text{GCR2O3} + 28048.1 + 54.4T$	[196]
${}^{\circ}G^{\text{Corundum}}_{Cr^{3+}:Cr^{3+}:O^{2-}} - 3H^{\text{SER}}_{Cr} - 3H^{\text{SER}}_{O} = +\text{GCR2O3} + \text{GHSERCR}$	[219]
${}^{\circ}G^{\text{Corundum}}_{Cr^{3+}:VA:O^{2-}} - 2H^{\text{SER}}_{Cr} - 3H^{\text{SER}}_{O} = +\text{GCR2O3}$	[239]
${}^{\circ}G^{\text{Corundum}}_{Cr^{2+}:Ni^{2+}:O^{2-}} - 2H^{\text{SER}}_{Cr} - H^{\text{SER}}_{Ni} - 3H^{\text{SER}}_{O} = +\text{GCR2O3} + 665910$	[196]
${}^{\circ}G^{\text{Corundum}}_{Cr^{2+}:Cr^{3+}:O^{2-}} - 3H^{\text{SER}}_{Cr} - 3H^{\text{SER}}_{O} = +\text{GCR2O3} + \text{GHSERCR} + 108305 - 5.2923T$	[219]
${}^{\circ}G^{\text{Corundum}}_{Cr^{2+}:VA:O^{2-}} - 2H^{\text{SER}}_{Cr} - 3H^{\text{SER}}_{O} = +\text{GCR2O3} + 108305 + 5.2923 * T$	[196]
${}^{\circ}G^{\text{Corundum}}_{Cr^{3+}:Ni^{2+}:VA} - 2H^{\text{SER}}_{Cr} - H^{\text{SER}}_{Ni} = +0.4\text{GCR2O3} + 28048.1 + 54.4T + \text{BCOR}$	this work
${}^{\circ}G^{\text{Corundum}}_{Cr^{3+}:Cr^{3+}:VA} - 3H^{\text{SER}}_{Cr} = +0.4\text{GCR2O3} + \text{GHSERCR} + \text{ACOR}$	this work
${}^{\circ}G^{\text{Corundum}}_{Cr^{3+}:VA:VA} - 2H^{\text{SER}}_{Cr} = +0.4\text{GCR2O3} + \text{ACOR}$	this work
${}^{\circ}G^{\text{Corundum}}_{Cr^{2+}:Ni^{2+}:VA} - 2H^{\text{SER}}_{Cr} - H^{\text{SER}}_{Ni} = +0.4\text{GCR2O3} + 665910 + \text{BCOR}$	this work
${}^{\circ}G^{\text{Corundum}}_{Cr^{2+}:Cr^{3+}:VA} - 3H^{\text{SER}}_{Cr} = +0.4\text{GCR2O3} + \text{GHSERCR} + 108305 - 5.2923T + \text{ACOR}$	this work
${}^{\circ}G^{\text{Corundum}}_{Cr^{2+}:VA:VA} - 2H^{\text{SER}}_{Cr} = +0.4\text{GCR2O3} + 108305 + 5.2923T + \text{ACOR}$	this work
${}^{\circ}T_C = -918$	[196]
${}^{\circ}\beta = -5.814$	[196]
Spinel	
$\left(Cr^{3+}, Cr^{2+}, Ni^{2+}\right)_1 \left(Cr^{3+}, Ni^{2+}, Va\right)_2 \left(Cr^{2+}, Va\right)_2 \left(O^{2-}, Va\right)_4$	
${}^{\circ}G^{\text{Spinel}}_{Cr^{3+}:Cr^{3+}:Cr^{2+}:O^{2-}} - 5H^{\text{SER}}_{Cr} - 4H^{\text{SER}}_{O} = +10.5\text{FFE3O4B} - 3.5\text{GFE3O4} - 0.5\text{BFE3O4} + \text{RFE3O4} + \text{ADDCR2}$	[232]
${}^{\circ}G^{\text{Spinel}}_{Cr^{3+}:Cr^{3+}:VA:O^{2-}} - 3H^{\text{SER}}_{Cr} - 4H^{\text{SER}}_{O} = +10.5\text{FFE3O4B} - 3.5\text{GFE3O4} - 0.5\text{BFE3O4} + \text{RFE3O4}$	[218]
${}^{\circ}G^{\text{Spinel}}_{Cr^{3+}:Ni^{2+}:Cr^{2+}:O^{2-}} - 3H^{\text{SER}}_{Cr} - 2H^{\text{SER}}_{Ni} - 4H^{\text{SER}}_{O} = +\text{GNICR2O4} + 71546 + \text{ADDCR2}$	[232]
${}^{\circ}G^{\text{Spinel}}_{Cr^{3+}:Ni^{2+}:VA:O^{2-}} - H^{\text{SER}}_{Cr} - 2H^{\text{SER}}_{Ni} - 4H^{\text{SER}}_{O} = +2\text{GNICR2O4} + 143092 - 10.5\text{FFE3O4B} + 3.5\text{GFE3O4} + 0.5\text{BFE3O4} - \text{RFE3O4}$	[196]
${}^{\circ}G^{\text{Spinel}}_{Cr^{3+}:VA:Cr^{2+}:O^{2-}} - 3H^{\text{SER}}_{Cr} - 4H^{\text{SER}}_{O} = +3.5\text{FFE3O4B} + 1.5\text{GFE3O4} - 0.5\text{BFE3O4} + \text{CFE3O4} + \text{RFE3O4} + \text{ADDCR2}$	[232]

Table 4.1 (continued)

Thermodynamic description	References
${}^{\circ}G^{\text{Spinel}}_{Cr^{3+}:VA:VA:O^{2-}} - H^{SER}_{Cr} - 4H^{SER}_{O} = +3.5FFE3O4B + 1.5GFE3O4 - 0.5BFE3O4 + CFE3O4 + RFE3O4$	[218]
${}^{\circ}G^{\text{Spinel}}_{Cr^{2+}:Cr^{3+}:Cr^{2+}:O^{2-}} - 5H^{SER}_{Cr} - 4H^{SER}_{O} = +10.5FFE3O4B - 3.5GFE3O4 - 0.5BFE3O4 + RFE3O4 + SFE3O4B + ADDCR2$	[232]
${}^{\circ}G^{\text{Spinel}}_{Cr^{2+}:Cr^{3+}:VA:O^{2-}} - 3H^{SER}_{Cr} - 4H^{SER}_{O} = +10.5FFE3O4B - 3.5GFE3O4 - 0.5BFE3O4 + RFE3O4 + SFE3O4B$	[218]
${}^{\circ}G^{\text{Spinel}}_{Cr^{2+}:Ni^{2+}:Cr^{2+}:O^{2-}} - 3H^{SER}_{Cr} - 2H^{SER}_{Ni} - 4H^{SER}_{O} = +14GFE2NIO4 - BFE2NIO4 + 3.5FFE3O4B - 10.5GFE3O4 + 1.5BFE3O4 + RFE3O4 + SFE3O4B + ADDCR2$	[232]
${}^{\circ}G^{\text{Spinel}}_{Cr^{2+}:Ni^{2+}:VA:O^{2-}} - H^{SER}_{Cr} - 2H^{SER}_{Ni} - 4H^{SER}_{O} = +14GFE2NIO4 - BFE2NIO4 + 3.5FFE3O4B - 10.5GFE3O4 + 1.5BFE3O4 + RFE3O4 + SFE3O4B$	[232]
${}^{\circ}G^{\text{Spinel}}_{Cr^{2+}:VA:Cr^{2+}:O^{2-}} - 3H^{SER}_{Cr} - 4H^{SER}_{O} = +3.5FFE3O4B + 1.5GFE3O4 - 0.5BFE3O4 + CFE3O4 + RFE3O4 + SFE3O4B + ADDCR2$	[232]
${}^{\circ}G^{\text{Spinel}}_{Cr^{2+}:VA:VA:O^{2-}} - H^{SER}_{Cr} - 4H^{SER}_{O} = +3.5FFE3O4B + 1.5GFE3O4 - 0.5BFE3O4 + CFE3O4 + RFE3O4 + SFE3O4B$	[218]
${}^{\circ}G^{\text{Spinel}}_{Ni^{2+}:Cr^{3+}:Cr^{2+}:O^{2-}} - 4H^{SER}_{Cr} - H^{SER}_{Ni} - 4H^{SER}_{O} = +GNICR2O4 + ADDCR2$	[232]
${}^{\circ}G^{\text{Spinel}}_{Ni^{2+}:Cr^{3+}:VA:O^{2-}} - 2H^{SER}_{Cr} - H^{SER}_{Ni} - 4H^{SER}_{O} = +GNICR2O4$	[196]
${}^{\circ}G^{\text{Spinel}}_{Ni^{2+}:Ni^{2+}:Cr^{2+}:O^{2-}} - 2H^{SER}_{Cr} - 3H^{SER}_{Ni} - 4H^{SER}_{O} = +21GFE2NIO4 - BFE2NIO4 - 14GFE3O4 + 2BFE3O4 + ADDCR2$	[232]
${}^{\circ}G^{\text{Spinel}}_{Ni^{2+}:Ni^{2+}:VA:O^{2-}} - 3H^{SER}_{Ni} - 4H^{SER}_{O} = +21GFE2NIO4 - BFE2NIO4 - 14GFE3O4 + 2BFE3O4$	[232]
${}^{\circ}G^{\text{Spinel}}_{Ni^{2+}:VA:Cr^{2+}:O^{2-}} - 2H^{SER}_{Cr} - H^{SER}_{Ni} - 4H^{SER}_{O} = +7GFE2NIO4 - 2GFE3O4 + CFE3O4 + ADDCR2$	[232]
${}^{\circ}G^{\text{Spinel}}_{Ni^{2+}:VA:VA:O^{2-}} - H^{SER}_{Ni} - 4H^{SER}_{O} = +7GFE2NIO4 - 2GFE3O4 + CFE3O4$	[232]
For compounds containing only Cr cations ${}^{\circ}T_C = 100$ and ${}^{\circ}\beta = 0.9$	[232]
For compounds containing only Ni cations ${}^{\circ}T_C = 858$ and ${}^{\circ}\beta = 0$	[232]
For compounds containing both Ni & Cr cations ${}^{\circ}T_C = 518$ and ${}^{\circ}\beta = 0.5$	[232]

Halite

$$\left(Cr^{3+}, Ni^{2+}, Ni^{3+}, Va\right)_1 \left(O^{2-}, Va\right)_1$$

${}^{\circ}G^{\text{Halite}}_{Cr^{3+}:O^{2-}} - H^{SER}_{Cr} - H^{SER}_{O} = +GCRWUSTI$	[218]
${}^{\circ}G^{\text{Halite}}_{Ni^{2+}:O^{2-}} - H^{SER}_{Ni} - H^{SER}_{O} = +GNIO$	[196]

Table 4.1 (continued)

Thermodynamic description	References
${}^{\circ}G^{\text{Halite}}_{\text{Ni}^{3+}:\text{O}^{2-}} - H^{\text{SER}}_{\text{Ni}} - H^{\text{SER}}_{\text{O}} = +\text{GNIO} + 132919.5 - 64.8855T$	[196]
${}^{\circ}G^{\text{Halite}}_{\text{VA:O}^{2-}} - H^{\text{SER}}_{\text{O}} = 0$	[196]
${}^{\circ}G^{\text{Halite}}_{\text{Cr}^{3+}:\text{VA}} - H^{\text{SER}}_{\text{Cr}} = +0.5\text{GCRWUSTI} + \text{AHAL} + \text{BCRHAL}$	this work
${}^{\circ}G^{\text{Halite}}_{\text{Ni}^{2+}:\text{VA}} - H^{\text{SER}}_{\text{Ni}} = +0.5\text{GNIO} + \text{AHAL} + \text{BNIHAL}$	this work
${}^{\circ}G^{\text{Halite}}_{\text{Ni}^{3+}:\text{VA}} - H^{\text{SER}}_{\text{Ni}} = +0.5\text{GNIO} + 66459.75 - 32.44275T + \text{AHAL}$	this work
${}^{\circ}G^{\text{Halite}}_{\text{VA:VA}} = +\text{AHAL}$	this work
${}^{\circ}T_C = 519$	[196]
${}^{\circ}\beta = 0.9873$	[196]

Definition of symbols

$$\text{GCR2O3}\,(298.15 < T < 1000) = -1177497.8 + 814.9138T - 132.046T\ln T + 5.256015\times10^{-3}T^2 - 1.38885\times10^{-6}T^3 + 1501761T^{-1}$$

$$\text{GCR2O3}\,(1000 < T < 2600) = -1166947.9 + 701.5624T - 115.5381T\ln T - 6.20492\times10^{-3}T^2 + 1.00698\times10^{-7}T^3 + 239949T^{-1}$$

$$\text{GCRWUSTI}\,(298.15 < T < 1000) = -563748.9 + 407.4569T - 66.02315T\ln T + 2.628\times10^{-3}T^2 - 6.944225\times10^{-7}T^3 + 750881T^{-1}$$

$$\text{GCRWUSTI}\,(1000 < T < 3000) = -558473.9 + 350.7812T - 57.76905T\ln T - 3.10246\times10^{-3}T^2 + 5.034917\times10^{-8}T^3 + 119974.7T^{-1}$$

$$\text{GNIO}\,(298.15 < T < 1000) = -254927.2 + 276.208T - 46.0391T\ln T - 9.31454\times10^{-3}T^2 + 1.29092\times10^{-6}T^3 + 382916T^{-1}$$

$$\text{GNIO}\,(1000 < T < 1800) = -256835.2 + 340.043T - 56.36068T\ln T + 2.54106\times10^{-3}T^2 - 8.11809\times10^{-7}T^3 + 1270T^{-1}$$

$$\text{GNIO}\,(1800 < T < 2600) = -259131.4 + 337.305T - 55.75758T\ln T + 2.20246\times10^{-3}T^2 - 7.80093\times10^{-7}T^3$$

$$\text{GNICR2O4}\,(298.15 < T < 2600) = -1442728.78 + 1005.1T - 167.1508T\ln T - 8.93284\times10^{-3}T^2 + 1052276T^{-1}$$

$$\text{GFE3O4}\,(298.15 < T < 3000) = -161731 + 144.873T - 24.9879T\ln T - 1.1952256\times10^{-3}T^2 + 206520T^{-1}$$

$$\text{GFE2NIO4} = -153200 + 173.55T - 28.259T\ln T - 3.2\times10^{-4}T^2 + 291000T^{-1}$$

$$\text{FFE3O4B}\,(298.15 < T < 3000) = -214607.7 + 138.83T - 23.28714T\ln T - 1.595929\times10^{-3}T^2 + 227729.3T^{-1}$$

$$\text{BFE3O4}\,(298.15 < T < 3000) = +46826 - 27.266T$$

$$\text{CFE3O4}\,(298.15 < T < 3000) = +120730 - 20.102T$$

Table 4.1 (continued)

Thermodynamic description	References
$\mathrm{DFE3O4}\,(298.15 < T < 3000) = +402520 - 30.529T$	
$\mathrm{RFE3O4}\,(298.15 < T < 3000) = +156000 - 3.37T$	
$\mathrm{SFE3O4B}\,(298.15 < T < 3000) = +46028.95 + 38.73173T - 11.58574T\ln T + 6.411774\times10^{-3}T^2$	
$\mathrm{BFE2NIO4} = +142000$	
$\mathrm{ADDCR2} = +2\mathrm{GFE3O4} + \mathrm{DFE3O4} - \mathrm{BFE3O4}$	
$\mathrm{VACR1} = +10000000$	
$\mathrm{VANI1} = +10000000$	
$\mathrm{ACOR} = +396559 - 200*T$	
$\mathrm{BCOR} = +236391 - 200*T$	
$\mathrm{AHAL} = +30T$	[22]
$\mathrm{BCRHAL} = +10000000$	
$\mathrm{BNIHAL} = +10000000$	

Table 4.2 Atomic mobility of assessed oxides in Ni-Cr-O system. Units are consistent with CALPHAD standard, see [22].

Mobility parameters	References
Corundum	
$\left(\mathrm{Cr^{3+}},\mathrm{Cr^{2+}}\right)_2\left(\mathrm{Ni^{2+}},\mathrm{Cr^{3+}},\mathrm{Va}\right)_1\left(\mathrm{O^{2-}},\mathrm{Va}\right)_3$	
Mobility of O	
$\phi^{\mathrm{Corundum\&O^{2-}\#3}}_{*:*:*} = -301704 + RT\ln\left(1.5\times10^{-3}\right)$	modified [90]
Mobility of Cr	
$\phi^{\mathrm{Corundum\&Cr^{2+}\#1}}_{*:*:*} = -10^9$	[90]
$\phi^{\mathrm{Corundum\&Cr^{2+}\#1}}_{*:*:*} = -10^9$	[90]
$\phi^{\mathrm{Corundum\&Cr^{3+}\#2}}_{*:*:*} = -214365 + RT\ln\left(2.3\times10^{-11}\right)$	modified [90]
Mobility of Ni	
$\phi^{\mathrm{Corundum\&Ni^{2+}\#2}}_{*:*:*} = -199455 + RT\ln\left(5.244\times10^{-12}\right)$	this work

Table 4.2 (continued)

Mobility parameters	References
Spinel	
$\left(Cr^{3+}, Cr^{2+}, Ni^{2+}\right)_1 \left(Cr^{3+}, Ni^{2+}, Va\right)_2 \left(Cr^{2+}, Va\right)_2 \left(O^{2-}, Va\right)_4$	
Mobility of O	
$\phi^{\text{Spinel\&O}^{2-}\#4}_{*:*:*:*} = -275784 + RT\ln\left(7.299\times10^{-7}\right)$	this work
Mobility of Cr	
$\phi^{\text{Spinel\&Cr}^{2+}\#1}_{*:*:*:*} = -10^9$	this work
$\phi^{\text{Spinel\&Cr}^{3+}\#1}_{*:*:*:*} = -10^9$	this work
$\phi^{\text{Spinel\&Cr}^{3+}\#2}_{*:*:*:*} = -153011 + RT\ln\left(1.15\times10^{-2}\right)$	this work
$\phi^{\text{Spinel\&Cr}^{2+}\#3}_{*:*:*:*} = -153011 + RT\ln\left(1.15\times10^{-2}\right)$	this work
Mobility of Ni	
$\phi^{\text{Spinel\&Ni}^{2+}\#1}_{*:*:*:*} = -10^9$	this work
$\phi^{\text{Spinel\&Ni}^{2+}\#2}_{*:*:*:*} = -113520 + RT\ln\left(2.222\times10^{-3}\right)$	this work
Halite	
$\left(Cr^{3+}, Ni^{2+}, Ni^{3+}, Va\right)_1 \left(O^{2-}, Va\right)_1$	
Mobility of O	
$\phi^{\text{Halite\&O}^{2-}\#2}_{*:*} = -263137 + RT\ln\left(4.956\times10^{-5}\right)$	this work
Mobility of Cr	
$\phi^{\text{Halite\&Cr}^{3+}\#1}_{*:*} = -194827 + RT\ln\left(1.412\times10^{-6}\right)$	this work
Mobility of Ni	
$\phi^{\text{Halite\&Ni}^{2+}\#1}_{*:*} = -118753 + RT\ln\left(4.658\times10^{-7}\right)$	this work
$\phi^{\text{Halite\&Ni}^{3+}\#1}_{*:*} = -118753 + RT\ln\left(4.658\times10^{-7}\right)$	this work

Table 4.3 R^2 of fit of predicted weight gain curves to the parabolic law.

Cr concentration (wt.%)	800 °C	900 °C	1000 °C
0	-	-	-
0.5	0.9926	-	0.94988

Table 4.3 (continued)

Cr concentration (wt.%)	800 °C	900 °C	1000 °C
2.5	0.99543	0.96237	-
5	0.98896	0.97038	0.91465
10	0.97561	0.97518	0.99616
15	0.98114	0.97481	1.00000
20	0.97212	0.99176	1.00000
25	0.98586	0.97879	-
30	0.97753	0.98298	1.00000
35	0.97497	0.99751	1.00000
40	0.97926	0.96238	1.00000
45	-	0.93115	-

Chapter 5

CO_2 Oxidation of 9Cr Steel

Summary

Fundamental insights into the mechanism of breakaway oxidation in Fe9Cr1Mo steel are deduced, through advanced characterisation and modelling. Degradation at 600 °C/∼42 bar CO_2 for ∼20,000 h is emphasised: conditions relevant to components such as the finned superheater tubes used for advanced gas-cooled nuclear reactors. It is shown that such conditions are sufficient to cause carbon saturation of the metallic substrate, as confirmed by direct observation of extensive carbide precipitation but also numerical analysis of the carbon transport. Thus the observation of graphite precipitation close to the scale/metal interface is rationalised. Nonetheless, the activity of carbon at the scale/metal interface does not reach unity – with respect to graphite – at time zero. A modelling method is proposed which accounts for this kinetic retardation of the attack; this can be used to interpolate across the regimes within which breakaway oxidation is prevalent. It is a plausible model for extrapolation to the lower temperatures relevant to service conditions and is suitable for lifetime estimation – so-called 'remnant life analysis' – of such safety-critical components when prone to this form of attack.

5.1 Introduction

Ferritic-martensitic 9Cr steels (P91, P92) possess good creep strength and adequate corrosion resistance in CO_2 environments at medium temperatures (400-700 °C). An important application is in CO_2 gas-cooled nuclear reactors, typically in the temperature range 480 to 520 °C [240]. Corrosive attack in these circumstances is characterised by an outer, duplex scale consisting of magnetite and Cr-rich spinel layers, accompanied by precipitation of Cr-rich carbides within the underlying steel [241]. Whilst the kinetics are close to parabolic at first, increasing carburisation leads to the onset of rapid linear kinetics. This 'breakaway' corrosion phenomenon is of practical significance, as it limits reactor lifetimes. It is also of fundamental significance, as the processes whereby a low carbon activity gas can carburise steels and ultimately produce graphite which mechanically disrupt the protective scale and potentially triggers the 'breakaway' kinetics are not well understood [242–244].

The ability of CO_2 to carburise Cr-rich alloys has long been recognised [245]. This is thermodynamically possible because the alloy is not in contact with the gas, but with the underside of an oxide scale, where the oxygen activity is controlled at a low value by the local metal-oxide equilibrium. If carbon is present, the relevant reactions are:

$$CO_2 = CO + {}^1\!/_2\, O_2 \qquad\qquad 2CO = CO_2 + C \tag{5.1}$$

and a low oxygen activity corresponds to a high P_{CO}/P_{CO_2} ratio, thereby producing an elevated carbon activity, a_C. It has been shown [246] that a model Fe-9Cr alloy exposed to CO_2 at 650 °C develops a steady-state carbide volume fraction at the alloy-scale interface corresponding to local equilibrium with the a_C value predicted for equilibration of the Boudouard reaction with the oxygen potential controlled by the alloy-scale equilibrium eq. (5.1). At lower temperatures, however, this state of local equilibrium is not quickly achieved. Exposure of T91/P92 to CO_2 at 550 °C leads to non-steady-state alloy carburisation beneath the usual duplex oxide scale [247, 248]. Measured carbon concentrations

near the alloy-scale interface increased slowly with time, reaching a value of 2.7 at.% after 1000 h. At the expected equilibrium value $a_C = 1$, the corresponding alloy carbon concentration is calculated to be $\sim$7 at.%. Thus the concentrations attained in short term laboratory experiments are approaching equilibrium, but are far removed from that state. The question then is how to predict when unit carbon activity will be reached, and the destructive consequences of graphite deposition can be anticipated.

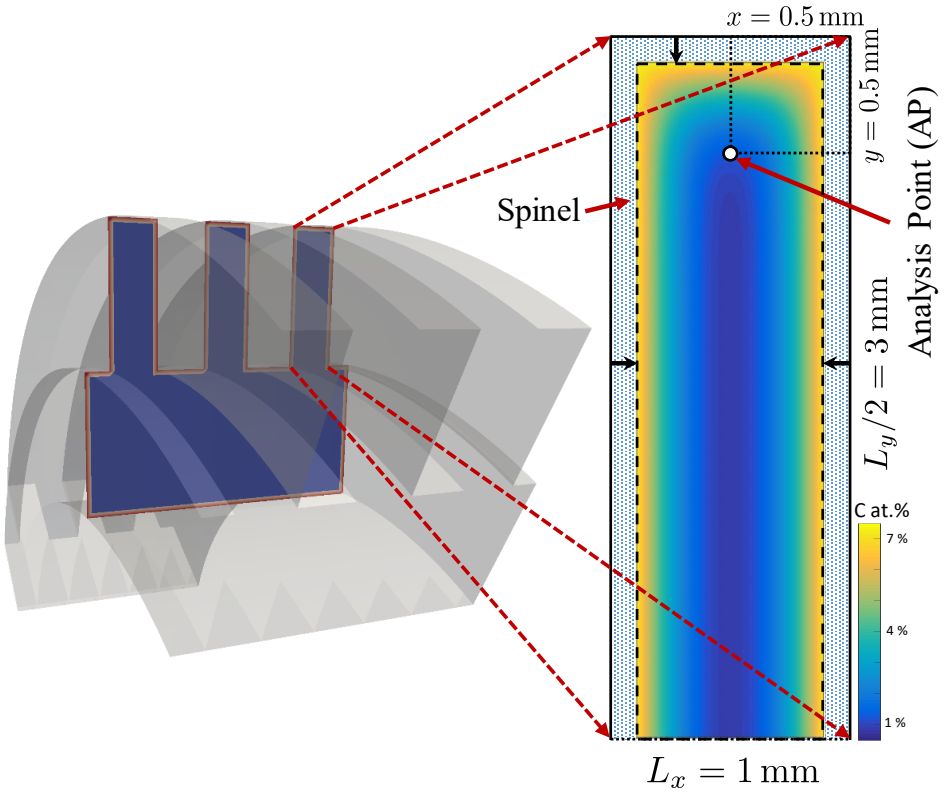
Prediction of the time needed for breakaway is of significant fundamental interest but also practical importance, since breakaway attack is aggressive: it results in significant loss of metal cross-section very quickly. Use can be made of long term accelerated tests at higher temperatures – 580 to 640 °C for example – to quantify the time for breakaway, but then one needs to identify the most appropriate means of extrapolation to service conditions for the purposes of the determination of component life [249]. Ideally, physics-based approaches rather than statistical means are preferred, but these do not exist as yet. Interestingly, the exact details of the rate-controlling steps leading to the 'breakaway' oxidation are still under considerable discussion and are controversial [246–248, 250, 251]. Quantitative numerical modelling is needed to address this situation, with the additional advantage of the possibility of a physics-based approach to the prediction of the reaction kinetics as a function of temperature.

In this chapter, Fe9Cr1Mo steel at/close to the point of breakaway is first characterised using modern analytical techniques in order to better understand the degradation mechanisms occurring. The observations are rationalised using thermodynamic and kinetic modelling. Calculations are carried out to compare the predicted rate of carbon uptake with that deduced by experiment – it is concluded that some form of surface-limited reaction causes a delay in carbon uptake. Numerical modelling is used to describe the approach of the metal substrate to carbon saturation, on the assumption that breakaway oxidation is associated with it. Predictions are made of the fraction of the mass gain associated with (i) oxidation and (ii) carburisation, assuming that no carbon can dissolve in the oxide scale.

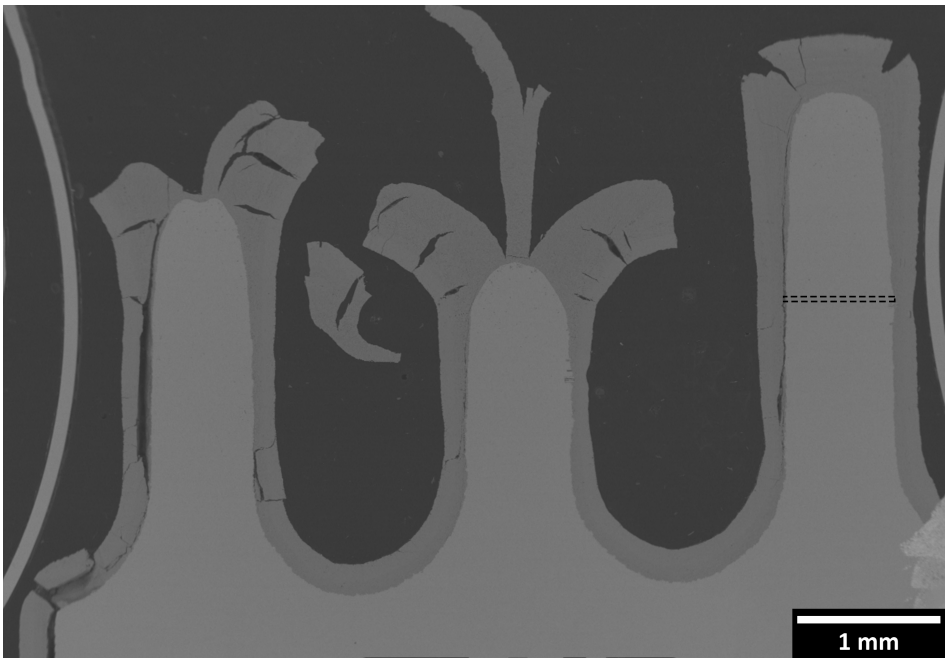
Finally, a method is proposed to allow for the extrapolation of the time to breakaway data from higher to lower temperatures, which will be of significant practical value.

5.2 Experimental Procedures

The material considered is Fe-9Cr1Mo steel of production-grade quality, see table 5.1. The 3D geometry of the specimen considered is shown in fig. 5.1a. Autoclaves (inner volume of ~ 22.5 l) were used to degrade the material at a gas pressure of 600 psig (42.38 bar), gas composition of 100 vppm H_2, 300 vppm CH_4, 1 vol% CO, 300 vppm H_2O and balance CO_2 and gas flow rate of 20 cc/min at standard temperature and pressure (STP). Four temperatures – 580, 600, 620 and 640 °C – were employed above the temperature of operation, to encourage accelerated breakaway. Figure 5.2 shows estimates for equilibrium oxygen activity (a_O) and carbon activity (a_C) for these conditions between 400 to 700 °C; Gibbs-energy minimisation was conducted using Thermo-Calc 2015b with SGTE Substances Database 5.1 including all assessed gaseous species. The a_O is predicted to be in the range 5×10^{-24} – 10^{-21} and a_C between 0.02 – 0.1. Specimen manufacture, autoclave operation and specimen examination were conducted by Amec Foster Wheeler on behalf of EDF Energy.



(a)



(b)

Fig. 5.1 (a) Illustration of the geometry of the fin tube specimen (left) with assumed fin dimension for life assessment as described in section 5.6.3 (right); (b) Backscattered SEM image of the cross-section of the fin tube exposed at 600 °C for 19,924 h. Note the right fin is just before breakaway initiation and the other two fins are during breakaway oxidation; measured profile of carbide volume fraction in black box region on the right fin is shown in fig. 5.13.

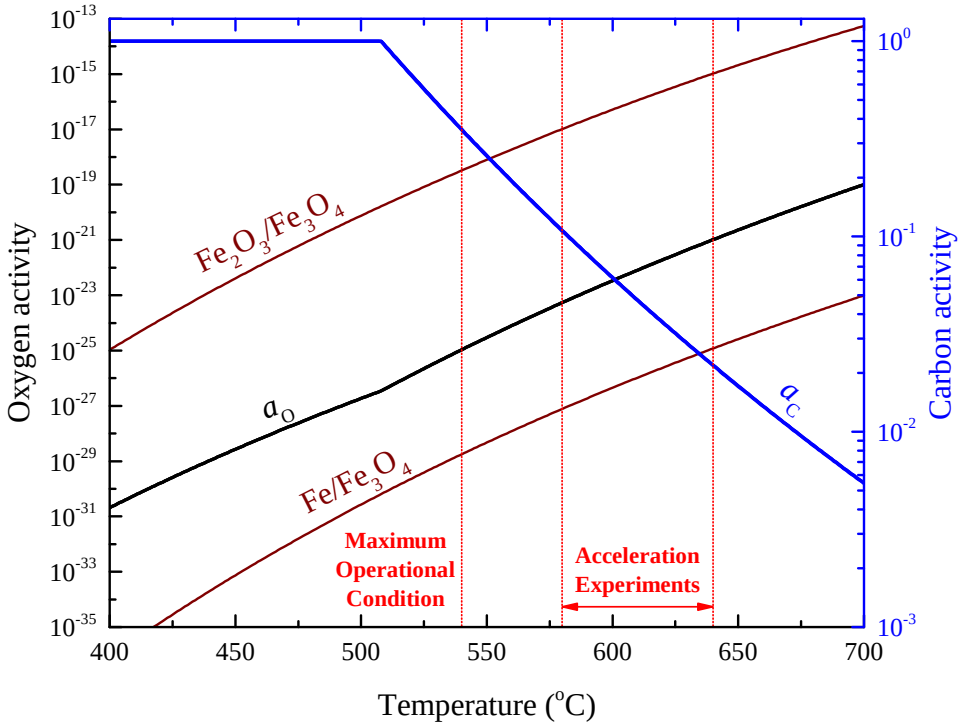


Fig. 5.2 Thermodynamic predictions of equilibrium activities of oxygen (black) and carbon (blue) for exposure gas condition (300 vppm H_2O, 100 vppm H_2, 300 vppm CH_4, 1 vol% CO and balance CO_2) at pressure of 600 psig (42.38 bar); equilibrium oxygen activities for typical iron oxides (brown); calculations were conducted using Thermo-Calc 2015b with SGTE Substances Database 5.1.

The exposure intervals were between 250 h and 5 kh, shorter exposure intervals being used at higher temperatures. The time to breakaway (TTB) was taken to be the exposure time at the moment of breakaway, as first observed on the fin tip of the samples; the weight gain at breakaway (WGB) was (conservatively) taken to be the weight gain observed immediately prior to visual observation of breakaway initiation. The WGB data were further corrected by using the oxidation rate obtained from the last protective region (i.e. when most recently the rate was still decreasing with time) to (a) account for the negative weight gains which can occur periodically from oxide spalls and to (b) correct for geometrical effects, i.e. specimens which have initiated breakaway oxidation at corners. The mass gain data are summarised in fig. 5.3: higher temperatures give larger weight gains but lower TTB; moreover the weight gain data exhibit more scatter as breakaway initiation is approached, suggesting large variance of TTB/WGB and post-breakaway kinetics.

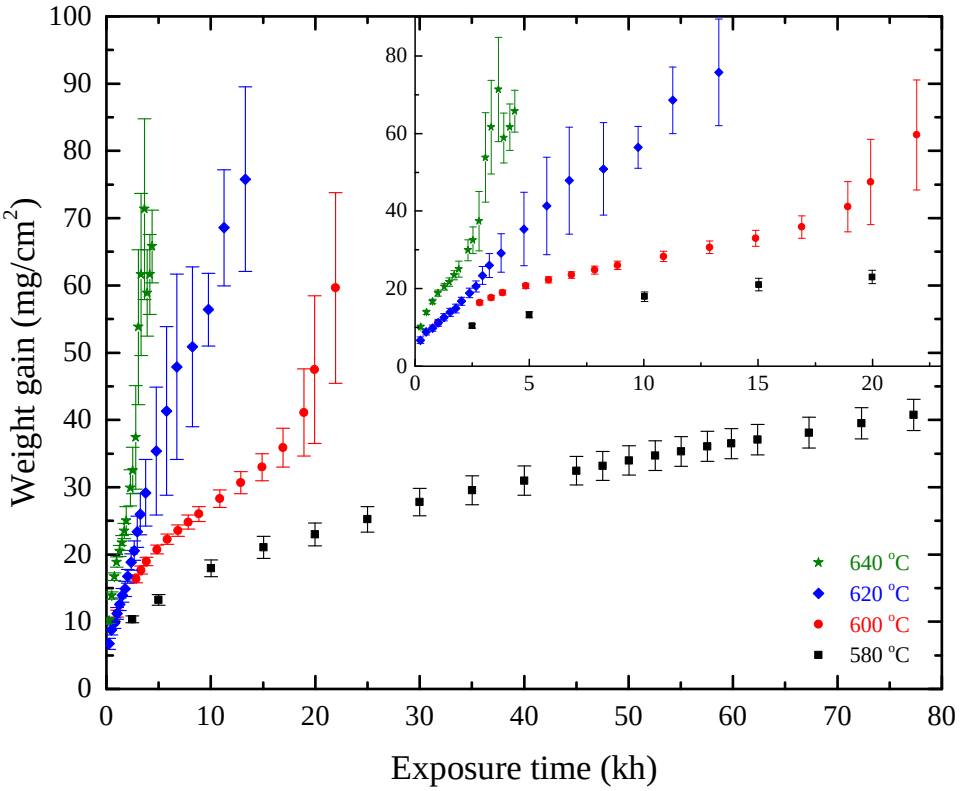


Fig. 5.3 Weight gain changes of experimental samples exposed at 580 °C (black), 600 °C (red), 620 °C (blue) and 640 °C (green) with gas compositions of 100 vppm H_2, 300 vppm CH_4, 1 vol% CO, 300 vppm H_2O and balance CO_2 at gas pressure of 600 psig (42.38 bar); one standard deviation from repeated tests is used to evaluate uncertainties. Raw data courtesy of Amec Foster Wheeler on behalf of EDF Energy.

A specimen exposed to 600 °C was chosen for detailed high-resolution microstructural characterisation, since a transition between protective/breakaway oxidation was observed, see fig. 5.1b; the specimen was exposed for 19,924 h while the first breakaway initiation of two fins was observed at 18,921 h. Thus the degree of degradation in the right hand fin can be assumed to approach that needed to initiate breakaway. A JEOL 6500F field emission gun scanning electron microscope (FEG-SEM) in back scattered electron imaging mode was used. In addition, energy dispersive X-Ray (EDX) chemical mapping was conducted at the internal oxide zone (IOZ) using a Zeiss Merlin FEG-SEM, with a beam of 5 keV energy and a probe current of 500 pA.

For site-specific analysis, samples were prepared for transmission electron microscopy (TEM) and atom probe tomography (APT) using a FEI Quanta 3D FEG FIB/SEM and an

NVision 40 dual beam FIB, respectively, following [252]. The TEM studies were carried out on a Talos F200 S/TEM operating at 200 keV. A Super-X EDS system with four silicon drift detectors (SDD) is integrated in the S-TWIN lens and offers the solid angle of 0.9 sr. Atom probe analysis was performed in a Cameca LEAP 3000X HR instrument operating in laser mode with pulse rate at 200 kHZ and pulse energy at 0.4 nJ, and a Cameca LEAP 5000 XR instrument operating in laser mode with pulse rate at 100 kHz and pulse energy at 50 pJ. In addition, the oxide region has been characterised by the nanoscale secondary ion mass spectrometry (NanoSIMS) using a Cameca NanoSIMS 50 system, following the methodology detailed in [253].

5.3 Theoretical Modelling

In what follows, we deal first with the kinetics of outer scale formation, in what is termed an oxide growth model (OGM). Second, we perform coupled thermodynamic/kinetic calculations in 1D using the DICTRA code and an associated homogenisation model. Finally, consideration is given to the modelling of carbon uptake in 2D in what is termed a substrate penetration model (SPM).

5.3.1 Oxide Growth Model (OGM)

The oxide growth model (OGM) is illustrated in fig. 5.4. As shown by inert marker experiments [254] iron diffuses outward to form the outer Fe_3O_4 layer, and the spinel layer grows inward. Solid-state diffusion of oxygen is far too slow to support the latter process [255], and another, faster process is in effect. The observation that the inner layer is porous has led to the proposal of gas phase molecular transport as part of the "available space model" [256, 257]. Partial pressures of O_2 within the scale are too low to provide sufficient mass transport. Instead, this role is filled by CO_2, as evidenced by $C^{18}O_2$ tracer experiments [258] and the simultaneous carburisation of the steel.

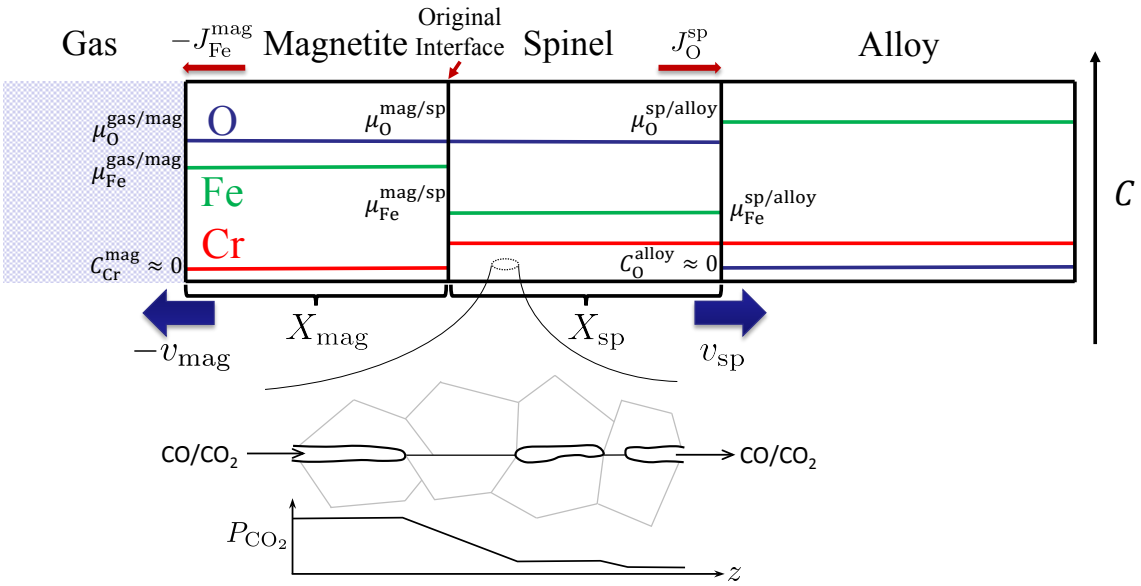


Fig. 5.4 Illustration of the oxide growth model (OGM) with defined physical parameters annotated. Inset shows proposed model for oxygen and carbon transport, involving gas phase mass transport within pores, and grain boundary diffusion between them.

Inward transport of CO_2 is not explicitly treated in the available space model, but has been recognised [250] as a diffusion controlled process. It is clear that a large gradient in CO_2 fugacity is maintained across the spinel layer (a) to allow local equilibrium with the oxygen activity profile, and (b) to account for the observed carburisation of the steel (a large value of P_{CO_2}) would cause its decarburisation). Accordingly, we propose that CO_2 transports via the gas phase within pores, but also via grain boundaries within the oxide separating the pores. It is this process which supports both oxide scaling and alloy carburisation.

The flux balance at the spinel/alloy interface can be written:

$$v_{sp}\left(C_{O,int}^{alloy} - C_{O,int}^{sp}\right) = J_{O,int}^{alloy} - J_{O,int}^{sp} \tag{5.2}$$

where v_{sp} is the velocity of the spinel/alloy interface measured relative to the original alloy/gas interface. The terms $C_{i,int}^{k}$ and $J_{i,int}^{k}$ are the interfacial concentrations and interfacial fluxes in a volume-fixed frame of reference of component i in phase k, respectively. Note that the $C_{i,int}^{k}$ are, here, evaluated as u_i^k/V_m where V_m is the molar volume and u_i^k are the

u-fractions which can be evaluated readily from the mole fractions x_i^k, consistent with

$$u_i^k = \frac{x_i^k}{\sum_{j \in S} x_j^k} \tag{5.3}$$

Note that by $j \in S$ one should infer that the summation is taken over the substitutional components only. Assuming negligible solubility of oxygen in the alloy and thus zero flux, eq. (5.2) reduces to

$$v_{\mathrm{sp}} = \frac{J_{\mathrm{O}}^{\mathrm{sp}}}{C_{\mathrm{O}}^{\mathrm{sp}}} \tag{5.4}$$

where v_{sp} can then be used to estimate the spinel thickness X_{sp} via:

$$X_{\mathrm{sp}} = \int_0^t v_{\mathrm{sp}} \, \mathrm{d}t \tag{5.5}$$

and $J_{\mathrm{O}}^{\mathrm{sp}}$ depends on the thermodynamic driving force and effective mobilities. Assuming the linearised gradient approximation, one has:

$$J_{\mathrm{O}}^{\mathrm{sp}} \simeq J_{\mathrm{O}}^{\mathrm{sp}\prime} = -M_{\mathrm{O}} C_{\mathrm{O}}^{\mathrm{sp}} \frac{\mu_{\mathrm{O}}^{\mathrm{sp/alloy}} - \mu_{\mathrm{O}}^{\mathrm{mag/sp}}}{X_{\mathrm{sp}}} (1 - f_{\mathrm{SiO_2}}) \tag{5.6}$$

where $J_{\mathrm{O}}^{\mathrm{sp}\prime}$, M_{O}, X and the μ denote the interfacial flux in a lattice-fixed frame of reference, the effective mobility of oxygen (as CO_2), oxide thickness and interfacial chemical potentials, respectively. Diffusional blocking by silica formed near the spinel/alloy interface [259] is explicitly recognised, and $f_{\mathrm{SiO_2}}^{\mathrm{int}}$ is the fraction of spinel/alloy interface across which diffusion is blocked in this way. The diffusion length is taken as X_{sp} and

$$\mu_{\mathrm{O}}^{\mathrm{mag/sp}} \simeq \mu_{\mathrm{O}}^{\mathrm{gas/mag}} \tag{5.7}$$

as the oxidation kinetics are dominated by the inner spinel layer; this assumption is supported by the negligible effect on the re-oxidation rate of the removal of the outer magnetite layer [260].

As Si diffusion is relatively slow in ferrite (its chemical diffusivity is less than $10^{-18}\,\mathrm{m^2/s}$ at 640 °C, see [261]), it is assumed that the amount of SiO_2 accumulated at the interface (mole per unit spinel/alloy surface area), n_{SiO_2}, is proportional to X_{sp}, as the inward growth of a spinel layer X_{sp} thick corresponds to consumption of an alloy zone of the same thickness. Hence

$$n_{SiO_2} = C_{Si} X_{sp} \tag{5.8}$$

where C_{Si} is the alloy concentration of Si. Assuming further that f_{SiO_2} is proportional to n_{SiO_2}, one has:

$$f_{SiO_2} = s C_{Si} X_{sp} \tag{5.9}$$

where $s[\mathrm{m^2 \cdot mol^{-1}}]$ is now termed the SiO_2 blocking factor. Equations (5.4) to (5.9) give the following implicit expression for X_{sp}

$$\exp\left\{sC_{Si}\left[\left(\mu_O^{sp/alloy} - \mu_O^{gas/mag}\right) sC_{Si} M_O t - X_{sp}\right]\right\} + sC_{Si}X_{sp} - 1 = 0 \tag{5.10}$$

Finally, by considering the flux of iron at the gas/magnetite interface – and using the same approximations as above – the following equations are obtained:

$$v_{mag} = \frac{J_{Fe}^{mag}}{C_{Fe}^{mag}} \tag{5.11}$$

$$J_{Fe}^{mag} \simeq J_{Fe}^{mag\prime} = -M_{Fe} C_{Fe} \frac{\mu_{Fe}^{sp/alloy} - \mu_{Fe}^{mag/sp}}{X_{sp}} (1 - f_{SiO_2}) \tag{5.12}$$

$$\mu_{Fe}^{mag/sp} \simeq \mu_{Fe}^{gas/mag} \tag{5.13}$$

$$X_{mag} = -\int_0^t (v_{mag} + v_{sp})\,\mathrm{d}t \tag{5.14}$$

yielding:

$$X_{mag} = -X_{sp}\left(\frac{\left(\mu_{Fe}^{sp/alloy} - \mu_{Fe}^{gas/mag}\right) M_{Fe}}{\left(\mu_O^{sp/alloy} - \mu_O^{gas/mag}\right) M_O} + 1\right) \tag{5.15}$$

Both M_{Fe} and M_{O} are written

$$M_k = \frac{M_k^{\circ}}{RT} \exp\left(\frac{-Q_k}{RT}\right) \tag{5.16}$$

Neither the activation energy nor the pre-exponential factor is known for iron or oxygen, because the microstructure of the spinel layer is not quantitatively defined, although the material is clearly fine-grained and porous. For this reason, the mobilities are treated as adjustable quantities in optimising the description of observed scaling rates.

5.3.2 DICTRA Simulations

To complement the above, the homogenisation model [190, 191] implemented in the 1D DICTRA diffusion code has been used to evaluate the phase evolution and diffusion within the underlying ferritic substrate in 1D. Details of the homogenisation model is described in section 4.3.3. Note that no attempt has been made to account for transport through the oxide scale; instead boundary conditions for oxygen and carbon are assumed to apply at the scale/metal interface. Version 2015b of the DICTRA code has been used, in conjunction with the thermodynamic database TCFE8 from Thermo-Calc. Consideration is given to the prescription of the boundary condition for carbon at the scale/metal interface. The increase of carbon content at the oxide/alloy interface expected as a consequence of the Boudouard reaction has been described previously by defining the inward flux of carbon across the oxide/alloy interface as being proportional to the difference of the actual (reduced) time-dependent concentration at the interface ($C_{\mathrm{C,int}}$) and the one arising as equilibrium is fully attained ($C_{\mathrm{C}}^{\mathrm{eq}}$) [248]:, so that

$$J_{\mathrm{C,int}} = \alpha_{\mathrm{C}} \left(C_{\mathrm{C}}^{\mathrm{eq}} - C_{\mathrm{C,int}}\right) \tag{5.17}$$

To be consistent with flux expression eq. (4.13) derived from thermodynamic driving force, we have here rewritten eq. (5.17) as:

$$J_{\mathrm{C,int}} V_m = \alpha_{\mu,\mathrm{C}} \left(\mu_{\mathrm{C}}^{\mathrm{eq}} - \mu_{\mathrm{C,int}} \right) \tag{5.18}$$

where $\alpha_{\mu,\mathrm{C}} \left[\mathrm{mol} \cdot \mathrm{m} \cdot \mathrm{s}^{-1} \cdot \mathrm{J}^{-1} \right]$ is termed the surface reaction coefficient of carbon, thus accounting for the finite rate of its surface reaction; V_m denotes the molar volume.

Taking the oxide/alloy interface as the reference, the outward flux of metallic components (e.g. Fe, Cr and Mo) are calculated based on the predictions of oxidation kinetics described in section 5.3.1. Hence the migration of the oxide/alloy interface is implicitly considered. The size of the computational domain is thus decreasing during simulations. Simulations have been coupled with thermodynamic descriptions of $M_{23}C_6$ carbide, M_7C_3 carbide, HCP_A3 (M_2(C,N)) and BCC_A2 (ferrite).

5.3.3 Substrate Penetration Model (SPM)

To enable approximate calculations of carbon penetration in particular at the fin tips when 2D soft-impingement effects become important, a simplified model for carbon diffusion has proven useful. It has been termed the substrate penetration model. Assuming a rectangular cross-section of each fin which is of dimensions $L_x \times L_y$, one can estimate the diffusion field of carbon in the alloy by considering

$$\dot{C}_{\mathrm{C}} = \nabla \cdot \left(D_{\mathrm{C}}^{\mathrm{eff}} \nabla C_{\mathrm{C}} \right) = D_{\mathrm{C}}^{\mathrm{eff}} \left(\frac{\partial C_{\mathrm{C}}^2}{\partial^2 z_x} + \frac{\partial C_{\mathrm{C}}^2}{\partial^2 z_y} \right) \tag{5.19}$$

where $D_{\mathrm{C}}^{\mathrm{eff}}$ is the effective chemical diffusion coefficient of carbon defined in eq. (5.22). In the alloy, only the concentration gradient of carbon is considered. In this case, the non-steady state carburisation described in eq. (5.17) can be approximated by:

$$\frac{C_{\mathrm{C,int}}(t) - C_{\mathrm{C}}^{\circ}}{C_{\mathrm{C}}^{\mathrm{eq}} - C_{\mathrm{C}}^{\circ}} = 1 - \exp(-\beta t) \tag{5.20}$$

where C_C°, $C_{C,int}$ and C_C^{eq} represent the initial, oxide/alloy interface and equilibrium concentration of carbon, respectively. C_C^{eq} is taken as the carbon concentration corresponding to $a_C = 1$ at different temperatures calculated from Thermo-Calc. Here β is a general 'lumped' factor describing the processes of carbon transport through the oxides, the kinetics of the Boudouard reaction [247, 250] and the kinetics of carbon transport across the oxide/alloy interface [248].

Note that then one can – provided the loss of section due to oxidation is ignored – use the method of eigenfunction expansions to determine a semi-analytical solution for the carbon concentration field. It is

$$\begin{aligned} C_C(z_x, z_y, t) = &\sum_{n=1}^{\infty}\sum_{m=1}^{\infty} \frac{4A\beta(C_C^\circ - C_C^{eq})\left[\exp(-\beta t) - \exp\left(-D_C^{eff}Bt\right)\right] X_n(z_x) Y_m(z_y)}{L_x L_y \left(D_C^{eff}B - \beta\right)} \\ &+ \left(C_C^{eq} - C_C^\circ\right)[1 - \exp(-\beta t)] + C_C^\circ \end{aligned} \tag{5.21}$$

where

$$\begin{aligned} X_n(z_x) &= \frac{\sin(\lambda_n z_x)}{\lambda_n} \\ Y_m(z_y) &= \frac{\sin(\lambda_m z_y)}{\lambda_m} \\ \lambda_n &= n\pi/L_x \\ \lambda_m &= m\pi/L_y \\ A &= [1 - (n\pi)][1 - \cos(m\pi)] \\ B &= \lambda_n^2 + \lambda_m^2 \end{aligned}$$

Diffusion in the carbides is assumed to be negligible [262]. In order to take the diffusion-blocking effect of the carbides into account, an effective diffusivity of carbon is assumed which is given by:

$$D_C^{eff} = f_\alpha D_C^\alpha \tag{5.22}$$

where f_α and D_{C}^{α} denote the volume fraction of the ferrite and the chemical diffusion coefficient of interstitial carbon in ferrite, respectively. Without explicitly treating the phase evolution, the inhomogeneous $D_{\mathrm{C}}^{\mathrm{eff}}$ across the spatial domain is taken as the one at the oxide/substrate interface, in this approach.

To account for the effect of oxidation on carbon penetration, the moving boundary problem can be treated – with the corner effects provided by the oxygen diffusion field ignored. Assuming a constant spinel/magnetite thickness ratio and by defining:

$$\begin{aligned} p_x &= \frac{z_x - X_{\mathrm{sp}}\{t\}}{L_x - 2X_{\mathrm{sp}}\{t\}} \qquad p_x \in [0,1] \\ p_y &= \frac{z_y - X_{\mathrm{sp}}\{t\}}{L_y - 2X_{\mathrm{sp}}\{t\}} \qquad p_y \in [0,1] \end{aligned} \tag{5.23}$$

Equation (5.19) can be rewritten in the following form:

$$\dot{C_{\mathrm{C}}} = D_{\mathrm{C}}^{\mathrm{eff}} \left(\frac{\partial^2 C_{\mathrm{C}}}{\partial p_x^2} + \frac{\partial C_{\mathrm{C}}}{\partial p_x} \right) \left[L_x - 2X_{\mathrm{sp}}\{t\} \right]^{-2} + D_{\mathrm{C}}^{\mathrm{eff}} \left(\frac{\partial^2 C_{\mathrm{C}}}{\partial p_y^2} + \frac{\partial C_{\mathrm{C}}}{\partial p_y} \right) \left[L_y - 2X_{\mathrm{sp}}\{t\} \right]^{-2} \tag{5.24}$$

Equation (5.24) has been solved by using the Finite Element Solver implemented in Mathematica 11 with the boundary condition given by eq. (5.20). This procedure allows the carbon diffusion field in the substrate to be estimated in 2D at minimal computational cost.

5.4 Experimental Results

The scale microstructure developed by the steel exposed to 600 °C for ∼20,000 h, at the point of breakaway, is shown in fig. 5.5a. A duplex oxide layer consisting of Fe-rich magnetite on the top and Cr-rich spinel phase at the bottom is present, and an internally oxidised zone (IOZ) between the protective scale and the substrate. Figure 5.5d shows the results of SEM-EDX mapping across the IOZ. Detailed compositional profiling across a typical precipitate core/shell structure in the IOZ (fig. 5.6(a)) is shown in fig. 5.6(b); the

core and the shell are identified by selected area diffractions (SAD), as shown in fig. 5.6(c), as $M_{23}C_6$ carbide and $FeCr_2O_4$ chromite, respectively. The phase formation sequence, the competition between oxidation & carburisation within the IOZ, and the associated diffusion paths are discussed in detail in section 5.6.1.

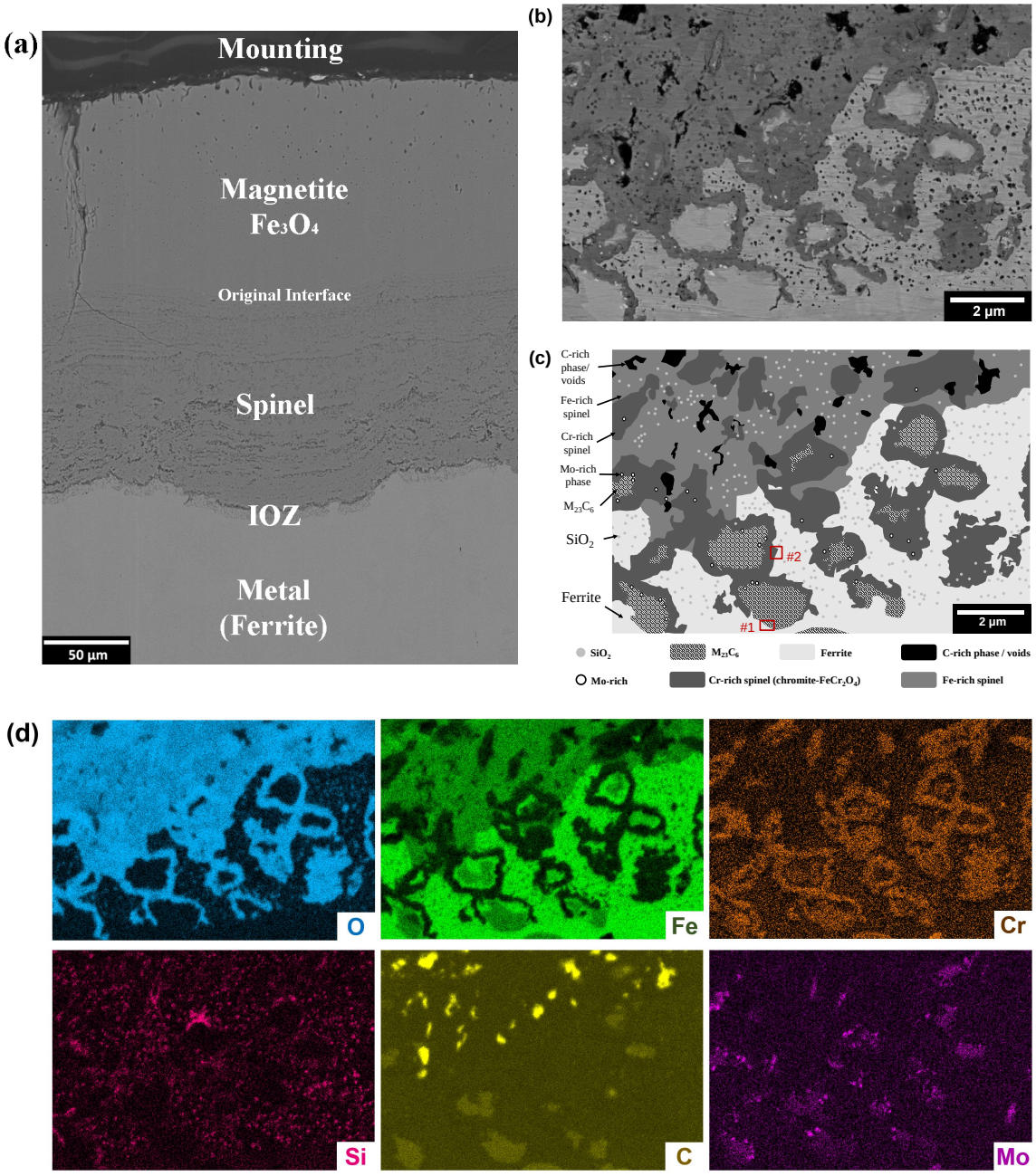


Fig. 5.5 (a) Backscattered SEM image of oxide cross-section showing layered structure consisting of magnetite-Fe_3O_4, banded spinel phase region and shallow IOZ; (b) Backscattered SEM and (d) EDX images of IOZ during the transition between protective/breakaway oxidation below (c) corresponding phase map with possible sites of atom probe analysis marked with red box.

Figure 5.7(a)&(b) compare typical microstructures taken from the centre of the fin before and after exposure. Severe carburisation is evident, with large blocky $M_{23}C_6$ type carbides and needle-shape $M_2(C,N)$ being present. The $M_2(C,N)$ phase was confirmed

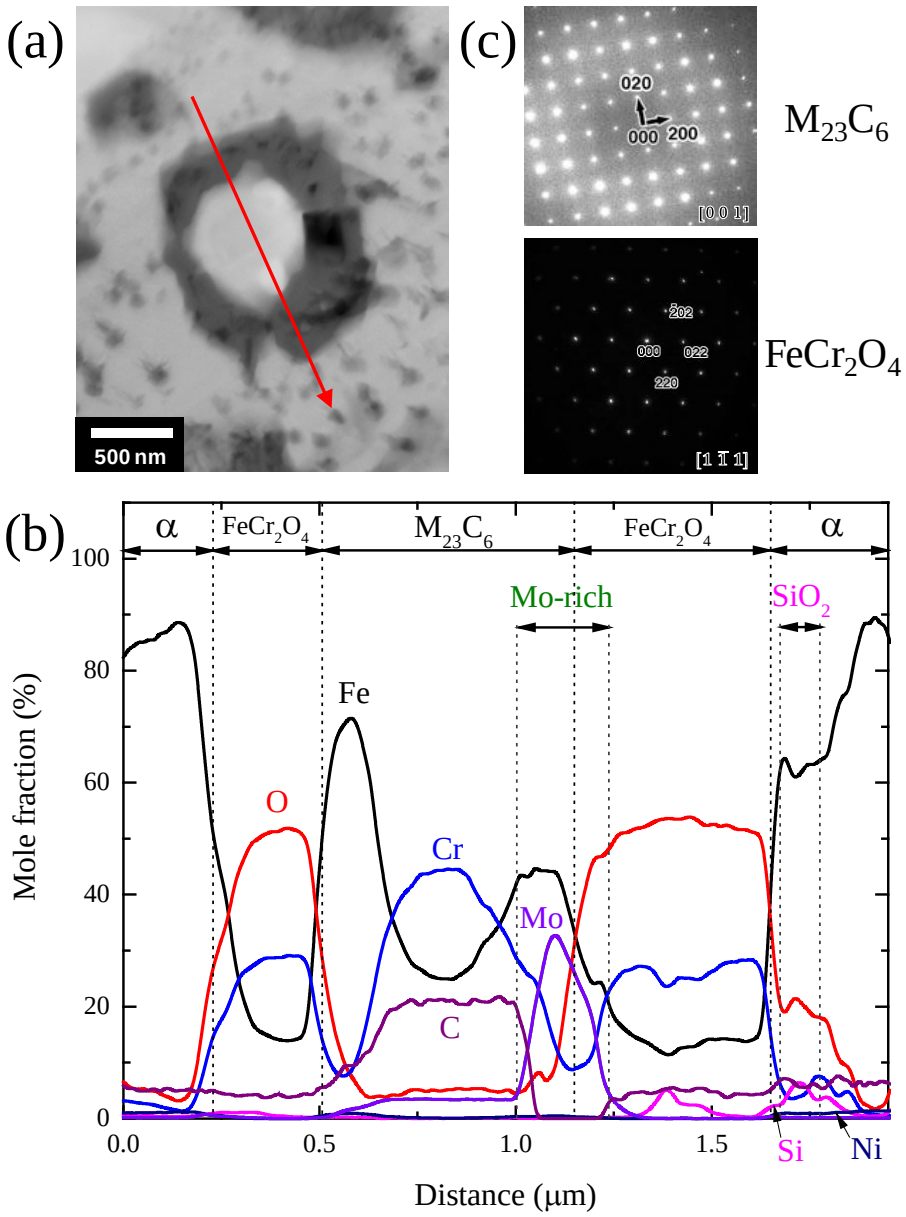


Fig. 5.6 (a) TEM dark field image taken from IOZ; (b) TEM-EDX line profile across the core/shell structure marked as red line in (a); (c) selected area diffraction patterns of $M_{23}C_6$ (core) and $FeCr_2O_4$ (shell). Measurements courtesy of Y.L. Chiu.

by SAD as shown in fig. 5.7(c) and TEM-EDX shown in table 5.2. The variation of the measured volume fraction of carbides across the fin tip is shown in fig. 5.13, and is compared with predicted carbide volume fraction corresponding to carbon activity of unity calculated from Thermo-Calc. It is seen that the measured carbide volume fraction corresponds to $a_C \sim 1$, suggesting that carbon deposition is imminent. Figure 5.8(a)&(b)

show a TEM image and EDX mapping taken from the IOZ. Elemental carbon has been identified inside the oxide region, with its carbon mole fraction at around 95% as suggested by EDX point analysis fig. 5.8(c). Figure 5.8(d) shows a high-resolution TEM (HRTEM) image of oxide/graphite interface and SAD patterns taken from the graphite region. One can clearly see the layered structure of crystalline graphite with a large inter planar spacing measured to be 3.37 Å, close to the accepted basal planar spacing of graphite of 3.35 Å.

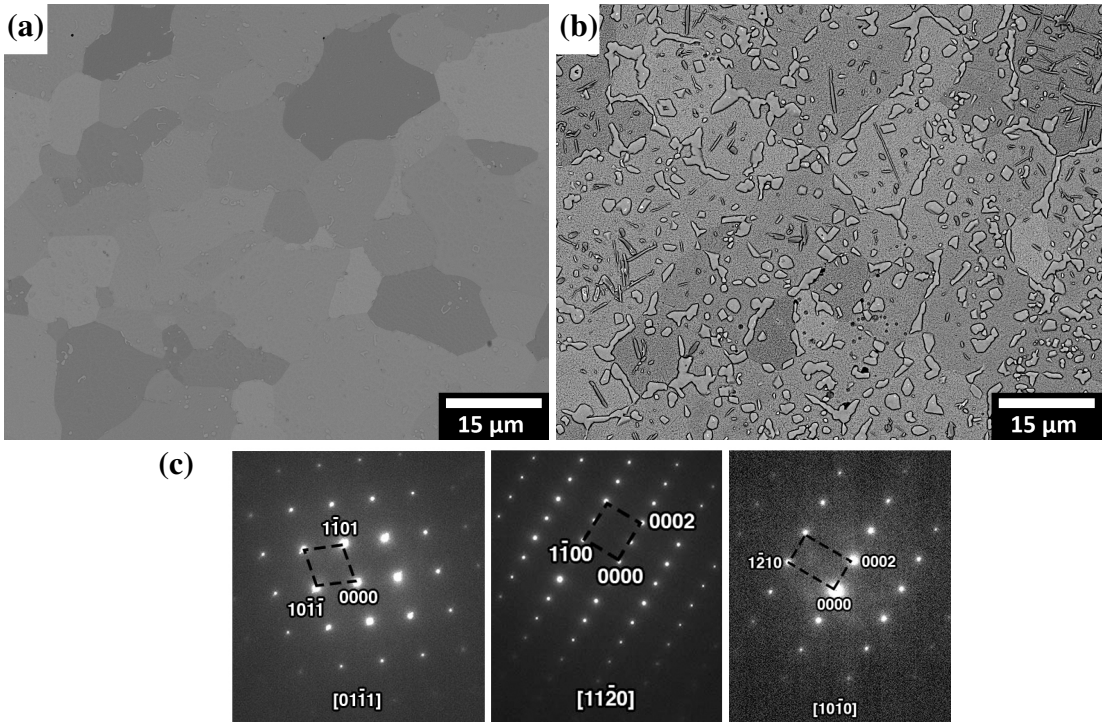


Fig. 5.7 Backscattered SEM images of the centre of the fin (a) before exposure and (b) at the transition between protective/breakaway oxidation during exposure, with large blocky $M_{23}C_6$ and needle shape M_2(C,N); (c) selected area diffraction patterns of M_2(C,N) phase present in (b).

Atom probe tomography (APT) was utilised to investigate in detail the chemical compositions of the various phases observed in the IOZ. Table 5.3 summarises the compositions of the chromite, ferrite and $M_{23}C_6$ phases which were confirmed by APT analysis. More specifically, two interfaces including $M_{23}C_6$/ferrite and chromite/ferrite were analysed, as marked in fig. 5.5c. The corresponding atom probe reconstructions are illustrated in

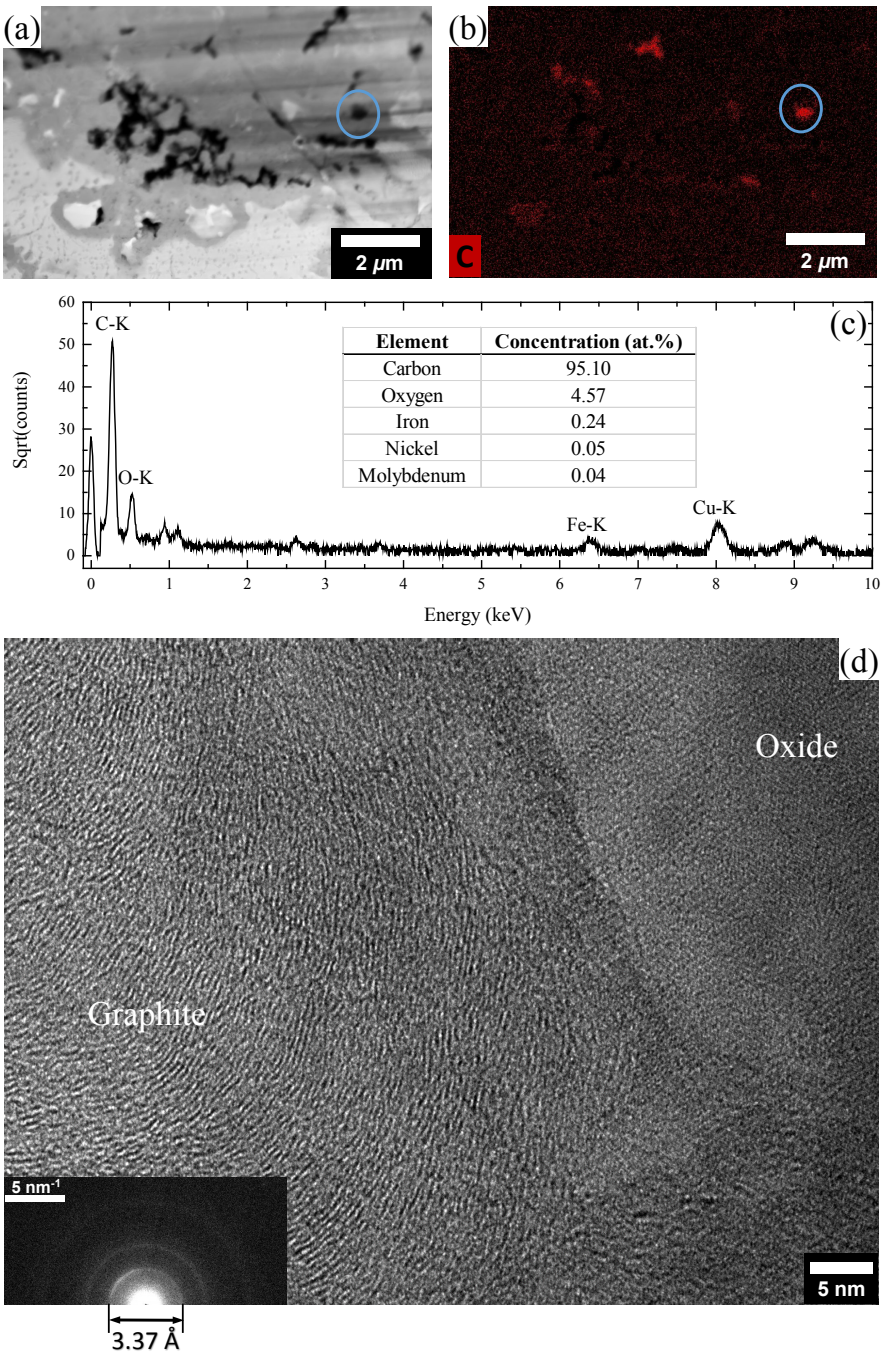


Fig. 5.8 (a) & (b) TEM dark field image & EDX carbon mapping taken from IOZ, respectively; (c) EDX spectrum taken from the carbon-rich region as marked in (a) & (b); (d) high-resolution TEM (HRTEM) image of oxide/graphite interface with SAD patterns of the graphite region. Measurements courtesy of Y.L. Chiu.

fig. 5.9. To enable comparisons of the degree of Cr depletion, the composition of ferrite from the fin centre is also listed in table 5.3.

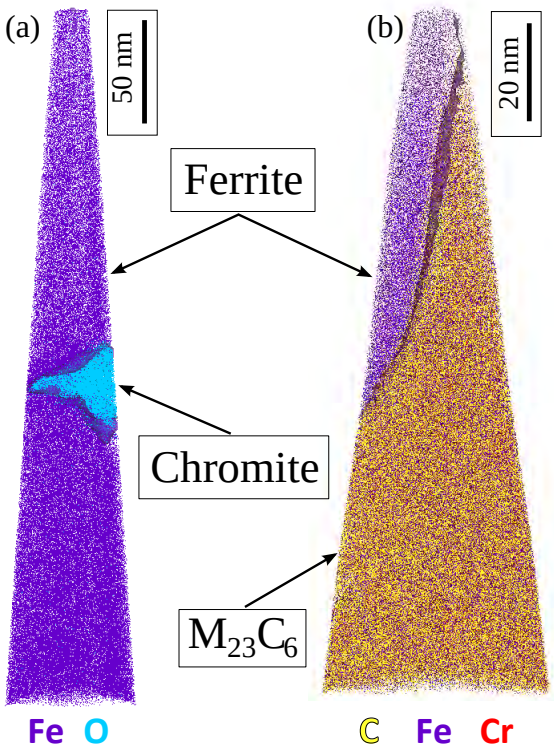


Fig. 5.9 Atom probe reconstructions of samples from the IOZ showing (a) the ferrite and chromite and (b) the ferrite and $M_{23}C_6$ phases. Isoconcentration surfaces at 90 and 67 at.% Fe highlight the ferrite/chromite and ferrite/$M_{23}C_6$ respectively. Measurements courtesy of P. Kontis.

Figure 5.10 shows the distribution of $^{56}Fe^{16}O^-$, $^{52}Cr^{16}O^-$, $^{28}Si^-$ and $^{12}C_2^-$ within the oxide region at the sub-micron resolution by using NanoSIMS. One can see more carbon in the spinel phase region close the the spinel/metal interface.

5.5 Modelling Results

5.5.1 Oxidation Kinetics

In fig. 5.11, experimental measurements of oxide layer thicknesses (the dimensional metrology is detailed in [263]) are compared with the predictions of eqs. (5.10), (5.15) and (5.16). Apparent in all the data is the approximately equal thicknesses of the outer magnetite and inner spinel layers. The inner layer occupies the space corresponding to alloy consumption as chromium in the product spinel is essentially immobile, and the equal

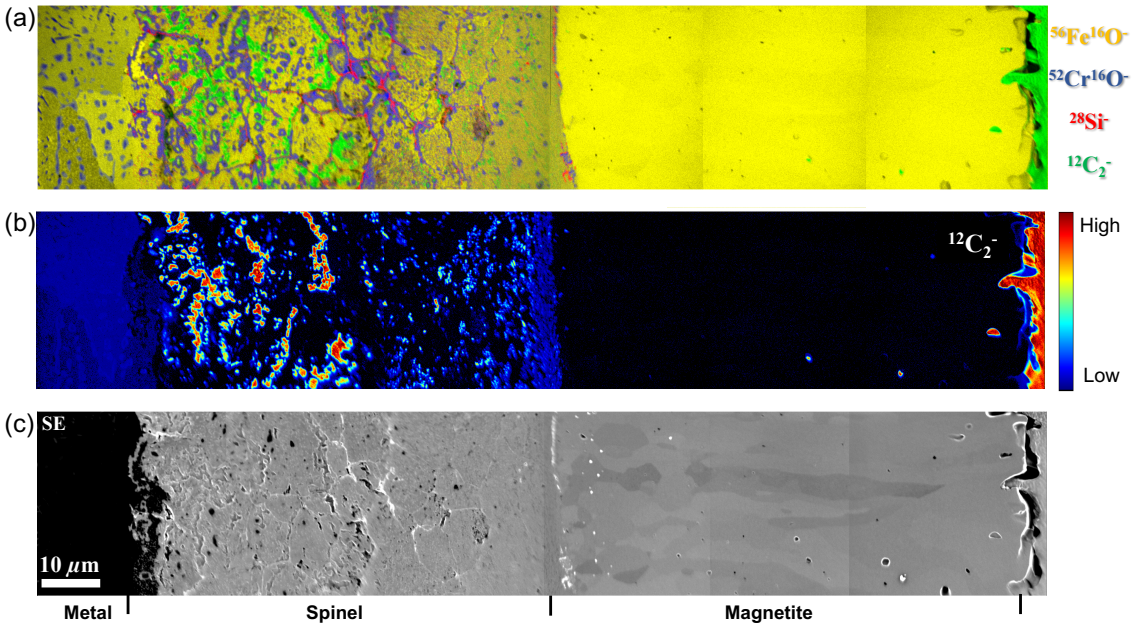


Fig. 5.10 Measurements of oxide phase regions by Nano-SIMS: (a) distribution of $^{56}Fe^{16}O^-$ (yellow), $^{52}Cr^{16}O^-$ (purple), $^{28}Si^-$ (red) and $^{12}C_2^-$ (green); (b) distribution of $^{12}C_2^-$; (c) secondary electron (SE) imaging. Measurements courtesy of K. Li.

layer thicknesses reflect the fact that the Fe/Cr ratio in the scale equals that in the alloy. During the course of this work, we have noticed a significant deviation away from purely parabolic kinetics – which can be modelled using a SiO_2 blocking factor $s = 5.2\,\mathrm{m^2{\cdot}mol^{-1}}$ – which we have attributed to the precipitation of this phase. Also shown are the predictions assuming $s = 0$. Predictions with $s = 5.2\,\mathrm{m^2{\cdot}mol^{-1}}$ show somewhat better agreement with the non-parabolic oxidation kinetics; the coefficient of determination (COD) is 0.83 for $s = 5.2\,\mathrm{m^2{\cdot}mol^{-1}}$ in comparison with 0.71 for $s = 0$; if this effect is not accounted for, the thicknesses are over/underpredicted at long times.

The activation energy for oxygen mobility (Q_O) and iron mobility (Q_Fe) deduced from the current experimental data are $276 \pm 10\,\mathrm{kJ/mol}$ and $264 \pm 11\,\mathrm{kJ/mol}$ respectively for $s = 5.2\,\mathrm{m^2{\cdot}mol^{-1}}$ and $255 \pm 19\,\mathrm{kJ/mol}$ and $243 \pm 18\,\mathrm{kJ/mol}$ respectively for $s = 0$. The obtained activation energies with/without considering Si effects are very close; this is due to the assumed temperature independency of the s parameter. Recent assessment [91, 264] describes the P_{O_2} dependent oxygen mobility $M_\mathrm{O} = y_\mathrm{Va} y_\mathrm{O} M_\mathrm{OVa}$, where y_Va and

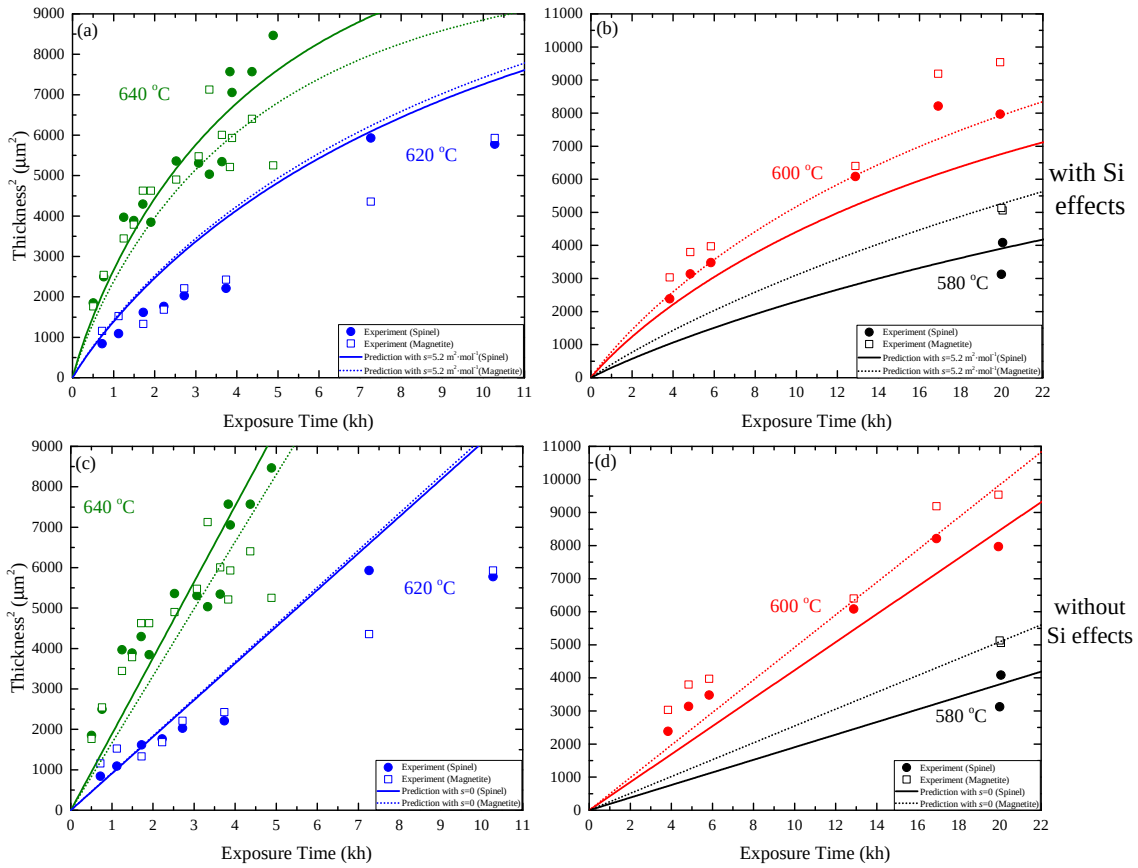


Fig. 5.11 Comparisons of predicted and measured thickness of spinel (solid line and solid circle) and magnetite (dash line and empty square) phase regions at (b) & (d) 580 & 600 °C and (a) & (c) 620 & 640 °C; predictions with SiO_2 blocking factor $s = 5.2\,\mathrm{m^2{\cdot}mol^{-1}}$ ((a) & (b)) and $s = 0$ ((c) & (d)) are compared. Measurements courtesy of J. Sumner and N. Simms.

y_O are site-fractions of vacancies and oxygen ions, respectively; it gives the activation energy of M_{OVa}, $Q_{OVa} \approx 140\,\mathrm{kJ/mol}$ if a reasonable oxygen vacancy formation energy is assumed [265, 255, 266, 264]. Obtained from the iron tracer diffusion in magnetite, Dieckmann *et al* [267] gives $Q_{Fe} = 613\,\mathrm{kJ/mol}$ for the iron interstitial regime and $Q_{Fe} = -140\,\mathrm{kJ/mol}$ (negative due to strong temperature dependency of defect equilibria, as discussed in [89]) for the iron vacancy regime between 900 to 1400 °C, and its extrapolation down to 500 °C is broadly consistent with measurements by Atkinson *et al* [268]. At 600 °C, the tracer diffusion coefficient $D^\star = MRT$ obtained from fitting the present model to observed scaling rates shows $D^\star_O \approx 10^{-17}\,\mathrm{m^2/s}$ and $D^\star_{Fe} \approx 10^{-15}\,\mathrm{m^2/s}$, compared with $D^\star_O = 2.2 \times 10^{-21}\,\mathrm{m^2/s}$ [264] and $D^\star_{Fe} = 8.2 \times 10^{-18}\,\mathrm{m^2/s}$ [269, 270] at $P_{O_2} = 10^{-20}$ atm,

interpolated from tracer diffusion experiments. The poor agreement between lattice diffusion activation energies and values found from scaling kinetics, for both oxygen and iron, indicates that mass transport in the present case is not via lattice diffusion. As proposed above, and shown schematically in the inset to fig. 5.1, transport is via a combination of gas phase and oxide grain boundaries. The equal activation energies reflect the stoichiometry controlled balance of metal and oxygen fluxes, and the ongoing adjustments in boundary P_{CO_2} and microstructure which achieve it.

Figure 5.12 shows the influence of temperature on oxide thickness at different times (200, 20, 2 and 0.2 kh) as predicted by the proposed model assuming $s = 5.2\,\mathrm{m}^2{\cdot}\mathrm{mol}^{-1}$. Higher temperatures lead to thicker oxides as expected, except for long exposure times when spinel growth reaches a saturation point due to a large predicted amount of SiO_2 blocking, and the magnetite thickness is reduced due to larger inward flux of oxygen than outward flux of iron at high temperatures. The spinel layer shows slightly smaller thickness than that of magnetite at low temperatures, but is slightly larger at high temperatures; this effect is supported by the experimental data of fig. 5.11.

5.5.2 Carburisation Kinetics

Figure 5.13 shows predicted profiles of carbide fractions across the component at different times made using the 1D-DICTRA model, alongside the experimental data determined using quantitative stereology. The simulations were conducted by applying either fixed activity $a_C = 1$ at the oxide/alloy interface (dashed lines) or else the time-varying surface reaction boundary conditions as described in eq. (5.18) (solid lines). Clearly the assumption of a unit carbon activity at time zero leads to gross overprediction of carburisation; carbon saturation would then be expected even at times as short as 3.8 kh. Using the surface reaction boundary condition ($\alpha_{\mu,C} = 1.2 \times 10^{-12}\,\mathrm{mol}\cdot\mathrm{m}\cdot\mathrm{s}^{-1}\cdot\mathrm{J}^{-1}$) gives much better agreement with the measurements; the time to carbon saturation is predicted to be close

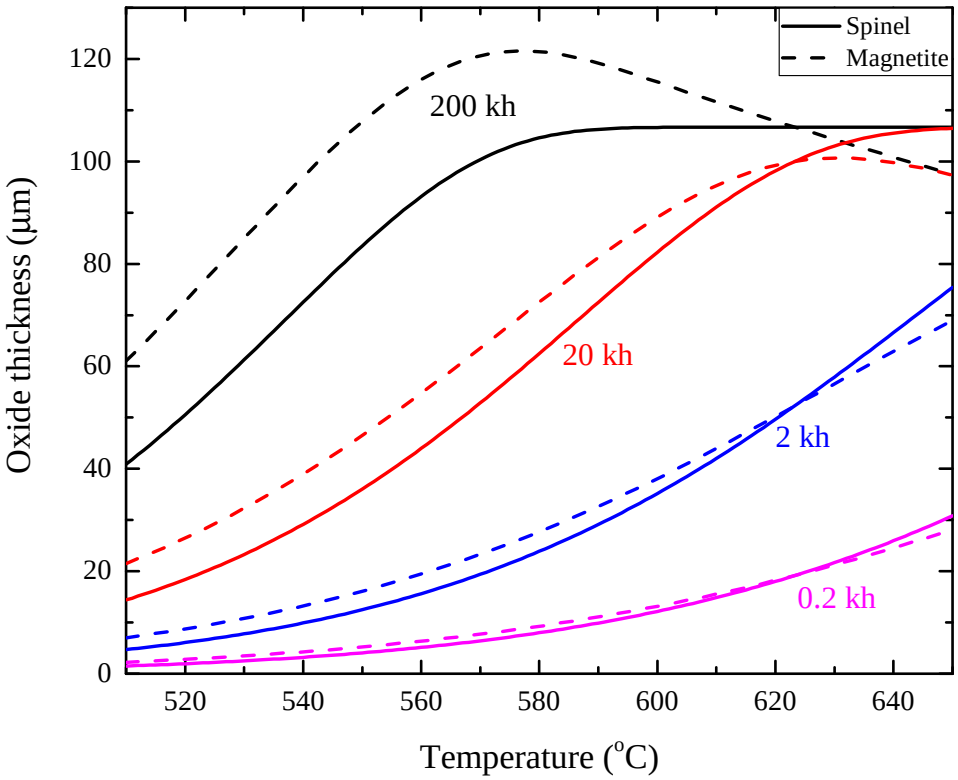


Fig. 5.12 Prediction of oxide thickness at different temperatures and different times; SiO_2 blocking factor $s = 5.2\,\mathrm{m^2{\cdot}mol^{-1}}$ is utilised.

to 20 kh. These calculations demonstrate that surface-limited reaction at the oxide/alloy interface delays carbon uptake.

Figure 5.14 compares the predicted evolution of carbon mole fraction (x_C) at the oxide/alloy interface and at the centre of the fin of 1 mm width for samples exposed at 600 °C, as predicted by a combination of the 1D-SPM ($\beta = 6.4 \times 10^{-8}\,\mathrm{s^{-1}}$) and 1D-DICTRA ($\alpha_{\mu,C} = 1.2 \times 10^{-12}\,\mathrm{mol \cdot m \cdot s^{-1} \cdot J^{-1}}$) models; the same oxidation kinetics model considering the SiO_2 blocking are used and loosely coupled together. The two 1D models show very close agreement except at the early stages when the effect of initial oxidation (and thus fast Fe & Cr loss from the metal) on carbon enrichment at the oxide/alloy interface is severe; this effect is obviously predicted only by 1D-DICTRA. Put another way, the DICTRA calculation predicts that when $t \sim 0$, the scale-alloy interface moves extremely fast, so rapidly that carbon cannot diffuse away from it into the metal, and is as a result concentrated at the interface. This erroneous result is an unavoidable consequence of

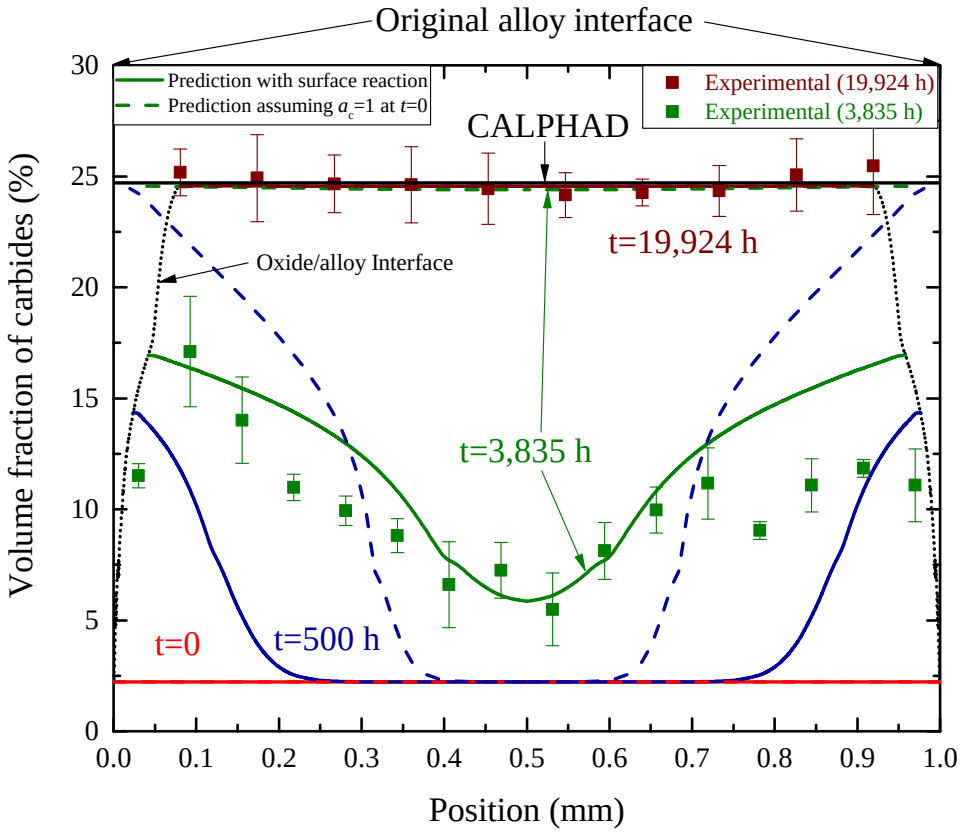


Fig. 5.13 Predicted profiles of volume fraction of carbides for a 1 mm fin exposed to experimental gas conditions at 600 °C at 0, 500 h, 3835 h and 19924 h, in comparison with measurements corresponding to black box marked in fig. 5.1b; simulations were conducted by 1D-DICTRA as described in section 5.3.2 treating migration of oxide/alloy interface and non-steady state carburisation with $\alpha_{\mu,\mathrm{C}} = 1.2 \times 10^{-12}\,\mathrm{mol \cdot m \cdot s^{-1} \cdot J^{-1}}$ (solid lines) or fixed $a_\mathrm{C} = 1$ at the oxide/alloy interface (dashed lines).

applying a model of diffusion control to very short times, when in fact other processes slow the oxidation rate.

Note that the two 1D models show predictions of carbon saturation (provided that the appropriate pairs of $\alpha_{\mu,\mathrm{C}}$ and β are chosen) which are consistent with each other. In particular, graphite precipitation is predicted by 1D-DICTRA after carbon saturation at around 18.8 kh; note however that such simulations are based on local-equilibrium assumptions and take no account of any energy barrier to nucleation of graphite. This will necessarily mean that the assumptions introduced are conservative with respect to graphite precipitation.

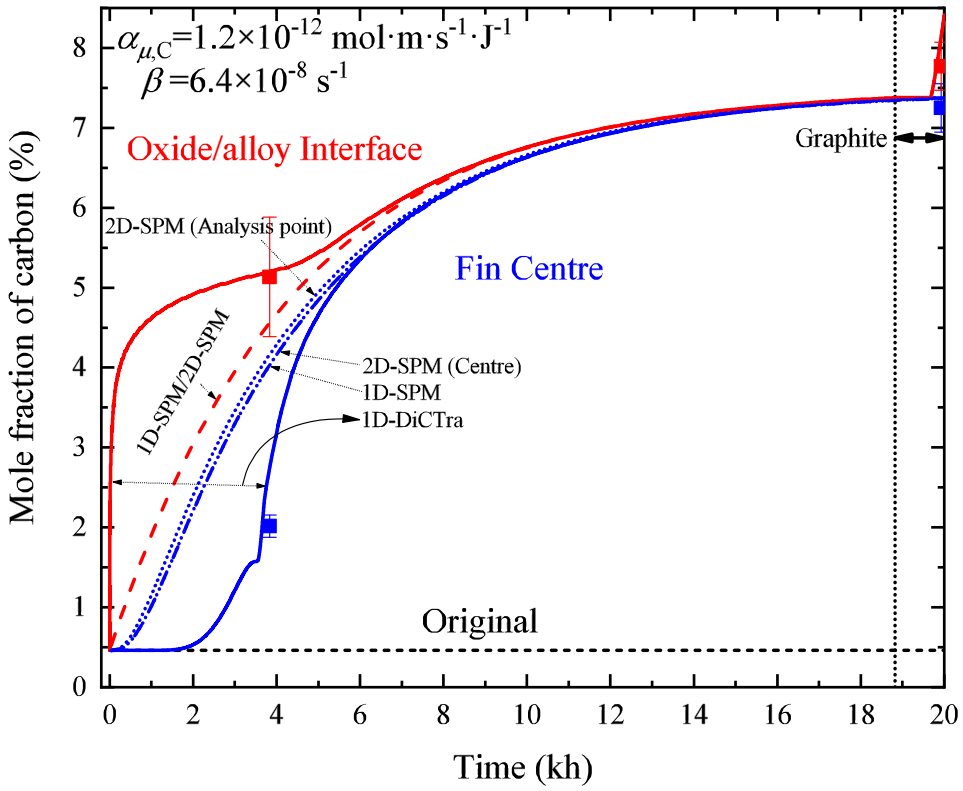


Fig. 5.14 Predicted evolution of carbon content at oxide/alloy interface and fin centre for a 1 mm width (6 mm long) fin exposed to experimental gas conditions at 600 °C, as predicted by 1D-DICTRA, 1D-SPM and 2D-SPM; above two carbon contents taken from the line profiles across the 2D fin tip (fig. 5.1(b)) through either the analysis point or the centre of y-axis are compared. Measured mole fraction of carbon (converted from carbide volume fraction) are labelled for comparisons.

Figure 5.14 reveals also a geometrical effect when one compares results from the 1D-SPM and 2D-SPM versions of the models; the 2D geometry is illustrated in fig. 5.1(a) with line profiles taken across the fin tip through either the analysis point or the centre of y-axis. The 1D-SPM and 2D-SPM (centre) predictions are very close, however the 2D-SPM profile at the analysis point considered shows an acceleration of carbon ingress due to corner (soft impingement) effects.

5.6 Discussion

5.6.1 On the Degradation Reactions Observed

Here, attack is characterised by a deep zone of internally precipitated Cr-rich carbides and a shallower zone containing internal oxides, principally Cr-rich chromite. There are similarities to what has been presented in [247, 271]. But the reactions occurring particularly in the subsurface alloy region are complex – see fig. 5.5c. Their rationalisation is warranted.

The conventional theory for the internal precipitation within an alloy attacked by different oxidants is due to Meijering (as reviewed in [241]) and its predictions are broadly in agreement with experiment [272]. Thus the less stable precipitate is expected to be found in the deeper zone, if formed, as the more stable one is formed near the surface where both oxidant activities are at their maximum value. In the present case, the Cr-rich spinel is much more stable than the carbide, and precipitates preferentially – consistent with accepted wisdom, such that within the internal oxide zone, a_O decreases with increasing depth until its value is too low to stabilise oxide with respect to carbide. Carbon does not react within the oxide precipitation zone, but diffuses rapidly through it to reach unreacted alloy, precipitating there as Cr-rich carbide. But there are subtle differences between what is observed here and the accepted theory. In the Meijering model, the internal carbide/internal oxide interface is assumed to be the site of instantaneous conversion of carbide to oxide, the carbon solute product diffusing inward to form more carbide at a greater depth. But here, as is clear in fig. 5.5c and from observations elsewhere [247, 271, 273], oxidation of the carbide takes time, and the interface is in fact somewhat diffuse implying the conversion of carbide to oxide is far from being instantaneous.

What has been observed here can be rationalised further in the following way. Within the carbide precipitation zone – which penetrates the full width of the fin – the amount of carbide varies with position (fig. 5.13), as does the matrix concentration of chromium

(table 5.3). This is a consequence of precipitation occurring under local equilibrium conditions:

$$23\underline{\mathrm{Cr}} + 6\underline{\mathrm{C}} = \mathrm{Cr}_{23}\mathrm{C}_6 \tag{5.25}$$

where for simplicity the iron content has been neglected; this reaction will be governed by a solubility product K_{sp}. Thus if local equilibrium is achieved, a gradient in a_{C} from its maximum at the oxide-carbide interface to a minimum at the fin centre is expected, accompanied by an increase in matrix chromium concentration accounting for the observed decrease in carbide fraction.

If local equilibrium is achieved, then the locus of compositions through the reaction zone can be represented by a diffusion path on the appropriate phase diagram. Because diffusion of interstitial species is so much faster than substitutional diffusion, the latter can be neglected, and the system examined with respect to variations in a_{C} and a_{O}. Schematic diffusion paths are shown in fig. 5.15 for relatively short times (t_1) and much longer times (t_2). The internal reaction product sequence of (α+$M_{23}C_6$), (α+$M_{23}C_6$+spinel), (α+SiO_2+spinel) observed in fig. 5.5c is seen to be consistent with a diffusion path (t_1) corresponding to the expected oxygen gradient, and a carbon activity profile with its maximum in the internal oxide-internal carbide region. At longer times (t_2), carbon uptake is greater, and no single-phase ferrite remains at the centre of the fin. Furthermore, the higher carbide, Cr-rich M_2(C,N) appears, as shown on the second diffusion path. Eventually, the carbon activity will rise above unity, and graphite will precipitate, initiating breakaway.

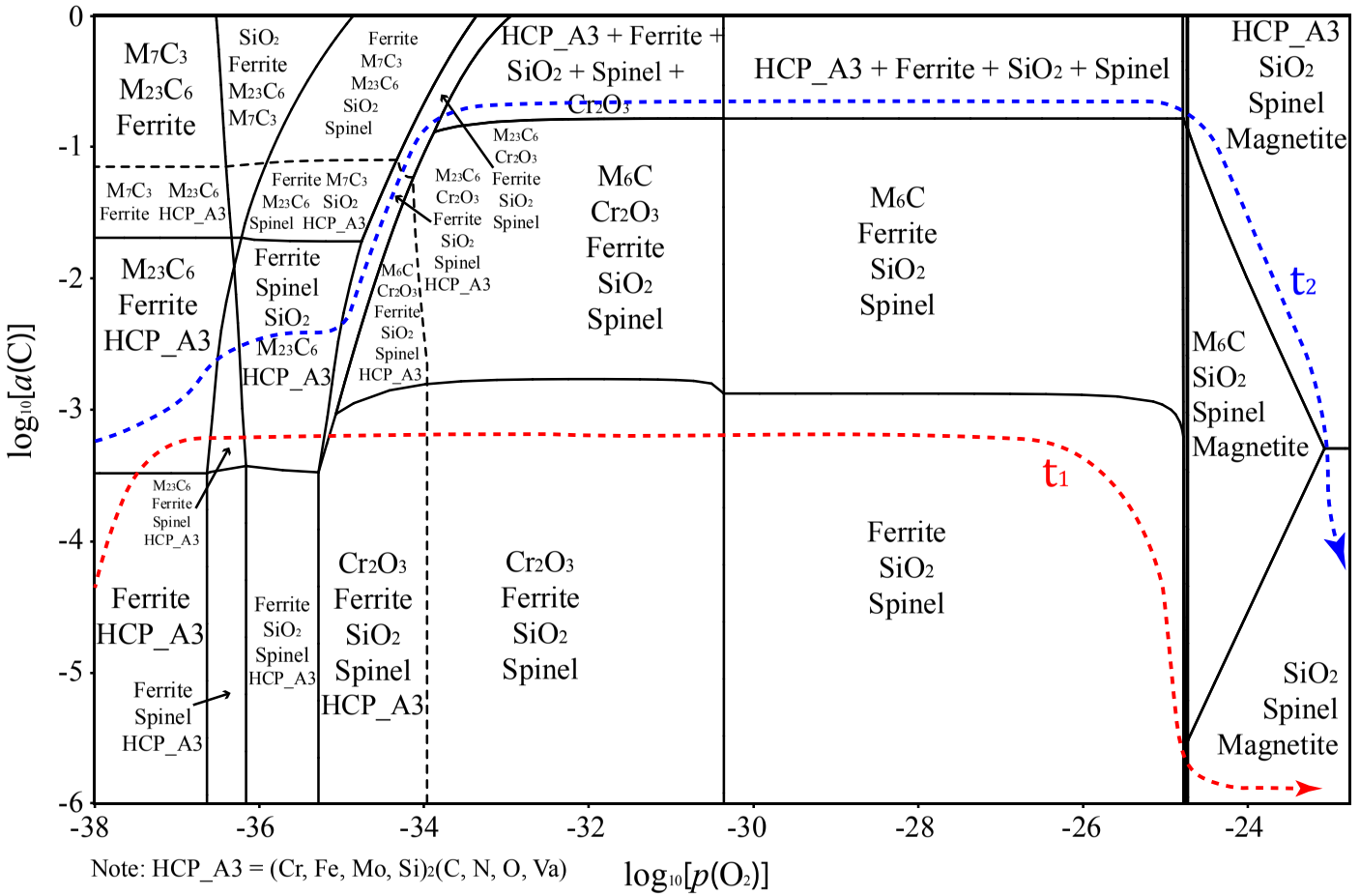


Fig. 5.15 Solid thermodynamic calculation predicting phase stable region at different P_{O_2} and a_C for virgin alloy with assumed molar nitrogen content of 10^{-6} at 600 °C; calculations were based on major phases included in TCFE8 and TCOX5 thermodynamic database; M_2(C, N, Va) introduced by nitrogen is predicted to present at bottom left of dashed black line, whose position is strongly dependent on nitrogen content; suggested diffusion paths for shorter times (t_1) and longer times (t_2) are marked as dashed lines.

A minor deficiency of this analysis arises from the assumption of zero metallic diffusion. In fact, chromium is locally depleted near the internal oxide, and Cr_2O_3 cannot form as would be predicted in the absence of depletion. One should note also that the predicted form of the phase diagram – particularly at low carbon and oxygen activities corresponding to the bottom left hand side of the figure – is very sensitive to the assumed levels of nitrogen in the steel. Increasing the assumed nitrogen level to 10^{-6} is enough to stabilise the (α+$M_{23}C_6$+M_2(C,N)) phase field. Since this is what is observed in the specimen centre after 20 kh exposure, it is concluded that the steel nitrogen content was of order 10^{-5}.

5.6.2 On the Role of Carbon and its Treatment in Numerical Modelling

Carbon plays a crucial role in the breakaway phenomenon studied here, but yet various aspects of its transport behaviour remain unclear. It has been found by atom probe tomography to segregate at grain boundaries of protective Cr_2O_3 grown on an Fe-20Cr alloy carburised at 650 °C in Ar-20CO_2 at 1 atm [251]. Although grain boundary diffusion is indicated, the precise transport mechanism through oxide layers has not been fully established: neither the chemical form of the carbon nor its interaction with the surrounding oxide are known.

This lack of understanding justifies the approach taken here. Rather than treating the diffusion of carbon through oxide and associated mass balance at the oxide/alloy interface explicitly, the strategy for the modelling approach adopted has been to treat two semi-coupled processes, consistent with the oxide growth model (OGM) and the substrate penetration model (SPM)/DICTRA. The former focusses on the kinetics of oxidation while the latter is concerned with the penetration of carbon into the substrate, formation of internal carbides, depletion of Cr in ferrite, and graphitisation at the substrate/oxide interface.

During the protective oxidation stage there is negligible carbon present in the oxide; most carbon generated by the Boudouard reaction is injected into the alloy which acts as a carbon sink, until it is fully (super-)saturated with carbon. The volume of the sink thus determines the time required for carbon saturation (TCS); oxidation, as seen from fig. 5.13, can reduce the volume of the sink by inward growth of the spinel. After the sink is fully (super-)saturated with carbon, carbon deposition and graphitisation (as predicted in fig. 5.14) will alter the properties of the oxide scale by mechanical disruption and facilitate the permeation of oxidants, causing the breakaway initiations – this is described and predicted in a practical manner as the carbon saturation model in section 5.6.3.

It is of interest to estimate the relative contributions of oxygen and carbon to the overall mass gain observed, and their variations with temperature. This becomes possible if one assumes that any contribution to the overall weight gain by carbon is due to its uptake in the metal alone – with any contribution within the oxide scale then being assumed negligible. Figure 5.16 shows predicted weight gain contributed by oxidation (by OGM) and carburisation (by SPM) at the predicted time to breakaway (predictions from section 5.6.3), in comparison with measured weight gain to breakaway (WGB) data. As seen, the contribution of carbon to the total weight gain is comparatively small, particularly at low temperatures with thicker oxide at the time to breakaway. It is also a constant net amount, corresponding to the amount precipitated in the steel fin, on account of the assumptions made in the modelling.

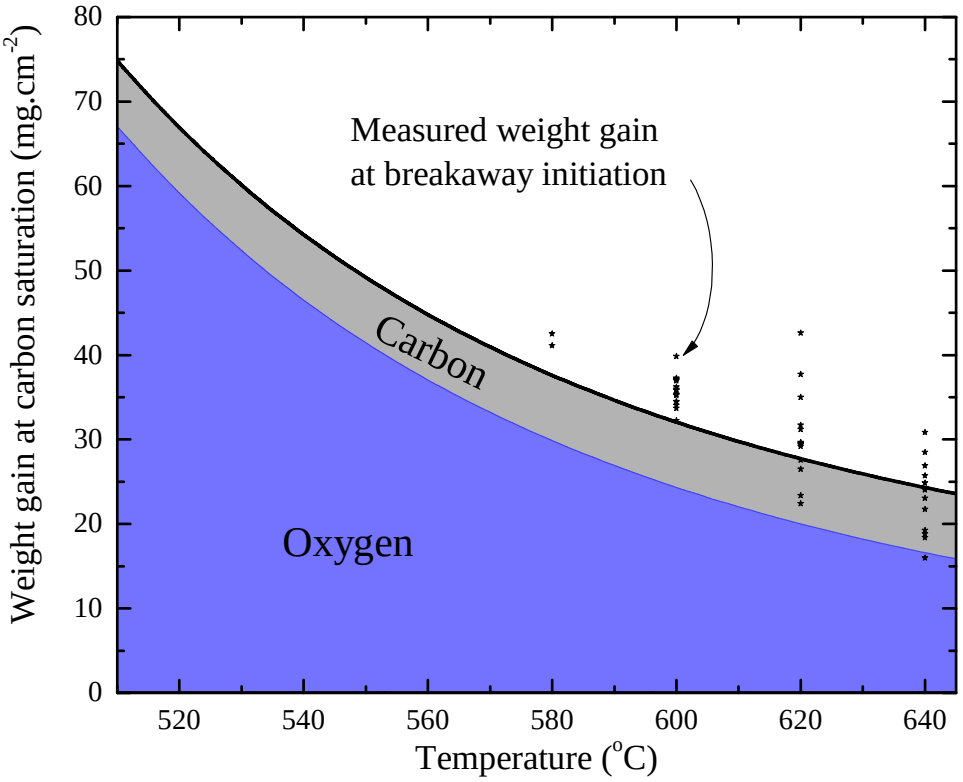


Fig. 5.16 Predicted weight gain contributed by oxidation and carburisation at the time of carbon saturation, in comparison with measured weight gain at breakaway (WGB) data. Note only carbon in the substrate and oxygen in the oxide scales are considered in the predictions. Measurements of WGB courtesy of Amec Foster Wheeler on behalf of EDF Energy.

5.6.3 Implications for Remnant Life Assessment

The present results provide plausible evidence that the point of breakaway initiation can be correlated with carbon saturation of the underlying substrate. Once carbon saturation is exceeded – and the necessary degree of supersaturation required for its nucleation reached – graphite (fig. 5.8) can precipitate at the spinel/alloy interface (even though layers' of carbon have been found in spinel phase region during protective region, as seen in fig. 5.10). By this stage, significant Cr depletion in ferrite due to formation of Cr-rich carbides will have occurred (table 5.3); the latter suppresses the formation of protective Cr-rich oxide while the former seems likely to decrease the fracture toughness of the oxide and the metal/oxide

interface. Such changes in reaction morphology need to be identified if the change in the reaction kinetics accompanying breakaway is to be quantified.

Using these arguments, it becomes possible to estimate the variation of time to breakaway (TTB) with temperature by assuming – somewhat conservatively – that it corresponds to the time needed for carbon saturation (TCS). This is done in the following way. First, one identifies an analysis point (AP) close to the tip of the fin, as illustrated in fig. 5.1a, and an associated assumed mean carbon concentration at saturation, denoted $X_{\mathrm{C}}^{\mathrm{crit}}$. Next, for each TTB datapoint available in the experimental dataset, one solves the diffusion equation described in section 5.3.3, to extract a value of the parameter β, which corresponds to the lumped parameter for both the transport kinetics of carbon through oxide and the kinetics of Boudouard reaction. Then, by extrapolating β, it is possible to predict TTB at the lower operational temperatures.

It is of interest first to determine the sensitivity of the times predicted in this way to the values of the critical parameters which are assumed. This is done in fig. 5.17 which represents a contour map for the time for carbon saturation as a function of the effective chemical diffusivity of carbon ($D_{\mathrm{C}}^{\mathrm{eff}}$) and surface reaction parameter (β) assuming $X_{\mathrm{C}}^{\mathrm{crit}} = 7\,\mathrm{at.\%}$ for the analysis point of (0.5 mm, 0.5 mm) in a fin geometry of 3 mm $\times$ 1 mm. Note that the solid contour lines account for the effect of oxidation kinetics via spinel growth kinetics at temperature of 600 °C as predicted in section 5.3.1, while the dashed contour lines do not consider any oxidation effects. Note that on the top left hand side of the figure, the sluggish surface reaction kinetics and high carbon diffusivity mean that the process is independent of carbon diffusivity, resulting in a surface reaction-controlled regime. Conversely, the bottom right region is controlled by carbon diffusion. Typical ranges of $D_{\mathrm{C}}^{\mathrm{eff}}$ and β suggest that it is the sluggish surface reaction which dominates in this case. One can also see that the oxidation (thinning of the fin) can reduce TCS predicted, i.e. shift contour lines towards right hand side; this is due to the decrease of the volume of the metal *sink* as discussed in section 5.6.2.

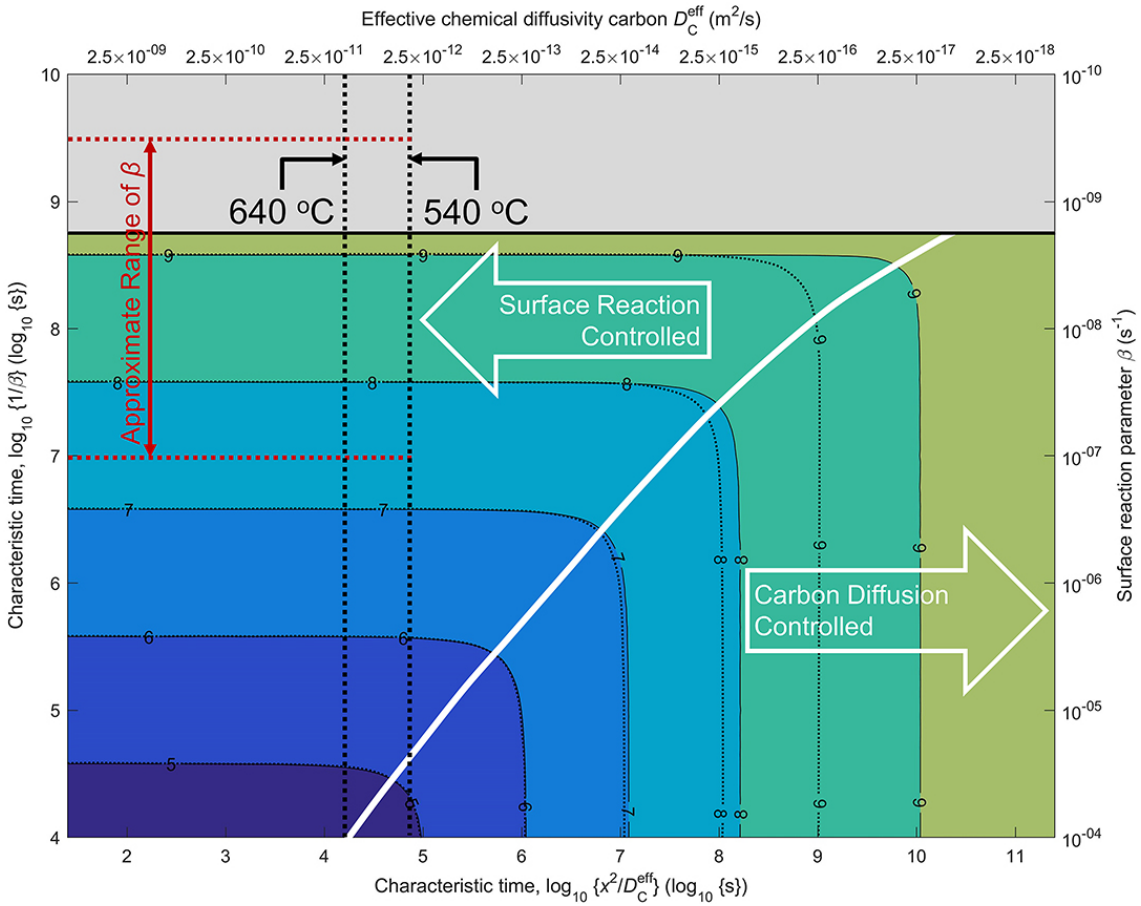


Fig. 5.17 Contour plot of time required for carbon saturation ($\log_{10}\{\mathrm{s}\}$) as a function of effective chemical diffusivity of carbon ($D_{\mathrm{C}}^{\mathrm{eff}}$) and surface reaction parameter (β); oxidation kinetics at 600 °C as predicted by section 5.3.1 is considered (solid contour lines), comparing with that without considering any oxidation kinetics (dash contour lines); typical ranges of $D_{\mathrm{C}}^{\mathrm{eff}}$ and β are marked as black dot lines and red dot lines, respectively; transition between $D_{\mathrm{C}}^{\mathrm{eff}}$-controlled region and β-controlled region is marked as white line; saturation criteria $X_{\mathrm{C}}^{\mathrm{crit}} = 7\,\mathrm{at.\%}$ for the analysis point of (0.5 mm, 0.5 mm) in a fin geometry of 3 mm × 1 mm is utilised; top grey region corresponds to situations where metal at the analysis point is oxidised before the carbon saturation criteria is reached.

Figure 5.18 shows calculated values of β from the temperature-dependent TTB measurements, for different assumed values of $X_{\mathrm{C}}^{\mathrm{crit}}$. For simplicity, the temperature dependency of $X_{\mathrm{C}}^{\mathrm{crit}}$ is ignored as the saturation level has very little difference over the temperature range of interest. The values of β are inter/extrapolated based on the Arrhenius equation, assuming that each of the processes included in the parameter follows Arrhenius behaviour; the corresponding activation energy (E_β) is found to be $345 \pm 14\,\mathrm{kJ/mol}$. One can see that higher $X_{\mathrm{C}}^{\mathrm{crit}}$ leads to lower E_β. This is due to a larger contribution of carbon diffusion in

the metal and the smaller contribution of the β processes to the net reaction if a higher X_C^{crit} is assumed.

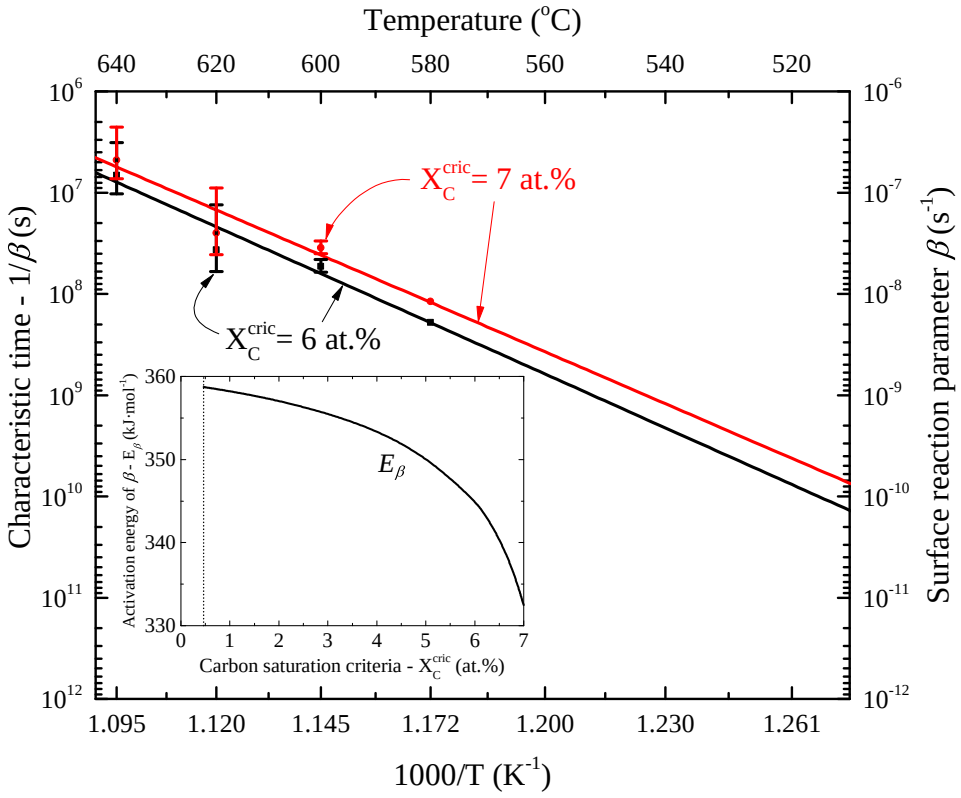


Fig. 5.18 Calculated surface reaction parameter β based on measured time to breakaway initiation and carbon saturation model with carbon saturation criteria $X_C^{crit} = 6\,at.\%$ (black) or $X_C^{crit} = 7\,at.\%$ (red); inter/extrapolation of β is based on the Arrhenius equation; corresponding activation energy E_β for different X_C^{crit} are plotted on the bottom left.

Figure 5.19 illustrates the predicted values of TTB against temperature along with measured data. Notice that the times to breakaway increase to very large values as the temperature falls, rising almost asymptotically as the temperature falls to the operational regime. The predicted time to breakaway initiation made with the carbon saturation model gives a higher life expectancy than that from an empirical ln{TTB}-1/T linear fitting, particularly at lower temperatures; this is more significant if a higher value of X_C^{crit} is assumed. Thus, at lower temperatures, the effect of a relatively smaller carbon diffusivity becomes more pronounced. Further future work is needed to assess the effect of any

non-Arrhenius behaviour of effective carbon diffusion caused by carbide precipitation, for example by the use of a Labyrinth factor.

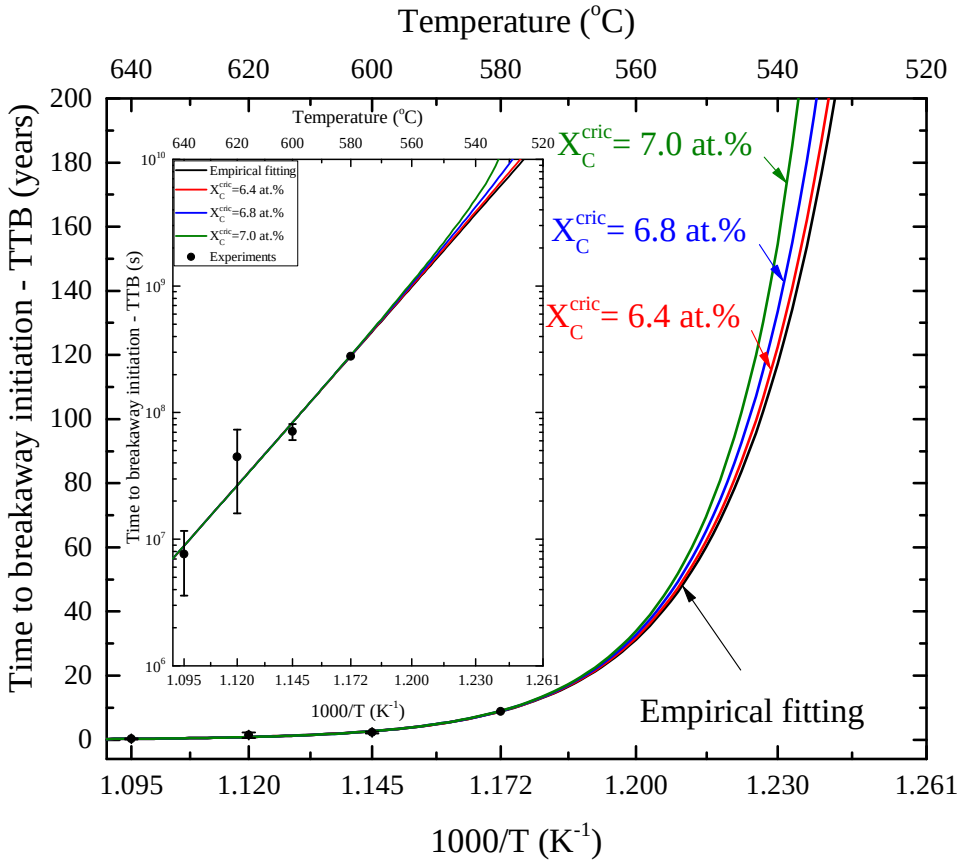


Fig. 5.19 Predicted time to breakaway initiation from an empirical ln{TTB}-1/*T* linear fitting and carbon saturation model with different carbon saturation criteria. Measurements of TTB courtesy of Amec Foster Wheeler on behalf of EDF Energy.

5.7 Summary & Conclusions

- A 9Cr1Mo steel subjected to degradation in high pressure (42.38 bar) CO_2 at 600 °C and 20 kh has been characterised. The component contains fins of initial thickness 1 mm and length 3 mm; the evidence confirms that the substrate is saturated with respect to carbon, as indicated by measurements of the very substantial carbide precipitation and thermodynamic calculations.

- The outer oxide scale consists of an Fe-rich magnetite/spinel and Cr-rich spinel; the former contains very little Cr and grows outwards with the latter growing inwards. The presence of graphite in the inner oxide scale of spinel close to the scale/metal interface has been confirmed by transmission electron microscopy.

- Attack of the metal substrate close to the scale/metal interface – termed the internally oxidised zone (IOZ) – involves Cr-rich $M_{23}C_6$ carbide forming but becoming progressively oxidised to a Cr-rich spinel as corrosion proceeds.

- It seems plausible that carbon saturation of the substrate is a precursor to the formation of graphite, which in turn is needed for breakaway attack. This is supported by the modelling. Thus, the time for carbon saturation is shorter than that needed to cause breakaway attack.

- Nevertheless, when calculations are made using diffusion theory for the rate of carbon ingress assuming a carbon activity of unity at the metal/scale interface at time zero, the measured rate of carbon ingress is severely overpredicted. Hence it is concluded that some form of kinetically-limiting process – such as gas ingress involving the Boudouard reaction, diffusion of carbon through the outer spinel or carbon transfer across the scale-alloy interface – causes a delay to the rate of carbon penetration.

- A physically-based model is proposed for the rate of carbon uptake, which accounts for both carbon diffusion in the substrate but also the kinetically-limiting processes. By consideration of the available data for the time to breakaway oxidation at higher temperatures – which is assumed to correlate with carbon saturation of the substrate at a chosen analysis point – extrapolation to lower temperatures can be accomplished.

- The modelling allows for the relative contributions to the overall mass gain from (i) carburisation and (ii) oxidation to be estimated. The fraction of the mass gain from carburisation is approximately 1/3 under conditions of accelerated higher

temperature testing but falls to substantially lower values at reactor temperatures. This is because carbon diffusion in the metal substrate starts to play a role in slowing the kinetics of attack at lower temperatures.

- The modelling presented represents a rationale for the estimation of the safe-working life of these components, and in particular extrapolation of high temperature testing to conditions more representative of operating conditions which are typically closer to 520 °C.

Tables & Figures

Table 5.1 Measured composition of steel (wt.%); carbon and sulphur are measured by the combustion analysis while the rest by the Inductively Coupled Plasma Optical Emission Spectometry (ICPOES). Data courtesy of EDF Energy.

C	Co	Cr	Cu	Fe	Mn	Mo	Nb	Ni	P	S	Si	Ti	V	W
0.093	0.02	9.2	0.16	Bal.	0.47	1.04	< 0.02	0.21	0.011	0.008	0.67	< 0.02	< 0.05	< 0.05

Table 5.2 Chemical composition (at.%) of $M_2(C,N)$ from internal oxidised zone (IOZ) as measured by TEM-EDX. Measurements courtesy of Y.L. Chiu.

C	Cr	Fe	Mo	N	V
24.73	61.83	0.73	1.84	10.59	0.25

Table 5.3 Chemical composition of chromite, $M_{23}C_6$ carbide and ferrite phase from the internal oxidised zone (IOZ) as measured by atom probe tomography (at.%). The chemical composition of ferrite from the centre of the right fin is also given. Measurements courtesy of P. Kontis.

Phase	C	Co	Cr	Cu	Fe	Mn	Mo	Ni	Si	O
Chromite[#2]	0.0	0.0	27.35 ± 0.043	0.0	12.98 ± 0.088	1.36 ± 0.037	0.05 ± 0.011	0.33 ± 0.021	4.55 ± 0.071	53.36 ± 0.077
$M_{23}C_6$[#1]	18.36 ± 0.017	0.0	29.63 ± 0.027	0.12 ± 0.002	46.38 ± 0.026	0.17 ± 0.004	4.23 ± 0.013	1.10 ± 0.011	0.01 ± 0.001	0.0
Ferrite[#2]	0.0	0.10 ± 0.001	0.0	0.15 ± 0.001	98.14 ± 0.005	0.0	0.09 ± 0.001	1.30 ± 0.004	0.0	0.0
Ferrite[#1]	0.34 ± 0.005	0.10 ± 0.005	0.80 ± 0.016	0.12 ± 0.006	97.26 ± 0.023	0.03 ± 0.003	0.22 ± 0.008	1.02 ± 0.020	0.03 ± 0.003	0.0
Ferrite[*]	0.0	0.01 ± 0.001	1.47 ± 0.004	0.12 ± 0.001	96.44 ± 0.007	0.29 ± 0.002	0.04 ± 0.001	0.15 ± 0.003	1.46 ± 0.003	0.0

[*] Ferrite from the centre of the right fin.

[#] Analysis from the IOZ with possible sites marked in fig. 5.5c.

Chapter 6

Summary, Conclusions and Future Directions

6.1 Summary

The aim of the work reported in this thesis has been to conduct basic, cutting-edge research aimed at improved predictions of diffusional phenomena and associated phase transformations during high performance applications of metals, particularly those used for high temperature applications.

Chapter 2 represents a literature review, in which state-of-art materials modelling techniques across various length scales linked to diffusional reactions, from CALPHAD approach, to DFT thermodynamics, are reviewed; the physical background and numerical implementations for diffusion both in metallic and oxide systems are considered in detail.

In chapter 3, the vacancy formation free energy in fcc-nickel is calculated by using highly-accurate *ab initio* thermodynamics. A modified TU-TILD (Two-stage Upsampled Thermodynamic Integration using Langevin Dynamics) method is employed, which hierarchically approaches the free energy surface by using a thermodynamic integration (TI) scheme and quantum perturbation theory, thus allowing excitation mechanisms to be included. Predictions show good agreement with available experimental measurements

and help to rationalise them. A significant non-Arrhenius behaviour of vacancy formation is also investigated and proven.

In chapter 4, oxidation kinetics for the Ni-Cr system are modelled and predicted by coupling CALPHAD thermodynamics and diffusional kinetics for both oxide and metallic phases. First, the defect structure, thermodynamic descriptions and diffusional mobilities are reviewed for oxide phases including (Ni,Cr)O-halite, $(Cr,Ni)_2O_3$-corundum and $NiCr_2O_4$-spinel; second, an improved homogenisation model – which is specifically optimised for diffusion in oxide and oxide/metal phase transformation – is developed and applied. The compositional dependency of oxidation kinetics has been successfully rationalised.

In chapter 5, fundamental insights into the mechanism of breakaway oxidation in Fe9Cr1Mo steel are deduced. High-resolution microstructural and chemical characterisations are conducted. Based upon theories of carbon diffusion in metals and Boudouard reaction, temperature-dependent lifetime of a critical nuclear component exposed to CO_2 – linked with carbon saturation – is predicted. A method for lifetime estimation of these critical components is proposed.

6.2 Future Directions

The following suggested future work arising from this study is divided into three main areas:

6.2.1 DFT Thermodynamics

One weakness of the calculations conducted for the free energy surface of Ni is that there is no totally accurate approach for the contribution from magnetic excitations (F^{mag}). One of the best approaches currently, as suggested by Körmann [274], seems to be the Quantum Monte Carlo simulation for an effective Heisenberg system, which has been

applied to Ni [275], Cr [276] and bcc-Fe [277] elsewhere. For the calculation of vacancy formation energy, another important contribution in magnetic systems is 'how to perform relaxations in the paramagnetic state'. There have been a few attempts for bcc-Fe [278], but this approach does not work for Ni as yet. However, recent studies of interatomic forces affected by going from the ferromagnetic to the paramagnetic state in Ni have suggested that the spin fluctuations are almost negligible; thus it is safe to assume that the relaxations around the vacancy are similar in the ferro- and paramagnetic regime for Ni.

Prediction of the vacancy formation energy is the first step toward the calculation of diffusional behaviour. As can be seen from assessed parameters for ionic systems (in chapter 4) and review for metallic systems [279], the vacancy formation energy is comparatively smaller than that of corresponding migration energy. It is thus important to calculate the temperature-dependent activation energies by extending current phonon calculations to the transition state theory coupling with, for example, the Nudged Elastic Band (NEB) method [280, 281]. It would also be interesting to extend current calculations to multicomponent systems using the Cluster Expansion method [282], or the Special Quasi-random Structures (SQS) [283] for disordered phases.

Apart from diffusional kinetics, the DFT thermodynamic method adopted in this work for metallic systems potentially allows also a wide range of materials properties to be predicted at finite-temperatures with high accuracy: (1) free energy, thus multi-component phase diagrams; (2) heat capacity, thermal expansion, phase transitions (solid/solid or solid/liquid), thermal conduction; (3) small-scale/high-symmetry defects such as vacancies, impurities, clustering, stacking faults, anti-phase boundary, micro-twinning, dislocation (no interaction), and grain boundaries; (3) low-symmetry defects such as crack tip and general grain boundary by the hybrid quantum mechanics/molecular mechanics (QM/MM) scheme [284, 285].

It is also important to extend current DFT thermodynamics to ionic systems such as oxides; this potentially allows better understanding of high temperature corrosion and

ceramic studies. Different interatomic potentials such as the *Buckingham* or *Hill* [286, 287] type potentials might be required for LD simulations.

6.2.2 Modelling of Oxidation Kinetics

Interface diffusion at IOZ In the work on the prediction of the critical Cr and/or Al concentrations for the formation of continuous/protection oxide scale in Ni-Cr-Al systems, much has been shown to depend upon the values assumed for the oxygen diffusivity within the internal oxide zone (IOZ), consistent with Wagner's internal oxidation theory. Because oxygen diffuses via a short circuit diffusion path such as internal oxide/metal interfaces, such data cannot readily be deduced by modelling and need to be obtained by experiments, e.g. by measurements of the evolution of IOZ thickness given a low P_{O_2} atmosphere for different alloys. Figure 6.1 illustrates the influence of local oxide fraction assumed within IOZ on the effective diffusivity of oxygen; oxygen solubility and diffusivity in metal and in oxide have been modelled within the current CALPHAD framework with parameters consistently being improved (see recently submitted paper [288] in Young's group which introduces binary interaction parameters for oxygen solubility/oxygen formation energy in fcc Fe-Ni); note that the flux description needs to be adjusted to account for interfacial diffusion. Prillieux and Young [289, 290] recently proposed a model describing the oxygen diffusivity within the IOZ, assuming spherical precipitates; this model can potentially be incorporated into the current modelling approach.

Grain boundary diffusion in oxides As transport in dense chromia and alumina is predominantly a grain boundary process, fundamental research is needed to model grain boundary diffusion taking into account e.g. space charge effects. Moreover, its link with lattice diffusion and its consistency with defect chemistry employed in current modelling approach needs to be addressed. Finally, the influence of (segregated) alloy solvent metal, reactive element metals and gas phase constituents also need to be studied [241].

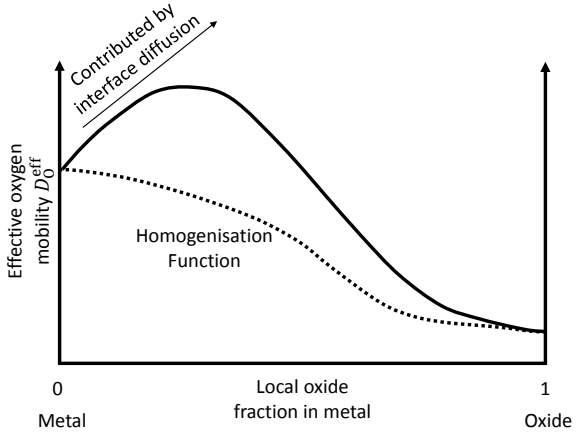


Fig. 6.1 Illustration of contribution of interface diffusion on effective oxygen mobility at the internal oxide zone (IOZ).

Nucleation As also pointed out by Young, nucleation needs to be considered for exposure at intermediate temperatures when the formation of the desired scale (at the steady-state) is difficult [241]. Either 2D or 3D simulation probably is the right way to go, although the coupling with stress field might be important as there is almost no plasticity in the oxide and the transformation stress is mainly accommodated in the metal or at the oxide/alloy interface; both have a strong influence on the diffusional behaviour.

Thermodynamic equilibrium solver One advantage arising from this piece of work – involving the storage of the whole pre-calculated starting values – is that it is potentially useful for alloy design purposes where most materials properties are defined at a fixed temperature; Gibbs-energy minimisation procedure (which is based on the Newton-Raphson scheme) can be very efficient once the starting values for a given range of compositions have been stored (it is even possible to skip the minimisation procedure for a rough calculation if a proper compositional discretisation is applied); further speed up by the interpolation scheme and parallisation is already available from this work.

6.2.3 CO_2 Oxidation of 9Cr Steel

The work reported on this topic is a good example of the research occurring in the corrosion community, which is seeing a transition from research of the empirical kind towards modelling backed up by targeted/guided experiments. Moreover, better higher-resolution characterisation such as APT plays an important role, opening a new window for studying complex phase transformation in ceramics and its interaction with metals.

The future fundamental study of CO_2 corrosion mostly requires clarification of the the transport mechanism of carbon through the oxide (which has been observed by APT in Cr_2O_3, but not yet in spinel) and its role at the oxide/alloy interface (which is phenomenologically explained by the Boudouard reaction in current work). However, as the microstructure of the spinel phase region is indeed very complex, more characterisation is needed. Figure 6.2 illustrates the microstructure in the spinel phase region based on preliminary characterisation. A trace of spinodal decomposition in spinel phase region has also been captured by ATP. No carbon in the oxide lattice/oxide grain boundary has been identified as yet, but care should be taken conducting *ex-situ* characterisation using APT due to the very small volumes analysed.

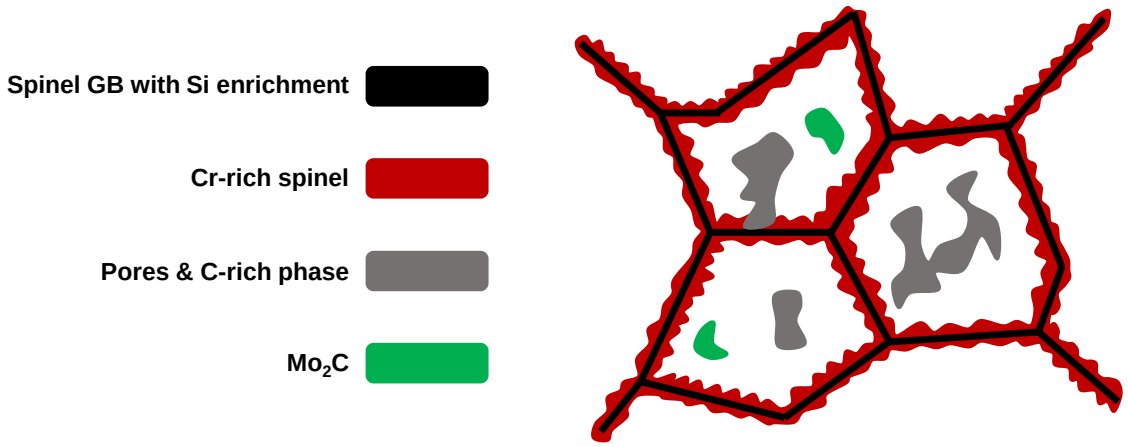


Fig. 6.2 Illustration of microstructure in spinel phase region, based on preliminary characterisation.

In terms of the modelling work, there are three main aspects required: (1) atomic-scale modelling is needed for the transport of carbon in oxide; (2) the current approach for carbon activity at the oxide/alloy interface utilises the exponential boundary condition; a more natural way would be to adapt the flux boundary conditions with their consistency with measured carbon profiles being checked carefully; (3) considering a Technology Readiness Levels (TRL) ladder shown below, the current approach needs to be incorporated/bladed into the statistical analysis which is used by industry.

- TRL 1: Observations and characterisation to inform modelling.
- TRL 2: Preliminary modelling of proposed mechanisms.
- TRL 3: Model development, testing and calibration.
- TRL 4: Proof of concept — lifetime prediction methodology (LPM).
- TRL 5: Study of sensitivity of prediction to input data and boundary conditions.
- TRL 6: Data structures and input/output to other codes.
- TRL 7: Interfacing to structural analysis codes (statistical analysis).
- TRL 8: Handover to industry.
- TRL 9: Used in anger by engineers at nuclear power plant.

The current status of the modelling is probably no greater than TRL 4.

References

[1] Michael Ashby, Hugh Shercliff, and David Cebon. *Materials: Engineering, Science, Processing and Design*. Butrworth Hinmamn, 2007.

[2] D. Tung and J. Lippold. Weld solidification behavior of Ni-base superalloys for use in advanced supercritical coal-fired power plants. In Eric S. Huron, R. C. Reed, Mark C. Hardy, Michael J. Mills, Rick E. Montero, P. D. Portella, and Jack Telesman, editors, *Superalloys 2012*, pages 563–567. John Wiley & Sons, 2012.

[3] Chester T. Sims. A contemporary view of nickel-base superalloys. *Journal of Metals*, 18(10):1119–1130, 1966.

[4] C. T. Sims and W. C. Hagel. *The Superalloys*. New York: John Wiley and Sons, 1972.

[5] C. T. Sims, N. S. Stoloff, and W. C. Hagel. *Superalloys II: High Temperature Materials for Aerospace and Industrial Power*. New York: John Wiley and Sons, 1987.

[6] L. R. Woodyatt, C. T. Sims, and Jr H. J. Beattie. Prediction of sigma-type phase occurrence from compositions in austenitic superalloys. *Transactions of the Metallurgical Society of the AIME*, 236(4):519–527, 1966.

[7] W. Betteridge and S. W. K. Shaw. Development of superalloys. *Materials Science and Technology*, 3(9):682–694, September 1987.

[8] Department for Business, Energy & Industrial Strategy, UK. Electricity: Chapter 5, Digest of United Kingdom Energy Statistics (DUKES), 2016.

[9] Wikipedia. Advanced gas-cooled reactor, 2016. [Online; accessed 03-September-2016].

[10] A. E. A. Bull and K. Hinds. Control of AGR coolant composition. Technical report, EDF Energy, 2012. Document Reference No. BEG/SPEC/ENG/BEOM/211, Rev. 002.

[11] RA Brierley and B J Handy. A survey of the oxidation induced carburisatilon of 9Cr-1Mo steel in AGR coolant atmospheres. Technical report, amec, 2007. Document Reference No. 13490/TR/001.

[12] Eleanor Laney. Report detailing the 9%Cr1%Mo samples available for analysis. Technical report, Chemistry & CO_2 Oxidation Group, EDF Energy Nuclear Generation Limited, Central Engineering Support, 2013. Document Reference No. E/REP/BPKB/0117/AGR/13.

[13] Roger C. Reed. *The Superalloys: Fundamentals and Applications*. Cambridge University Press, 2006.

[14] Atsushi Sato. *Nickel-based single crystal superalloys for industrial gas turbines*. PhD thesis, The University of Birmingham, 2011.

[15] Paraskevas Kontis. *A Study on the Effect of Grain Boundary Elements on Polycrystalline Superalloys*. PhD thesis, University of Oxford, 2016.

[16] Sakalawalli Acharige Mudith Karunaratne. *Diffusional Phenomena In Nickel Base Superalloys*. PhD thesis, Cambridge University, 2000.

[17] M. F. Ashby. Physical modelling of materials problems. *Materials Science and Technology*, 8(2):102–111, 1992.

[18] Aaron Oaks. Development of generalized KMC code to study defect mobility in ceramic materials towards nuclear fuel applications. Technical report, University of Illinois Urbana-Champaign, 2010.

[19] P.J. Spencer. A brief history of CALPHAD. *Calphad*, 32(1):1–8, 2008.

[20] Otto Redlich and A. T. Kister. Algebraic representation of thermodynamic properties and the classification of solutions. *Industrial & Engineering Chemistry*, 40(2):345–348, 1948.

[21] Mats Hillert. *Phase equilibria, phase diagrams and phase transformations: their thermodynamic basis*. Cambridge University Press, 2007.

[22] Hans Leo Lukas, Suzana G. Fries, and Bo Sundman. *Computational Thermodynamics: The CALPHAD Method*. Cambridge University Press, 2007.

[23] Mats Hillert. The compound energy formalism. *Journal of Alloys and Compounds*, 320(2):161–176, 2001.

[24] Gerhard Inden. Determination of chemical and magnetic interchange energies in BCC alloys II. Applications to non-magnetic alloys. *Z. Metallkd*, 66:577–581, 1975.

[25] Mats Hillert and Magnus Jarl. A model for alloying in ferromagnetic metals. *Calphad*, 2(3):227–238, 1978.

[26] Bo Jansson. Computer operated methods for equilibrium calculations and evaulation of thermochemical model parameters. Technical report, The Royal Institute of Technology (KTH), 1984.

[27] J-O Andersson, Thomas Helander, Lars Höglund, Pingfang Shi, and Bo Sundman. Thermo-Calc & DICTRA, computational tools for materials science. *Calphad*, 26(2):273–312, 2002.

[28] Bo Sundman, Ursula R. Kattner, Christophe Sigli, Matthias Stratmann, Romain Le Tellier, Mauro Palumbo, and Suzana G. Fries. The OpenCalphad thermodynamic software interface. *Computational Materials Science*, 125(Supplement C):188–196, 2016.

[29] S.-L. Chen, S. Daniel, F. Zhang, Y.A. Chang, X.-Y. Yan, F.-Y. Xie, R. Schmid-Fetzer, and W.A. Oates. The PANDAT software package and its applications. *Calphad*, 26(2):175–188, 2002.

[30] E. Schrödinger. An undulatory theory of the mechanics of atoms and molecules. *Phys. Rev.*, 28:1049–1070, Dec 1926.

[31] M. Born and R. Oppenheimer. Zur quantentheorie der molekeln. *Annalen der Physik*, 389(20):457–484, 1927.

[32] P. Hohenberg and W. Kohn. Inhomogeneous electron gas. *Phys. Rev.*, 136:B864–B871, Nov 1964.

[33] W. Kohn and L. J. Sham. Self-consistent equations including exchange and correlation effects. *Phys. Rev.*, 140:A1133–A1138, Nov 1965.

[34] John P. Perdew, Adrienn Ruzsinszky, Jianmin Tao, Viktor N. Staroverov, Gustavo E. Scuseria, and GÃ¡bor I. Csonka. Prescription for the design and selection of density functional approximations: More constraint satisfaction with fewer fits. *The Journal of Chemical Physics*, 123(6), 2005.

[35] D. M. Ceperley and B. J. Alder. Ground state of the electron gas by a stochastic method. *Phys. Rev. Lett.*, 45:566–569, Aug 1980.

[36] J. P. Perdew and Alex Zunger. Self-interaction correction to density-functional approximations for many-electron systems. *Phys. Rev. B*, 23:5048–5079, May 1981.

[37] John P. Perdew, Kieron Burke, and Matthias Ernzerhof. Generalized gradient approximation made simple. *Phys. Rev. Lett.*, 77:3865–3868, Oct 1996.

[38] John P. Perdew and Yue Wang. Accurate and simple analytic representation of the electron-gas correlation energy. *Phys. Rev. B*, 45:13244–13249, Jun 1992.

[39] Stewart J Clark, Matthew D Segall, Chris J Pickard, Phil J Hasnip, Matt IJ Probert, Keith Refson, and Mike C Payne. First principles methods using CASTEP. *Zeitschrift für Kristallographie-Crystalline Materials*, 220(5/6):567–570, 2005.

[40] G. Kresse and J. Furthmüller. Efficiency of ab-initio total energy calculations for metals and semiconductors using a plane-wave basis set. *Computational Materials Science*, 6(1):15–50, 1996.

[41] G. Kresse and J. Furthmüller. Efficient iterative schemes for *ab initio* total-energy calculations using a plane-wave basis set. *Phys. Rev. B*, 54:11169–11186, Oct 1996.

[42] Paolo Giannozzi, Stefano Baroni, Nicola Bonini, Matteo Calandra, Roberto Car, Carlo Cavazzoni, Davide Ceresoli, Guido L Chiarotti, Matteo Cococcioni, Ismaila Dabo, Andrea Dal Corso, Stefano de Gironcoli, Stefano Fabris, Guido Fratesi, Ralph Gebauer, Uwe Gerstmann, Christos Gougoussis, Anton Kokalj, Michele Lazzeri, Layla Martin-Samos, Nicola Marzari, Francesco Mauri, Riccardo Mazzarello, Stefano Paolini, Alfredo Pasquarello, Lorenzo Paulatto, Carlo Sbraccia, Sandro Scandolo, Gabriele Sclauzero, Ari P Seitsonen, Alexander Smogunov, Paolo Umari, and Renata M Wentzcovitch. QUANTUM ESPRESSO: a modular and open-source software project for quantum simulations of materials. *Journal of Physics: Condensed Matter*, 21(39):395502, 2009.

[43] Y Wang, J J Wang, H Zhang, V R Manga, S L Shang, L-Q Chen, and Z-K Liu. A first-principles approach to finite temperature elastic constants. *Journal of Physics: Condensed Matter*, 22(22):225404, 2010.

[44] F. Körmann, B. Grabowski, A.V. Ruban, T. Hickel, Y. Gong, R.C. Reed, and J. Neugebauer. Finite-temperature stacking-fault Gibbs energies in Al, Cu, and Ni. *Phys. Rev. B*, 2017.

[45] D.J. Crudden, A. Mottura, N. Warnken, B. Raeisinia, and R.C. Reed. Modelling of the influence of alloy composition on flow stress in high-strength nickel-based superalloys. *Acta Materialia*, 75:356 – 370, 2014.

[46] C. Woodward. First-principles simulations of dislocation cores. *Materials Science and Engineering: A*, 400–401:59–67, 2005. Dislocations 2004–An International Conference on the Fundamentals of Plastic Deformation.

[47] Xi Zhang, Blazej Grabowski, Fritz Körmann, Christoph Freysoldt, and Jörg Neugebauer. Accurate electronic free energies of the $3d, 4d$, and $5d$ transition metals at high temperatures. *Phys. Rev. B*, 95:165126, Apr 2017.

[48] Daan Frenkel and Berend Smit. *Understanding Molecular Simulation: From Algorithms to Applications*. Academic Press, San Diego, second edition, 2002.

[49] A. Einstein. Die plancksche theorie der strahlung und die theorie der spezifischen wärme. *Annalen der Physik*, 327(1):180–190, 1906.

[50] Mauro Palumbo, Suzana G Fries, Andrea Dal Corso, Fritz Körmann, Tilmann Hickel, and Jörg Neugebauer. Reliability evaluation of thermophysical properties from first-principles calculations. *Journal of Physics: Condensed Matter*, 26(33):335401, 2014.

[51] Max Born. *Dynamik der Kristallgitter*. Leipzig / Berlin, 1915.

[52] Max Born and Kun Huang. *Dynamical Theory of Crystal Lattices*. Oxford University Press, 1954.

[53] Duane C. Wallace. *Thermodynamics of Crystals*. Dover Publications, 1998.

[54] K. Parlinski, Z. Q. Li, and Y. Kawazoe. First-principles determination of the soft mode in cubic ZrO_2. *Physical Review Letters*, 78:4063–4066, May 1997.

[55] Blazej Grabowski. *Towards ab initio assisted materials design: DFT based thermodynamics up to the melting point*. PhD thesis, University of Paderborn, Paderborn, Germany, 2009.

[56] Atsushi Togo and Isao Tanaka. First principles phonon calculations in materials science. *Scripta Materialia*, 108:1–5, Nov 2015.

[57] Fei Zhou, Weston Nielson, Yi Xia, and Vidvuds Ozoliņš. Lattice anharmonicity and thermal conductivity from compressive sensing of first-principles calculations. *Phys. Rev. Lett.*, 113:185501, Oct 2014.

[58] Yue Chen, Xinyuan Ai, and C. A. Marianetti. First-principles approach to nonlinear lattice dynamics: Anomalous spectra in PbTe. *Phys. Rev. Lett.*, 113:105501, Sep 2014.

[59] D. Alfè, G. D. Price, and M. J. Gillan. Thermodynamics of hexagonal-close-packed iron under earth's core conditions. *Phys. Rev. B*, 64:045123, Jul 2001.

[60] G J Ackland. Calculation of free energies from *ab initio* calculation. *Journal of Physics: Condensed Matter*, 14(11):2975, 2002.

[61] Lars Ismer. *First principles based thermodynamic stability analysis of the secondary structure of proteins*. PhD thesis, Universität Paderborn, 2008.

[62] B. Grabowski, L. Ismer, T. Hickel, and J. Neugebauer. *Ab initio* up to the melting point: Anharmonicity and vacancies in aluminum. *Phys. Rev. B*, 79:134106, Apr 2009.

[63] Murray S. Daw and M. I. Baskes. Semiempirical, quantum mechanical calculation of hydrogen embrittlement in metals. *Phys. Rev. Lett.*, 50:1285–1288, Apr 1983.

[64] M. I. Baskes. Application of the embedded-atom method to covalent materials: A semiempirical potential for silicon. *Phys. Rev. Lett.*, 59:2666–2669, Dec 1987.

[65] M. I. Baskes, J. S. Nelson, and A. F. Wright. Semiempirical modified embedded-atom potentials for silicon and germanium. *Phys. Rev. B*, 40:6085–6100, Sep 1989.

[66] Byeong-Joo Lee, M.I. Baskes, Hanchul Kim, and Yang Koo Cho. Second nearest-neighbor modified embedded atom method potentials for bcc transition metals. *Phys. Rev. B*, 64:184102, Oct 2001.

[67] Andrew Ian Duff, Theresa Davey, Dominique Korbmacher, Albert Glensk, Blazej Grabowski, Jörg Neugebauer, and Michael W. Finnis. Improved method of calculating *ab initio* high-temperature thermodynamic properties with application to ZrC. *Phys. Rev. B*, 91:214311, Jun 2015.

[68] N. David Mermin. Thermal properties of the inhomogeneous electron gas. *Phys. Rev.*, 137:A1441–A1443, Mar 1965.

[69] G. Kresse and D. Joubert. From ultrasoft pseudopotentials to the projector augmented-wave method. *Phys. Rev. B*, 59:1758–1775, Jan 1999.

[70] N. W. Ashcroft and N. D. Mermin. *Solid State Physics*, chapter The Sommerfeld Theory of Metals, pages 29–56. Harcourt College Publishers, 1976.

[71] M. Methfessel and A. T. Paxton. High-precision sampling for brillouin-zone integration in metals. *Phys. Rev. B*, 40:3616–3621, Aug 1989.

[72] Adolf Fick. Ueber diffusion. *Annalen der Physik*, 170(1):59–86, 1855.

[73] Torsten Teorell. Studies on the "diffusion effect" upon ionic distribution. some theoretical considerations. *Proceedings of the National Academy of Sciences of the United States of America*, 21(3):152–161, March 1935.

[74] A. Einstein. Über die von der molekularkinetischen theorie der wärme geforderte bewegung von in ruhenden flüssigkeiten suspendierten teilchen. *Annalen der Physik*, 322(8):549–560, 1905.

[75] Lars Onsager. Reciprocal relations in irreversible processes. I. *Phys. Rev.*, 37:405–426, Feb 1931.

[76] Lars Onsager. Reciprocal relations in irreversible processes. II. *Phys. Rev.*, 38:2265–2279, Dec 1931.

[77] John Ågren. Diffusion in phases with several components and sublattices. *Journal of Physics and Chemistry of Solids*, 43(5):421–430, 1982.

[78] Jan-Olof Andersson and John Ågren. Models for numerical treatment of multicomponent diffusion in simple phases. *Journal of Applied Physics*, 72(4):1350–1355, 1992.

[79] Henry Eyring. The activated complex in chemical reactions. *The Journal of Chemical Physics*, 3(2):107–115, 1935.

[80] Carl Wagner. Beitrag zur theorie des anlaufvorgangs. *Z. Phys. Chem. B*, 21:25–41, 1933.

[81] Carl Wagner. Equations for transport in solid oxides and sulfides of transition metals. *Progress in Solid State Chemistry*, 10:3–16, 1975.

[82] Per Kofstad. *High Temperature Corrosion*. Elsevier Applied Science, 1988.

[83] Per Kofstad and Truls Norby. *Defects and transport in cryscrystal solids*. University of OSLO, 2007.

[84] Ferdinand Anne Kröger and FA Kröger. *The chemistry of imperfect crystals*. North-Holland Amsterdam, 1964.

[85] Neil Birks, Gerald H. Meier, and Frederick S. Pettit. *Introduction to the High-Temperature Oxidation of Metals*. Cambridge University Press, 2nd edition, 2006.

[86] Reza Naraghi, Lars Höglund, and John Ågren. Application of compound energy formalism to the parabolic growth of solid metal oxides, June 2014.

[87] Per Kofstad. Defect in inorganic compounds. In *High Temperature Corrosion*, chapter 2, pages 26–60. Elsevier Applied Science, 1988.

[88] Samuel Hallström, Lars Höglund, and John Ågren. Modeling of diffusion in wustite and simulation of oxidation of iron at 600 °C. In Pentti Karjalainen and Staffan Hertzman, editors, *6th European Stainless Steel Conference*, pages 273–278, 2008.

[89] Samuel Hallström, Lars Höglund, and John Ågren. Modeling of iron diffusion in the iron oxides magnetite and hematite with variable stoichiometry. *Acta Materialia*, 59(1):53–60, 2011.

[90] Samuel Hallström, Mats Halvarsson, Lars Höglund, Torbjörn Jonsson, and John Ågren. High temperature oxidation of chromium: Kinetic modeling and microstructural investigation. *Solid State Ionics*, 240(0):41–50, 2013.

[91] Henrik Larsson, Torbjörn Jonsson, Reza Naraghi, Yilun Gong, Roger C Reed, and John Ågren. Oxidation of iron at 600 °C – experiments and simulations. *Materials and Corrosion*, 68(2):133–142, 2017.

[92] Ken Dill and Sarina Bromberg. *Molecular driving forces: statistical thermodynamics in biology, chemistry, physics, and nanoscience*. Garland Science, second edition, 2010.

[93] N.L. Peterson, W.K. Chen, and D. Wolf. Correlation and isotope effects for cation diffusion in magnetite. *Journal of Physics and Chemistry of Solids*, 41(7):709–719, 1980.

[94] Samuel Hallström. *On high temperature oxidation resistance: Towards the materials genome of high temperature alloys*. PhD thesis, KTH Royal Institute of Technology, 2014.

[95] Arthur H. Heuer, Maryam Zahiri Azar, Hannes Guhl, Matthew Foulkes, Brian Gleeson, Tsubasa Nakagawa, Yuichi Ikuhara, and Mike W. Finnis. The band structure of polycrystalline Al_2O_3 and its influence on transport phenomena. *Journal of the American Ceramic Society*, 99(3):733–747, 2016.

[96] A.H. Heuer and M. Zahiri Azar. A disconnection mechanism of enhanced grain boundary diffusion in Al_2O_3. *Scripta Materialia*, 102:15–18, jun 2015.

[97] A.H. Heuer, T. Nakagawa, M.Z. Azar, D.B. Hovis, J.L. Smialek, B. Gleeson, N.D.M. Hine, H. Guhl, H.-S. Lee, P. Tangney, W.M.C. Foulkes, and M.W. Finnis. On the growth of Al_2O_3 scales. *Acta Materialia*, 61(18):6670–6683, 2013.

[98] Arthur H. Heuer, David B. Hovis, James L. Smialek, and Brian Gleeson. Alumina scale formation: A new perspective. *Journal of the American Ceramic Society*, 94:s146–s153, 2011.

[99] A. Atkinson and R. I. Taylor. The diffusion of ^{63}Ni along grain boundaries in nickel oxide. *Philosophical Magazine A*, 43(4):979–998, 1981.

[100] Benjamin Berkels, Andreas Rätz, Martin Rumpf, and Axel Voigt. Identification of grain boundary contours at atomic scale. In Fiorella Sgallari, Almerico Murli, and Nikos Paragios, editors, *Scale Space and Variational Methods in Computer Vision*, volume 4485 of *Lecture Notes in Computer Science*, pages 765–776. Springer Berlin Heidelberg, 2007.

[101] Theodoros Karakasidis and Madeleine Meyer. Grain-boundary diffusion of cation vacancies in nickel oxide: A molecular-dynamics study. *Phys. Rev. B*, 55:13853–13864, May 1997.

[102] Yinkai Lei, Yu Gong, Zhiyao Duan, and Guofeng Wang. Density functional calculation of activation energies for lattice and grain boundary diffusion in alumina. *Phys. Rev. B*, 87:214105, Jun 2013.

[103] A G Van Der Geest, M M Islam, T Couvant, and B Diawara. Energy ordering of grain boundaries in Cr_2O_3 : insights from theory. *Journal of Physics: Condensed Matter*, 25(48):485005, 2013.

[104] Alain Chartier, Bogdan Golovchuk, Stéphane Gossé, and Laurent Van Brutzel. Disordering and grain boundaries of (Ni,Fe)Cr_2O_4 spinels from atomistic calculations. *The Journal of Chemical Physics*, 139(13):134702, 2013.

[105] A. F. Acton and M. Bevis. The geometry of coincidence-site lattices. *Acta Crystallographica Section A*, 27(2):175–179, Mar 1971.

[106] H. Grimmer, W. Bollmann, and D. H. Warrington. Coincidence-site lattices and complete pattern-shift in cubic crystals. *Acta Crystallographica Section A*, 30(2):197–207, Mar 1974.

[107] A.M. Meirmanov. *The Stefan Problem*, volume 3. Walter De Gruyter Inc, 1992.

[108] John Ågren. Numerical treatment of diffusional reactions in multicomponent alloys. *Journal of Physics and Chemistry of Solids*, 43(4):385–391, 1982.

[109] William D Murray and Fred Landis. Numerical and machine solutions of transient heat-conduction problems involving melting or freezing. *ASME Journal of Heat Transfer*, 81:106–112, 1959.

[110] Sabine Crusius, Gerhard Inden, Ursula Knoop, Lars Höglund, and John Ågren. On the numerical treatment of moving boundary problems. *Zeitschrift für Metallkunde*, 83(9):673–678, 1992.

[111] N. Matan, H.M.A. Winand, P. Carter, M. Karunaratne, P.D. Bogdanoff, and R.C. Reed. A coupled thermodynamic/kinetic model for diffusional processes in superalloys. *Acta Materialia*, 46(13):4587–4600, 1998.

[112] H. Larsson and R.C. Reed. On the numerical simulation of diffusion-controlled reactions under local equilibrium conditions. *Acta Materialia*, 56(15):3754–3760, 2008.

[113] Henrik Larsson, Henrik Strandlund, and Mats Hillert. Unified treatment of Kirkendall shift and migration of phase interfaces. *Acta Materialia*, 54(4):945–951, 2006.

[114] Henrik Larsson and Annika Borgenstam. Trans-interface diffusivity in the Fe-Ni system. *Scripta Materialia*, 56(1):61–64, 2007.

[115] Henrik Larsson. A model for 1D multiphase moving phase boundary simulations under local equilibrium conditions. *Calphad*, 47(0):1–8, 2014.

[116] H. S. Carslaw and J. C. Jaeger. *Conduction of Heat In Solids*. Oxford Science Publications, 1959.

[117] Michel Rappaz, Michel Bellet, and Michel Deville. *Numerical Modeling in Materials Science and Engineering*. Springer Berlin Heidelberg, 2003.

[118] S.D. Conte and C.W.D. Boor. *Elementary numerical analysis: an algorithmic approach*. McGraw-Hill Higher Education, 1980.

[119] Henrik Larsson. Implementation of a model for 1D multicomponent, multiphase diffusion process simulations. Technical report, The Royal Institute of Technology (KTH), 2006. ISRN KTH/MSE–06/74–SE+METO/FOU.

[120] Henrik Larsson and Magnus Jansson. Rate of change at equilibrium. *Calphad*, 51:220–223, 2015.

[121] A. Glensk, B. Grabowski, T. Hickel, and J. Neugebauer. Breakdown of the arrhenius law in describing vacancy formation energies: The importance of local anharmonicity revealed by *Ab initio* thermodynamics. *Phys. Rev. X*, 4:011018, Feb 2014.

[122] Michot, G. and Deviot, B. Influence de l'oxydation sur la trempe des lacunes dans le nickel–durcissement du a la trempe. *Rev. Phys. Appl. (Paris)*, 12(12):1815–1817, 1977.

[123] Heinz-Peter Scholz. *Messungen der absoluten leerstellenkonzentration in nickel und geordneten intermetallischen nickel-legierungen mit einem differentialdilatometer*. PhD thesis, University of Göttingen, 2001.

[124] Wolfram Wycisk and Monika Feller-Kniepmeier. Quenching experiments in high purity Ni. *Journal of Nuclear Materials*, 69:616–619, 1978.

[125] Arnaud Metsue, Abdelali Oudriss, Jamaa Bouhattate, and Xavier Feaugas. Contribution of the entropy on the thermodynamic equilibrium of vacancies in nickel. *The Journal of Chemical Physics*, 140(10), 2014.

[126] R. Nazarov, T. Hickel, and J. Neugebauer. Vacancy formation energies in fcc metals: Influence of exchange-correlation functionals and correction schemes. *Phys. Rev. B*, 85:144118, Apr 2012.

[127] Z. Zhu, H. Basoalto, N. Warnken, and R.C. Reed. A model for the creep deformation behaviour of nickel-based single crystal superalloys. *Acta Materialia*, 60(12):4888–4900, 2012.

[128] M. Kolbe. The high temperature decrease of the critical resolved shear stress in nickel-base superalloys. *Materials Science and Engineering: A*, 319:383 – 387, 2001.

[129] L. Kovarik, R.R. Unocic, Ju Li, P. Sarosi, C. Shen, Y. Wang, and M.J. Mills. Microtwinning and other shearing mechanisms at intermediate temperatures in Ni-based superalloys. *Progress in Materials Science*, 54(6):839–873, 2009.

[130] D. Barba, E. Alabort, S. Pedrazzini, D.M. Collins, A.J. Wilkinson, P.A.J. Bagot, M.P. Moody, C. Atkinson, A. Jérusalem, and R.C. Reed. On the microtwinning mechanism in a single crystal superalloy. *Acta Materialia*, 135:314–329, 2017.

[131] F Seitz. On the porosity observed in the kirkendall effect. *Acta Metallurgica*, 1(3):355–369, 1953.

[132] Carl Wagner. Passivity and inhibition during the oxidation of metals at elevated temperatures. *Corrosion Science*, 5(11):751–764, 1965.

[133] D.R. Clarke, , and C.G. Levi. Materials design for the next generation thermal barrier coatings. *Annual Review of Materials Research*, 33(1):383–417, aug 2003.

[134] C.M.F. Rae and R.C. Reed. The precipitation of topologically close-packed phases in rhenium-containing superalloys. *Acta Materialia*, 49(19):4113–4125, nov 2001.

[135] B. Grabowski, P. Söderlind, T. Hickel, and J. Neugebauer. Temperature-driven phase transitions from first principles including all relevant excitations: The fcc-to-bcc transition in Ca. *Phys. Rev. B*, 84:214107, Dec 2011.

[136] George H. Vineyard. Frequency factors and isotope effects in solid state rate processes. *Journal of Physics and Chemistry of Solids*, 3(1):121–127, 1957.

[137] M. Mantina, Y. Wang, R. Arroyave, L. Q. Chen, Z. K. Liu, and C. Wolverton. First-principles calculation of self-diffusion coefficients. *Phys. Rev. Lett.*, 100:215901, May 2008.

[138] J. Wolff, M. Franz, J.-E. Kluin, and D. Schmid. Vacancy formation in nickel and α-nickel-carbon alloy. *Acta Materialia*, 45(11):4759 – 4764, 1997.

[139] P. Ehrhart. *Atomic Defects in Metals*, volume 25, chapter Atomic Defects in Metals · Ni, pages 242–250. Springer-Verlag Berlin Heidelberg, 1991.

[140] W. Wycisk and M. Feller-Kniepmeier. Quenching experiments on high-purity nickel. *physica status solidi (a)*, 37(1):183–191, 1976.

[141] AA Mamalui, TD Ositinskaya, VA Pervakov, and VI Khotkevich. Determination of the energy of formation of vacancies in nickel by the technique of quenching in liquid helium II. *Soviet Physics Solid State*, 10(9), 1969.

[142] G Dlubek, O Brummer, N Meyendorf, P Hautojarvi, A Vehanen, and J Yli-Kauppila. Impurity-induced vacancy clustering in cold-worked nickel. *Journal of Physics F: Metal Physics*, 9(10):1961, 1979.

[143] S Nanao, K Kuribayashi, S Tanigawa, and M Doyama. Studies of defects at thermal equilibrium and melting in Cu and Ni by positron annihilation. *Journal of Physics F: Metal Physics*, 7(8):1403, 1977.

[144] J L Campbell, C S Schulte, and J A Jackman. Temperature dependence of positron trapping in silver and nickel. *Journal of Physics F: Metal Physics*, 7(10):1985, 1977.

[145] H. Matter, J. Winter, and W. Triftshäuser. Phase transformations and vacancy formation energies of transition metals by positron annihilation. *Applied physics*, 20(2):135–140, 1979.

[146] K. Maier, M. Peo, B. Saile, H. E. Schaefer, and A. Seeger. High-temperature positron annihilation and vacancy formation in refractory metals. *Philosophical Magazine A*, 40(5):701–728, 1979.

[147] K G Lynn, C L Snead Jr, and J J Hurst. Positron lifetime studies of pure Ni from 4.2 to 1700 K. *Journal of Physics F: Metal Physics*, 10(8):1753, 1980.

[148] L C Smedskjaer, M J Fluss, D G Legnini, M K Chason, and R W Siegel. The vacancy formation enthalpy in Ni determined by positron annihilation. *Journal of Physics F: Metal Physics*, 11(11):2221, 1981.

[149] H. E. Schaefer. Equilibrium defects in metals. In P. G. Coleman and S. C. Sharma, editors, *Proceedings of 6th International Conference on Positron Annihilation*, page 369. Amsterdam: North-Holland, 1982.

[150] H. E. Schaefer. Investigation of thermal equilibrium vacancies in metals by positron annihilation. *physica status solidi (a)*, 102(1):47–65, 1987.

[151] R.W. Siegel. Positron annihilation spectroscopy of defects in metals: A critical assessment and comparison with other techniques. In P. G. Coleman, S. C. Sharma, and L. M. Diana, editors, *Proceedings of 6th International Conference on Positron Annihilation*, 1982.

[152] H. Ullmaier, editor. *Atomic Defects in Metals / Atomare Fehlstellen in Metallen*, volume 25 of *Condensed Matter*. Springer-Verlag Berlin Heidelberg, 1 edition, 1991.

[153] M J Fluss, L C Smedskjaer, B Chakraborty, and M K Chason. Positron annihilation in solid and liquid Ni. *Journal of Physics F: Metal Physics*, 13(4):817, 1983.

[154] S. Yu. Glazkov. Point defect formation and thermal properties of nickel at high temperatures. *Teplofizika Vysokikh Temperatur*, 25(1):59–64, 1987.

[155] T. Troev, Ch. Angelov, and I. Mincov. Positron annihilation measurements of quenched-in defects in Ni. *Physics Letters A*, 138(1):65–68, jun 1989.

[156] P.H. Dederichs, T. Hoshino, B. Drittler, K. Abraham, and R. Zeller. Total-energy calculations for point defects in metals. *Physica B: Condensed Matter*, 172(1):203–209, 1991.

[157] T. Korhonen, M. J. Puska, and R. M. Nieminen. Vacancy-formation energies for fcc and bcc transition metals. *Phys. Rev. B*, 51:9526–9532, Apr 1995.

[158] P. A. Korzhavyi, I. A. Abrikosov, B. Johansson, A. V. Ruban, and H. L. Skriver. First-principles calculations of the vacancy formation energy in transition and noble metals. *Phys. Rev. B*, 59:11693–11703, May 1999.

[159] T Mizuno, M Asato, T Hoshino, and K Kawakami. First-principles calculations for vacancy formation energies in Ni and Fe: non-local effect beyond the LSDA and magnetism. *Journal of Magnetism and Magnetic Materials*, 226–230, Part 1:386–387, 2001. Proceedings of the International Conference on Magnetism (ICM 2000).

[160] El Hocine Megchiche, Simon Pérusin, Jean-Claude Barthelat, and Claude Mijoule. Density functional calculations of the formation and migration enthalpies of mono-vacancies in Ni: Comparison of local and nonlocal approaches. *Phys. Rev. B*, 74:064111, Aug 2006.

[161] Chelsey Z. Hargather, Shun-Li Shang, Zi-Kui Liu, and Y. Du. A first-principles study of self-diffusion coefficients of fcc Ni. *Computational Materials Science*, 86:17–23, 2014.

[162] W. M. Haynes. *CRC Handbook of Chemistry and Physics*. CRC Press, Taylor & Francis Group, Boca Raton, 2015.

[163] B. Legendre and M. Sghaier. Curie temperature of nickel. *Journal of Thermal Analysis and Calorimetry*, 105(1):141, mar 2011.

[164] Andrei V Ruban, S Khmelevskyi, Peter Mohn, and Börje Johansson. Temperature-induced longitudinal spin fluctuations in Fe and Ni. *Phys. Rev. B*, 75(5):054402, feb 2007.

[165] Fritz Körmann, Pui-Wai Ma, Sergei L Dudarev, and Jörg Neugebauer. Impact of magnetic fluctuations on lattice excitations in fcc nickel. *Journal of Physics: Condensed Matter*, 28(7):076002, jan 2016.

[166] Pui-Wai Ma and S. L. Dudarev. Constrained density functional for noncollinear magnetism. *Phys. Rev. B*, 91(5):054420, feb 2015.

[167] P. E. Blöchl. Projector augmented-wave method. *Phys. Rev. B*, 50:17953–17979, Dec 1994.

[168] P. Vinet, J. Ferrante, J. H. Rose, and J. R. Smith. Compressibility of solids. *Journal of Geophysical Research: Solid Earth*, 92(B9):9319–9325, 1987.

[169] G. Kresse, J. Furthmüller, and J. Hafner. Ab initio force constant approach to phonon dispersion relations of diamond and graphite. *EPL (Europhysics Letters)*, 32(9):729, 1995.

[170] Blazej Grabowski, Tilmann Hickel, and Jörg Neugebauer. *Ab initio* study of the thermodynamic properties of nonmagnetic elementary fcc metals: Exchange-correlation-related error bars and chemical trends. *Phys. Rev. B*, 76(2):024309, Jul 2007.

[171] Andrew Ian Duff, M.W. Finnis, Philippe Maugis, Barend J. Thijsse, and Marcel H.F. Sluiter. MEAMfit: A reference-free modified embedded atom method (RF-MEAM) energy and force-fitting code. *Computer Physics Communications*, 196:439–445, 2015.

[172] Fritz Körmann, Tilmann Hickel, and Jörg Neugebauer. Influence of magnetic excitations on the phase stability of metals and steels. *Current Opinion in Solid State and Materials Science*, 20(2):77–84, apr 2016.

[173] G. Inden. Computer calculation of the free energy contributions due to chemical and/or magnetic ordering. In *Proc. Calphad V*, pages 1–13, Düsseldorf, 1976.

[174] Duancheng Ma, Blazej Grabowski, Fritz Körmann, Jörg Neugebauer, and Dierk Raabe. *Ab initio* thermodynamics of the CoCrFeMnNi high entropy alloy: Importance of entropy contributions beyond the configurational one. *Acta Materialia*, 100:90–97, 2015.

[175] Fritz Körmann, Abed Al Hasan Breidi, Sergei L. Dudarev, Nathalie Dupin, Gautam Ghosh, Tilmann Hickel, Pavel Korzhavyi, Jorge A. Muñoz, and Ikuo Ohnuma. Lambda transitions in materials science: Recent advances in CALPHAD and first-principles modelling. *physica status solidi (b)*, 251(1):53–80, 2014.

[176] Mats Hillert and Magnus Jarl. A model for alloying in ferromagnetic metals. *Calphad*, 2(3):227–238, jan 1978.

[177] G Inden. The role of magnetism in the calculation of phase diagrams. *Physica B+C*, 103(1):82–100, jan 1981.

[178] Andrei V Ruban, Anatoly B Belonoshko, and Natalia V Skorodumova. Impact of magnetism on Fe under earth's core conditions. *Phys. Rev. B*, 87(1):014405, jan 2013.

[179] Sergii Khmelevskyi. Longitudinal integration measure in classical spin space and its application to first-principle based simulations of the high temperature magnetism of Fe and Ni. *ArXiv e-prints*, 2017.

[180] Thomas Schuler, Caroline Barouh, Maylise Nastar, and Chu-Chun Fu. Equilibrium vacancy concentration driven by undetectable impurities. *Phys. Rev. Lett.*, 115:015501, Jun 2015.

[181] Damien Connétable, Matthieu David, Aurélien Prillieux, David Young, and Daniel Monceau. Impact of the clusterization on the solubility of oxygen and vacancy concentration in nickel: A multi-scale approach. *Journal of Alloys and Compounds*, 708:1063–1072, 2017.

[182] R. Nazarov, T. Hickel, and J. Neugebauer. First-principles study of the thermodynamics of hydrogen-vacancy interaction in fcc iron. *Phys. Rev. B*, 82:224104, Dec 2010.

[183] Döme Tanguy, Yu Wang, and Damien Connétable. Stability of vacancy-hydrogen clusters in nickel from first-principles calculations. *Acta Materialia*, 78:135–143, 2014.

[184] Caroline Barouh, Thomas Schuler, Chu-Chun Fu, and Maylise Nastar. Interaction between vacancies and interstitial solutes (C, N, and O) in $\alpha-$Fe: From electronic structure to thermodynamics. *Phys. Rev. B*, 90:054112, Aug 2014.

[185] C.S. Giggins and F.S. Pettit. Oxidation of Ni-Cr alloys between 800 °C and 1200 °C. *Transactions of the Metallurgical Society of AIME*, 245(4):2495–2507, 1969.

[186] D.L. Douglass. The oxidation mechanism of dilute Ni-Cr alloys. *Corrosion Science*, 8(9):665–678, 1968.

[187] G. C. Wood and F. H. Stott. Oxidation of alloys. *Materials Science and Technology*, 3(7):519–530, 1987.

[188] Inderjeet Kaur and Wolfgang Gust. *Fundamentals of grain and interphase boundary diffusion*. Stuttgart, West Germany: Ziegler Press, 2nd edition, 1989.

[189] E.W. Hart. On the role of dislocations in bulk diffusion. *Acta Metallurgica*, 5(10):597–597, 1957.

[190] Henrik Larsson and Anders Engström. A homogenization approach to diffusion simulations applied to $\alpha+\gamma$ Fe-Cr-Ni diffusion couples. *Acta Materialia*, 54(9):2431–2439, 2006.

[191] Henrik Larsson and Lars Höglund. Multiphase diffusion simulations in 1D using the DICTRA homogenization model. *Calphad*, 33(3):495–501, 2009.

[192] M Hillert. The discrete lattice model for diffusion revisited. *Scripta Materialia*, 44(7):1095–1097, 2001.

[193] Henrik Larsson and Lars Hoglund. A scheme for more efficient usage of CALPHAD data in simulations. *Calphad*, 50:1–5, 2015.

[194] R. Pillai, T. Galiullin, A. Chyrkin, and W.J. Quadakkers. Methods to increase computational efficiency of CALPHAD-based thermodynamic and kinetic models employed in describing high temperature material degradation. *Calphad*, 53:62–71, 2016.

[195] C. Bradford Barber, David P. Dobkin, and Hannu Huhdanpaa. The Quickhull Algorithm for Convex Hulls. *ACM Transactions on Mathematical Software*, 22(4):469–483, December 1996.

[196] Jeffrey R. Taylor and Alan T. Dinsdale. A thermodynamic assessment of the Ni-O, Cr-O and Cr-Ni-O system using the ionic liquid and compound enerygy models. *Z. Metallkd.*, 81:354–366, 1990.

[197] S. Chevalier, F. Desserrey, and J. P. Larpin. Oxygen transport during the high temperature oxidation of pure nickel. *Oxidation of Metals*, 64(3):219–234, 2005.

[198] C. Dubois, C. Monty, and J. Philibert. Oxygen self-diffusion in NiO single crystals. *Philosophical Magazine A*, 46(3):419–433, 1982.

[199] C. Dubois, C. Monty, and J. Philibert. Influence of oxygen pressure on oxygen self-diffusion in NiO. *Solid State Ionics*, 12:75–78, 1984.

[200] Michael O'Keeffe and Walter J. Moore. Diffusion of oxygen in single crystals of nickel oxide. *The Journal of Physical Chemistry*, 65(8):1438–1439, 1961.

[201] M. Meyer, S. Barbezat, C. El Houch, and R. Talon. Diffusion study of oxygen implanted in nickel oxide. *J. Phys. Colloques*, 41(C6):C6–327–C6–330, 1980.

[202] J. Carrera-caño, A. Dominguez-rodriguez, R. Marquez, J. Castaing, and J. Philibert. Point defects and high-temperature creep of non-stoichiometric NaCl-type oxide single crystals I. NiO. *Philosophical Magazine A*, 46(3):397–409, 1982.

[203] A. Atkinson, A. E. Hughes, and A. Hammou. The self-diffusion of Ni in undoped and Al-doped NiO single crystals. *Philosophical Magazine A*, 43(5):1071–1091, 1981.

[204] A. Atkinson and R. I. Taylor. The self-diffusion of Ni in NiO and its relevance to the oxidation of Ni. *Journal of Materials Science*, 13(2):427–432, 1978.

[205] R. Lindner and A. Akerstro. Diffusion of nickel-63 in nickel oxide (NiO). *Discuss. Faraday Soc.*, 23:133–136, 1957.

[206] Milton L. Volpe and John Reddy. Cation self-diffusion and semiconductivity in NiO. *The Journal of Chemical Physics*, 53(3):1117–1125, 1970.

[207] Jae Shi Choi and Walter J. Moore. Diffusion of nickel in single crystals of nickel oxide. *The Journal of Physical Chemistry*, 66(7):1308–1311, 1962.

[208] Kazuo Fueki and J. Bruce Wagner. Studies of the oxidation of nickel in the temperature range of 900° to 1400 °C. *Journal of The Electrochemical Society*, 112(4):384–388, 1965.

[209] Moon Taik Shim and Walter J. Moore. Diffusion of nickel in nickel oxide. *The Journal of Chemical Physics*, 26(4):802–804, 1957.

[210] S. Mrowec and Z. Grzesik. Oxidation of nickel and transport properties of nickel oxide. *Journal of Physics and Chemistry of Solids*, 65(10):1651–1657, 2004.

[211] B. Lesage, A.M. Huntz, and P. Lacombe. Autodiffusion cationique dans l'oxyde de nickel monocristallin sous pression partielle d'oxygene voisine de la pression de dissociation de l'oxyde. *Journal of Physics and Chemistry of Solids*, 42(8):705–712, 1981.

[212] B. Lesage, A.M. Huntz, and P. Lacombe. Relation between cationic self-diffusion in nickel oxide and nickel oxidation. *Solid State Ionics*, 12:359–363, 1984.

[213] C. Greskovich. Kinetics of $NiCr_2O_4$ formation and diffusion of Cr^{3+} ions in NiO. *Journal of the American Ceramic Society*, 53(9):498–502, 1970.

[214] W.K. Chen, N.L. Peterson, and L.C. Robinson. Chromium tracer diffusion in NiO crystals. *Journal of Physics and Chemistry of Solids*, 34(4):705–709, 1973.

[215] M. S. Seltzer. Diffusion of ^{51}Cr in NiO single crystals. *Journal of The Electrochemical Society*, 118(5):802–805, 1971.

[216] A. C. S. Sabioni, A. M. Huntz, J. N. V. Souza, M. D. Martins, and F. Jomard. Diffusion of nickel in single- and polycrystalline Cr_2O_3. *Philosophical Magazine*, 88(3):391–405, 2008.

[217] A. Atkinson and R.I. Taylor. Impurity diffusion in NiO grain boundaries. *Journal of Physics and Chemistry of Solids*, 47(3):315–323, 1986.

[218] Jeffrey R. Taylor and Alan T. Dinsdale. A thermodynamic assessment of the Cr-Fe-O system. *Z. Metallkd.*, 84:335–345, 1993.

[219] Erwin Povoden, A. Nicholas Grundy, and LudwigJ. Gauckler. Thermodynamic reassessment of the Cr-O system in the framework of solid oxide fuel cell (SOFC) research. *Journal of Phase Equilibria and Diffusion*, 27(4):353–362, 2006.

[220] John J. Carey, Merid Legesse, and Michael Nolan. Low valence cation doping of bulk Cr_2O_3: Charge compensation and oxygen vacancy formation. *The Journal of Physical Chemistry C*, 120(34):19160–19174, 2016.

[221] Corinne Gray, Yinkai Lei, and Guofeng Wang. Charged vacancy diffusion in chromium oxide crystal: DFT and DFT+U predictions. *Journal of Applied Physics*, 120(21):215101, 2016.

[222] A. C. S. Sabioni, A. M. Huntz, F. Millot, and C. Monty. Self-diffusion in Cr_2O_3 III. chromium and oxygen grain-boundary diffusion in polycrystals. *Philosophical Magazine A*, 66(3):361–374, 1992.

[223] S.C. Tsai, A.M. Huntz, and C. Dolin. Growth mechanism of Cr_2O_3 scales: oxygen and chromium diffusion, oxidation kinetics and effect of yttrium. *Materials Science and Engineering: A*, 212(1):6–13, 1996.

[224] William C. Hagel. Anion diffusion in α-Cr_2O_3. *Journal of the American Ceramic Society*, 48(2):70–75, 1965.

[225] A. C. S. Sabioni, A. M. Huntz, F. Millot, and C. Monty. Self-diffusion in Cr_2O_3 II. oxygen diffusion in single crystals. *Philosophical Magazine A*, 66(3):351–360, 1992.

[226] Wayne E. King and J.H. Park. Anion grain boundary diffusion in Cr_2O_3 and Cr_2O_3-0.09 weight percent Y_2O_3. In M.H. Yoo, W.A.T. Clark, and C.L. Briant, editors, *Interfacial structure, properties and design – MRS Symposium Proceedings*, pages 193–198. Materials Research Society (MRS), Cambridge University Press, 1988.

[227] A. C. S. Sabioni, B. Lesage, A. M. Huntz, J. C. Pivin, and C. Monty. Self-diffusion in Cr_2O_3 I. chromium diffusion in single crystals. *Philosophical Magazine A*, 66(3):333–350, 1992.

[228] R. Lindner and Å. Åkerström. Selbstdiffusion und Reaktion in Oxyd- und Spinellsystemen. *Zeitschrift für Physikalische Chemie*, 6(3_4):162–177, feb 1956.

[229] W. C. Hagel and A. U. Seybolt. Cation diffusion in Cr_2O_3. *Journal of The Electrochemical Society*, 108(12):1146–1152, 1961.

[230] Kazutomo Hoshino and N. L. Peterson. Cation self-diffusion in Cr_2O_3. *Journal of the American Ceramic Society*, 66(11):c202–c203, 1983.

[231] JONG-HEE Park, WAYNE E. KING, and STEVEN J. ROTHMAN. Cation tracer diffusion in Cr_2O_3 and Cr_2O_3-0.09 wt% Y_2O_3. *Journal of the American Ceramic Society*, 70(12):880–885, 1987.

[232] Lina Kjellqvist, Malin Selleby, and Bo Sundman. Thermodynamic modelling of the Cr-Fe-Ni-O system. *Calphad*, 32(3):577–592, 2008.

[233] W.D. Kingery, D.D. Hill, and R.P. Nelson. Oxygen mobility in polycrystalline $NiCr_2O_4$ and α-Fe_2O_3. *Journal of the American Ceramic Society*, 43(9):473–475, 1960.

[234] N S Gorbunov and V I Izvekov. The investigation of diffusion in metal oxides by means of radioactive tracers. *Soviet Physics Uspekhi*, 3(5):778, 1961.

[235] R. Lindner and Å. Åkerström. Diffusion von Ni-63 in nickelspinellen. *Zeitschrift für Physikalische Chemie*, 18(5_6):303–307, dec 1958.

[236] Daniel Monceau and Bernard Pieraggi. Determination of parabolic rate constants from a local analysis of mass-gain curves. *Oxidation of Metals*, 50(5-6):477–493, 1998.

[237] H. V. Atkinson. A review of the role of short-circuit diffusion in the oxidation of nickel, chromium, and nickel-chromium alloys. *Oxidation of Metals*, 24(3):177–197, 1985.

[238] Langli Luo, Lianfeng Zou, Daniel K. Schreiber, Donald R. Baer, Stephen M. Bruemmer, Guangwen Zhou, and Chong-Min Wang. In-situ transmission electron microscopy study of surface oxidation for Ni–10Cr and Ni–20Cr alloys. *Scripta Materialia*, 114:129–132, 2016.

[239] M. Kowalski and P.J. Spencer. Thermodynamic reevaluation of the C-O, Fe-O and Ni-O systems: Remodelling of the liquid, BCC and FCC phases. *Calphad*, 19(3):229–243, 1995.

[240] World Nuclear News. UK nuclear plant gets ten-year extension, 2015. [Online; accessed 28-September-2016].

[241] David J. Young. *High Temperature Oxidation and Corrosion of Metals*. Elsevier, second edition, 2016.

[242] S. B. Newcomb and W. M. Stobbs. The initiation of breakaway oxidation of Fe-9Cr-1Mo in a high pressure CO_2 atmosphere. *Oxidation of Metals*, 26(5):431–466, 1986.

[243] Keitarou Kaya, Shigenari Hayashi, and Shigeharu Ukai. High-temperature oxidation behavior of 9Cr ferritic-steel in carbon dioxide. *ISIJ International*, 54(6):1379–1385, 2014.

[244] F. Rouillard and T. Furukawa. Corrosion of 9-12Cr ferritic-martensitic steels in high-temperature CO_2. *Corrosion Science*, 105:120–132, 2016.

[245] C. T. Fujii and R. A. Meussner. Carburization of Fe-Cr alloys during oxidation in dry carbon dioxide. *Journal of The Electrochemical Society*, 114(5):435–442, 1967.

[246] Thomas Gheno, Daniel Monceau, Jianqiang Zhang, and David J. Young. Carburisation of ferritic Fe-Cr alloys by low carbon activity gases. *Corrosion Science*, 53(9):2767–2777, 2011.

[247] F. Rouillard, G. Moine, M. Tabarant, and J.C. Ruiz. Corrosion of 9Cr steel in CO_2 at intermediate temperature II: Mechanism of carburization. *Oxidation of Metals*, 77(1-2):57–70, 2012.

[248] D. J. Young, P. Huczkowski, T. Olszewski, T. Hüttel, L. Singheiser, and W. J. Quadakkers. Non-steady state carburisation of martensitic 9-12%Cr steels in CO_2 rich gases at 550 °C. *Corrosion Science*, 88:161–169, 2014.

[249] G. B. Gibbs and L. A. Popple. Oxidation of structural-steels in CO_2 cooled reactors. *Nuclear Energy-Journal of the British Nuclear Energy Society*, 21(1):51–55, 1982.

[250] F. Rouillard, G. Moine, L. Martinelli, and J.C. Ruiz. Corrosion of 9Cr steel in CO_2 at intermediate temperature I: Mechanism of void-induced duplex oxide formation. *Oxidation of Metals*, 77(1-2):27–55, 2012.

[251] David J. Young, Thuan Dinh Nguyen, Peter Felfer, Jianqiang Zhang, and Julie M. Cairney. Penetration of protective chromia scales by carbon. *Scripta Materialia*, 77(0):29–32, 2014.

[252] K. Thompson, D. Lawrence, D.J. Larson, J.D. Olson, T.F. Kelly, and B. Gorman. In situ site-specific specimen preparation for atom probe tomography. *Ultramicroscopy*, 107:131–139, 2007.

[253] Katie L. Moore, Markus Schröder, and Chris R. M. Grovenor. *Imaging Secondary Ion Mass Spectroscopy*, pages 709–744. Wiley-VCH Verlag GmbH & Co. KGaA, 2012.

[254] E.C. Potter and G.M.W. Mann. In *Proc. 2nd Int. Congress Metallic Corros, NACE*, page 872, New York, 1963.

[255] Francis Millot and Yan Niu. Diffusion of O^{18} in Fe_3O_4: An experimental approach to study the behavior of minority defects in oxides. *Journal of Physics and Chemistry of Solids*, 58(1):63–72, 1997.

[256] G. B. Gibbs. A model for mild steel oxidation in CO_2. *Oxidation of Metals*, 7(3):173–184, 1973.

[257] J. Robertson and M. I. Manning. Criteria for formation of single layer, duplex, and breakaway scales on steels. *Materials Science and Technology*, 4(12):1064–1071, 1988.

[258] M. R. Taylor, J. M. Calvert, D. G. Lees, and D. B. Meadowcroft. The mechanism of corrosion of Fe-9%Cr alloys in carbon dioxide. *Oxidation of Metals*, 14(6):499–516, 1980.

[259] Thuan Dinh Nguyen, Jianqiang Zhang, and David J. Young. Effects of silicon on high temperature corrosion of Fe-Cr and Fe-Cr-Ni alloys in carbon dioxide. *Oxidation of Metals*, 81(5):549–574, 2014.

[260] P. C. Rowlands, D. R. Holmes, A. Whittaker, R. A. Brierley, and J. C. P. Garrett. The oxidation behaviour of Fe-9Cr-1Mo steels. In *Proceedings symposium on gas-cooled reactors today*, volume 4, pages 173–181, United Kingdom, 1983. British Nuclear Energy Society.

[261] J Fridberg, LE Torndahl, and M Hillert. Diffusion in iron. *Jernkontorets Annaler*, 153(6):263, 1969.

[262] Anders Engström, Lars Höglund, and John Ågren. Computer simulation of diffusion in multiphase systems. *Metallurgical and Materials Transactions A*, 25(6):1127–1134, 1994.

[263] Joy Sumner, Nigel Simms, Aya Shin, and Jonathan Pearson. Kinetics of duplex oxide growth on 9Cr steels exposed in CO_2: Application of dimensional metrology. *Oxidation of Metals*, 87:617–629, 2017.

[264] Reza Naraghi. *Mobility assessment of Fe-O system*. PhD thesis, KTH Royal Institute of Technology, 2017.

[265] James E. Castle and P. L. Surman. Self-diffusion of oxygen in magnetite. Effect of anion vacancy concentration and cation distribution. *The Journal of Physical Chemistry*, 73(3):632–634, 1969.

[266] F. Millot, J. C. Lorin, B. Klossa, Y. Niu, and J. R. Tarento. Oxygen self-diffusion in Fe_3O_4: An experimental example of interactions between defects. *Ber. Bunsen-Ges.*, 101(9):1351–1354, September 1997. Discussion Meeting on Solute Point Defect Interactions in Crystals, Lower Saxony, Germany, Apr 07-09, 1997.

[267] R. Dieckmann and H. Schmalzried. Defects and cation diffusion in magnetite (i). *Berichte der Bunsengesellschaft für physikalische Chemie*, 81(3):344–347, 1977.

[268] A. Atkinson, M. L. O'Dwyer, and R. I. Taylor. ^{55}Fe diffusion in magnetite crystals at 500 °C and its relevance to oxidation of iron. *Journal of Materials Science*, 18(8):2371–2379, 1983.

[269] R. Dieckmann and H. Schmalzried. Defects and cation diffusion in magnetite (vi): Point defect relaxation and correlation in cation tracer diffusion. *Berichte der Bunsengesellschaft für physikalische Chemie*, 90(7):564–575, 1986.

[270] J. Töpfer, S. Aggarwal, and R. Dieckmann. Point defects and cation tracer diffusion in $(Cr_xFe_{1-x})_{3-\delta}O_4$ spinels. *Solid State Ionics*, 81(3–4):251–266, 1995.

[271] J. Pirón Abellán, T. Olszewski, H. J. Penkalla, G. H. Meier, L. Singheiser, and W. J. Quadakkers. Scale formation mechanisms of martensitic steels in high CO_2/H_2O-containing gases simulating oxyfuel environments. *Materials at High Temperatures*, 26(1):63–72, 2009.

[272] D. J. Young and S. Watson. High-temperature corrosion in mixed gas environments. *Oxidation of Metals*, 44(1):239–264, 1995.

[273] Thuan Dinh Nguyen, Jianqiang Zhang, and David J. Young. Effects of cerium and manganese on corrosion of Fe-Cr and Fe-Cr-Ni alloys in Ar-20CO_2 and Ar-20CO_2-20H_2O gases at 650 °C. *Corrosion Science*, 100:448–465, 2015.

[274] F. Körmann. *Personal Communication*, 2016.

[275] F. Körmann, A. Dick, T. Hickel, and J. Neugebauer. Role of spin quantization in determining the thermodynamic properties of magnetic transition metals. *Phys. Rev. B*, 83:165114, Apr 2011.

[276] F Körmann, B Grabowski, P Söderlind, M Palumbo, S G Fries, T Hickel, and J Neugebauer. Thermodynamic modeling of chromium: strong and weak magnetic coupling. *Journal of Physics: Condensed Matter*, 25(42):425401, 2013.

[277] N. Sandberg, Z. Chang, L. Messina, P. Olsson, and P. Korzhavyi. Modeling of the magnetic free energy of self-diffusion in bcc Fe. *Phys. Rev. B*, 92:184102, Nov 2015.

[278] A. V. Ruban and V. I. Razumovskiy. Spin-wave method for the total energy of paramagnetic state. *Phys. Rev. B*, 85:174407, May 2012.

[279] Shun-Li Shang, Bi-Cheng Zhou, William Y. Wang, Austin J. Ross, Xuan L. Liu, Yong-Jie Hu, Hua-Zhi Fang, Yi Wang, and Zi-Kui Liu. A comprehensive first-principles study of pure elements: Vacancy formation and migration energies and self-diffusion coefficients. *Acta Materialia*, 109:128–141, 2016.

[280] Graeme Henkelman, Blas P. Uberuaga, and Hannes Jónsson. A climbing image nudged elastic band method for finding saddle points and minimum energy paths. *The Journal of Chemical Physics*, 113(22):9901–9904, 2000.

[281] Graeme Henkelman and Hannes Jónsson. Improved tangent estimate in the nudged elastic band method for finding minimum energy paths and saddle points. *The Journal of Chemical Physics*, 113(22):9978–9985, 2000.

[282] J.M. Sanchez, F. Ducastelle, and D. Gratias. Generalized cluster description of multicomponent systems. *Physica A: Statistical Mechanics and its Applications*, 128(1):334–350, 1984.

[283] Alex Zunger, S.-H. Wei, L. G. Ferreira, and James E. Bernard. Special quasirandom structures. *Phys. Rev. Lett.*, 65:353–356, Jul 1990.

[284] Liam Huber, Blazej Grabowski, Matthias Militzer, Jörg Neugebauer, and Jörg Rottler. A QM/MM approach for low-symmetry defects in metals. *Computational Materials Science*, 118:259 – 268, 2016.

[285] Liam Huber, Blazej Grabowski, Matthias Militzer, Jörg Neugebauer, and Jörg Rottler. Ab initio modelling of solute segregation energies to a general grain boundary. *Acta Materialia*, 132:138–148, jun 2017.

[286] Terrell L. Hill. Steric effects. I. Van der Waals potential energy curves. *The Journal of Chemical Physics*, 16(4):399–404, 1948.

[287] Frank Jensen. *Introduction to Computational Chemistry*. John Wiley & Sons, Inc, 3rd edition, 2017.

[288] Domingo Jullian, Jianqiang Zhang, D. Brynn Hibbert, and David J. Young. Oxygen solubility in austenitic Fe-Ni alloys at high temperatures. *submitted*, 2017.

[289] Aurelien Prillieux. *Hydrogen and water vapour effects on oxygen solubility and diffusivity in high temperature Fe-Ni alloys*. PhD thesis, University of New South Wales, 2017.

[290] Aurélien Prillieux, Domingo Jullian, Jianqiang Zhang, Daniel Monceau, and David J. Young. Internal oxidation in dry and wet conditions for oxygen permeability of Fe-Ni alloys at 1150 and 1100 °C. *Oxidation of Metals*, 87(3):273–283, Apr 2017.